COMPUTATIONAL MODELLING OF STRUCTURE–FROZEN SOIL/ICE INTERACTION

BY

UDENI G. ANURUDDHA PUSWEWALA

A Dissertation
Submitted to The University of Manitoba
in Partial Fulfillment of the Requirements
for the Degree of

DOCTOR OF PHILOSOPHY

Department of Civil Engineering
University of Manitoba
Winnipeg, Manitoba, Canada.

ISBN 0-315-76950-5

COMPUTATIONAL MODELLING OF STRUCTURE-FROZEN SOIL/ICE INTERACTION

by

UDENI G. ANURUDDHA PUSWEWALA

A thesis submitted to the Faculty of Graduate Studies of the University of Manitoba in partial fulfillment of the requirements of the degree of

DOCTOR OF PHILOSOPHY

To the memory of my father and to my mother

ACKNOWLEDGEMENTS

I am sincerely grateful to my thesis advisor Prof. R.K.N.D. Rajapakse, for suggesting the topic of the research and providing continued expert guidance up to the completion of the investigation. Encouragement and support received from Prof. Rajapakse throughout this work is greatly appreciated.

I convey my sincere thanks to Prof. L. Domaschuk and Prof. D.H. Shields for providing much assistance and many useful ideas, and for their constructive criticism. Appreciation is also extended to Prof. A.H. Shah and Prof. B. Stimpson for providing helpful comments and serving in the advisory committee. I am grateful to Prof. R. Frank for devoting his time to serve as the external examiner.

The assistance received from Mr. P. Macdonald and the staff of the Central Computing Services, in the form of computer facilities needed for the extensive numerical simulations, is much appreciated. Thanks are extended to Mr. Y.M. Desai for helping with UNIX operating system in a few instances, Mr. R.P. Lach for providing pressuremeter test data, Dr. R. Zhang for preparing a few figures for the manuscript, and all of my friends for their encouragement.

This work was made possible by the financial support received in the form of a research assistantship from the NSERC operating grant of Prof. Rajapakse, a graduate fellowship from The University of Manitoba, and a teaching assistantship from the Department of Civil Engineering, all of which I greatly appreciate.

I wish to take this opportunity to acknowledge the moral support received from my family, especially Uncle Samson, throughout my higher studies, and the influence of Prof. P. Karasudhi of The Asian Institute of Technology in developing my interest in research.

July 1991

Udeni G. Anuruddha Puswewala
Winnipeg, Canada.

TABLE OF CONTENTS

LIST OF TABLES:

LIST OF FIGURES

NOMENCLATURE

a = denotes a radius;

$\mathbf{a}$ = nodal displacement vector;

$\mathbf{a}_k$ = nodal displacement vector at time t_k;

$\mathbf{a}_{k+1}^0$ = initial guess for nodal displacement vector at time t_{k+1};

$\Delta\mathbf{a}_{k+1}^n$ = incremental correction of displacement vector at the nth iterate at time t_{k+1};

A = coefficient in power law creep equation;

A_1 = coefficient in Fish's model;

b = parameter in equation for creep of laterally loaded piles; also denotes a breadth;

$\mathbf{b}_k$ = body force at time t_k;

B = parameter in power law creep equation;

$[B]$ = matrix relating nodal dispacements to strain;

C = parameter in power law creep equation;

C_o = parameter in Fish's model;

C_1 = coefficient in equation for lateral creep displacement of piles;

C_2 = parameter in equation for lateral creep displacement of piles;

$\widetilde{C}$ = a material constant in Fish's model;

C_n = bond modulus for normal stress-relative displacement relations;

C_s = bond modulus for adfreeze strength;

$[C]$ = constitutive matrix for interface element (eq. 6.8);

d = denotes a buried depth; also clear distance between two cores;

$\dot{d}$ = denotes a rate of displacement;

d_n = relative displacement normal to bond interface;

d_s = relative displacement parallel to bond interface;

d_s^c = relative creep displacement parallel to bond interface;

$\mathbf{d}$ = vector of relative displacements at mid-plane of interface element;

$\bar{D}$ = defined by eq. 5.23b;

$[D]$ = constitutive matrix for isotropic linear elasticity;

$[\bar{D}]$ = incremental constitutive matrix in Domaschuk's model;

$[\bar{D}]^n$ = matrix defined by eq. 3.51;

e_d = resultant deviatoric strain in Domaschuk's model;

E = Young's modulus;

E_p = Young's modulus of pile material;

E_s = Young's modulus of frozen material;

$\mathbf{f}_k$ = applied force vector at time t_k;

$\Delta\mathbf{f}_k$ = increment of applied load during time Δt_k;

$F(\bar{t})$ = dimensionless shape function in Fish's model

g = parameter in creep equation for bond interface (eq. 6.4);

G = matrix defined by eq. 6.6;

G_c = Shear creep function in Domaschuk's model;

h = parameter in creep equation for bond interface (eq. 6.4);

H = coefficient in creep equation for bond interface;

I = second moment of area of a cross-section;

k = denotes time increment number;

k_w = Winkler coefficient for beams on elastic foundations;

K = a quantity defined by eq. 3.66b;

K_o = material constant in Domaschuk's model;

K_c = Bulk creep function in Domaschuk's model;

l = denotes a length of a pile (beam) element;

$[L]$ = a differential operator matrix (eq. 3.1);

m_1 = material constant in Domaschuk's model;

$[M]$ = matrix defined by eq. 6.9, 6.10;

n = denotes iterate number;

n_1 = material constant in Domaschuk's model;

$[N]$ = denotes shape function matrix;

p = denotes an applied pressure; as subscript, denotes load increment number;

P = denotes an applied load;

q = denotes an applied pressure;

$\mathbf{q}$ = vector of nodal deformations for a beam;

r = radial coordinate (cylindrical);

R = lateral ice reaction defined by eq. 5.3;

ΔR^n_{k+1} = incremental correction of lateral ice reaction at nth iterate at time t_{k+1};

s = denotes a local coordinate measure (eq. 5.13b);

s_{ij} = components of deviatoric stress tensor;

S = surface of the domain;

S_d = resultant deviatoric stress in Domaschuk's model;

$[S]^n$ = matrix obtained by differentiating strain rate vector by stress vector (eq. 3.48);

t = denotes elapsed time;

t_0 = denotes initial time; also a parameter in Fish's model (eq. 3.24);

t_k = time at the end of k time steps;

t_m = time to failure in Fish's model (eq. 3.21);

$\bar{t}$ = dimensionless time in Fish's model;

Δt_k = time increment at the $(k+1)$ th time step;

T = denotes temperature;

$\mathbf{T}_k$ = surface traction forces at time t_k;

u_r = radial displacement in cylindrical coordinates;

u_x = horizontal displacement in cartesian coordinates;

u_y = vertical displacement in cartesian coordinates;

u_z = vertical displacement in cylindrical coordinates;

$\mathbf{u}$ = displacement vector;

v, v_1, v_2 = variables used to convert governing beam equation to Galerkin's form (eq. 5.7 onwards);

V = volume of domain;

w = total lateral displacement at a point on a pile;

w_c = lateral creep displacement at a point on a pile;

x = coordinate (cartesian);

y = coordinate (cartesian);

z = vertical coordinate (cartesian or cylindrical);

α, β = material constants in Domaschuk's model;

$\boldsymbol{\alpha}$ = vector of rate of relative creep displacements at mid-plane of interface element;

$\boldsymbol{\beta}$ = strain rate vector;

γ_0 = instantaneous strain;

$\dot{\gamma}$ = steady creep displacement rate of axially loaded piles;

δ = dimensionless parameter in Fish's model;

δ_{ij} = Kronecker delta;

$\dot{\delta}$ = rate of vertical deflection of beam at mid-span;

ϵ^c = creep strain;

ϵ_{ij} = component of strain tensor;

$\dot{\epsilon}_c$ = a selected, arbitrary, value of creep strain rate;

$\dot{\epsilon}_m$ = minimum strain rate in Fish's model;

$\dot{\epsilon}_e^c$ = equivalent creep strain rate;

$\dot{\epsilon}_{ij}^c$ = component of creep strain rate tensor;

ϵ = strain vector (tensor);

ϵ^c = creep strain vector (tensor);

ϵ^e = elastic strain vector (tensor);

ϵ^p = plastic strain vector (tensor);

ϵ_k = strain vector at time k;

ϵ_k^c = creep strain vector at time t_k;

η, ζ = parameters in Fish's model;

$\dot{\eta}$ = rate of relative displacement at interface;

θ = parameter for interpolation of stress within a time interval;

ϑ = denotes an orientation angle;

κ, ϱ, ϕ, φ = parameters used in Domaschuk's model;

λ = denotes fraction of load; also used in non-dimensional parameter for beams on elastic foundations;

ν = Poisson's ratio;

ν_p = Poisson's ratio for pile material;

ν_s = Poisson's ratio for frozen material;

σ = stress;

σ_0 = instantaneous stress in Fish's model;

σ_c = a proof stress;

σ_e = equivalent stress;

σ_{ij} = component of stress tensor;

σ_n = normal stress at interface;

Chapter 1

INTRODUCTION

1.1 Preliminary

Cold regions of the world consist of the northern (or Arctic) and southern parts of the world, centered around the poles. About one-half the land area of Canada and the Soviet Union, more than 60% of Alaska, about 22% of the People's Republic of China, and large areas of northern Eurasia as well as Greenland and Antarctica can be categorized as cold climatic regions (Johnston 1981). In the northern hemisphere, the southern limit of the cold region extends approximately to the 40th parallel. Seasonal and permanently frozen ground, and large ice bodies like glaciers, ice cover over lakes, sea ice, ice islands, and ice-bergs, are common features of cold regions which require special attention of the geotechnical and civil engineer (Tsytovich 1975, Andersland and Anderson 1978, Johnston 1981). In recent times, the rapid increase in the utilization of abundant natural resources found in the the cold regions has generated much interest in frozen soil and ice engineering, and consequently, attention has been focussed on structure-frozen soil/ ice interaction problems in these environments. In these regions, a large number of structures like natural gas pipe-lines, buildings, highways, electricity transmission towers, oil rigs, artificial islands etc. had already been constructed, while many more are being scheduled for construction. Some of these structures, specially many drilling platforms, are located offshore and are based on frozen earth at the ocean bottom.

Of the two categories of frozen ground in cold regions, the first is the seasonally frozen ground, which is the top layer of soil that is subjected to alternate freezing and thawing processes every year. Known as the active layer, it has important implications to the field engineer as all infrastructural, geotechnical and various other problems concerned with the yearly freezing and thawing processes manifest in this layer. In the far north, the active layer is as shallow as 150 mm, while farther south from the North Pole, it can be as much as 3 m in thickness. The second category of frozen ground is permafrost, which is generally defined as a ground

of any kind which stays colder than the freezing temperature of water throughout several years, and is usually found, although not always, underlying the active layer. It may consist of a dry sand with no ice at all, but much of the permafrost is not only cemented by ice but interbedded with large ice masses, whose melting could bring about subsidence, erosion and structural distress. The permafrost layer is very thick in polar regions (e.g. 390 m at Resolute, NWT, Canada; 74°N), and gradually becomes thinner towards the lower latitudes, until the layer becomes first discontinuous and then fragmented at its southern boundary. Permafrost exists in some mountainous regions, and its occurrence may vary with the local topography. Due to the effect of the geothermal gradient, permafrost would not exist to an infinite depth, but will have a bottom boundary below which the soil or rock is no longer frozen. Thus, for engineering purposes, permafrost can be considered as a geological layer of finite thickness.

Geotechnical and civil engineering problems concerned with the frozen ground (and ice) can be categorized in general as: (a) those involving steady-state frozen ground or ice, where time dependent settlement of structures, freezing of buried water and other utility pipes, etc. are encountered, (b) those due to the freezing process, where problems caused by frost action are seen, and (c) those due to the the thawing process, which causes thaw settlement and weakening of the soil. Numerous complications of problems may arise due to the combined effects of two or all of above categories. Permafrost degradation (or melting), a larger scale phenomenon compared with individual cases of structure-active layer interaction, is an important geo-environmental problem in cold climates. This may be caused by climatic changes, changes of vegetation cover, building of new structures or modification of the conditions existing in the active layer in any other manner, and its consequences, such as subsidence and erosion, will continue for a long time after the initiation of such action. A considerable amount of literature is available where many aspects of geotechnical and geo-environmental problems encountered in cold regions are discussed at length (Jumikis 1966, Tsytovich 1975, Andersland and Anderson 1978, Johnston 1981, Lunardini 1981).

Some of the beneficial aspects of frozen ground are its stability and strength.

Permafrost provides excellent bearing capacity (provided thawing or excessive time-dependent settlement under load is avoided), stabilizes the ground due to the bond strength of the frozen moisture, and (sometimes artificial) ground freezing can be useful in building cofferdams, tunnelling work, and other similar activities (see, for eg: Jessberger (ed.) 1978, Frivik et al. (eds.) 1980). Ice bodies like glaciers, lake or sea ice cover, etc. provide bearing surface for many permanent and temporary structures like oil drills, roads and weather stations.

As far as geotechnical considerations of frozen soils and ice (specially its interaction with man-made structures) are concerned, study of the mechanical properties of these frozen geomaterials assumes a fundamental importance. In the ensuing sections of this Chapter, an overview of the mechanical properties of frozen soils/ice, and the experimental work as well as numerical modelling that have been conducted in this respect, are presented, as preliminaries for the objective of this thesis discussed in §1.4.

1.2 Mechanical Properties of Frozen Soils and Ice

In general, frozen soils consist of four components, i.e. soil (mineral) particles, gaseous components, frozen water and unfrozen water. Classification systems for identification of frozen soils and ice have been developed (Andersland and Anderson 1978). At lower temperatures, frozen soils are known to have a strength comparable to that of weak concrete. However, these frozen geomaterials show time dependent settlement under constant load, a characteristic known as "creep", and their mechanical properties are highly susceptible to temperature variations. Pure ice and ice with soil particle inclusions have creep and other mechanical properties very similar to those of frozen soils. A great difference in strength between frozen and unfrozen soils has been noted, which is generally attributed to the cementing action of the ice component in the frozen soil. Usually, ice deformation characteristics form the upper bound for deformation of frozen soils, while ice-poor soils with high solids concentrations may display interparticle friction and particle interlocking, or cohesion, depending on the size of the soil particles, much as in unfrozen soils.

The mechanical properties of frozen soil are sensitive to stress, strain-rate, temperature, confining pressure, particle size, particle orientation and packing, frozen and unfrozen water contents, and impurities (air bubbles, salts or organic matter) in the water-ice matrix. Similar sensitvity to ambient conditions is shown by ice, which, being in general a polycrystalline material, in addition shows a dependence of its mechanical properties on crystal and grain shapes, sizes, and orientation, as well as on the concentration of impurities (soil particles, pores etc.) contained in the ice, and its density. Dependence of mechanical and thermo-mechanical properties of frozen soils and ice on different physical and ambient factors are discussed in many texts and research/review articles (Tsytovich and Sumgin 1959, Sanger and Kapler 1963, Vyalov 1965a and 1965b, Goughnour and Andersland 1968, Sayles 1968 and 1973, Gold 1970 and 1977, Sayles and Haines 1974, Tsytovich 1975, Andersland and Anderson 1978, Assur 1980, Jessberger 1980a and 1980b, Mellor 1980, Czurda 1983, Hooke 1981, Yuanlin and Carbee 1984).

Creep of frozen soils is described macroscopically as caused by a combination of phenomena such as pressure melting of the ice due to stresses at points of contact between soil particles, movement of unfrozen water to regions of lower stress under differences of water surface tensions, refreezing of melted water, consequent breakdown of the ice and bonds with the soil grains, and readjustment of soil particles. (Andersland and Anderson 1978). Vyalov (1973) listed three basic types of deformation occurring in a mass of frozen soil under load as: mutual displacement of the mineral particles, flow of the ice and movement of the adhesive water, and the formation and development of microcracks and other structural defects. In materials like ice, because of the grain orientation, preferable planes of slip may occur, whereby creep would take place in a particular direction (along these glide planes) more easily. Attempts have been made to explain the creep process at the atomic or molecular level, where creep is described as a thermally activated process (Andersland and Akili 1967, Andersland and Douglas 1970, Assur 1980, Fish 1984) governed by the theory of rate process (Glasstone et al. 1941). According to this approach, molecular particles participating in a deformation process, termed 'flow units', are 'activated' by acquiring a sufficient amount of energy to surmount the en-

ergy barrier which separates the adjacent equilibrium positions of the units. Under no applied directed potentials, the atomic particles vibrate about their equilibrium positions and the energy barriers are crossed in all directions with equal frequency. However, an applied directed potential such as a shear stress distorts the energy barriers, and a net frequency of activation of the flow units in the direction of the applied stress is created (Mitchell et al. 1968). This results in a steady state of flow in the direction of the applied potential (stress), and can be seen as creep.

Time-dependent (creep) deformations of frozen soils/ice are generally preceded by an elastic deformation, which is usually small in comparison with the creep movements. Many studies had been conducted to evaluate elastic properties of frozen soils/ice (Gold 1977, Traetterberg et al. 1975, Tsytovich 1975, Sinha 1977, Bragg and Andersland 1982, Mellor and Cole 1983). Typical creep strain-time curves of frozen soils, observed in uniaxial compression tests, are as shown in Figure 1.1. Figure 1.1a shows variations in creep curves due to the composition of frozen soils. Figure 1.1b shows a basic creep curve, and Figure 1.1c shows the variation of strain rate with time, plotted by obtaining the time-derivative of the creep curve in Figure 1.1b. The basic creep curves in Figures 1.1b and 1.1c are applicable to ice samples as well, tested under constant uniaxial stress. It is generally accepted that the standard creep curve in Figure 1.1b consists of three parts or stages. In the first part decelerating creep takes place, and is known as the primary creep stage, or, alternately, as a strain hardening stage. Creep deformation takes place at a constant rate during the second part of the curve, which is known as the steady or secondary creep stage. The final part is the tertiary or accelerating creep stage (strain softening stage), where the rate of creep strain increases up to the point of rupture, denoted by point R in Figure 1.1b. The corresponding time-rate of creep strain is as in Figure 1.1c. The shape of the creep curve for a given material depends strongly on temperature and magnitude of stress. For low stresses, creep may occur in attenuating (decaying) manner, and the curve may never enter a secondary or tertiary stage. In other instances, the material may fail in the secondary creep stage due to excessive deformation, and not enter the tertiary stage. Entry into the tertiary creep stage automatically signifies the failure of the material through

accelerating creep deformations.

Vyalov (1963, 1965b) depicted the stress-dependence of creep deformation of frozen soils (and ice) at constant temperature as shown in Figure 1.2, and the temperature dependence of creep deformation of these materials at a constant stress as shown in Figure 1.3. It is known that the relationships between creep strain and stress, and between creep strain and temperature, are highly non-linear. Glen (1955) observed that uniaxial, constant stress compression tests on polycrystalline ice yielded an initial primary creep stage followed by a secondary creep stage. Glen (1955), Mellor and Testa (1969), etc. noted the sensitivity of strain rate to temperature. Subsequent uniaxial test programs by Mellor and Cole (1983), Sego and Morgenstern (1983), Fish (1984), Jacka (1984), etc. have contributed much to the understanding of the behaviour of ice. Among the main features noted were the momentary development of a minimum creep strain rate under constant stress tests, and a similar development of a maximum stress under constant strain rate tests, as schematically depicted in Figures 1.4a and 1.4b. Experimental programs have also been conducted using step-wise increasing stresses (Andersland and Akili 1967, Eckardt 1979, Fish 1981).

Based on one dimensional long-term creep tests on frozen soils, Vyalov (1963) reported that the lower the stress, the longer is the time to reach failure. This observation is depicted in Figure 1.5, where the curve had been obtained by plotting the failure loads versus the time to failure. In Figure 1.5, σ_o is the momentary compressive failure stress, σ_∞ is the ultimate, continuous strength, and ordinate at any point, $\sigma(t)$, is the long-term strength or resistance to failure for a given load duration. If the applied stress does not exceed σ_∞, the material will not fail for any unlimited duration of time. Hooke (1981) discussed long-term uniaxial testing (e.g. Kamb 1972) of ice, and suggested the possibility that strain softening of ice in the tertiary creep stage (which occurs due to recrystallization) may not continue indefinitely, or that it may alternate with a strain hardening process. Investigations on tensile strength properties of frozen soils/ice are also reported in the literature (eg: Bragg and Andersland 1982, Jessberger 1980a).

Among different types of multi-axial tests conducted on frozen soils and ice are triaxial tests (Sayles 1968 and 1973, Andersland and Alnouri 1970, Chamberlain et al. 1972, Domaschuk et al. 1985, Domaschuk et al. 1991), pressuremeter tests (Ladanyi and Johnston 1973, Kjartanson et al. 1988, Murat et al. 1989, Shields et al. 1989), plate tests (Lach 1989), penetration of rigid bodies into ice (Domaschuk et al. 1989), and model pile tests (Parameswaran 1979). Results obtained from these multi-axial testing programs have in general been in agreement with the findings from uniaxial tests. Figure 1.6, taken from Kjartanson et al. 1988, and Figure 1.7, taken from Shields et al. (1989), show the behaviour of polycrystalline ice under pressuremeter testing; both these figures are in agreement with the uniaxial behaviour of ice depicted in Figure 1.4a. In many field tests, emphasis had generally been placed on investigating the performance of particular foundation elements in permafrost; examples are the tests for performance of vertically and laterally loaded piles (Rowley et al. 1973), rod anchors (Johnston and Ladanyi 1972), and penetration tests (Ladanyi 1976). Effect of mean normal pressure on frozen soil/ice deformations had also been investigated (Vyalov 1963 and 1965b, Chamberlain et al. 1972, Domaschuk et al. 1991). Figure 1.8 (after Vyalov 1965b), depicts the hypothesized shape of stress curves (in the octahedral shear stress-strain space) for different durations of load and different mean normal stresses.

Among other factors affecting the mechanical properties of frozen soils and ice are the particular geological and freezing processes by which permafrost/ice was created, and micro-cracking (Gold 1966, Fish and Sayles 1981) and healing of cracks. In addition, factors like freezing effects and frost heave (Penner 1970, Yong and Osler 1971, Czurda 1983), thaw consolidation (Nixon and McRoberts 1973), and adfreeze strengths (Parameswaran 1978 and 1981, Alwahhab 1983, Soo 1983) may have a direct influence on soil-structure interaction problems, depending on the situation.

As in the case of any other material, stress-deformation relations become paramount in engineering analyses of frozen media, since tests cannot be performed to simulate each and every situation which involves deformation of such media. In a practical sense, the need for constitutive relations for frozen soils/ ice arises in

the case of predicting settlements of structures founded on permafrost and ice. At the design and construction stages of any structure, measures should be taken to ensure that the creep settlement during its service life will not exceed the allowable service limit. Using the test data collected over the past many years, many researchers had proposed constitutive relations to describe certain classes of deformation phenomena observed in frozen geomaterials. The multiple complexity of frozen soils, and the high sensitivity of frozen soils/ice to ambient conditions, stress magnitudes and stress/strain rates etc. had presented innumerable obstacles to the process of developing a general stress-strain relationship applicable over all stress and temperature ranges. As a result, there is no single constitutive relation that can be universally applied to describe the observed creep behaviour of frozen soils and ice over all ranges of stress, strain, temperature, and other relevant parameters, although many constitutive models exist to describe the creep process under several specified constraints. Some of these constitutive relations are discussed in Chapter 2.

1.3 Review of Numerical Analysis of Structure-Frozen Soil/Ice Interaction

A very important role of numerical analysis of structure-frozen soil/ice interaction is the prediction of creep settlements of various foundation elements. Constitutive models for creep of frozen soils/ice (Chapter 2) are pertinent in this regard. In view of the non-linearity of the material models and the complicated geometry involved in these interaction problems, the Finite Element Method (Zienkiewicz 1977, Owen and Hinton 1980, for example) is undisputably a very versatile and powerful technique that can be applied to the solution of such boundary-value problems. In the literature, there are several previous occasions where numerical analyses of structure-frozen soil/ ice interaction have been performed.

Klein (1979) used the Finite Element Method (FEM) to apply the generalized power law creep model (see §2.1, §3.3.1) to solve a problem involving a tunnel made of frozen earth. Plane stress/strain formulations were used in a FE program based on successive elastic solutions (Greenbaum and Rubinstein 1968). Klein and

Jessberger (1979) applied the same approach to analyze the bending of a simply-supported beam of frozen sand. These FE treatments were based on a fully explicit time integrating technique, and thus depended on small time increments for accuracy. Chehayeb et al. (1987) employed the generalized power law creep model to study the indentation of an ice sheet by a cylindrical body, by using plane stress FE analysis. They used a secant-type iterative solution algorithm on the global equation of motion, and a Newton-Raphson type iterative algorithm coupled with α-type time incrementing on the constitutive model at each Gauss point. Chehayeb et al. (1987) reports that 4 to 6 cycles of iteration at the global equation level and not more than 4 cycles of iteration at the element level, per time step, were required to satisfy the specified convergence. Emery and Mirza (1980) used the FEM to simulate the flow of a large ice mass, using a power law-type constitutive model. Soo et al. (1987) used the FEM to analyze reinforcement in frozen earth structures, including plain and reinforced frozen sand beams, and similar frozen earth walls. They used plane stress/ strain elements, bond interface elements, weighting functions to account for difference in tensile and compressive strengths of frozen soils, and the concept of yield functions, in a fully-explicit FE code (similar to Klein 1979) to solve these creep problems. Klein (1979) and Soo (1983) also provided relevant axisymmetric formulations.

An important class of structure-frozen soil/ice interaction problems involve laterally loaded piles. In the literature, laterally loaded piles have been treated as beams supported by spring - dashpot systems (i.e. Maxwell mechanical model). Neukirchner and Nixon (1987) proposed an elementary secondary creep model where the pile is modelled as a beam on a system of dashpots. They obtained solutions by using the finite difference technique. Foriero and Ladanyi (1990) used the FEM in an explicit time incremental algorithm to solve this problem, by assuming the pile to be laterally supported by a spring-dashpot system.

Numerical treatment of adfreeze/bond strength phenomena in structure-frozen soil/ ice interaction has been reported only rarely. Chehayeb et al. (1987) used an indirect method, without using any interface elements, to study the effect of adfreeze strength in sea-ice indentation problems. Soo (1983) used a material model,

conforming to the power law-type model, to develop an interface element which was incorporated in a fully explicit finite element code and used to simulate the bond between reinforcement and frozen earth.

1.4 Objectives of the Research

This research was undertaken for the purpose of complementing the substantial experimental work which has been conducted on the creep deformation of frozen soils/ice with a fairly comprehensive computational (i.e. numerical) treatment of the subject. Therefore this work is classifiable as an applied research effort, the objectives of which can be listed as:

1. Development of appropriate finite element codes for the following purposes: implement several selected creep constitutive models for ice/frozen soil-structure interaction analyses; investigate laterally loaded piles in creeping media; and model adfreeze strength phenomena.

2. Investigation (by computational means and comparison with corresponding experimental results where available) of the suitability of each of the selected constitutive models to represent the observed behaviour of frozen soils/ice in situations of interaction with structures.

3. Demonstrate use of the computer codes as predictive tools applicable in analyses of a wide range of structure-frozen soil/ice interaction problems encountered in the engineering field.

1.5 Scope of the Thesis

In the present study, finite element codes for structure-frozen soil/ice interaction analyses will be developed within the confines of small displacement theory. Out of the many constitutive models proposed to describe the creep behaviour of frozen soils/ice, three models are selected for implementation in the codes. These models are the Power Law Creep Model, Fish's Unified Model, and Domaschuk's Model. The reasons for selecting these particular models and their basic functional

forms are discussed in **Chapter 2.**

Development of appropriate finite element codes and the implementation of the three selected constitutive models in the codes are detailed in **Chapter 3.** The first two models are incorporated in an iterative, time-incrementing finite element code, and the third (Domaschuk's model) is implemented in an iterative, load-incrementing finite element code. Phenomenological extensions of the power law model to multi-step loads are also discussed. Details of time/load incrementing finite element algorithms, explicit forms of various matrices involved, details of the structure of the codes, and verification of the codes for accuracy and reliability with respect to each constitutive model and each class of element, are all provided under Chapter 3. The codes are capable of performing the materially non-linear finite element analyses of structure-frozen soil/ice interaction problems in conditions of plane stress/strain, axisymmetry, plane strain axisymmetry, and in three dimensions.

The use of the above finite element codes in computational analyses of several structure-frozen soil/ice interaction problems under plane and axisymmetric conditions is detailed in **Chapter 4.** Analyses are performed for creep deformations as well as for stress distributions. In the first part of Chapter 4, axisymmetric analyses are used to investigate the applicability and limitations of two extended versions of the power law model by simulating multi-stage pressuremeter tests on a frozen sand, and by comparing the predictions with test data (Lach 1989). The power law is also used to establish a correspondence between numerical simulations and test data (Domaschuk et al. 1989) in the case of penetration of laterally loaded cores in ice, by using plane strain analyses. The numerical results are used to develop a relationship for an equivalent spring-dashpot to represent the ice medium. Interaction between a group of rigid cores in ice is similarly investigated. Axisymmetric analyses and the power law model are used to investigate settlement of footings on frozen ground, and to simulate several rate-controlled penetration problems in frozen soils; both these classes of problems correspond to situations commonly encountered in the field. In the second part of Chapter 4, generalized Fish's model is used in axisymmetric analyses to re-simulate several uniaxial creep tests on ice reported

by Jacka (1984), followed by analyses of several examples involving interaction of structures with frozen ground, these being plane strain axisymmetric analyses of pressuremeter tests, axisymmetric analyses of footings, and plane strain analyses of laterally loaded, embedded, rigid cores. Correspondence of the numerical results with the generally observed characteristics of creep deformation of ice/frozen soils reported in the literature is discussed, and capabilities of the model in this regard are emphasized. In the third part of Chapter 4, use of Domaschuk's model to simulate pressuremeter tests and plate tests on a selected frozen sand is discussed. These analyses are performed under axisymmetric conditions.

Chapter 5 discusses the treatment of laterally loaded piles in ice and frozen soils. A simple pile element, supported laterally by a spring-dashpot system, is developed and implemented in an appropriate finite element code. The non-linear dashpot relationship developed earlier by analyzing laterally loaded rigid cores (Chapter 4) is used to characterize the dashpot here. Laterally loaded piles are analyzed using this code under different restraint conditions. A series of completely three-dimensional analyses of laterally loaded piles in ice is conducted using the power law constitutive model. These results are compared with the results obtained using the simple pile element.

In **Chapter 6**, the development of an appropriate finite element to model the adfreeze/ bond strength phenomena in frozen soils/ice is discussed. This element is incorporated in a finite element code developed earlier (Chapter 3), and several demonstration problems are conducted to investigate its behaviour.

The conclusions of the study are summarized in **Chapter 7**, along with a discussion of contributions made to the field of computational analyses of structure-frozen media interaction problems during the course of the research.

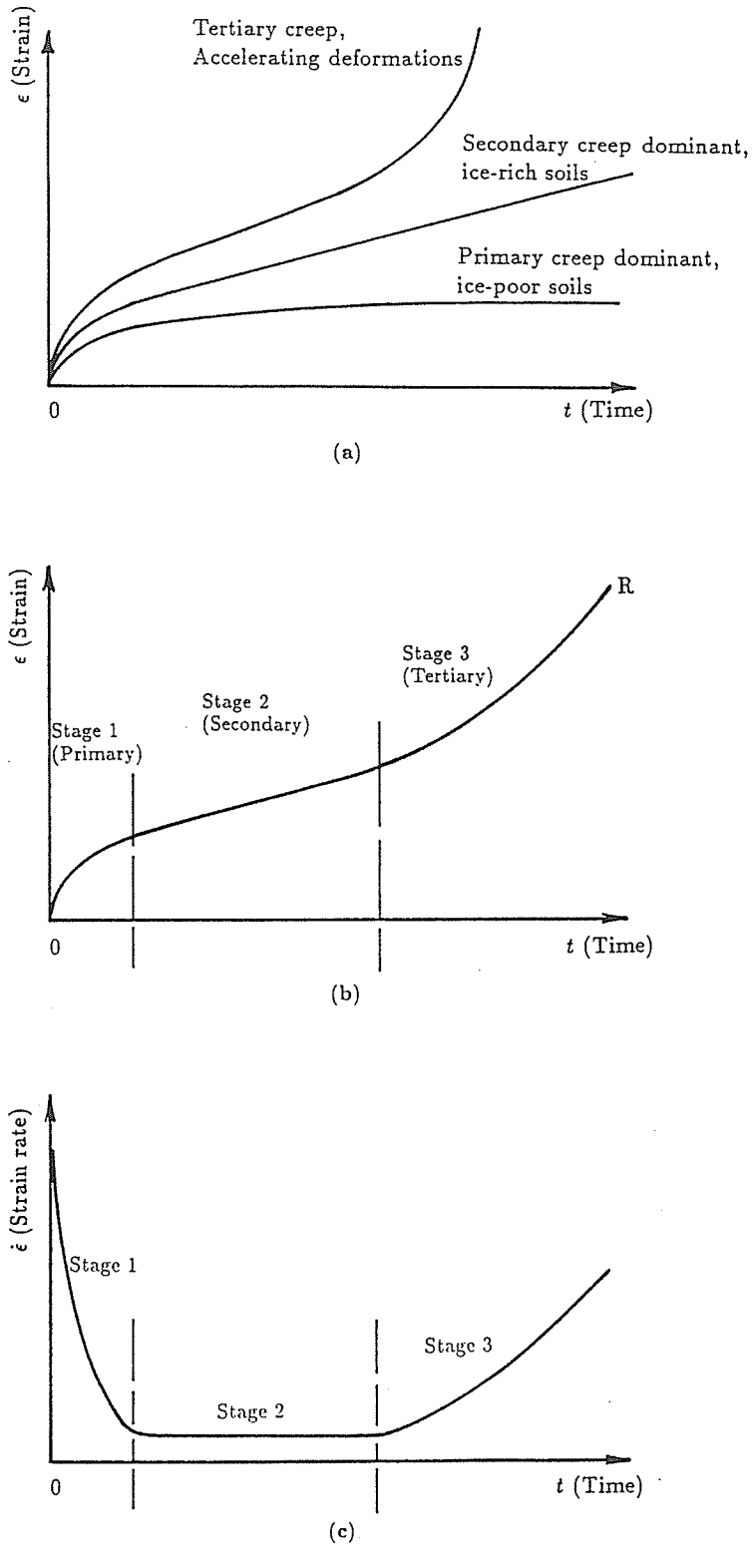

Figure 1.1 Typical creep curves for frozen soils/ice.

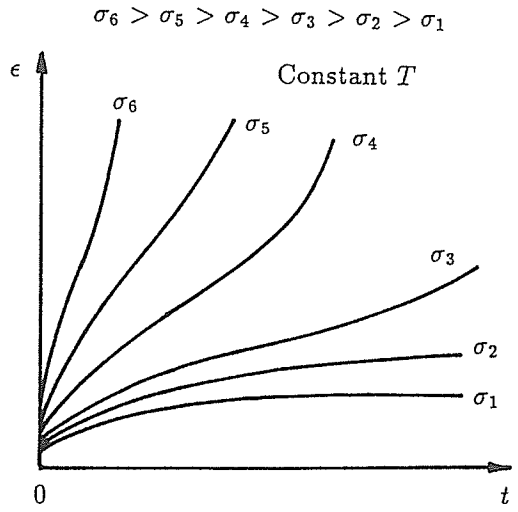

Figure 1.2. Stress dependence of creep deformation of frozen soils (and ice).

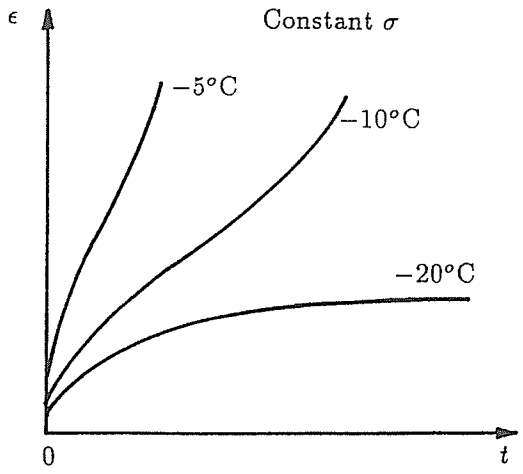

Figure 1.3. Temperature dependence of creep deformation of frozen soils (and ice).

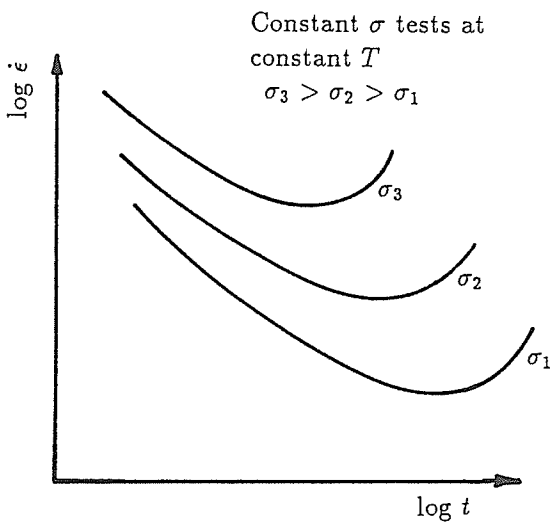

(a)

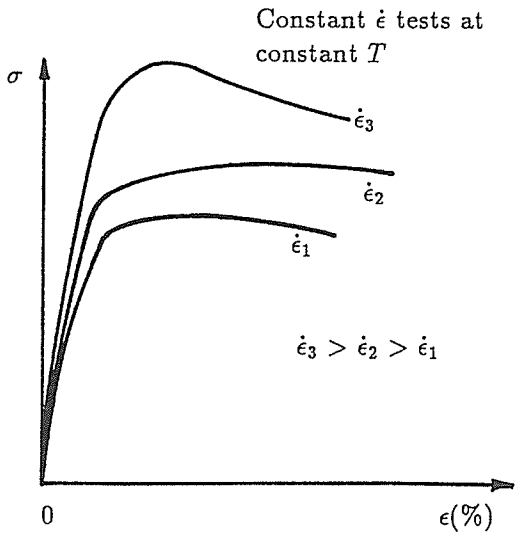

(b)

Figure 1.4 Creep behaviour of ice: (a). Constant stress tests. (b). Constant strain-rate tests.

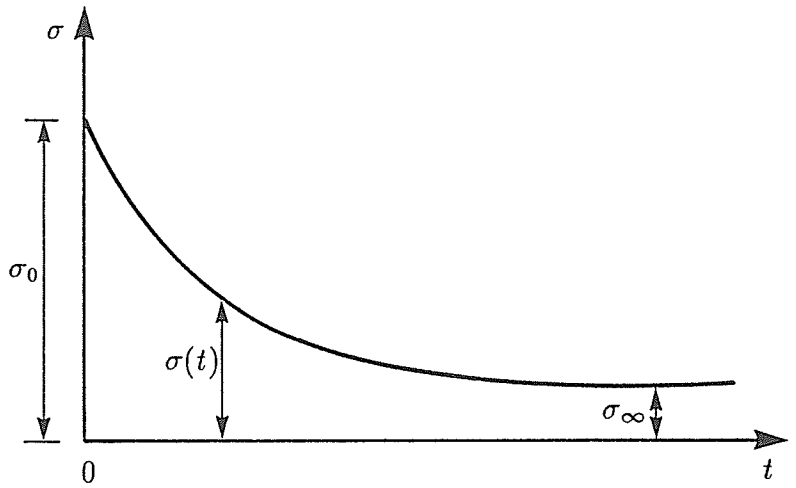

Figure 1.5. Long-term strength of frozen soils (after Vyalov 1963).

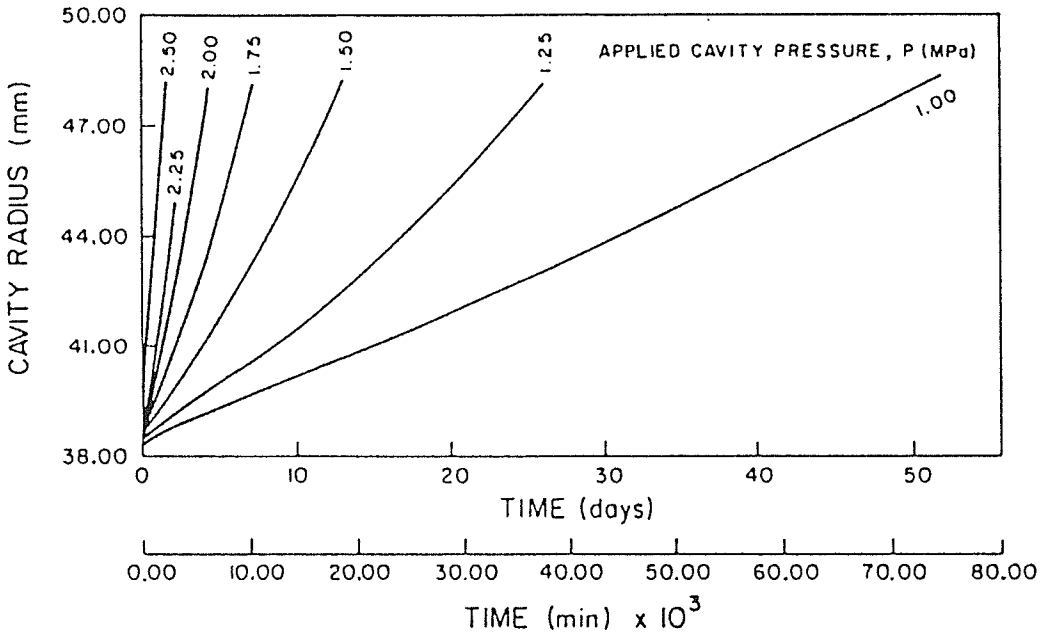

Figure 1.6 Results of pressuremeter tests on ice, after Kjartanson, Shields, Domaschuk, and Man (1988).

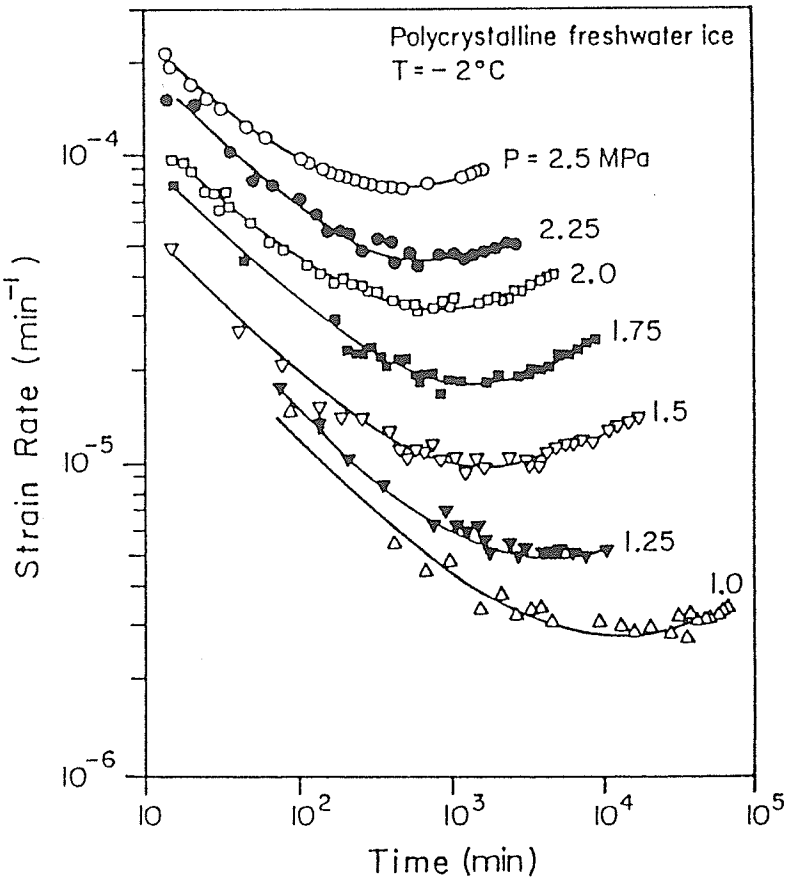

Figure 1.7 Results of pressuremeter tests on ice, after Shields, Domaschuk, Azizi and Kjartanson (1989).

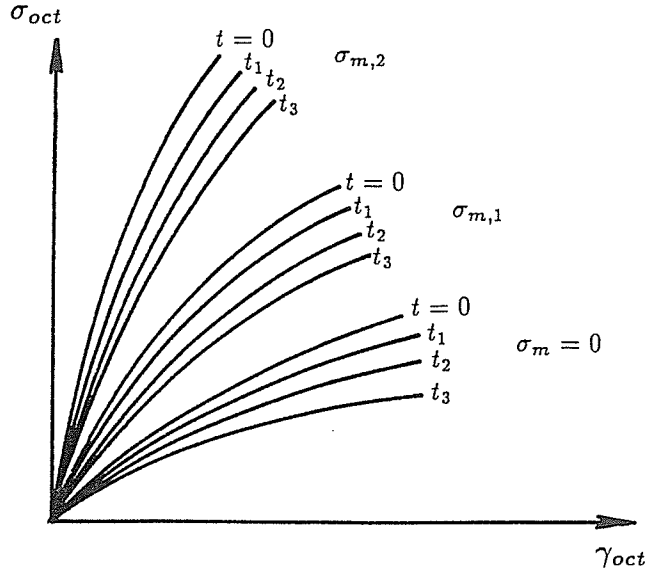

Figure 1.8 Effect of mean normal stress (σ_m) on octahedral shear stress (σ_{oct})–octahedral shear strain (γ_{oct}) behaviour of frozen soils (after Vyalov 1965b).

Chapter 2

REVIEW OF CONSTITUTIVE RELATIONS FOR FROZEN SOILS/ICE

2.1 General

Different researchers have followed different approaches to develop constitutive relations to describe the creep of frozen soils and ice. Some constitutive models are based on purely phenomenological behaviour of frozen soils and ice observed in experiments, while others are based on physical (thermo-mechanical) processes that are believed to take place within the creeping material. In all approaches, the models need to be verified against observed deformation characteristics of the material. In a broader sense, a model is a mathematical formulation that translates the physical or microscopic creep process into a macroscopical phenomenon. It is most desirable that such engineering models be mathematically as simple as possible, but a cost would be involved here in that the simpler the model, the narrower may be its range of application. Given the multiple complexity of the actual rheological processes of frozen soils and ice, a simple model that can simulate a large number of frequently observed creep deformation processes within an acceptable margin of deviation can be called a successful engineering model. Predictions made using such a model can be used for design and construction purposes by applying a suitable factor of safety, provided the same general class of deformation as simulated by the model is known to occur in the material under consideration. Several creep constitutive models proposed for frozen soils/ice are described below.

2.2 Power Law Model

The power law creep model, in its basic form, is a time-hardening law originally proposed to describe the uniaxial creep of metals at high temperatures (Norton 1929, Dorn 1954). This has been later adopted to describe the creep of frozen soils/ice under uniaxial stress-strain states (Glen 1955, Vyalov 1965b, Klein 1979), and relates the creep strain to stress and elapsed time by a power type relationship

of the form:

$$\epsilon^c = A\,\sigma^B\,t^C\ , \qquad C \leq 1\ , \tag{2.1}$$

where ϵ^c is the creep strain, σ the applied stress, t the elapsed time, and A, B, C are material parameters. Parameter A is dependent on temperature and has units $(\text{stress})^{-B}(\text{time})^C$, while B, C are dimensionless and vary only slightly with the temperature. For $C < 1$, equation (2.1) describes the primary or attenuating creep modes, and for $C = 1$ it describes the secondary creep stage. Glen (1955) proposed that the minimum creep strain rate in ice is related to applied constant stress as,

$$\dot{\epsilon}^c = A\,\sigma^B\ , \tag{2.2}$$

where superposed dot denotes the time derivative of the relevant quantity, and all other notations are as before. Nye (1956) generalized equation (2.2) to multi-dimensions (see §3.2.1). Vyalov (1963, 1965b) expressed the stress-strain relationship for frozen soils/ice as,

$$\sigma = K(t)\,\epsilon^m\ , \qquad \text{or,} \qquad \epsilon = \left[\frac{\sigma}{K(t)}\right]^{\frac{1}{m}}\ , \tag{2.3}$$

which are forms equivalent to equation (2.1), and where $K(t)$ is a time dependent parameter. Note that Vyalov (1963, 1965b) thereafter described the use of these equations to develop a theory of hereditary creep. Klein and Jessberger (1979) showed the equivalence of parameters used in equations (2.1) and (2.3). Based on an experimental program, Klein (1979) gave values of parameters A, B, C for several frozen soils at a selected temperature (see Table 2.1). Hooke (1981) reviewed the application of equation (2.2) to represent the steady creep of ice.

Generalization of equation (2.1) to multi-dimensions is discussed at length by Hult (1966) and Odqvist (1966), with respect to modelling of creep in metals; Odqvist (1966) also hypothesized the extension of equation (2.1) to time varying stresses. Application of identical processes with regard to frozen soils and ice are discussed later in Chapter 3 (§3.2.1) of this dissertation.

It is noteworthy that the term *secondary creep stage* is used in a different context than the term *steady creep stage* (Odqvist 1966). Secondary creep stage is the second stage in Figures 1.1b or 1.1c, where strain rate remains constant with time, whereas *steady* and *non-steady* creep stages, respectively, are defined according to whether the current stress distribution remains constant or varies with time. Thus it is possible to obtain a long-term attenuating creep behaviour (similar to the primary creep behaviour) under a steady state stress field. When a viscoelastic material is stressed, an initial (elastic) stress distribution is set up, which will thereafter change gradually towards a long-term, steady-state stress distribution. The time period during which this stress change takes place is known as the *transient* or non-steady stress stage. These transient stress stages are generally inevitable in a multi-dimensional boundary value problem, and the practically significant duration of the transient stage would be determined according to the particular creep model used.

Ladanyi (1972) presented the generalized power law in the context of an engineering theory specifically directed at solving the problems of footings and anchors buried in frozen soils. Following Hult (1966), Ladanyi (1972) wrote the secondary creep model in uniaxial stress state as,

$$\frac{d\epsilon}{dt} = \dot{\epsilon} = \dot{\epsilon}_c \left[\frac{\sigma}{\sigma_c}\right]^{\bar{n}} , \tag{2.4}$$

where ϵ denotes the creep strain, σ_c is a temperature dependent proof (uniaxial) stress for an arbitrarily selected creep strain rate ($\dot{\epsilon}_c$), $\dot{\epsilon}_c$ is selected to express equation (2.4) in normalized form, $\bar{n}$ is a temperature dependent exponent, and other notations are as given before. The initial (instantaneous) strains were assumed to consist of a reversible elastic portion and a non-reversible plastic portion. Equation (2.2) is based on the assumption of linearization of creep curves (Hult 1966), and is valid when strains encountered in the secondary creep stage are much larger than those in the primary creep stage. A uniaxial, time-hardening, primary creep model was proposed identical to equation (2.1), and an equivalent primary strain-hardening model was given as (Ladanyi 1972),

$$\frac{d(\epsilon)^{\frac{1}{C}}}{dt} = A^{\frac{1}{C}} \sigma^{\frac{B}{C}} . \tag{2.5}$$

Extension of the models above to multi-dimensions in the case of incompressible materials followed the methods of Hult (1966) and Odqvist (1966) earlier (see §3.2.1). Ladanyi (1972) described an empirical method to include the effect of hydrostatic stress in the generalized creep model, by using the test results of Sayles (1968), and gave expressions to estimate either the creep strength or the time to failure, when one of the two quantities are known.

2.3 Fish's Unified Model

A creep constitutive model was proposed by Fish (1984), based on the thermodynamic considerations of the creep process (Fish 1980, 1981). Experimental data from uniaxial constant stress (CS) tests and uniaxial constant strain rate (CSR) tests on ice and frozen soil samples were used to develop the theory. This model is written as (Fish 1984):

$$\dot{\epsilon} = \widetilde{C}\,\frac{kT}{h}\,\exp\Big(-\frac{E_1}{R_1 T}\Big)\,\exp\frac{\Delta S}{k}\,\Big(\frac{\sigma}{\sigma_o}\Big)^{\zeta+\eta}\,, \tag{2.6}$$

where $\widetilde{C}$, $\zeta \geq 0$, and $\eta \geq 1$ are dimensionless parameters (independent of temperature), σ_o is the ultimate strength of soil (temperature dependent) in MPa, E_1 is activation energy in kJ/mole, k is Boltzmann's constant (1.38×10^{-23} J/K), h is Planck's constant (6.63×10^{-34} Js), R_1 is the gas constant (8.31×10^{-3} kJ/mole K), T is absolute temperature in K, kT/h is frequency of vibration of elementary particles around their equilibrium positions, and ΔS is the change of entropy given by Fish (1984) as,

$$\frac{\Delta S}{k} = \frac{\Delta S(\bar{t})}{k} = \delta\, f(\bar{t})\,, \tag{2.7}$$

where δ is a dimensionless parameter (independent of temperature), and $f(\bar{t})$ is a function of normalized (dimensionless) time, given by,

$$f(\bar{t}) = \bar{t} - \ln \bar{t} - 1\,, \qquad \text{and} \qquad \bar{t} = t/t_m\,, \tag{2.8}$$

where t_m is the time to failure. Fish (1984) assumed the creep process to be isothermal and volumetric and instantaneous strains to be small. In this model, deformation and failure were considered as a single thermo-activated process in which the dominant role belongs to the change of entropy (Fish 1984). Failure was assumed

to occur when the entropy change became zero. The point where entropy change reached zero was interpreted to coincide with the instant when strain rates in CS tests reach the minima and stress in CSR tests reach the maximum (peak) values. Time to failure t_m was linked to applied stress σ as (Fish 1984):

$$t_m = t_o \left(\frac{\sigma}{\sigma_o} \right)^{-\eta} , \qquad \text{for } \sigma \leq \sigma_o , \tag{2.9}$$

where t_o is the mean duration of the "settled life" of an elementary particle in a position of equilibrium (Frenkel 1947) given by,

$$t_o \approx \frac{h}{kT} \exp\left[\frac{E_1}{R_1 T} \right] , \tag{2.10}$$

where all notations are as defined earlier. The minimum strain rate (secondary creep stage) was described by (Fish 1984):

$$\dot{\epsilon}_m = \frac{\widetilde{C}}{t_m} \left(\frac{\sigma}{\sigma_o} \right)^{\zeta} . \tag{2.11}$$

The creep model for constant stress situations was given as (Fish 1984):

$$\dot{\epsilon} = \dot{\epsilon}_m \exp\{\delta \, f(\bar{t})\} , \tag{2.12}$$

where $\dot{\epsilon}_m$ is defined by equation (2.11), $f(\bar{t})$ is defined by equation (2.8), δ is the dimensionless parameter defined earlier and $\dot{\epsilon}$ is the creep strain rate. Primary creep occurs for $\bar{t} < 1$, secondary creep for $\bar{t} = 1$, and tertiary creep for $\bar{t} > 1$.

For CSR tests, the strain rate is constant, i.e. $\dot{\epsilon} = \dot{\epsilon}_m$. The constitutive equation was written as (Fish 1984):

$$\sigma = \sigma(\bar{t}) = \sigma_{max} \exp\left\{ -\frac{\delta \, f(\bar{t})}{\eta} \right\} , \tag{2.13}$$

where σ_{max} is the maximum (peak) stress observed in CSR tests, and all other notations are as defined earlier. The failure criterion was given as,

$$t_m = \frac{\epsilon_m}{\dot{\epsilon}} = t_o \left(\frac{\sigma_{max}}{\sigma_o} \right)^{-\eta} \qquad \text{or,} \qquad \dot{\epsilon} = \dot{\epsilon}_m = \frac{\epsilon_m}{t_o} \left(\frac{\sigma_{max}}{\sigma_o} \right)^{\eta} , \tag{2.14}$$

where ϵ_m is the strain accumulated up to time t_m. By defining $\bar{\sigma} = \sigma/\sigma_{max}$, equation (2.13) was rewritten as (Fish 1984):

$$(\bar{\sigma})^{\eta} = \exp\{-\delta\, f(\bar{t})\}\ , \tag{2.15}$$

and it was defined that primary, secondary, and tertiary creep occurs, respectively, for $\bar{t} < 1$ ($\bar{\sigma} < 1$), $\bar{t} = 1$ ($\bar{\sigma} = 1$), and $\bar{t} > 1$ ($\bar{\sigma} < 1$). Fish (1984) showed the equivalence of creep data from CS and CSR tests by superposing these data on a single normalized diagram [see Fig. 17 of Fish (1984)]. The entire creep model was summarized as shown in Figure 2.1 (after Fish 1984). Fish (1984) also described methods to determine parameters of the model based on either type of test (CS or CSR).

Fish (1987) proposed a new method to determine the creep parameters for the model, specially the time to failure t_m, using creep test data. The time to secondary creep stage, which appears as a momentary phenomenon on the strain-time curve, denotes the above time to failure. He also emphasized that the shape of the creep curve predicted by the model in equation (2.12) is influenced by the value of parameter δ, which lies between $0 < \delta < 1$ for a large number of materials. This influence is illustrated by Figure 2.2, where results obtained by numerical integration of equation (2.12), in view of equation (2.8), are shown for three values of δ (δ = 0.3, 0.5, 0.7). Largest deviations between the curves occur during the primary creep stage and well after failure, while the differences diminish close to the failure point.

The above constitutive model of Fish has the significant advantage of being able to predict all three stages of creep. However, it is necessary to generalize the model to multi-dimensions if it is to be used for prediction of soil-structure interaction problems found in practice. Concurrent to this generalization, it is necessary to hypothesize that the model in equation (2.12) holds for time-varying stresses, since a transient stress stage is generally encountered in boundary value problems. Further discussion of this model, including generalization to multi-dimensions is made later in Chapter 3 (§3.2.2) of this dissertation.

2.4 Domaschuk's Model

The constitutive model for frozen soils proposed by Domaschuk et al. (1985), Rahman (1988) and Domaschuk et al. (1991) is based on the concept of separating the response of the material under isotropic compression and under shearing stress. For unfrozen soils, previous studies had been conducted to obtain bulk modulus (K) using isotropic compression tests, and shear modulus (G) using mean normal stress triaxial tests (Domaschuk and Wade 1969, Valliappan 1974); these K and G modulii were then substituted in the usual isotropic, linear elastic relationships to obtain the constitutive model for the materials. The same approach had been continued (Domaschuk et al. 1985, Rahman 1988) to obtain generalized solutions for the K and G modulii of a frozen sand; however, these modulii would no longer be constants, but functions of stress state, time, temperature, ice and unfrozen water content, grain size, etc. Thus the two modulii were named as bulk creep function K_c, and shear creep function G_c, respectively.

Domaschuk et al. (1985) proposed the use of isotropic compression tests to determine the K_c function defined as,

$$\sigma_m = K_c \, \epsilon_v \ , \tag{2.16}$$

where σ_m is the mean normal stress and ϵ_v the volumetric stain, and the use of triaxial compression tests with σ_m held constant to determine the G_c function defined as,

$$S_d = G_c \, e_d \ , \tag{2.17}$$

where,

$$S_d = \sqrt{(\sigma_1 - \sigma_m)^2 + (\sigma_2 - \sigma_m)^2 + (\sigma_3 - \sigma_m)^2} \ , \tag{2.18a}$$

and

$$e_d = 2\sqrt{(\epsilon_1 - \epsilon_m)^2 + (\epsilon_2 - \epsilon_m)^2 + (\epsilon_3 - \epsilon_m)^2} \ , \tag{2.18b}$$

where ϵ_m is the mean volumetric strain, σ_i (i = 1,2,3) are principal stresses, and ϵ_i are principal strains (in the context of triaxial testing).

Samples of a quartz, carbonate medium grain sand, saturated and maintained at -3^oC, were used in the tests to evaluate the creep functions (Rahman 1988). Data

collected from a multi-stage isotropic compression creep test on a sand sample were used to construct curves of ϵ_v versus σ_m after various elapsed times (Rahman 1988). It was assumed that the total strain at any particular time was the sum of all the instantaneous strains and creep strains that the sample had undergone prior to the time under consideration. This data linearized on a σ_m/ϵ_v versus σ_m plot, and a secant bulk creep function (K_{cs}) was derived as (Rahman 1988),

$$\frac{\sigma_m}{\epsilon_v} = K_{cs} = K_0 + \phi \exp\{-\kappa t\}\, \sigma_m \ , \tag{2.19}$$

where K_o, ϕ, κ are parameters obtained from the plots, and t is the elapsed time. By manipulating equation (2.19), Rahman (1988) obtained the following expression for tangent bulk creep function K_c:

$$K_c = K_0 \left(1 + \frac{1}{K_0}\, \phi \exp\{-\kappa t\} \sigma_m\right)^2 \ . \tag{2.20}$$

In order to determine the shear creep function, multi-stage triaxial tests at constant mean normal stresses were conducted (Rahman 1988). A constant σ_m was maintained by complementing the increases in axial stresses by appropriate decreases in cell pressure, at each stage of the step-wise increases in deviatoric stress. Using the test data, curves of resultant deviatoric stress (S_d) versus resultant deviatoric strain (e_d) were prepared for different elapsed times. As before, it was assumed that the total strain at any particular time was the sum of all the instantaneous strains and creep strains that the sample had undergone prior to the time under consideration. Shear creep function G_c was defined as the momentary slope of the resultant deviatoric stress-strain curve, at a given time. Rahman (1988) graphically evaluated G_c from the S_d vesus e_d curves at selected points, and replotted the G_c versus σ_m/S_d curves at different elapsed times. Noting the fact that the further transformed plots of $(\sigma_m/S_d)/G_c$ versus (σ_m/S_d) were linear for different elapsed times, the following hyperbolic expression was proposed for the shear creep function G_c (Rahman 1988):

$$G_c = \frac{\sigma_m/S_d}{\varphi + \varrho(\sigma_m/S_d)} \ , \tag{2.21}$$

where, by manipulating the data curves and noting several characteristics which were consequently evident, the parameters φ and ϱ were evaluated as,

$$\varphi = c t^{\alpha} \ , \qquad \text{and} \qquad \varrho = m_1\, \sigma^{\beta}\, t^{n_1} \ . \tag{2.22}$$

Thus the creep function G_c in equation (2.21) was written as (Rahman 1988):

$$G_c = \left(m_1\, \sigma_m^{\beta}\, t^{n_1} + ct^{\alpha}\, \frac{S_d}{\sigma_m}\right)^{-1} . \tag{2.23}$$

It was then suggested that the same concept as in incremental elasticity should be employed, by using K_c and G_c to model, respectively, the bulk creep behaviour and the shear creep behaviour of the frozen sand. Numerical implementation of the model is discussed in Chapter 3 (§3.2.3).

2.5 Other Models

In addition to the three constitutive models discussed so far, many other models for creep of frozen soils and ice are available in the literature. Only a brief reference to some of these models will be made here.

Yuanlin and Carbee (1983) proposed a constitutive model for frozen silt, based on the results of a series of unconfined compression creep tests on remolded, saturated Fairbanks silt at constant stress and temperature conditions. For various test temperatures, a sudden change in the slope of $\log \dot{\epsilon}$ versus $1/\sigma$ curves was noticed at almost the same minimum strain rate (about 10^{-6} s^{-1}). Based on this observation, they classified creep of frozen silt into two types as short-term and long-term creep, and proposed expressions to describe minimum creep strain rate, time to failure, and loss of strength, for each type of creep. Based on suggestions of Assur (1980), a constitutive equation was proposed to relate creep strain to other relevant parameters (time to failure, current time, and strain to failure). Definition of failure was similar to that in the case of Fish's model (§2.3).

Sinha (1983) proposed a creep model of ice for monotonically increasing stress. This was basically a numerical integration method to predict the strain path corresponding to a given stress history. The model was applicable to previously undeformed polycrystalline materials where grain boundary diffusional process did not play a major role. It incorporated the grain size effect, and strain was predicted in terms of elastic, delayed elastic, and viscous (permanent) strains.

Several constitutive models (specifically for ice) have been proposed based on the "second order fluid model" (Morland and Spring 1981, McTigue et al. 1985, Man et al. 1985, Sun 1987). Pertinent to these approaches is a general theory of stress-deformation relations of isotropic materials, presented by Rivlin and Ericksen (1955). McTigue et al. (1985) discussed a special case of a more general constitutive model based on the second order fluid model proposed by Morland and Spring (1985). Man et al. (1985) suggested a new model that could capture the advantages of both the second order fluid model (McTigue et al. 1985) and the secondary creep model (Glen 1955, Nye 1956). Sun (1987) further extended above work and proposed two modified fluid models for ice.

Ting (1983) proposed a tertiary creep model for frozen sands. Gardner et al. (1984) derived a constitutive equation for primary and secondary creep of ice and frozen soils. Morland (1979), Gold and Sinha (1980), Le Gac and Duvall (1980), Williams (1984), Ashby and Duvall (1985), and Szyszkowski and Glockner (1985) are among other researchers who had proposed constitutive models for ice.

2.6 Relations for Interface Behaviour

The behaviour at the interface between a foundation element and surrounding frozen medium assumes importance in several situations, specially in the case of axially loaded piles in permafrost and ice. Most of the pile foundations are of timber, while steel and concrete piles are also in use. The advantages of pile foundations in cold regions include their ability to carry even extremely large loads in difficult permafrost conditions, ability to transfer the loads to a suitable stratum (that remains structurally and thermally stable for the service life of the structure) some distance below the active layer, ability to provide an air space between heated buildings and permafrost to avoid permafrost degradation, possibility to mobilize the adfreeze bond strength to carry part or all of the load, and the ability of installation with minimum disturbance to the ground thermal regime (Johnston 1981).

Axially loaded piles embedded in permafrost carry most of the load due to the shear adfreeze bond strength developed at the pile-soil (or ice) interface. Resistance

due to end bearing can be significant only when the pile bottom rests on a hard base. The load-resisting mechanism for laterally loaded piles is different, where the loads are carried mainly by the lateral soil (or ice) reaction. Based on test observations as well as theoretical predictions of creep of ice, several relationships had been proposed to describe the creep of piles in permafrost/ice and the closely related adfreeze strength phenomena.

Parameswaran (1979) found that the steady state creep displacement rate $\dot{\gamma}$ of axially loaded piles in frozen soils was related to the applied shear stress (τ) at the pile-soil interface as,

$$\dot{\gamma} \propto (\tau)^{\tilde{n}} \ , \tag{2.24}$$

where $\tilde{n}$ varied between 6.7 and 9.1 for various types of piles (wood, concrete and steel piles with different surface finishes). These findings generally agreed with those of Johnston and Ladanyi (1972). Nixon and McRoberts (1976) gave the following steady state relation for creep of axially loaded piles in permafrost, based on theoretical considerations of creep of permafrost:

$$\dot{\gamma} = B_1 \, \tau^{n_1} + B_2 \, \tau^{n_2} \ , \tag{2.25}$$

where B_1, B_2, n_1, n_2 are parameters, and other notations are as before. Morgenstern et al. (1980) reviewed some long-term creep tests on ice to propose the following expression for the steady state pile velocity ($\dot{u}_a$):

$$\dot{u}_a = \frac{a \, 3^{(n_1+1)/2} \, B_1}{n_1 - 1} \, \tau^{n_1} \ , \tag{2.26}$$

where B_1, n_1 are parameters and a is pile radius.

The shear stress (τ) at the pile-ice (or -soil) interface in equations (2.24)–(2.26) is referred to as the adfreeze bond strength of ice/permafrost to pile. Numerical values for adfreeze strength of piles in ice and frozen soils at different pile velocities are available in the literature (Tsytovich and Sumgin 1956, Vyalov 1965, Frederking 1979, Parameswaran 1978 and 1981). Parameswaran (1978) and Alwahhab (1983) observed that for relatively smooth model pile surfaces, the bond strength (under constant displacement rates) reached a peak and dropped thereafter, indicating a

break in the bond. Material models for bond behaviour at the interface can be hypothesized (Soo 1984) based on such observed behaviour.

2.7 Selection of Constitutive Models for Present Study

The three constitutive models described in §2.2, §2.3 and §2.4, respectively, were selected for implementation in the finite element codes developed in the course of this research (see Chapter 3). The basis for selecting these models for the present research is as described below.

The power law creep model (§2.2) is widely accepted and used as applicable to describe the primary, secondary, and attenuating creep of frozen soils/ice, by experimentalists as well as numerical analysts in this field (Glen 1955, Nye 1956, Vyalov 1963 and 1965b, Ladanyi 1972, Klein 1979, Klein and Jessberger 1979, Hooke 1981, etc.). Numerical values of the material parameters involved in the model have been reported for different frozen soils and ice at different temperatures (Glen 1955, Klein 1979, Hooke 1981, etc.). Major advantages of the model are its simple mathematical form, the involvement of only three material parameters (only two parameters for secondary creep), and the availability of a large base of experimental data. The origin of the power law model can be traced to the field of modelling of creep in metals (Norton 1929, Hult 1966, Odqvist 1966), and substantial literature is available on various aspects of the model, including its generalization to multi-axial states of stress and strain. These considerations formed the main reasons for the selection of the power law model for implementation in the computer codes.

Fish's (1984, 1987) unified creep model (§2.3) is different from the power law in two respects: i.e., it is based on a thermodynamic consideration of the creep process, and it is able to simulate the entire creep process, including the primary, secondary, and tertiary creep stages. Here, secondary creep is considered as a momentary phenomenon, represented by a point of inflexion in the creep curve. This type of behaviour has been confirmed also in multi-axial tests on ice (see Figures 1.6, 1.7) and frozen soils (Yuanlin and Carbee 1983). The failure of the material is signalled by the onset of the tertiary creep stage, and there arise many occasions

when such failure critically affects the structural performance of the material, and therefore the serviceability of structures founded on it. Considerations of above type were the prime reason for implementing this model in the computer codes here. Generalization, and assumption of validity of the model for varying stresses, will be made similar to the case of the power law model.

Among the conceptual differences between the models discussed above and Domaschuk's model (§2.4, Domaschuk et al. 1991) are the consideration of compressibility of the material in the latter model, and the fact that the latter model is not expressed explicitly in a rate form. (Incompressibility of the material is assumed during the generalization of the power law and Fish's model, as shown in Chapter 3 later). Compressibility of the material has important implications with respect to the creep process, and a model which takes it into account may be more realistic than the models which depend on the incompressibility of the material. Since Domaschuk's model is based on multi-axial test data, the need of generalization does not arise. These considerations, and the availability of necessary parameters for a particular frozen sand, were the main reasons for implementing the model in an appropriate finite element code here.

Table 2.1:
Power law creep parameters for different frozen soils
(After Klein, 1979)

Material at $-10°C$	A	B	C
Ottawa Sand	3.5×10^{-4}	1.28	0.44
Bat-Baioss Clay	1.6×10^{-3}	2.50	0.45
Emscher-Marl	7.6×10^{-5}	4.00	0.10
Callovian Sandy Loam	5.5×10^{-4}	3.70	0.37
Karlsruher Sand	1.3×10^{-3}	2.00	0.40

Note: A in $(\mathrm{mm}^2/\mathrm{N})^B \mathrm{hr}^{-C}$

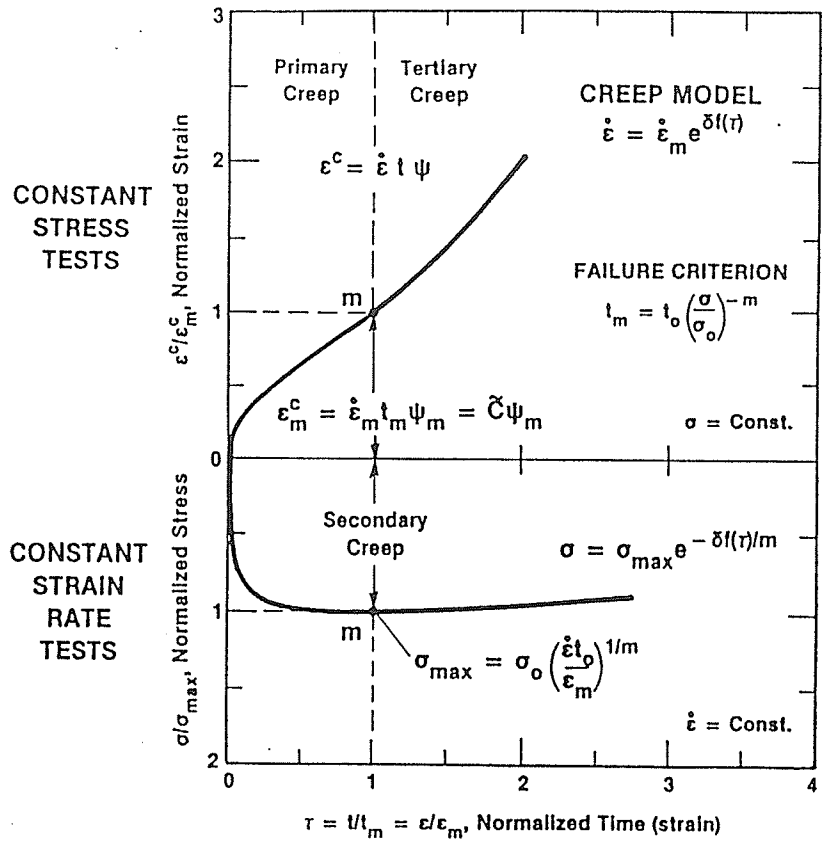

Figure 2.1 Creep model of Fish (1984).

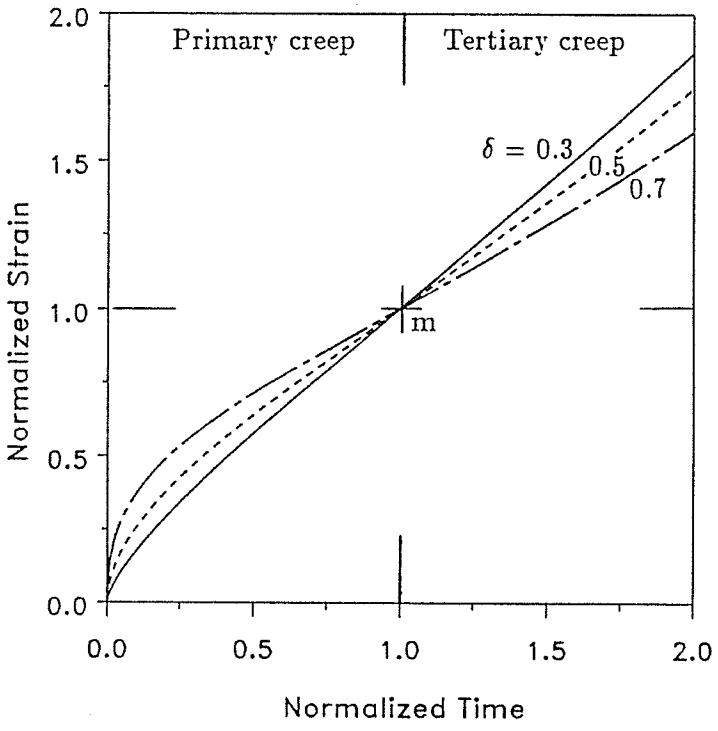

Figure 2.2 Effect of δ on shape of creep curve.

Chapter 3

FINITE ELEMENT CODES FOR CREEP OF ICE AND FROZEN SOILS

3.1 General

The development of appropriate finite element codes for the computational analyses of structure-frozen soil/ ice interaction (which, as outlined in §1.4, constitutes the main objective of this research) is detailed in this Chapter. The results of this development effort are several finite element codes which would be readily usable for the settlement predictions and computational analyses of a wide variety of structure-frozen soil/ ice interaction problems encountered in engineering practice. As discussed later in §3.6, much effort was expended to establish the accuracy and the reliability of the codes developed here. The range of applicability of these finite element codes has been greatly broadened by presenting a choice of three different (basic) constitutive models, and by allowing for the incorporation of additional models in the future, as and when such need arises.

Due to the variety of creep constitutive models and structure-frozen media problems considered, it became apparent that the most convenient procedure would be to develop several finite element codes, with each code confined to a certain class of problems and/or models. The broadest such division was made between continuum analyses (which are based on 2-D and 3-D continuum elements), and beam analyses (based on 1-D beam elements on viscous media). Thus the present Chapter is restricted to codes for continuum analyses, whereas codes developed for beam elements on viscous media are discussed in Chapter 5 (§5.2.2, 5.2.3, and 5.2.4). Although finite elements developed for the modelling of adfreeze/bond phenomena were ultimately incorporated into a code based on continuum analysis, all details concerning computational modelling of adfreeze/bond strength are given in Chapter 6, mainly because of the slight variation in the numerical approach involved in the development of such elements.

As mentioned in Chapter 2, creep constitutive models considered in this dissertation are the power law model (Glen 1955, Nye 1956, Vyalov 1963, Klein 1979), Fish's unified model (Fish 1984, 1987), and Domaschuk's model (Rahman 1988, Domaschuk et al. 1991). The numerical algorithm to be used in the case of each model is governed by the mathematical form of the respective model. Thus the first two models are incorporated in an iterative, time-incrementing finite element algorithm, while the latter model is incorporated in an iterative, load-incrementing finite element algorithm. These algorithms and the numerical considerations with respect to each model are discussed in the ensuing sections of this Chapter. However, basic relationships in the Finite Element Method (Zienkiewicz 1977, Chap. 5) apply regardless of the incremental algorithm used, and as such, these would be briefly outlined here.

A continuum material domain of volume V and surface area S is considered to be discretized by a mesh of finite elements. At any point within the material domain, the displacement vector will be denoted by $\mathbf{u}$, strain vector by $\boldsymbol{\epsilon}$ and stress vector by $\boldsymbol{\sigma}$. The vector of nodal displacements will be denoted by $\mathbf{a}$. Vectors $\mathbf{u}$, $\boldsymbol{\epsilon}$, and $\mathbf{a}$ are related to each other as follows:

$$\boldsymbol{\epsilon} = [L]\,\mathbf{u}, \qquad \mathbf{u} = [N]\,\mathbf{a} \qquad \text{and} \qquad \boldsymbol{\epsilon} = [L]\,[N]\,\mathbf{a} = [B]\,\mathbf{a}. \tag{3.1}$$

In (3.1), $[N]$ is the shape function matrix and $[L]$ is a differential operator matrix obtained through standard formulations of solid mechanics (see Appendix A). Equilibrium of the material domain at any given time t_k can be written as,

$$\int_V [B]^T \boldsymbol{\sigma}_k \, dV + \mathbf{f}_k = \mathbf{0}, \tag{3.2}$$

where subscript k denotes that the relevant quantity is considered at time t_k, $\mathbf{f}_k$ is the known force vector made up of the prescribed surface traction forces $\mathbf{T}_k$ on the surface S and of the body forces $\mathbf{b}_k$, given by,

$$\mathbf{f}_k = -\int_V [N]^T \mathbf{b}_k \, dV - \int_S [N]^T \mathbf{T}_k \, dS\,, \tag{3.3}$$

and all other notations are as given earlier.

3.2 Numerical Implementation of Creep Constitutive Models

It is possible to base creep constitutive models on different concepts or hypotheses (Nye 1956, Vyalov 1965b, Hult 1966, Odqvist 1966, Christensen 1971, Fish 1984, Domaschuk et al. 1991). A broad class of creep constitutive models have been presented on the basis of elastic visco-plasticity (Vyalov 1965b, Odqvist 1966). One concept used to describe the constitutive behaviour of these materials is to decompose the total deformation into a recoverable elastic component, and non-recoverable plastic and viscous components. Plastic deformations are time-independent and viscous deformations are considered as time- (or strain-) dependent. Variations in the consideration of these components exist, since, for example, it is possible to define a linear, non-linear, isotropic, or anisotropic elastic component, or delete the elastic component altogether and consider only a non-recoverable plastic deformation component, in addition to the pertinent viscous deformation component. Many functional forms are available to describe the plastic deformation component (Odqvist 1966, Zienkiewicz and Cormeau 1974).

Under the concept where the total deformation is decomposable into individual components, the total current strain tensor $\epsilon(t)$ can be written as,

$$\epsilon(t) = \epsilon^e(t) + \epsilon^p(t) + \epsilon^c(t) \ , \tag{3.4}$$

where $\epsilon^e(t)$ is the current elastic strain tensor, $\epsilon^p(t)$ is the current plastic strain tensor, $\epsilon^c(t)$ is the current creep strain tensor, and t is the current time (measured from the commencement of the deformation process). For the case of frozen soils and ice, $\epsilon^p(t)$ is assumed to be insignificant (Klein 1979), and $\epsilon^e(t)$ is related to stress $\sigma(t)$ as,

$$\sigma(t) = [D]\,\epsilon^e(t) \ , \tag{3.5}$$

where $[D]$ is the isotropic linear elastic (Hooke's) constitutive matrix (Timoshenko and Goodier 1951, and Appendix A). The viscous (or creep) component of the strain tensor is most conveniently expressed in a rate form, as is the case with respect to the power law model (see equation 3.16) or the unified model of Fish (see equation 3.28). It is noted that equations (3.4)–(3.5), in the absence of $\epsilon^p(t)$, represent a

mechanical model consisting of a linear elastic spring connected in series with a dash-pot, which represents the viscous deformations.

An alternate class of creep constitutive models can be proposed analogous to incremental elasticity or hypoelasticity (Truesdell 1955), where the pertinent constitutive relationship can be stated as,

$$d\epsilon = [\hat{C}]\, d\sigma \ , \tag{3.6}$$

where $d\epsilon$ and $d\sigma$ are infinitesimal strain and stress tensors, and $[\hat{C}]$ is the constitutive matrix. The elements of $[\hat{C}]$ above are not constants but are functions of stress, temperature, etc., whereas time occurs to the same order in all terms implying that the relationship is time-independent. Equation (3.6) had been adopted by Domaschuk et al. (1985), Rahman (1988), and Domaschuk et al. (1991) to propose an incremental constitutive model for creep of frozen sands.

In order to implement the selected creep constitutive models in finite element schemes, it is necessary to obtain the relationship between the components of stress and strain tensors in an explicit manner. Since the original forms of the power law model and Fish's unified model are restricted to uniaxial stress-strain fields, the generalization of these models to multi-axial states of stress and strain will be briefly discussed in the ensuing sub-sections, and the componential form of constitutive relations for each model will be derived in turn. Domaschuk's model is proposed for multi-axial stress and strain fields, and requires no further generalization. Tensorial notation will be used in the following work to denote tensor components.

3.2.1 Power Law Model

The basic concept of the constitutive model used here is that the total strain vector consists of an elastic strain component and a creep strain component, i.e.

$$\epsilon(t) = \epsilon^e(t) + \epsilon^c(t) \ , \tag{3.7}$$

where $\epsilon(t)$, $\epsilon^e(t)$, $\epsilon^c(t)$, and t are all as defined earlier (see equation 3.4). The elastic strain tensor can be related to the stress vector through the use of a linear elastic constitutive matrix $[D]$ as given by equation (3.5).

For uniaxial straining of viscoelastic materials in the secondary creep stage, Odqvist (1966) presented Norton's power law (Norton 1929) as,

$$\frac{d\epsilon^c(t)}{dt} = \dot{\epsilon}_c \left(\frac{\sigma}{\sigma_c} \right)^{\rho} , \tag{3.8}$$

where $\epsilon^c(t)$ is the current creep strain, σ the stress, and $\dot{\epsilon}_c$ an arbitrary standard value of the creep strain rate for which $\sigma = \sigma_c$, and σ_c and ρ are material constants depending on temperature, particularly in the case of σ_c. Odqvist (1966) hypothesized equation (3.8), originally stated for a constant stress σ, to hold also for a time-dependent stress $\sigma(t)$, and presented the following expression to describe total deformation (in the absence of plastic deformations):

$$\epsilon(t) = \epsilon^e + \int_0^t \dot{\epsilon}_c \left(\frac{\sigma}{\sigma_c} \right)^{\rho} dt \ . \tag{3.9}$$

A more general version of equation (3.9) which accounts for plastic deformations has also been given by Odqvist (1966). For frozen soils and ice, materials which show creep properties (not restricted to secondary creep), the equation (3.8) can be written in an equivalent form as,

$$\dot{\epsilon}^c(t) = AC\, \sigma(t)^B\, t^{C-1} \ , \tag{3.10}$$

where $\dot{\epsilon}^c(t)$ denotes creep strain rate, $\sigma(t)$ is as defined earlier, t is the elapsed time from the instant of stressing of the material, and A, B, C are creep parameters. A has units of $(\text{stress})^{-B}(\text{time})^{-C}$ while B and C are dimensionless. For a constant stress σ, integration of equation (3.10) with respect to time yields the following widely used form of the uniaxial, constant stress creep equation:

$$\epsilon^c \ = \ A\, \sigma^B\, t^C \ , \tag{3.11}$$

In the field of frozen geomaterials, equation (3.11) is the model used by experimental research workers (Glen 1955, Vyalov 1963, Klein 1979) to evaluate the material parameters A, B, and C. For frozen soils, A is strongly dependent on the

temperature while B and C vary only slightly with it. For $C < 1$, equations (3.10) or (3.11) describe the primary creep stage of a standard creep (ϵ vs σ) curve, or, alternately, the entire creep curve of an attenuating creep example, which occurs when the material is subjected to a low stress level.

Generalization of equation (3.10) to cases of three-dimensional stress and strain has been performed in the literature (Nye 1956, Vyalov 1963 & 1965b, Hult 1966, Odqvist 1966, Klein and Jessberger 1979) through several approaches. Pertinent assumptions used for the generalization are that the material is isotropic and incompressible, creep strain rate is uninfluenced by a superposed hydrostatic pressure, tensors of stress and strain rate are coaxial, equation (3.10) holds for the uniaxial case, and elastic strains are very small compared to creep strains. An exception to the incompressibility requirement during creep was suggested by Vyalov (1963). In most cases (Nye 1956, Hult 1966, Odqvist 1966, Klein and Jessberger 1979), the generalization is made using the same concepts as for the Von Mises hypothesis in the theory of plasticity (Hill 1950). Accordingly, use is made of an equivalent stress σ_e and an equivalent creep strain rate $\dot{\epsilon}^c_e$, respectively, given by,

$$\sigma_e \;=\; \sqrt{(3/2)\, s_{ij}\, s_{ij}} \quad \text{and} \quad \dot{\epsilon}^c_e \;=\; \sqrt{(2/3)\, \dot{\epsilon}^c_{ij}\, \dot{\epsilon}^c_{ij}}\;, \tag{3.12}$$

where summation is implied over indices i and j, $(i, j = 1, 2, 3)$, $\dot{\epsilon}^c_{ij}$ denotes the components of the creep strain rate tensor and s_{ij} denotes the deviatoric stress tensor (Hill 1950, Hult 1966, Odqvist 1966) given by,

$$s_{ij} \;=\; \sigma_{ij} \;-\; 1/3\, \delta_{ij}\, \sigma_{kk}\;, \tag{3.13}$$

where σ_{ij} is the stress tensor and δ_{ij} is the Kronecker delta. Generalization is achieved by assuming that equation (3.10) is applicable to equivalent stress and equivalent strain rate (Hult 1966, Odqvist 1966, Klein and Jessberger 1979, Chehayeb et al. 1987), i.e.,

$$\dot{\epsilon}^c_e(t) \;=\; AC\, \sigma_e(t)^B\, t^{C-1}\;. \tag{3.14}$$

In view of the assumed non-influence of hydrostatic stress on the creep process, it is hypothesized that creep occurs due to the deviatoric stress tensor. Hence it is as-

sumed that the components of the creep strain rate tensor are directly proportional to the corresponding components of the deviatoric stress tensor (Prandtl-Reuss relations, Hill 1950). Thus the following relationship is obtained, under the condition that it yields the correct expression (equation 3.10) when reduced to the uniaxial case:

$$\dot{\epsilon}^c_{ij}(t) = \frac{3}{2}\frac{\dot{\epsilon}^c_e(t)}{\sigma_e(t)} s_{ij}(t) \ . \tag{3.15}$$

Substitution of equations (3.14) and (3.12) in equation (3.15) yields the following expression for the components of strain-rate tensor (Hult 1966, Odqvist 1966, Klein and Jessberger 1979):

$$\dot{\epsilon}^c_{ij}(t) = \frac{3}{2} AC \left[\frac{3}{2} s_{kl}(t)\, s_{kl}(t)\right]^{\frac{B-1}{2}} s_{ij}(t)\, t^{C-1} \ . \tag{3.16}$$

Equation (3.16) above is in an appropriate form to be implemented in a time incrementing finite element algorithm, and its time integral represents $\epsilon^c(t)$ used in equations (3.7) or (3.4). Explicit expressions of $\dot{\epsilon}^c_{ij}(t)$ for different continuum elements are given in Appendix A.

Equations (3.10), (3.14) and (3.16) have been hypothesized for situations of time dependent stresses, and therefore one may naturally assume that these equations need no modifications when applied to situations of loads applied in distinct steps. Unfortunately, experimental evidence (Ladanyi and Johnston 1973, Eckardt 1979, Thimus 1988) indicates otherwise, and sharp increases in the deformation rates observed immediately following the application of a new load step dictate a modification or extension of equations (3.14) and (3.16) to cover such situations as multiple-step loadings. A similar requirement is addressed by Hult (1966) in his treatment of creep in metals. Thus on phenomenological grounds alone, extension of the basic model in equations (3.14) and (3.16) to multiple loads may be undertaken in such a manner as to reasonably simulate the observed creep behaviour. In so doing, the rationale for maintaining a time-dependent stress in equations (3.14) or (3.16) should now be interpreted as accommodation of transient stresses within a single load step, or as accounting for quasi-static loading cases where the time rates

of load variations are very low. As Hult (1966) notes, such modified phenomenological creep models may assume different forms depending on the accuracy that is required from their predictions, and no claims are made that the laws of such theories are derivable from other laws of physics. Two such modified models are considered in this dissertation, and these modifications will be denoted by **Power Law Extension I**, and **II**, respectively, in the following work. It is noted that the classical theory of viscoelasticity (Christensen 1971) accounts for multiple load steps and/or varying stresses through the use of the hypothesis of fading memory, by which the history of deformation is made more dependent on the recent than the distant deformation events. However, this approach had not been followed in most of the experimental programs on frozen soils and ice.

Power Law Extension I:

Thimus (1988) proposed a modified power law model for a uniaxial, multi-step load case, which, for two-step loads can be written as:

$$\text{for } t < t_1 \; ; \qquad \epsilon^c(t) = A\,\sigma_1^B\,t^C \quad , \tag{3.17a}$$

$$\text{and} \qquad \text{for } t > t_1 \; ; \qquad \epsilon^c = A\left[\sigma_1^{\frac{B}{C}}\,t_1 + (\sigma_1+\sigma_2)^{\frac{B}{C}}\,(t-t_1)\right]^C \quad . \tag{3.17b}$$

In the above, σ_1 is the stress applied initially (at $t = 0$), σ_2 is the stress increment applied at $t = t_1$ and t is the current time measured from $t = 0$. Equation (3.17a) was generalized to yield an equation similar to (3.14), and the time derivative of equation (3.17b) was generalized as:

$$\dot{\epsilon}_e^c = AC\left[\sigma_{1e}(t_1)^{\frac{B}{C}}\,t_1 + \sigma_e(t)^{\frac{B}{C}}\,(t-t_1)\right]^{C-1}\sigma_e(t)^{\frac{B}{C}} \quad , \tag{3.18}$$

where $\sigma_e(t)$ is the total equivalent stress at the current time t and $\sigma_{1e}(t_1)$ is the equivalent stress that existed at t_1 prior to the application of the second load increment. Using equation (3.15), expressions for components of the creep strain rate tensor can be derived for $t < t_1$ and $t > t_1$, respectively, and are given in Appendix A. These latter expressions serve as the appropriate flow model. Thimus (1988) presents the extension of the above model for more than two load steps. Due to the

form in which equation (3.17b) is written, the power term of stress is not B and the power term of time is not C, except for the special case where $C = 1$.

Power Law Extension II:

It is possible to propose an alternate extension of the basic generalized power law to account for multiple load steps, based on a hypothesis that each time a new load step is introduced, creep mechanism manifests as a fresh response depending on the total stress existing at the moment and the time elapsed from the start of the latest load increment (see Hult 1966 for a similar interpretation). Under this model, the generalized form of the creep strain rate during the ith load step can be written as:

$$\dot{\epsilon}_e^c(t) = AC\sigma_e(t)^B \left(t - t_{i-1}\right)^{C-1} , \tag{3.19}$$

where $\sigma_e(t)$ is the resultant equivalent stress at the current time t, and t_{i-1} $(i = 1, 2, ..)$ is the time at which the ith load step is applied. As before, expressions for components of the strain rate tensor $\dot{\epsilon}_{ij}^c(t)$ can be derived (see Appendix A), and $\epsilon^c(t)$ in equations (3.7) or (3.4) now represents the total time integral of $\dot{\epsilon}_{ij}^c(t)$ from $t = 0$ to the current time.

3.2.2 Fish's Unified Model

Fish's unified creep model (Fish 1984, 1987) is incorporated in a finite element algorithm, using the constitutive concept in equation (3.7) as the basis. For this purpose, componential expressions for creep strain rate tensor $\dot{\epsilon}_{ij}^c(t)$ are obtained by generalizing the uniaxial creep model of Fish (1987). Fish's uniaxial creep model is proposed in such a way that the flow equation is separated from the shape function. Such separation was possible due to the fact that creep curves for a great majority of solids show a similarity, with the major difference between each other being the magnitude of the parameters used in the flow equation. It was noted that this type of separation is most suitable for ice and frozen soils. Accordingly, Fish (1984, 1987) suggested the following product of two functions to describe the uniaxial strain rate

of ice in the case of constant stress and temperature:

$$\dot{\epsilon}^c(t) = \dot{\epsilon}_m \, F(\bar{t}) \ , \tag{3.20}$$

where $\dot{\epsilon}^c(t)$ is the current creep strain rate which is a function of time, stress and temperature, $\dot{\epsilon}_m$ is the minimum strain rate, $F(\bar{t})$ is a dimensionless shape function, and $\bar{t}$ is the dimensionless time given by,

$$\bar{t} = t/t_m \ , \tag{3.21}$$

where t is the actual elapsed time and t_m is the time to failure as defined by Fish. The model proposed by Fish for the uniaxial constant stress and temperature is as shown in Figure 2.1, where the failure is defined to occur at point 'm'. The time to reach point 'm' is defined as the failure time t_m. As discussed in §2.3 (Figure 2.1), the material first shows a primary creep response during which the strain rate consistently decreases, followed by a momentary creep stage (point 'm') which is hereafter referred to as the failure point, and a final stage of tertiary or accelerating creep. The shape function $F(\bar{t})$ in equation (3.20) is given as,

$$F(\bar{t}) = \exp\left\{\delta(\bar{t} - \ln \bar{t} - 1)\right\} \ , \tag{3.22}$$

where δ is a dimensionless parameter of the shape. For $t = t_m$, equations (3.22) and (3.20) yield $F(\bar{t}) = 1$ and $\dot{\epsilon}^c = \dot{\epsilon}_m$, indicating the secondary creep stage or the failure point, while for primary creep ($t < t_m$) and tertiary creep ($t > t_m$) it is seen that $F(\bar{t}) > 1$. Fish (1984, 1987) stated that for a great number of materials the value of δ is within the limits $0 < \delta < 1$, and evaluated $\delta \approx 0.47$ for ice by considering the test data of Jacka (1984) and Ashby and Duval (1985) within the stress and temperature ranges considered. No definite dependency of δ upon stress and temperature for polycrystalline ice was found, whereas such dependency was quoted to be more certain for frozen soils (Fish 1987).

It is seen that both the failure strain rate $\dot{\epsilon}_m$ and the time to failure t_m are functions of stress and temperature. The functional forms given by Fish (1984) for

the above relationships are:

$$\dot{\epsilon}_m = \frac{\widetilde{C}}{t_m} \left(\frac{\sigma}{\sigma_0} \right)^{\zeta} \quad , \tag{3.23}$$

and

$$t_m = t_0 \left(\frac{\sigma}{\sigma_0} \right)^{-\eta} \quad , \qquad \text{for} \quad \sigma \leq \sigma_0 \ , \tag{3.24}$$

where $\widetilde{C}$ is a material constant, ζ and η are parameters to be evaluated from experiments, t_0 is the mean duration of the settled life of an elementary particle in a position of equilibrium (Frenkel 1947) which in turn depends on temperature, and σ_0 is known as the instantaneous strength of soil (the stress that will cause failure at time $t_m = t_0$). Equations (3.23) and (3.24) can be combined to show that $\dot{\epsilon}_m$ is proportional to σ^{μ}, where $\mu = \eta + \zeta$. The dependence of $\dot{\epsilon}_m$ and t_m on the stress σ is evident from published test data (e.g. Yuanlin and Carbee 1983, Jacka 1984, Shields et al. 1989). Therefore, when the model given here (equation 3.20) is used for prediction purposes, it is necessary to determine the relationship between σ and $\dot{\epsilon}_m$ as well as that between σ and t_m within different stress ranges (assuming isothermal conditions).

The above uniaxial model of Fish (1984, 1987) can be generalized to multiaxial states of stress and strain, by assuming that the material is isotropic and incompressible, and by following a procedure identical to that used for generalizing the power law earlier (§3.2.1). Such an approach is possible since the generalization procedure is independent of the particular form of the creep law, provided the latter is expressed in a time-rate form. Therefore, under the same assumptions as made for the power law model earlier, an equivalent stress σ_e and an equivalent creep strain rate $\dot{\epsilon}_e^c$ are defined as given by equations (3.12) and (3.13), and the Prandtl-Reuss relations (Hill 1950) are hypothesized as given by equation (3.15). Similar to the earlier case, the generalization of Fish's uniaxial model is achieved by assuming that equations (3.20) and (3.22) can be applied to the equivalent stress and equivalent creep strain rate, i.e.,

$$\dot{\epsilon}_e^c = \dot{\epsilon}_{me} \ \exp\left\{\delta(\bar{t} - \ln \bar{t} - 1)\right\} \quad , \tag{3.25}$$

where

$$\bar{t} = \frac{t}{t_m} \ , \qquad \dot{\epsilon}_{me} = \frac{\widetilde{C}}{t_m} \left(\frac{\sigma_e}{\sigma_0} \right)^{\zeta} \ , \qquad \text{and} \qquad t_m = t_0 \left(\frac{\sigma_e}{\sigma_0} \right)^{-\eta} \ , \quad \text{for} \ \ \sigma_e \leq \sigma_0 \ . \tag{3.26}$$

In the above, $\dot{\epsilon}_{me}$ is an equivalent minimum strain rate, and $\widetilde{C}$, t_0, σ_0 and t_m are as defined for the uniaxial case. It is convenient to write approximate expressions for $\dot{\epsilon}_{me}$ and t_m in the following form:

$$\dot{\epsilon}_{me} = C_o \, \sigma_e^{\mu} \qquad ; \qquad t_m = A_1 \, \sigma_e^{-\eta} \ , \tag{3.27}$$

with $\mu = \zeta + \eta$. For particular values of η and μ, relations in equations (3.27) would be usually applicable within the stress and temperature range considered. Substituting equations (3.27) and (3.25) in equation (3.15), the following expression is obtained for the components of the creep strain rate tensor:

$$\dot{\epsilon}^c_{ij}(t) = \frac{3}{2} \, C_o \, \sigma_e^{\mu - 1} \, \exp\{\delta(\bar{t} - \ln \bar{t} - 1)\} \, s_{ij}(t) \ . \tag{3.28}$$

With $\bar{t}$ given by equations (3.26) and (3.27), above equation (3.28) serves as the multi-axial creep constitutive model for the present numerical study. The appropriate time integral of equation (3.28) represents $\epsilon^c(t)$ in equations (3.7) or (3.4). Explicit expressions for $\dot{\epsilon}^c_{ij}(t)$ for different continuum elements are given in Appendix B.

3.2.3 Domaschuk's Model

The multi-axial creep model proposed by Domaschuk (Rahman 1988, Domaschuk et al. 1991) requires no generalization, unlike the two previous originally uniaxial models (§3.2.1 and §3.2.2). An additional advantage in the case of this model is the incorporation of volumetric creep deformations, which implies that the compressibility of frozen materials is being taken into account here.

The model has been discussed in several instances (Domaschuk et al. 1985, Rahman 1988, Domaschuk et al. 1991). However, the following re-presentation of

the model appears to be more consistent with the original differential stress-strain concept in equation (3.6) and the standard conventions in geomechanics:

$$d\sigma_m = K_c \, d\epsilon_v \ , \tag{3.29a}$$

$$dS_d = G_c \, de_d \ , \tag{3.29b}$$

where,

$$d\sigma_m = d\sigma_{ii}/3 \quad ; \quad de_v = d\epsilon_{ii} \ , \tag{3.30}$$

and,

$$dS_d = \sqrt{ds_{ij} \, ds_{ij}} \quad ; \quad de_d = 2\sqrt{de_{ij} \, de_{ij}} \ . \tag{3.31}$$

In above, a prefix d denotes that a differential or infinitesimal amount of the relevant quantity is being considered; σ_m, ϵ_v, S_d, and e_d are referred to as volumetric mean stress, volumetric strain, resultant deviatoric stress, and resultant deviatoric strain, respectively; K_c denotes the Bulk Creep Function; G_c denotes the Shear Creep Function; and, ds_{ij} is a differential deviatoric stress tensor and de_{ij} a differential deviatoric strain tensor, which can be defined, respectively, as,

$$ds_{ij} = d\sigma_{ij} - 1/3 \, \delta_{ij} \, d\sigma_{kk} \ , \quad \text{and} \quad de_{ij} = d\epsilon_{ij} - 1/3 \, \delta_{ij} \, d\epsilon_{kk} \ . \tag{3.32}$$

Both K_c and G_c are tangent modulii, the functional form of which had been derived as (Rahman 1988),

$$K_c = K_0 \left(1 + \frac{1}{K_0} \, \phi \exp\{-\kappa t\} \sigma_m\right)^2 \ , \tag{3.33}$$

and,

$$G_c = \left(m_1 \, \sigma_m^{\beta} \, t^{n_1} + c t^{\alpha} \, \frac{S_d}{\sigma_m}\right)^{-1} \ , \tag{3.34}$$

where, t is the current time, K_0, ϕ, κ, m_1, β, n_1, c, and α can be referred to as material constants which are evaluated by manipulating the curves fitted to test

data (Rahman 1988), and σ_m and S_d are, respectively, the current volumetric mean stress and current resultant deviatoric stress, defined as,

$$\sigma_m = \sigma_{ii}/3 \ , \qquad \text{and} \qquad S_d = \sqrt{s_{ij}\, s_{ij}} \ . \tag{3.35}$$

Equations (3.33) and (3.34) show that both K_c and G_c are functions of the current stress state $\boldsymbol{\sigma}$, and the current time t measured from the commencement of the deformation process. Therefore, in the numerical implementation of the above model, equations (3.29), (3.33) and (3.34) should be integrated with respect to the loading (i.e., by incrementing the applied load in several small steps), and the solutions thus obtained would hold for a given elapsed time t under a given loading system. Accordingly, this model is incorporated in the load-incrementing finite element scheme detailed in §3.4. In view of equations (3.29)–(3.32), the componential form of the stress-strain relationship, which is required for the finite element scheme, can be written as,

$$d\sigma_{ij} = K_c\, d\epsilon_{kk}\, \delta_{ij} + 2G_c\, (d\epsilon_{ij} - 1/3\, d\epsilon_{kk}\, \delta_{ij}) \ . \tag{3.36}$$

The matrix form of equation (3.36) is given in Appendix C. It should be noted that equation (3.36) represents the isotropic form of the constitutive behaviour, which was assumed by Rahman (1988) and Domaschuk et al. (1991) at the outset. Inclusion of anisotropy (by assuming coupling between normal stresses and shear strains, and between shear stresses and normal strains) is possible, although it complicates the model; a possible extension of the above model (equations 3.29 and 3.36) to anisotropy is discussed by Yin (1990).

3.3 Time-Incrementing, Iterative, Finite Element Algorithm

The time-incrementing, iterative, finite element algorithm, used for the implementation of the power law creep model (§3.2.1) and Fish's unified creep model (§3.2.2), will be discussed in this section. The algorithm presented here is based on previous treatments of this subject by Zienkiewicz (1977) and Hughes and Taylor (1978). Recalling the material domain under consideration (§3.1), equilibrium at

any time t_k is as given in equation (3.2), and, in view of equations (3.5) and (3.7), the stress-strain relationship is:

$$\boldsymbol{\sigma}_k = [D]\{\boldsymbol{\epsilon}_k - \boldsymbol{\epsilon}_k^c\} , \tag{3.37}$$

where all notations are as given earlier. For time incrementing algorithms, the time history is assumed to be discretized by time intervals or steps, and the time t_k is reached after the accumulation of k time steps starting from the initial time $t = 0$. Thus, at the end of the next interval Δt_k, the total elapsed time will be $t_{k+1} = t_k + \Delta t_k$. The solution needed is the evaluation of $\mathbf{a}_{k+1}$ and $\boldsymbol{\sigma}_{k+1}$ at the time t_{k+1}, given that $\mathbf{a}_k$ and $\boldsymbol{\sigma}_k$ at time t_k are known. Equilibrium at time t_{k+1} can be written as,

$$\int_V [B]^T \boldsymbol{\sigma}_{k+1}\, dV \;+\; \mathbf{f}_{k+1} \;=\; \mathbf{0}. \tag{3.38}$$

In view of equations (3.1) and (3.37), the expression for the difference between the stress vectors $\boldsymbol{\sigma}_{k+1}$ and $\boldsymbol{\sigma}_k$ can be expressed in the following form:

$$\boldsymbol{\psi}_{k+1} \;\equiv\; \boldsymbol{\sigma}_{k+1} - \boldsymbol{\sigma}_k - [D]\,[B]\,\{\mathbf{a}_{k+1} - \mathbf{a}_k\} + [D]\,\Delta t_k\,\boldsymbol{\beta}(\boldsymbol{\sigma}_{k+\theta}) \;=\; \mathbf{0}. \tag{3.39}$$

In the above, the following relationship has been used:

$$\boldsymbol{\epsilon}_{k+1}^c - \boldsymbol{\epsilon}_k^c \;=\; \boldsymbol{\beta}(\boldsymbol{\sigma}_{k+\theta}) \cdot \Delta t_k \;, \tag{3.40}$$

where $\boldsymbol{\beta}$ denotes the strain rate vector given by equation (3.16) in the case of the power law model (see Appendix A for the Power Law Extensions I and II), and by equation (3.28) in the case of Fish's unified model, and,

$$\boldsymbol{\sigma}_{k+\theta} \;=\; (1-\theta)\,\boldsymbol{\sigma}_k \;+\; \theta\,\boldsymbol{\sigma}_{k+1} \;, \qquad (0 \le \theta \le 1) \;. \tag{3.41}$$

Starting from the known values of $\boldsymbol{\sigma}_k$ and $\mathbf{a}_k$, the Newton-Raphson procedure (see Zienkiewicz 1977) is used to iterate within the time interval Δt_k for the unknowns $\boldsymbol{\sigma}_{k+1}$ and $\mathbf{a}_{k+1}$. The iteration number is denoted by a superscript numeral, and the iterations are started from the following initial guesses:

$$\boldsymbol{\sigma}_{k+1}^0 = \boldsymbol{\sigma}_k \qquad \text{and} \qquad \mathbf{a}_{k+1}^0 = \mathbf{a}_k. \tag{3.42}$$

After successive iterations, the iteration cycle n can be reached, while the selected convergence criterion (given by equation 3.53) may not yet be satisfied. Thus equations (3.38) and (3.39) can be written as,

$$\boldsymbol{\chi}^{n}_{k+1} \;=\; \int_V [B]^T \boldsymbol{\sigma}^{n}_{k+1}\, dV \;+\; \mathbf{f}_{k+1} \;\neq\; \mathbf{0}, \tag{3.43}$$

and,

$$\boldsymbol{\psi}^{n}_{k+1} \;=\; \boldsymbol{\sigma}^{n}_{k+1} - \boldsymbol{\sigma}_k - [D]\,[B]\,\{\mathbf{a}^{n}_{k+1} - \mathbf{a}_k\} + [D]\,\Delta t_k\,\boldsymbol{\beta}(\boldsymbol{\sigma}^{n}_{k+\theta}) \;\neq\; \mathbf{0}, \tag{3.44}$$

where

$$\boldsymbol{\sigma}^{n}_{k+\theta} \;=\; (1-\theta)\,\boldsymbol{\sigma}_k + \theta\,\boldsymbol{\sigma}^{n}_{k+1}\;, \qquad (0 \le \theta \le 1)\;. \tag{3.45}$$

In the above, use of $\theta = 1,\ 1/2$ or 0 results in, respectively, a fully implicit iterative, an implicit-explicit (where iterations may or may not be incorporated), or a fully explicit, numerical scheme. Using the curtailed Taylor expansion on equations (3.43) and (3.44), the following expressions can be written:

$$\boldsymbol{\chi}^{n+1}_{k+1} \;=\; \boldsymbol{\chi}^{n}_{k+1} \;+\; \int_V [B]^T\,\Delta\boldsymbol{\sigma}^{n}_{k+1}\, dV\;, \tag{3.46}$$

and,

$$\boldsymbol{\psi}^{n+1}_{k+1} \;=\; \boldsymbol{\psi}^{n}_{k+1} \;+\; \Delta\boldsymbol{\sigma}^{n}_{k+1} - [D]\,[B]\,\Delta\mathbf{a}^{n}_{k+1} + [D]\,\Delta t_k\,[S]^n\,\theta\,\Delta\boldsymbol{\sigma}^{n}_{k+1}\;, \tag{3.47}$$

where matrix $[S]^n$ given by,

$$[S]^n \;=\; \left(\frac{\partial\boldsymbol{\beta}}{\partial\boldsymbol{\sigma}}\right)\;, \tag{3.48}$$

is evaluated for $\boldsymbol{\sigma}^{n}_{k+\theta}$. By assuming that solutions have converged at the $(n+1)$th iteration, the above expressions (3.46) and (3.47) can be set equal to zero. This results in the following two equations which would yield the incremental corrections $\Delta\boldsymbol{\sigma}^{n}_{k+1}$ and $\Delta\mathbf{a}^{n}_{k+1}$ upon solution:

$$\Delta\boldsymbol{\sigma}^{n}_{k+1} = [\bar{D}]^n\Big[[B](\Delta\mathbf{a}^{n}_{k+1} + \mathbf{a}^{n}_{k+1} - \mathbf{a}_k) - [D]^{-1}(\boldsymbol{\sigma}^{n}_{k+1} - \boldsymbol{\sigma}_k) - \Delta t_k\,\boldsymbol{\beta}(\boldsymbol{\sigma}^{n}_{k+\theta})\Big], \tag{3.49}$$

and,

$$\int_V [B]^T[\bar{D}]^n[B]\,\Delta\mathbf{a}_{k+1}^n\,dV = \int_V [B]^T[\bar{D}]^n\Big\{[D]^{-1}(\boldsymbol{\sigma}_{k+1}^n - \boldsymbol{\sigma}_k) - [B](\mathbf{a}_{k+1}^n - \mathbf{a}_k) + \Delta t_k\,\boldsymbol{\beta}(\boldsymbol{\sigma}_{k+\theta}^n)\Big\}\,dV - \int_V [B]^T\boldsymbol{\sigma}_{k+1}^n\,dV - \mathbf{f}_{k+1}\ , \quad (3.50)$$

where matrix $[\bar{D}]^n$ is given by,

$$[\bar{D}]^n = \Big[[D]^{-1} + \Delta t_k[S]^n\theta\Big]^{-1}\ . \quad (3.51)$$

The solution is now updated as

$$\boldsymbol{\sigma}_{k+1}^{n+1} = \boldsymbol{\sigma}_{k+1}^n + \Delta\boldsymbol{\sigma}_{k+1}^n \qquad \text{and} \quad \therefore\ \mathbf{a}_{k+1}^{n+1} = \mathbf{a}_{k+1}^n + \Delta\mathbf{a}_{k+1}^n\ . \quad (3.52)$$

If convergence has occurred at the above $(n+1)$ th iteration, we set $\boldsymbol{\sigma}_{k+1} = \boldsymbol{\sigma}_{k+1}^{n+1}$ and $\mathbf{a}_{k+1} = \mathbf{a}_{k+1}^{n+1}$, and proceed to the next time step; otherwise iteration is continued.

As per the basic constitutive concept in equations (3.5) and (3.7), the solution process is initiated by obtaining the instantaneous elastic deformations and stress distribution at the time of application of the initial load ($t = 0$). These displacement and stress vectors are then used to obtain the incremental displacement and stress vectors during the first time interval Δt_0, by solving equations (3.49) and (3.50) through the iterative process outlined earlier. For the iterative scheme, the following convergence criterion is used:

$$\|\Delta\mathbf{a}_k^n\| \ < \ 0.01 \times \|\Delta\mathbf{a}_k^{n-1}\|\ , \quad (3.53)$$

where $\|\mathbf{x}\|$ denotes the Euclidean norm of the relevant vectorial quantity $\mathbf{x}$. It should be noted that many alternative convergence criteria may be employed (Owen and Hinton 1980). The solution process is repeated for each time interval, until the final time instance is reached where the analysis is terminated.

Explicit expressions for the matrices $\boldsymbol{\sigma}$, $\boldsymbol{\epsilon}$, $[D]$, $\boldsymbol{\beta}$, $[\bar{D}]$, $[S]^n$, etc. for different types of finite elements (plane stress, plane strain, axisymmetry, plane strain axisymmetry, three-dimensional, and simple one dimensional) are given in Appendix

A for the case of Power Law models, and in Appendix B for the case of Fish's unified creep model.

3.4 Load-Incrementing, Iterative, Finite Element Algorithm

The load incrementing, iterative, finite element algorithm used to implement the model of Domaschuk (§3.2.3) is detailed in this section. In fact, this algorithm is usable for all problems with pure material non-linearity where no time integration is required (Zienkiewicz 1977, Owen and Hinton 1980). Therefore, as far as the numerical implementation is considered, Domaschuk's model can be categorized under the class of non-linear elasticity problems. The time of solution (which is a pertinent quantity for a creep model) appears merely as an input data equivalent to a material parameter, in the constitutive functions of Domaschuk's model (equations 3.33, 3.34 and Appendix C).

Let the incremental constitutive relationship postulated by Domaschuk's model be denoted by (see Appendix C):

$$d\boldsymbol{\sigma} = [\bar{D}]\, d\boldsymbol{\epsilon} \ . \tag{3.54}$$

Let $\mathbf{f}$ be the total load applied on the system. Since the load is applied on the system in steps (or increments), it is possible to consider the system at any given fraction λ of the total load, denoted by $\lambda\mathbf{f}$. Thus after the application of the pth load increment, the equilibrium of the continuum domain (originally expressed by equation 3.2) can be re-written as,

$$\boldsymbol{\chi}_p \equiv \int_V [B]^T \boldsymbol{\sigma}_p \, dV + \lambda_p \mathbf{f} = \mathbf{0} \ , \qquad 0 < \lambda \leq 1 \ . \tag{3.55}$$

Note that the use of a subscript p in this section denotes that the relevant quantity is being considered at the pth load increment, and that the present fraction of the applied load $\lambda_p\mathbf{f}$ could be equivalently denoted by $\mathbf{f}_p$. Because of the functional form of the constitutive functions K_c and G_c (Appendix C), performance of iterative corrections within each load increment is essential for accurate solutions.

Thus the equilibrium at the nth iteration during a given $(p+1)$th load increment can be written as,

$$\boldsymbol{\chi}_{p+1}^{n} \equiv \int_V [B]^T \boldsymbol{\sigma}_{p+1}^{n}\, dV + \lambda_{p+1}\mathbf{f} \neq \mathbf{0}\ , \tag{3.56}$$

where a superscript n denotes that the nth iteration is being considered, and the unequal sign has been used to denote that exact equilibrium has not been achieved yet. By applying the curtailed Taylor series expansion, the above equation can be written as,

$$\boldsymbol{\chi}_{p+1}^{n+1} \equiv \boldsymbol{\chi}_{p+1}^{n} + \int_V [B]^T \Delta\boldsymbol{\sigma}_{p+1}^{n}\, dV = \mathbf{0}\ , \tag{3.57}$$

which, in view of equation (3.56), can be re-written by collecting the accumulated incremental corrections during the $(p+1)$th load increment for the stress vector in one term, as follows:

$$\boldsymbol{\chi}_{p+1}^{n+1} \equiv \int_V [B]^T \delta\boldsymbol{\sigma}_{p+1}^{n}\, dV + \int_V [B]^T \boldsymbol{\sigma}_p\, dV + \lambda_{p+1}\mathbf{f} = \mathbf{0}\ . \tag{3.58}$$

The incremental stress-strain relation (equation 3.54) yields:

$$\delta\boldsymbol{\sigma}_{p+1}^{n} = [\bar{D}(\boldsymbol{\sigma}_{p+1}^{n}, t)]\, \delta\boldsymbol{\epsilon}_{p+1}^{n}\ , \tag{3.59}$$

where, in view of equations (3.1),

$$\delta\boldsymbol{\epsilon}_{p+1}^{n} = [B]\, \delta\mathbf{a}_{p+1}^{n}\ . \tag{3.60}$$

By substituting equations (3.59) and (3.60) in equation (3.58), the following equation is obtained to yield the incremental nodal displacement vector $(\delta\mathbf{a}_{p+1}^{n})$ for the nth iteration, upon solution:

$$\int_V [B]^T[\bar{D}(\boldsymbol{\sigma}_{p+1}^{n}, t)][B]\, \delta\mathbf{a}_{p+1}^{n}\, dV + \int_V [B]^T \boldsymbol{\sigma}_p\, dV + \lambda_{p+1}\mathbf{f} = \mathbf{0}\ . \tag{3.61}$$

After $\delta\mathbf{a}_{p+1}^{n}$ is evaluated from equation (3.61), the incremental stress vectors are computed by using equations (3.59) and (3.60). Once the specified convergence criterion is satisfied, the solutions are updated as,

$$\boldsymbol{\sigma}_{p+1} \equiv \boldsymbol{\sigma}_{p+1}^{n+1} = \boldsymbol{\sigma}_p + \delta\boldsymbol{\sigma}_{p+1}^{n} \qquad \text{and} \qquad \mathbf{a}_{p+1} \equiv \mathbf{a}_{p+1}^{n+1} = \mathbf{a}_p + \delta\mathbf{a}_{p+1}^{n}\ . \tag{3.62}$$

A convergence criterion identical to that given in equation (3.53) was used. The solution process is repeated for each load increment until the total load is reached ($\lambda = 1$). The explicit forms of matrices $d\sigma$, $d\epsilon$, $[B]$, $[\bar{D}]$, etc., involved in this section, are given in Appendix C.

3.5 On the Development of Finite Element Codes

In order to develop computer codes for this research, the elementary Finite Element Analysis Program (FEAP), developed by R.L. Taylor of the University of California, Berkeley (Zienkiewicz 1977, Chap. 24), was used as the basic skeleton. In its basic form, FEAP is capable of solving linear elastic problems using the finite element method. Later, FEAP was extended by Kanok-Nukulchai (1984) to solve static and dynamic problems under linear and non-linear elasticity. However, none of these versions of FEAP is capable of handling creep problems, or the accompanying complexities such as changes of boundary conditions during the analysis of a given problem. Therefore, only the basic algorithms needed for the mesh input reading, and solution of a symmetric or unsymmetric system of linear equations were extracted from the FEAP program. Time-incrementing schemes, iterative solution algorithms, necessary assembling and localization algorithms for arrays, ability to change boundary conditions or material properties during an analysis, etc. were incorporated to develop the time-incrementing computer codes here. Thus a complete new set of Macro commands were defined to control the execution of these codes. For load-incrementing codes, the same basic structure of FEAP as modified by Kanok-Nukulchai (1984) could be used, but considerable changes were necessary, e.g. to maintain stress values with respect to loading history.

As shown schematically in Figure 3.1, all computer codes developed here can be divided into the following two major components:

A. Main program section with system subroutines.

B. Element subroutines.

The main program section contains all system subroutines to perform the fol-

lowing tasks:

1. Read control parameters for each problem, and set up arrays for global and localized (elemental) arrays.
2. Read mesh input data, including boundary conditions.
3. Establish necessary identification data arrays (element nodal connections, equation numbers, etc.) and set up the skyline profile for global stiffness (or tangent stiffness) matrix.
4. Localization of quantities for each element, and assembly of global arrays from localized arrays.
5. Iterative solution of the resulting simultaneous equation system, and check for convergence.
6. Output of solutions, as specified by the user.
7. Progression of the solution process through each iterative/ time/ load cycle, and accumulation of time- or load-integrated quantities.

Element subroutines are written for each type of element, and these subroutines are attached to the routines of the main section. For example, an element subroutine was written (with a given name) to represent the axisymmetric continuum element under the power law model, another for the axisymmetric continuum element under Fish's model, another for the three dimensional continuum element for the power law model, and so on. Each element subroutine performs the following tasks:

1. Read input material properties for the particular type of element.
2. Compute tangent stiffness matrix, right hand side force vector, and incremental stresses for each element per each iteration cycle in each time step. (Also calculates additional quantities like incremental reactions, when required).

Figure 3.2 shows a general modular chart for the incremental solution process used in the programs developed here. The method of programming used above

allows for the incorporation of new element subroutines (e.g. using new constitutive relations) into relevant codes with minimum effect on the rest of the codes, and thus is referred to as the concept of 'program modules'.

As mentioned before, the execution of these codes is by the use of a set of macro commands which allows the user to select the desired solution process. Macro commands control the number and lengths of the time steps or load steps, the iterative process, computation and solution of the global system of equilibrium equations, computing stress increments and updating the stresses, input of boundary conditions and its changes, computing reactions, output of required quantities, and stopping the analysis at an intermediate stage in order to restart it later.

For the analyses of structure-frozen soil/ice interaction problems in the continuum, the following codes were developed in FORTRAN77, by incorporating the creep constitutive models and solution algorithms described above:

3.5.1 Computer Code ITFECC-A

(Iterative Time-incrementing Finite Element analysis code
for Creep in Continuum - A)

This code is capable of analyzing interaction problems using the constitutive models of Power Law Extension II (which reduces to the classical power law for a single load step), and Fish's unified model. A total of 17 element subroutines are incorporated for analyses of problems in conditions of plane stress, plane strain, axisymmetry, plane strain axisymmetry, three dimensional analysis, one dimensional analysis, and situations where adfreeze/bond phenomena (Chapter 6) are involved. Over 50 macro commands are available to control the execution of the program. Control parameters are used to determine, among other things, whether to use an iterative or a non-iterative process, and the value of θ (equation 3.45) if the iterative process is used. Further details regarding this code are provided in Appendix D.

ITFECC-A is the master program developed in the course of this research, and is an entirely self-sustained code with approximately 11,000 source lines. Algorithms

incorporated in this code were used as the bases for developing subsequent codes used in this study.

3.5.2 Computer Code ITFECC-B

(Iterative Time-incrementing Finite Element analysis code
for Creep in Continuum - B)

This code is capable of analyzing interaction problems using the constitutive model of Power Law Extension I (obtained by generalizing the model of Thimus, 1988), and incorporates 2 element subroutines for analysis of problems in axisymmetric conditions. Macro commands and control parameters are similar to those used in ITFECC-A. The need for a separate code for the Power Law Extension I arose because of the requirement to maintain stresses for different load steps independently. For a single load step, this code yields results identical to those given by ITFECC-A under Power Law Extension II.

3.5.3 Computer Code ILFENP

(Iterative Load-incrementing Finite Element analysis code
for Non-linear Problems)

This code incorporates the model of Domaschuk, and has 6 element subroutines to analyze interaction problems in conditions of axisymmetry, plane strain, and three dimensional analysis. As compared to the codes ITFECC-A and ITFECC-B above, macro commands used here define slightly different computational procedures, because of the absence of time incrementing process in this case.

In the codes developed above, capabilities to use between 2 to 4 nodes per element in the case of plane strain axisymmetry (or one dimensional analysis), between 3 to 9 nodes per element for two dimensional elements (plane stress/strain or axisymmetry), and either 8 or 20 nodes per element in the case of three dimensional finite elements, were incorporated. Numerical integration of order between 1 and 3 can be selected in each coordinate direction. Further details regarding these codes, including lists of available elements and macro commands, can be found in

Appendix D. Sample input data and output files for code ITFECC-A are given in Appendix E. Further computer codes developed in conjunction with this research are referenced in Chapter 5, §5.3.2.

All codes developed in this project are totally independent, and do not depend on any external software packages for the computations, except for the standard subfunction features provided by FORTRAN77 compilers. For extensive details regarding these computer codes, reference should be made to the user manuals prepared separately (Puswewala and Rajapakse, 1991b and 1991c).

3.6 Verification of Codes

The accuracy and reliability of these computer codes were verified by simulating several problems involving viscoelastic deformations in continuum domains, and by comparing the predicted values with the corresponding, available analytical solutions. It should be noted that, during the verification process, emphasis is placed on the power law model, since the available analytical solutions are based on this model, and therefore on the main code ITFECC-A. Once the basic time incrementing algorithms are verified for the power law model, the identical algorithms used for Fish's model (and for the Power Law Extension I in code ITFECC-B) are automatically confirmed, and only a few additional checks would be sufficient to test whether the particular constitutive assumption is being correctly modelled. The verification of code ILFENP for Domaschuk's model was also carried out by performing basic checks on the load incrementing algorithm.

The capabilities to be established with regard to these codes are: (a). The reliability of the codes as a whole, by verifying whether the time integration (or load integration) actually takes place as expected. (b). The influence of time discretization (or load discretization) on the accuracy of the predicted solutions. (c). The reliability of the codes over long periods of analysis history. (d). The accuracy of each type of element. The details of code verifications performed are as given below:

3.6.1 Verification of Code ITFECC-A

Basic checks for the correct performance of iterative and time-incrementing algorithms of the code were performed by using the simple one-dimensional elements to simulate situations involving creep under several load steps in the case of the Power Law Extension II, and under a single load step in the case of Fish's unified model. In one example, a rod of length 60 mm and axial area 1.6 mm^2 was considered. Under the power law, creep parameters for Bat-Baioss clay in Table 2.1, along with Young's modulus (E) = 8000 MPa were used, and three load steps of 0.8, 2.0, and 3.5 N were applied. Under Fish's model, E = 8000 MPa, $\delta = 0.5$ and parameters given by equation (4.11) were used, and a load of 1.2 N was applied. Numerical results for the above simulations are as shown in Figure 3.3, along with analytical solutions in the case of Power Law Extension II (obtained by integrating equation 3.19, and adding the initial elastic deformation), and solutions obtained by independent numerical integration of Fish's model in equation (3.28) for the uniaxial case under a single load step. A total of 7200 time steps were used in an iterative solution process in the case of both models. Excellent agreement between the results predicted by the code and those obtained by independent means confirm the validity of the basic time-integration algorithm used in the code. It is noted that several thousand time steps were used mainly to confirm the ability of the code to perform time integration over a large number of time intervals. By using a constant time step of 10 hrs throughout, results with -6.5% deviation from the analytical value were obtained after 1300 hours. The relative insensitivity of the results to the time discretization in this case is due to the constant stress condition within each load step. One-dimensional elements, in the case of each model, were developed for the primary purpose of performing basic verifications on the algorithms of the code. Subsequently, verifications were performed using multi-dimensional elements where generalization of stress and strain had been utilized.

By using the classical power law of creep (equation 3.16), Odqvist (1966) obtained an idealized solution for the cavity expansion of a long, thick-walled cylinder of visco-elastic material. The assumptions made by Odqvist (1966) in this case are that creep takes place under steady state conditions, the material is incompressible,

and initial transient creep stage has no influence on the steady creep stage. The steady state analytical solution obtained by Odqvist (1966) under the assumptions mentioned above can be adopted to describe the radial velocity of a cavity wall in an infinite medium where the far field pressure is zero, assuming that the creep of the medium is described according to equation (3.14) with $C = 1$. The analytical solution can then be written as (from Odqvist 1966):

$$\frac{du_r}{dt} = \frac{\sqrt{3}}{2} Aa\Big(\frac{\sqrt{3}p}{B}\Big)^B , \tag{3.63}$$

where u_r denotes the radial displacement of the cavity wall, a is the radius of the cavity, A, B are creep parameters described earlier, p is the pressure applied on the cavity wall, and t is the time variable. Under the theory of small displacements, equation (3.63) yields a constant radial velocity. Equation (3.63) can be extended to primary creep situations ($C < 1$) by using a convenient transformation of the time variable as $\tau = t^C$. Assuming that long-term attenuating creep occurs under the steady state, equation (3.63) can be written as,

$$\frac{du_r}{dt} = \Big(\frac{\sqrt{3}}{2}\Big)^{B+1} Aa\Big[\frac{2p}{B}\Big]^B Ct^{C-1} . \tag{3.64}$$

Above problem was selected for the purpose of verification of the code here. The radii of the internal and external walls of the cylinder were considered to be 10 and 3000 mm, respectively, and a pressure of 1.0 MPa was applied on the internal wall. Initially, the cavity expansion problem was analyzed under secondary creep conditions. The values for A and B in equation (3.63) were obtained from Shields et al. (1989), assuming that $C = 1$, as:

$$A = 0.001745\Big(\frac{\text{mm}^2}{\text{N}}\Big)^B \text{hrs}^{-1} , \qquad B = 2.43 . \tag{3.65}$$

The problem was simulated using the code and a mesh of 200 plane strain axisymmetric elements. The outer boundary was assumed to be fully restrained. A Poisson's ratio (ν) of 0.47 was used to represent incompressibility, and a very high Young's modulus (E) of 200 GPa was used to minimize the elasticity effects

in the numerical solution (since elastic effects had been completely eliminated from the analytical solution). The rate of radial displacement predicted by the code was computed by plotting the time-radial displacement curve for 70 hours and by computing the slope of the resulting curve (a straight line), and the value obtained was 6.967×10^{-3} mm/hr. The constant radial velocity computed from equation (3.63) for this case is 6.637×10^{-3} mm/hr. Thus the predicted value over-estimates the analytical value by 4.96%, and the closeness of the two results can be used as a positive verification indicator. In this case, the difference between the numerical and the analytical solutions is expected, mainly because of the presence of elasticity effects in the code, whereas these were eliminated from the analytical solution. In addition, the existence of σ_{zz} (the normal stress in the vertical direction) is taken into account in the formulation of the plane strain axisymmetric element here, unlike in the analytical approach. The presence of σ_{zz} makes this particular element somewhat sensitive to the value of Poisson's ratio, and it behaves very stiffly at values of ν very close to 0.5.

A case of attenuating creep was considered using the same cavity expansion example, in order to compare the numerical results with the analytical solution in equation (3.64). Identical elastic and creep parameters as earlier were selected, along with $C = 0.64$. The finite element simulation was carried out for a long time span (up to 1.5 years) using a fully restrained outer boundary, and the numerical results for the cavity radius are presented in Figure 3.4, along with the values computed using the analytical solution in equation (3.64). The two curves are very close to one another, and the numerical value underestimates the analytical prediction by only about 3% after 12000 hours. This analysis shows that the numerical algorithm remains stable and accurate for long periods of time span. For the time span of 12000 hrs., the analysis was performed using approximately 17000 time steps, starting with a step length of 0.0001 hrs. which was gradually lengthened to 2.2 hours as displacement rate decreased.

A further simulation of the identical problem was performed by considering larger time steps, starting with a time step of 1 hour and increasing the time step to 10 hours as the analysis progressed. The results of this simulation are shown

in Figure 3.5 along with the corresponding analytical result, and it can be seen that even this comparatively coarse time discretization yields a good comparison with the analytical result. It is noted that the reason for this good comparison lies in the stability of the numerical algorithm used, and in the fact that the initial transient creep stage has a negligible effect on the long-term steady state solution for displacements. However, it will be shown later that this type of coarse time discretization is not suitable for studies of some other types of phenomena, such as the initial stress redistribution process.

The steady-state analytical solution for the vertical deflection at the center of a simply supported beam under the action of a central concentrated load has been obtained by Odqvist (1966), under the identical assumptions as used for the cavity expansion problem earlier. A similar problem has previously been treated by Klein and Jessberger (1979). The present code is used to simulate this problem, by using eight node (Serendipity) plane stress elements to model the beam. The idealized analytical solution for the rate of vertical deflection at the mid-span (due to steady creep) in a centrally loaded, simply-supported beam made of incompressible creeping material (Odqvist 1966) can be rewritten as,

$$\dot{\delta} = \frac{K P^B L^{B+2} \left(\frac{1}{2}\right)^{2B+2}}{B+2} , \tag{3.66a}$$

$$\text{where,} \qquad K = \frac{A}{\left[b\left(\frac{h}{2}\right)^{2+1/B} \frac{2B}{2B+1}\right]^B} . \tag{3.66b}$$

In the above, $\dot{\delta}$ is the rate of the vertical deflection at the centre of the beam, P is the applied concentrated load, L, h, b, are the span length, height, and breadth, respectively, of the beam, and A, and B are creep parameters as defined earlier. Using the values of A and B given by Klein and Jessberger (1979) for Karlsruher sand at -10^oC (see Table 2.1) along with $E = 200$ GPa and $\nu = 0.47$, the above problem was simulated using the code for $P = 400$ N. The simulation was carried out using a mesh of 10, eight-node plane stress finite elements, with two layers of 5 elements each spanning one-half of the span of the beam considered ($L = 1$ m; $h = 0.15$ m; $b = 0.1$ m), as shown in Figure 3.6. Based on an analysis performed

for 70 hours, the constant rate of the vertical creep deflection at the mid-span (at the level of the neutral axis) obtained from the numerical results (by computing the slope of the displacement-time curve) was 5.75×10^{-2} mm/hr, compared with the analytical value of 5.35×10^{-2} mm/hr obtained from equations (3.66). The difference between the two values is 7.5%. These differences are expected for several reasons: (a). As earlier, the results of the code are influenced by the value of E, whereas such effects were eliminated from the analytical solution. (b). The numerical simulation was performed with plane stress elements, while the analytical solution was derived through the beam theory.

The beam problem was next analyzed under primary (or attenuating) creep conditions. The analytical solution of equations (3.66) can be adopted for primary creep situations by incorporating the transformed time parameter $\tau = t^C$, and the expression would be,

$$\dot{\delta} = \frac{K P^B L^{B+2} \left(\frac{1}{2}\right)^{2B+2}}{B+2} C t^{C-1} \ , \tag{3.67}$$

where K is given by equation (3.66b), and all other quantities are as defined before. The beam problem was analyzed using the code for $E = 200$ GPa, $\nu = 0.47$, and the creep parameters for Karlsruher sand as given in Table 2.1. The comparison of the numerical results (for the vertical deflection at the neutral axis at mid-span) with those obtained from the analytical expression in equation (3.67) is presented in Figure 3.7. The finite element simulation was performed for 20000 hours, using approximately 17000 time steps. Figure 3.7 shows that the numerical and analytical solutions agree with a deviation of approximately 8.8% after a time span of 20000 hours, indicating the reliability of the code over long time spans. The causes for deviation should be the same as given for the steady creep case earlier.

Further verifications were performed to investigate the ability of the code to simulate transient stress behaviour, with respect to the power law model. At the same time, these verifications could be used to check the validity of formulations used for the axisymmetric and three dimensional elements. For this purpose, a uniaxial Maxwell viscoelastic model (Christensen 1971) was considered, with spring

constant K_1 and a general dash-pot described by equation (3.10). If this model is subjected to a constant strain γ_o applied instantaneously, an initial stress $K_1\gamma_o$ would be set up, which would thereafter 'relax' according to the equation,

$$[\sigma(t)]^{1-B} = (B-1)\,K_1 A t^C + (K_1\gamma_o)^{1-B}\ , \qquad B \neq 1\ . \tag{3.68}$$

(Note that for a linear dash-pot ($B = 1$, $C = 1$), the relaxation equation is given by $\sigma(t) = K_1\gamma_o \exp\{-tAK_1\}$). In order to simulate the above problem using the code, a thin rod with cross sectional radius of 0.2 mm and a length of 60 mm was modelled by using ten equal-depth axisymmetric elements (two layers of elements in radial direction, each layer with equal radial thickness). Properties used were $K_1 = 8000$ MPa, ν (Poisson's ratio) $= 0$, $A = 0.35 \times 10^{-3}$ (MPa)$^{-B}$(hr)$^{-C}$, $B = 1.28$, and $C = 0.44$ (A, B, C from Table 2.1). The problem was analyzed for a prescribed constant strain of 1/600. The closed-form analytical solution given by equation (3.68) is shown in Figure 3.8, along with the corresponding numerical results for stress relaxation obtained from the code using different constant time step lengths of 0.0001, 0.005 and 0.01 hours, respectively. Numerical solutions were obtained by using the iterative procedure with $\theta = 0.5$. Figure 3.8 shows an excellent agreement between the stress behaviour predicted by the numerical scheme for the small time steps (of 0.0001 hours) and those predicted by the closed-form solution, indicating the ability of the numerical scheme to represent the assumed constitutive model almost exactly. As seen from Figure 3.8, errors appear (particularly during the initial period when stress rates are high) when a larger time step length is used. The excellent agreement shown for the constant time step of 0.0001 hours was repeated when variable time step lengths, starting with a step of 0.0001 hours and increasing the step length by a ratio of 1.25 after every 0.05 hours, were used. Similar agreement was seen for a linear dash-pot model. The accuracy of the stress relaxation behaviour predicted by the axisymmetric element indicates the validity of the generalization process, the reliability of the numerical scheme, and the ability of the constitutive model to simulate transient stress states. The length of the time step to be employed depends on the stress rate, which in turn is dependent on the magnitudes of creep parameters used. In the example in Figure 3.8, magnitude of

stress decreases by 94% during the first 0.5 hours, thus requiring the use of small time steps for accuracy.

A similar numerical example was repeated to confirm the validity of the three dimensional elements developed here. A thin column of length 60 mm, and cross-sectional dimensions of 0.2mm $\times$ 0.2mm was modelled by ten brick elements with 8 nodes for each element, and using two columns of five equal-depth elements to model one-half of the column. The material properties used were identical to those used in the axisymmetric example above. The problem was analyzed for a prescribed constant strain of 1/600. The simulation was carried out using variable time step lengths, starting with a step of 0.0001 hours and increasing the step length by a ratio of 1.25 after every 500 time steps. The comparison of the closed-form solution given by equation (3.68) with that predicted by the code is as shown in Figure 3.9, where excellent agreement between the two results can be seen. As in the case of the axisymmetric element earlier, this comparison confirms the validity of the algorithm used to develop the three dimensional elements. Similar agreement was seen when 20 node elements were used to model the column. As before errors appear in the values predicted for stresses when coarser time discretizations are used.

Analytical closed-form solutions are unavailable for Fish's model. Therefore, verifications can be performed only by comparing the results predicted by the code with those evaluated by independent numerical means (as shown earlier in Figure 3.3). In order to verify the axisymmetric element under Fish's model, the same thin rod geometry considered earlier (length = 60 mm; radius = 0.2 mm) was modelled by a column made of 3 axisymmetric elements stacked one upon another, with 8 nodes per element, and this mesh was subjected to a constant vertical stress of 0.75 MPa. Values of E = 8000 MPa, ν = 0, and creep parameters for Fish's model given by equation (4.11) were used. The results obtained by this example are compared with independent numerical integration of equation (3.28), as shown in Figure 3.10. The excellent agreement between the two results can be used to validate the axisymmetric element in the case of Fish's model, including the generalization process applied in the case of the uniaxial expression. Since routines of the main section of the code, which are common to all types of elements and both creep

models, have already been validated by the simulations conducted under the power law earlier, no further verification under the model of Fish are presented here.

Above verification examples were deemed to be sufficient for validation of the code ITFECC-A, including all its element subroutines. However, during the simulations of various interaction problems presented in later chapters, it would be seen that several additional occasions of verification with regard to the algorithms and constitutive models of the code ITFECC-A do occur.

3.6.2 Verification of Code ITFECC-B

Code ITFECC-B gives results identical to those of the code ITFECC-A considered earlier, for the case of a single load step considered under the power law. The difference between the predictions of the two codes arise only after a subsequent load step is applied. The algorithm of the code was checked by using the relevant one dimensional element to simulate creep under a loading history with two load steps. The same rod geometry, material parameters and first two load steps as used for Power Law Extension II in Figure 3.3 were used. The results of the simulation for Power Law Extension I are as shown in Figure 3.11, along with the results obtained by analytical integration of equations (3.17). The agreement of the two results shows that the actual creep model of Thimus (1988) is properly incorporated in the code. In Figure 3.11, the corresponding results for Power Law Extension II, obtained using the code ITFECC-A, are also shown for comparison. A multi-dimensional simulation using Power Law Extension I is discussed later, in Chapter 4. Since time-incrementing algorithms used here are identical to those in ITFECC-A, no further verifications were deemed necessary with respect to the code ITFECC-B.

3.6.3 Verification of Code ILFENP

Computer code ILFENP was developed mainly for the purpose of implementing Domaschuk's model. However, any other hypoelastic model can be similarly incorporated in the code, without any difficulty. Since analytical solutions are not

available in the case of Domaschuk's model, an equivalent one-dimensional problem was simulated using a thin rod geometry modelled by axisymmetric elements. The same element configuration as used earlier for the stress relaxation simulation was used here, and the axial creep displacement under a constant applied load was simulated. These results were compared with independent numerical integration of an equivalent one dimensional problem, defined as,

$$d\,\sigma = \left(K_c + 4/3\,G_c\right) d\,\epsilon\ . \tag{3.69}$$

The comparison of the two results, obtained by using identical parameters (given by equations 4.12) are shown in Figure 3.12. A comparatively small deviation between the two results can be seen from the figure, but the agreement is satisfactory for practical purposes. The only usefulness of Figure 3.12 is the indication that the relevant model has been correctly implemented. Subsequently, plane strain axisymmetric elements were used to model a fictitious pressuremeter test. Analyses were conducted for a specified load using 50, 200 and 600 load steps (load steps were of equal size in each problem), and for the material parameters given in equations 4.12. It was seen that regardless of the number of load steps used, the final result was nearly identical (less than 0.5% deviation). Therefore, it can be concluded that the sensitivity of the algorithm to load discretization is not appreciable, at least for the material parameters used in this comparison. Because of the iterative process in the algorithm, this observation may be deemed to hold for a considerable range of values of the material parameters. These verifications were deemed sufficient to validate the code ILFENP, especially since it involves an algorithm which is similar to many algorithms widely used for problems in non-linear elasticity.

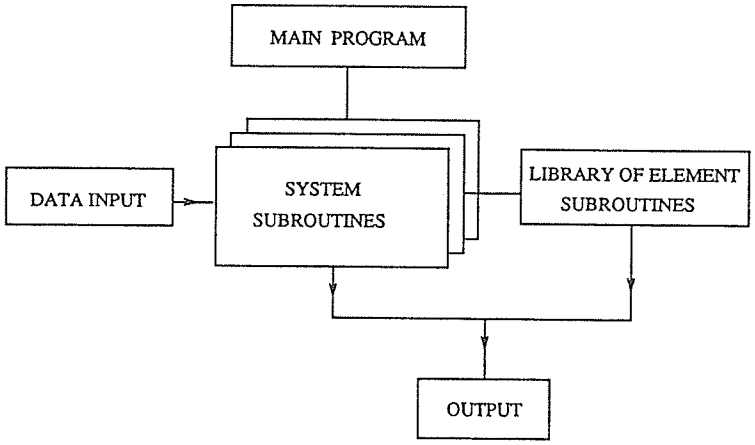

Figure 3.1. Schematic diagram for computer codes.

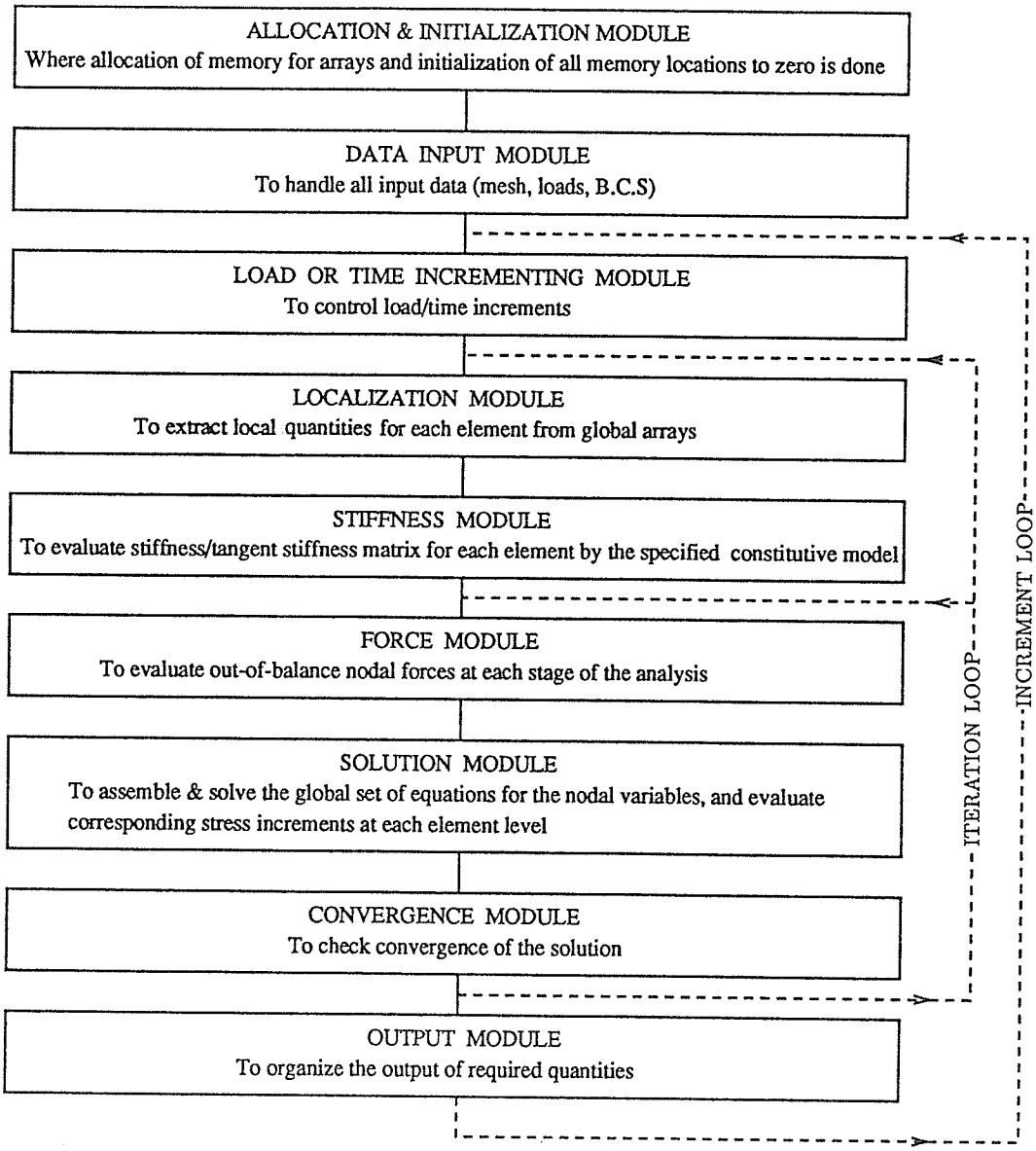

Figure 3.2. Modular diagram for computer codes.

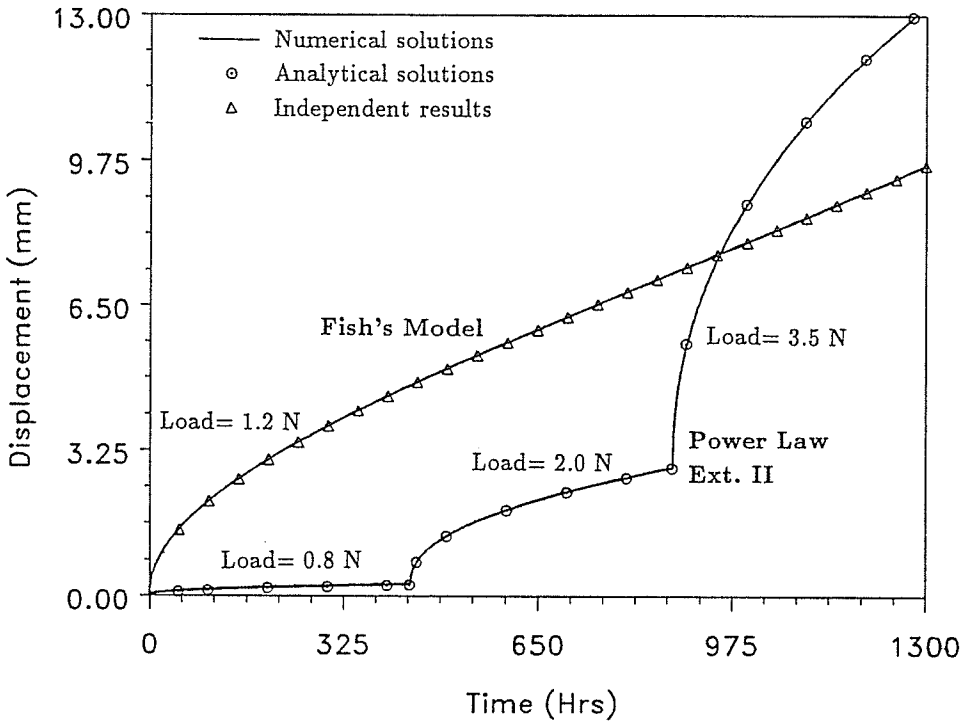

Figure 3.3. Results using 1-D elements under Power Law Ext. II and Fish's Model.

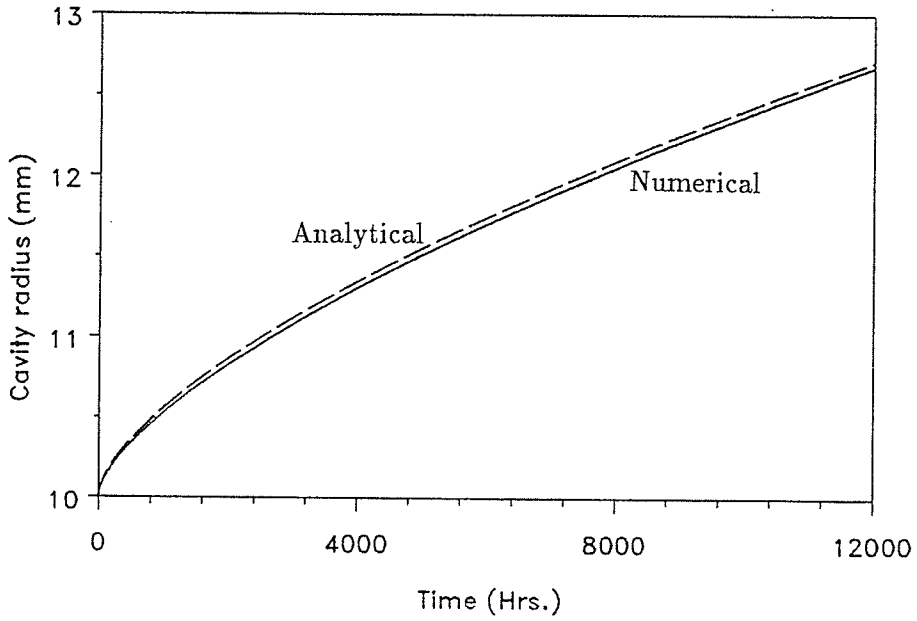

Figure 3.4. Comparison of numerical and analytical solutions for radial displacement of the inner wall of thick-walled viscoelastic cylinder under internal pressure.

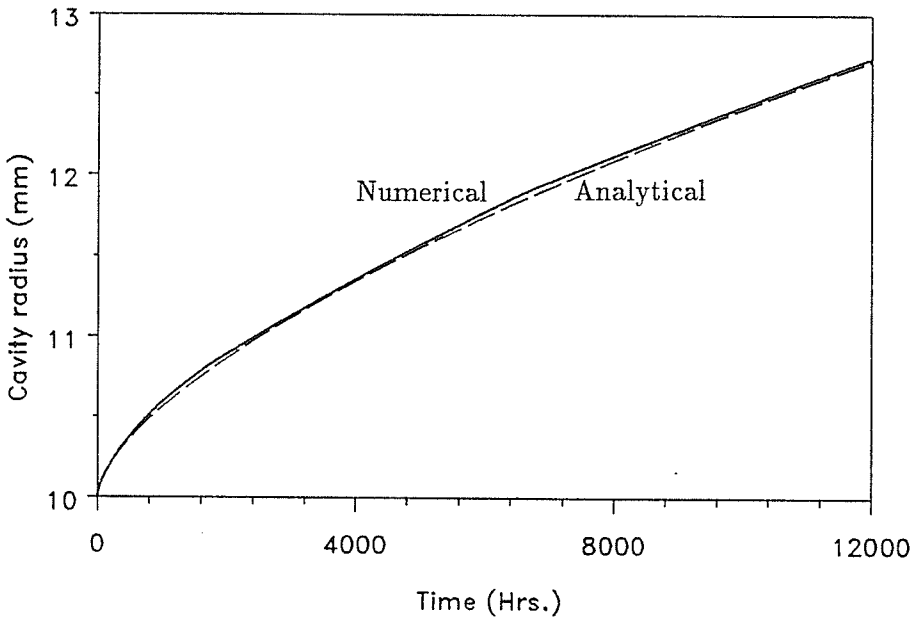

Figure 3.5. Comparison of numerical results using coarse time discretization and analytical solution for radial displacement of the inner wall of thick-walled viscoelastic cylinder under internal pressure.

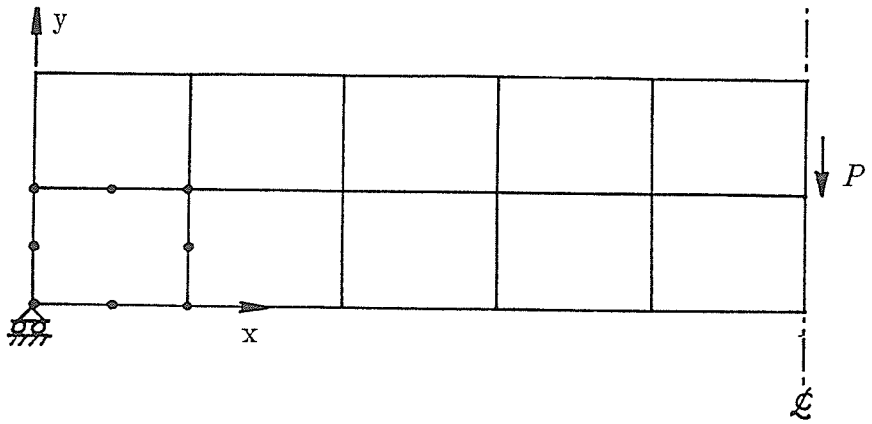

Figure 3.6. Finite element discretization of half-span length of beam.

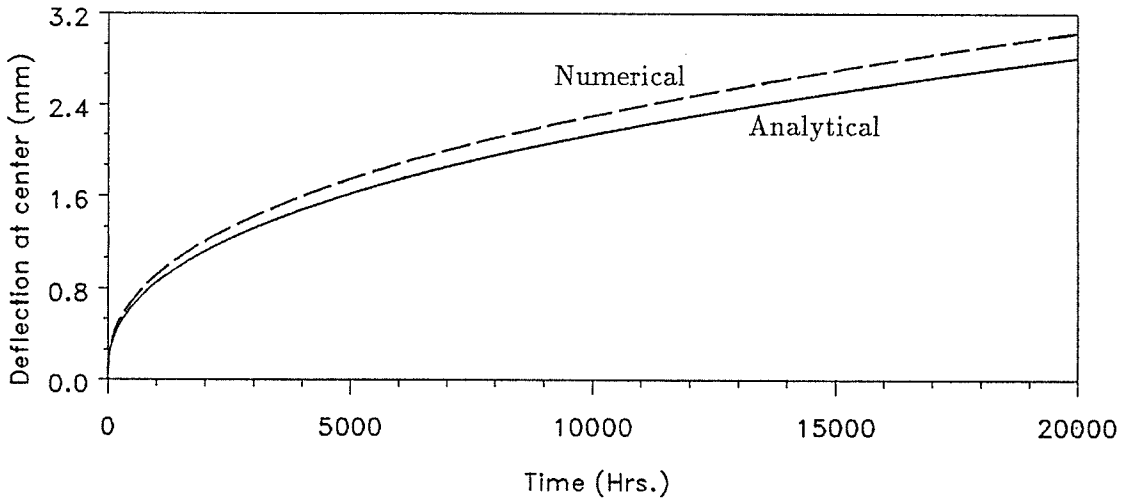

Figure 3.7. Comparison of numerical and analytical solutions for vertical deflection at mid-span of viscoelastic beam under central concentrated load

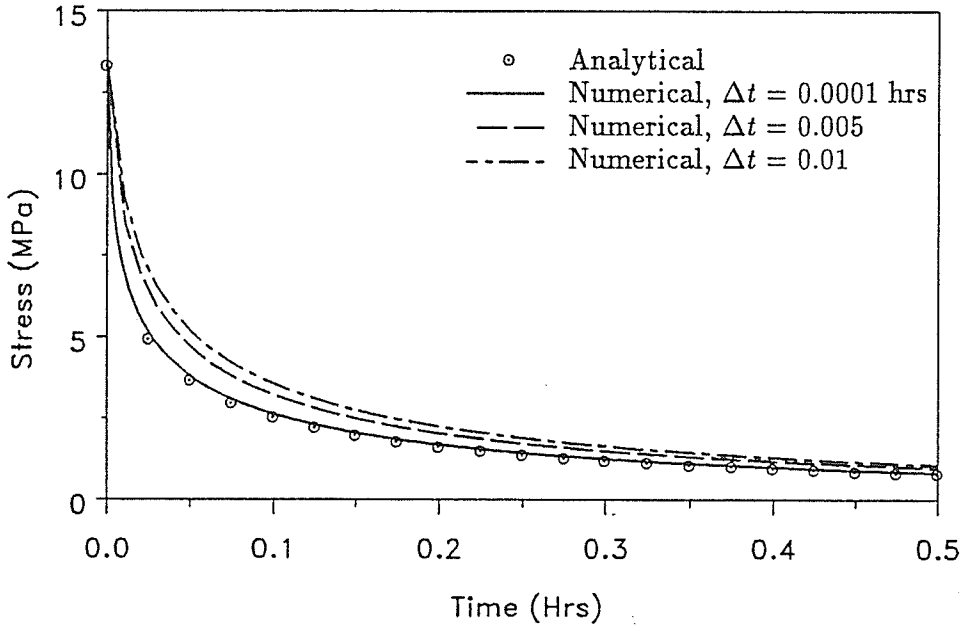

Figure 3.8. Comparison of numerical and analytical solutions for stress relaxation (numerical solutions using axisymmtric elements).

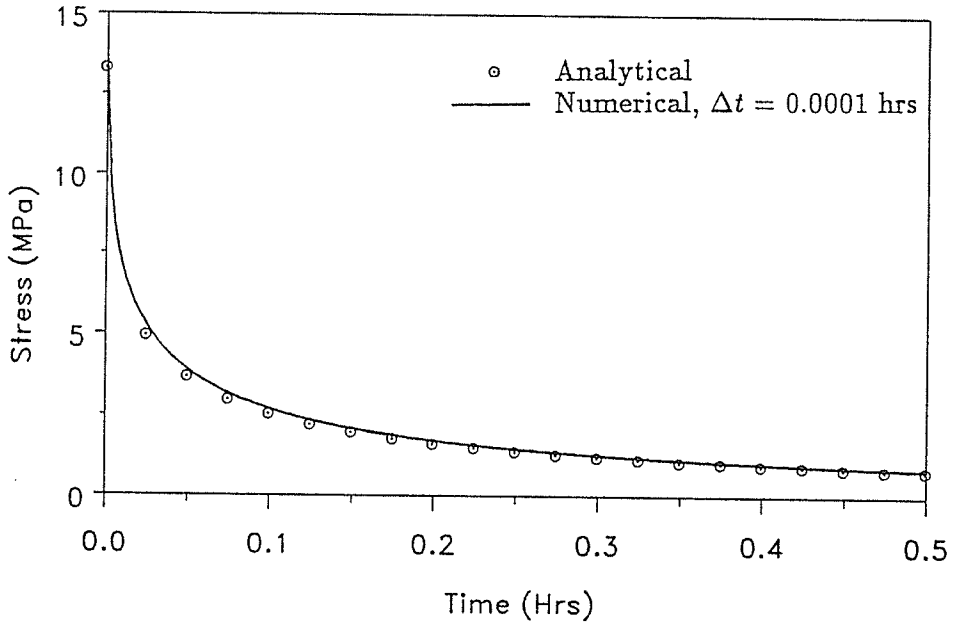

Figure 3.9. Comparison of numerical and analytical solutions for stress relaxation (numerical solutions using 3-D elements).

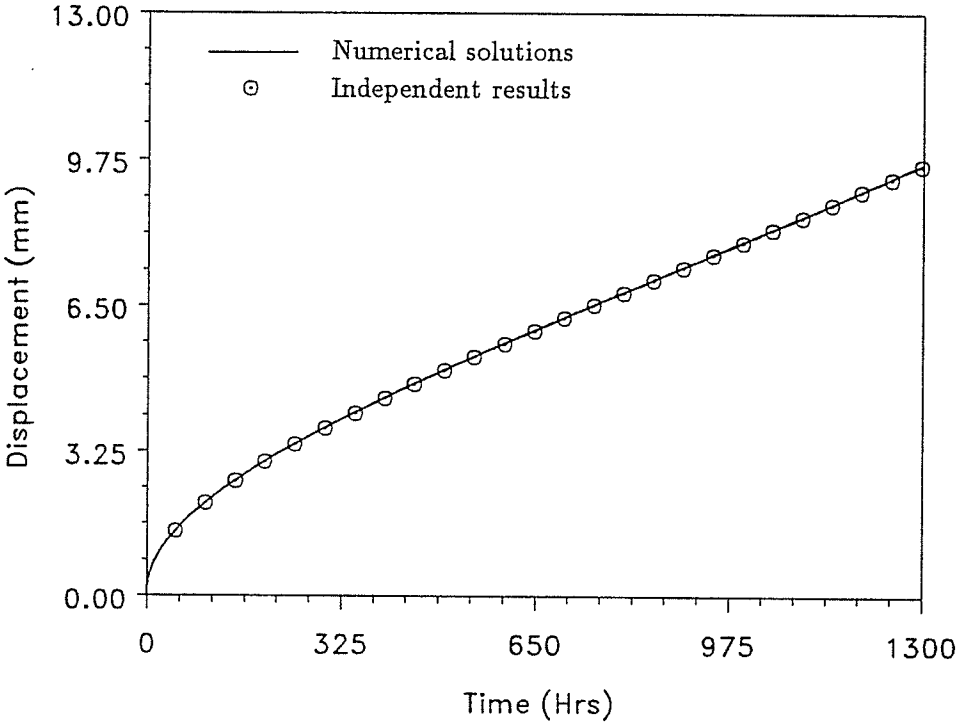

Figure 3.10. Comparison of FE results using axisymmetric elements under Fish's model with independent evaluation of the model.

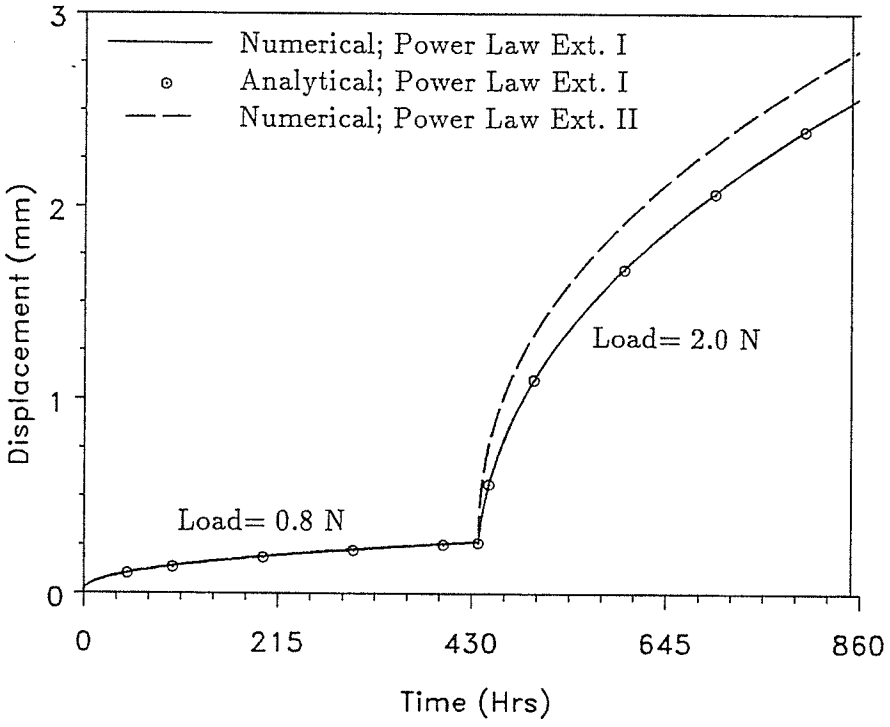

Figure 3.11. Results using 1-D elements under Power Law Extensions I and II.

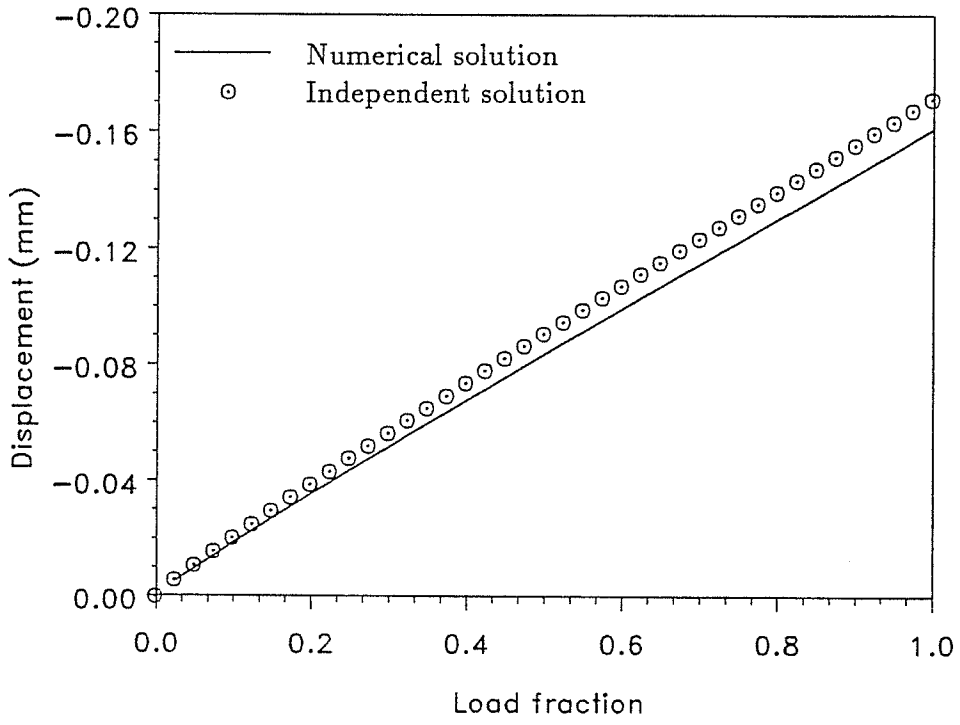

Figure 3.12. Comparison of FE results using axisymmetric elements under Domaschuk's model with independent evaluation of an equivalent 1-D model.

Chapter 4

ANALYSES OF PLANE AND AXISYMMETRIC INTERACTION PROBLEMS

4.1 General

There is a large number of structure-frozen soil/ ice interaction problems which can be conveniently analyzed using a two dimensional coordinate frame. Under this category are problems of plane strain, plane stress, and axisymmetry. Plane strain conditions are assumed to occur if no deformations take place in the direction perpendicular to the coordinate frame, and therefore in such cases when the same deformation field exists in every plane parallel to the coordinate plane, taken along an axis extending to a comparatively large distance in directions perpendicular to the coordinate frame. An example for plane strain conditions is a long, strip footing placed on frozen ground. Plane stress conditions prevail in plate type domains (with small thickness in the direction perpendicular to the coordinate frame), and stresses in the direction perpendicular to the coordinate frame are assumed to be non-existent. Plane stress conditions can be approximately assumed in such situations as in frozen soil beams (§3.6). Axisymmetric conditions are said to prevail when both the geometry and loading system of an interaction problem have axial symmetry about a pertinent axis, and deformation field in any coordinate plane defined by the symmetry axis and a given radial line is identical to that in any other such plane obtained by considering a different radial line. Axially loaded cylindrical footing or pile problems are examples for axisymmetric conditions. There are certain problems that can be assumed to have the combined effect of plane strain and axisymmetry, and hence can be referred to as plane strain axisymmetric problems. Such conditions may be assumed to exist, for example near the center of the probe in pressuremeter tests.

This Chapter will be entirely devoted to discussion of computational analyses of interaction problems in two dimensional coordinate frames, using the computer codes described in Chapter 3. Only continuum analyses will be discussed here, and

the three creep models (Power law, Fish's model and Domaschuk's model) will be considered in turn. The numerical analyses presented here were performed in double precision. The SUN/4 280 computers at The University of Manitoba were used for most of the analyses, while the AMDAHL 5870 mainframe was used occasionally.

4.2 Analysis Using Power Law Creep Model

Computer codes ITFECC-A and ITFECC-B are capable of analyzing interaction problems using the power law creep model (see §3.5). Of the above codes, ITFECC-B would be useful only when the Power Law Extension I (§3.2.1) is being investigated. Using these codes, computational analyses of a variety of problems were performed, as detailed in ensuing subsections. In §4.2.1, the applicability and limitations of the two extended power law models are investigated by comparing computational results with experimental data (Lach 1989) for pressuremeter tests on frozen sand. In the remaining sub-sections, the power law model and the code ITFECC-A is used as a predictive tool to obtain the deformation behaviour in several situations of practical importance encountered in geotechnical engineering. Out of these, in §4.2.3, a correspondence is established with another set of test data on laterally loaded steel rods in ice, obtained by Domaschuk et al. (1989).

4.2.1 Pressuremeter Tests on Frozen Soils

As mentioned above, the codes ITFECC-A and ITFECC-B were used to investigate the applicability and limitations of the two versions of the power law model (extended to multiple load steps based on phenomenological observations, as given in §3.2.1) as the constitutive models for the long term behaviour of frozen soil by simulating two multiple-load step pressuremeter tests conducted by Lach (1989). Pressuremeter tests involve axisymmetric, multi-axial stress conditions that exist in many practical situations, and thus present a suitable stress distribution to investigate the predictive ability of a multi-axial constitutive model under multiple load steps. For the simulations, the appropriate creep parameters will be evaluated, as detailed later, by a suitable graphical method, using test data. The response predicted by the two models for the subsequent load steps will be compared with the

test data, in order to determine which model possesses a better ability to reasonably predict the actual response.

The two pressuremeter tests considered for simulation are schematically depicted in Figure 4.1. The frozen soil used in the tests (Lach 1989) was a uniform, quartz, carbonate, medium grain sand with an average moisture content of approximately 22%. The soil was maintained at an average temperature of $-3°C$ in a pit 2.5m square, filled to a height of 1.8m. Both tests were conducted in the same pit. The diameter of both pressuremeter boreholes was approximately 76 mm and the length of the pressuremeter probe was 390 mm. In the first test, the pressuremeter probe was centered at a depth of 550 mm below the surface of the frozen sand, and four load steps were applied by pressurizing the probe in the following sequence: 0.86 MPa during the first 121 hours, 1.77 MPa during the next 869 hours, 2.83 MPa during the following 1410 hours, and 3.47 MPa thereafter. In the second test, the pressuremeter probe was centered at a depth of 1050 mm below the surface of the frozen sand and loaded by three load steps in the following sequence: 0.85 MPa during the first 410 hours, 1.79 MPa during the following 1220 hours, and 2.78 MPa thereafter. In all cases, the subsequent load step was applied when the response to the previous load step had attenuated, and the response to the final load step in both tests indicated a tendency to failure by accelerating creep. The tests yielded smooth time-radial displacement data, except for a slight discontinuity of approximately 0.3 mm in the displacement-time curve during the second load step of the first pressuremeter test, caused by a temperature rise in the pit. For the analyses here, the test results were corrected by removing this perturbation. The test results presented here had already been corrected for membrane thickness and resistance, as well as for calibration of the data acquisition equipment.

For the numerical analysis, it was necessary to evaluate the creep parameters A, B, and C for the frozen sand. Ladanyi and Johnston (1973) suggested a graphical method to evaluate these parameters, based on the plane strain analytical solution given by Odqvist (1966) for the cavity expansion of a thick-walled, infinitely long viscoelastic cylinder. For this purpose, the idealized, closed-form solution for the

above problem given in equation (3.64) can be expressed as:

$$\frac{V}{V_{i-1}} = \exp\left[2\left(\frac{\sqrt{3}}{2}\right)^{B+1} A\left(\frac{2}{B}\right)^{B} (p_c - p_0)^B t^C\right] , \tag{4.1}$$

where V_{i-1} denotes the cavity volume at the start of a given ith load step, V is the cavity volume at any time t after the pressure had been increased to $(p_c - p_0)$, p_c is the pressure on the cavity wall, p_0 the pressure at the outer boundary, and all other notations are as before. By taking first the natural and then the ordinary logarithm of equation (4.1), it can be seen that the pressuremeter creep curves for each load step should linearize when $\ln\left(\frac{V}{V_{i-1}}\right)$ is plotted against t in log-log plot. The slope of these straight lines is C. When the intercept (denoted by M_1 hereafter) of each of these lines at unit time is plotted against the corresponding total applied pressure value in log-log plot, another straight line should materialize with a slope of B. From its intercept read at unit value of pressure, and using the value of B, the magnitude of A can be calculated.

The above graphical method was applied to the results of the first three load steps of the first pressuremeter test. Figure 4.2 shows the $\log\left(\ln \frac{V}{V_{i-1}}\right)$ vs. $\log t$ plot for the test results, on which the $\log M_1$ vs. $\log(p_c - p_0)$ plot is superposed. The pressure at a sufficiently large distance from the bore-hole wall (p_0) was approximated as zero. Figure 4.2 shows that the test data do not exactly linearize on the $\log\left(\ln \frac{V}{V_{i-1}}\right)$ vs. $\log t$ plot. There is no guarantee that such linearization should happen exactly for any material, and therefore the application of the power law flow model to such materials is an approximation. By approximating the three curves with straight lines, the following values were obtained for the slopes (parameter C):

$$^1C = 0.1433 , \qquad ^2C = 0.2049 , \qquad ^3C = 0.2707 , \tag{4.2}$$

where, ^iC denotes the parameter C evaluated for the ith step. The average value for C is,

$$C = 0.2063 \tag{4.3}$$

The slope of the $\log M_1$ vs. $\log p_c$ plot gives,

$$B = 0.6844 \tag{4.4}$$

It is noted that the value of B (< 1) above is rather low in comparison to values of B (> 1) reported elsewhere (Ladanyi and Johnston 1973, Klein 1979). The reason for this may be the attempt here to fit the power law model to long-term test results (total duration of 100 days), with most of it showing a highly attenuating behaviour, as compared to mostly short-term tests used elsewhere (Ladanyi and Johnston 1973, Klein 1979, Murat et al. 1989). While noting this point, the value of equation (4.4) will be used subsequently as the present investigation is focussed on long-term response of frozen soils, characterized by the values computed here. For the value given in equation (4.4), the average value for A is:

$$A = 0.00575 \left(\frac{\text{mm}^2}{\text{N}}\right)^B \text{hr}^{-C} \tag{4.5}$$

Based on the values for Young's modulus (E) given by Andersland and Anderson (1978), E of the frozen sand considered here at $-3°$C was estimated as 6000 MPa. A Poisson's ratio (ν) of 0.47 was selected to represent almost total incompressibility.

The computer codes ITFECC-A and ITFECC-B were used, depending on the particular extended version of the power law used, to simulate the two pressuremeter tests using the above material parameters. Each load step was simulated using small time steps (in the order of 10^{-5} hours) at the beginning when the strain (and stress) rates were high, which were gradually lengthened to the order of one hour as the strain rates diminished. Reference can be made to §3.6 for a discussion of appropriate time-step lengths, depending on the problem to be modelled and the magnitudes of creep parameters.

For the analysis of the first pressuremeter test, the frozen soil domain was discretized in the r-z plane using a finite element mesh of 200 axisymmetric elements with a total of 1232 active degrees of freedom, as shown in Figure 4.3. All elements were of Serendipity type (8 nodes), and numerical integration of order two was used in both directions. The outer diameter of the frozen sand domain considered was 16.5 times the diameter of the bore hole. Stresses needed for the incremental analysis were maintained at four Gauss points in each element, these being identical to

the points where stiffness evaluations were performed. For the second pressuremeter test, a mesh of 198 axisymmetric elements with a total of 1224 active degrees of freedom was used; all other details were as for the earlier test. Alternatively, the tests were analyzed under plane strain axisymmetry, using a mesh of 201 nodes and 100 elements along a radial line, each element consisting of 3 nodes. Numerical integration of order 2 was used in the radial direction, and stresses were maintained at two Gauss points in each element. It was found that the plane strain axisymmetric and fully axisymmetric analyses yielded results which varied by less than 3% from each other, but due to its formulation method, the plane strain axisymmetric element showed some sensitivity to the value of Poisson's ratio (indicating a stiffer response when ν was very close to 0.5).

The results of the simulation of the first pressuremeter test using Power Law Extension I (§3.2.1, equation 3.18) is shown in Figure 4.4, where the cavity radius at the center of the pressuremeter probe is plotted against time, and shown along with the corresponding test results (Lach 1989). The simulation was performed for the first two load steps using fully axisymmetric analysis and by back-substituting the creep parameters evaluated using the same test results, given in equations (4.3)–(4.5). It is seen that the simulation of the first load step, where the basic generalized power law was used, compares closely with the observed results. However, the predicted radial displacement follows a path different from the test results during the second load step, and overestimates it by about 40% at the end of the load step. This indicates that the generalized version of the Power Law Extension I is unable to predict the response to a subsequent load step when the creep parameters evaluated here are used.

The first pressuremeter test was re-simulated using the Power Law Extension II (§3.2.1, equation 3.19), and the creep parameters in equations (4.3)–(4.5). The creep parameters had been evaluated using the same test results, then averaged, and were back-substituted in the numerical algorithm. Therefore, one cause for any discrepencies that appear between the numerical and observed results may be the "averaging" effect, since a flow model of the type given in equations (3.19) had already been used for the evaluation of creep parameters, assuming ideal creep con-

ditions to prevail. The simulation was performed for the first three load steps, and the numerical results are presented in Figure 4.5 along with the test results (Lach 1989), where, as earlier, the cavity radius of the center point of the pressuremeter probe is plotted against time. Figure 4.5 shows an almost exact agreement between the numerical and observed results for the first two load steps, but the predicted radial displacement during the third load step underestimates the test result by about 40%. Thus the use of averaged creep parameters fails to yield a good agreement with test data during the third load step in this case. The fourth load step of the test, in which the response shows tertiary creep behaviour, is not considered for simulation here.

Alternatively, creep parameters evaluated individually for each load step in the first pressuremeter test were back-substituted to simulate the corresponding load step. Thus, ${}^1C$ in equation (4.2) was used for the first load step, ${}^2C$ for the second load step, and ${}^3C$ for the third load step. B and A are as given in equations (4.4) and (4.5). The results of the numerical simulation are as shown in Figure 4.6, which shows good agreement with observed data for all load steps. The predicted displacement slightly underestimates the test data during the three load steps, but the comparison shows that the predictive ability of the constitutive model is acceptable for practical purposes.

The results of the simulation of the second pressuremeter test using the averaged parameters from the first test (equations 4.3–4.5) are as shown in Figure 4.7, where the corresponding test data (Lach 1989) are also presented. The comparison between the numerical and observed values during the first load step is good. However, the predicted radial displacement underestimates the test data by about 30% during the second load step. The observed response during the third load step cannot be correctly simulated by the power law since failure of the frozen soil had occurred through accelerating creep, although this simulation is also presented in Figure 4.7.

Figures 4.5–4.7 show the limitations of the time-hardening power law when extended to multi-step loading. The Power Law Extension II represented the con-

stitutive behaviour of the frozen soil better than did the Power Law Extension I. However, the performance of the latter model may improve in the case of a different set of constitutive parameters. The value of C affects this type of long-term predictions considerably, as seen by comparing Figures 4.5 and 4.6. A higher value of C (0.2707 vs. 0.2063) used for the third load stage was solely responsible for the improved agreement with the observed results in Figure 4.6. Therefore it is plausible to suggest a stress dependence for the value of C. Unfortunately, a functional form of this relationship cannot be provided here due to lack of adequate data. The ability to satisfactorily simulate the first load stage in all cases here indicates the suitability of the classical power law model for single load-step situations. Regarding the performance of the Power Law Extension I, Thimus (1990) does not agree with the use of graphical methods to evaluate the creep parameters. Inaccuracies are involved in parameter evaluation since idealized, steady-state analytical solutions are applied to test results which may still be in transient creep stage, while a model of the type given in equation (3.19) had been assumed a-priori in Figure 4.2.

The following factors have an effect on the comparison between the predicted and observed results, and thus on the estimation of suitability of the constitutive model used here: (1) Repeatability of test results. From the test results for the initial load stage in the two tests, different C values can be obtained using the method in Figure 4.2, although nearly the same pressure was applied in both cases. This may be caused by the attempt to fit power law formula to tests of very different durations (5 and 17 days, respectively). (2) Differences in assumptions. The analytical solution used to evaluate the creep parameters was developed using plane strain conditions involving only σ_{rr} and $\sigma_{\theta\theta}$, by eliminating the elasticity effects, and by assuming a stationary stress distribution. None of these conditions are satisfied in the numerical analysis or in reality, since additional stresses (i.e. σ_{zz}), elasticity effects, and transient stress behaviour are involved in the creep process. (3) Use of the small displacement theory to simulate fairly large displacements, these being as large as 10% of the borehole radius. (4) Anomalies in the test results. The somewhat irregular shape of the radius-time curve at about 60 days in the first test (Figure 4.6) indicates possible fracturing or slippage which cannot be predicted by

power law models as used here.

Figure 4.8 shows the predicted displacement profiles of the borehole wall at different time instances during the simulation of the first pressuremeter test using individual C values for each load step. The displacement profiles maintain a concave shape towards the axis of axisymmetry (center-line of the borehole), and move outwards with time. The maximum radial displacement was not at the center point of the pressuremeter probe but slightly above it. This, most probably, was due to the end effect caused by the bottom of the borehole. This feature is not noticeable in the figure because of the scale used, but was evident from the numerical results.

Figures 4.9a and 4.9b, respectively, show the distributions of stresses σ_{rr} and $\sigma_{\theta\theta}$ along a radial line at the center of the probe for the first pressuremeter test simulated using individual C parameters for each load step. (Note that the plots commence from the first Gauss point close to the borehole wall). In the figures, numerically obtained stress distributions at $t = 0$ hours (initial elastic), $t = 121$ hours (prior to the application of the second load step), $t = 990$ hours (prior to the application of the third load step), and at $t = 2400$ hours are shown against the radius. Also shown are the linear elastic stress distributions computed by using plane strain axisymmetric analysis for the three applied pressures of 0.86 MPa, 1.77 MPa and 2.83 MPa. The stress at any instant during the creep process decay with increasing radius, similar to the behaviour of the analytical linear elastic stress distributions. By comparing the numerical solutions at $t = 0$ (initial elastic) and $t = 121$ hours, it is seen that the change in magnitude of stress is as much as 100% at some locations in the domain. The difference between the initial elastic stress distribution obtained by numerical simulation and the analytical solution is caused by the differences in assumptions regarding the stress state (fully axisymmetric vs. plane strain) involved in the two approaches. Away from the center of the probe (eg: at the top or bottom of the probe), magnitudes or profiles of stresses during the creep process do not show any resemblance to the analytical linear elastic solutions obtained by plane strain axisymmetry. A study of variation of stress with time showed that stresses change from an initial elastic state towards a long-term, quasi-stationary creep state, and that the stress variation rates depend on the magnitudes

of creep parameters.

The process of stress redistribution seen from the numerical analyses can be interpreted in the context of the basic assumption of the constitutive model (in equation 3.7), i.e. that the total strain tensor consists of an elastic and a creep component. Thus a change in the magnitude of stress indicates a change in the magnitude of the elastic component of the strain tensor. Stress analyses using the model (Figures 4.9, 3.8, 3.9) show that transient stress stages are accounted for in the constitutive model. It was seen that an initial, comparatively rapid change in elastic strain components, indicating the transient creep stage, is later followed by a quasi-stationary creep stage where the creep strains predominate (with very small further changes in stress magnitudes) and control the flow process.

One advantage of the power law over many other creep models is its simplicity for computational purposes, and the involvement of only three material parameters. This investigation indicated that the constitutive model in equations (3.7) and (3.5) has the overall capability to model deformations in frozen geomaterials, and is able to simulate transient as well as stationary creep situations. The numerical algorithm of the code is reliable over long periods of time history (100 days in this case), and the code is a convenient predictive tool for complicated interaction problems provided the constitutive assumption is valid. Caution is needed in the selection of applicable creep parameters for the power law model.

A note is added regarding plane strain analysis as opposed to fully axisymmetric analysis. Figure 4.6 shows results using a fully axisymmetric simulation, but an alternate simulation using plane strain axisymmetry yielded a curve almost identical to this, with deviations of about 2%. Thus it is reasonable to assume plane strain conditions at the center level of the probe, and end-effects due to the top surface of the frozen soil and the bottom of the borehole, as well as effects due to the depth of the probe, are not so pronounced. Furthermore, plane strain finite element analysis using the mesh of 100 elements consumed less than 5% of the CPU time required for the fully axisymmetric simulation using the mesh of 200 Serendipity elements, for the same time history of deformation. However, fully axisymmetric analyses are

essential for a complete study of the problem, such as progression of the borehole wall profile with time, deformations at the upper surface of the frozen soil medium, stress distributions at locations other than the center of the probe, etc.

4.2.2 Footings on Frozen Ground

The code was used to predict creep in three separate examples involving interaction between footings and frozen sand. All problems in this subsection were conducted using axisymmetric FE analyses.

The first investigation was on the creep behaviour of a frozen sand half-space subjected to a uniformly distributed vertical load acting over a circular area on the surface of the domain. The radius of the patch load was taken as one meter. This example is similar to the case of a fully flexible footing on frozen soil, a situation commonly encountered in geotechnical engineering. The analytical solution for the elastic behaviour of a half-space of isotropic homogeneous material under a load of above type is given by Terzaghi and Peck 1948, (based on the Boussinesq's solution). The finite element simulation was conducted using a mesh consisting of 128 elements, each having 8 nodes, and a total of 750 active degrees of freedom, as shown in Figure 4.10. The radius of the material domain was 18.5 times the footing radius and its depth 27.9 times the footing radius. These outer boundaries represented distances where the influence of the load was negligible. Two different sands were used for the half-space, with the following creep parameters for the first material:

$$A = 0.55 \times 10^{-2} \left(\frac{\text{mm}^2}{\text{N}} \right)^B \text{hrs}^{-C} \ , \qquad B = 0.83 \ , \qquad C = 0.31 \ , \qquad (4.6)$$

where the values were obtained by using creep data from all the load steps of the two pressuremeter tests (Lach 1989) in the graphical method described earlier (§4.2.1). The second material is considered to be frozen Ottawa sand, and the parameters are obtained from Table 2.1 (following Klein 1979). For the two sands, E was estimated (Andersland and Anderson 1978) as 6000 MPa and 25000 MPa, respectively, and $\nu = 0.47$ was assumed for both cases.

For the simulations, a load of intensity 0.17 MPa and another of 0.283 MPa were applied independently on the half space consisting of frozen soil given by equation (4.6). Figure 4.11 shows the distribution of σ_{zz} along an axis very close to the symmetry axis at $t = 0$ hours (elastic stress) and at $t = 3323$ hours for both load cases, together with the analytical elastic solution along the symmetry axis. It can be seen that the difference in stress at $t = 0$ and $t = 3323$ hours is indistinguishable in the figure, and that the analytical distribution is almost identical to the numerical result. A similar behaviour was observed for Ottawa sand, and hence diagrams are not presented. Predominantly uniaxial straining, as characterized by the uniaxial Maxwell rheological model (Christensen 1971), occurring under the center of the circular load appears to be the cause for the above constant stress condition with time. Further, this occurrence of constant stress can be considered as an additional verification of the code and the axisymmetric element. Figure 4.12a shows the time dependent settlement profiles at the surface for the two loads on the frozen soil characterized by equation (4.6). A similar settlement analysis was performed for Ottawa sand under 0.85 MPa, and a comparison of the settlement profiles for the two sands is shown in Figure 4.12b. It can be seen that Ottawa sand, although subjected to a higher load, experiences a smaller settlement rate and a smaller long-term settlement than the other sand subjected to a smaller load. This is a consequence of the lower temperature at which the properties of Ottawa sand were evaluated. Material properties of frozen soils (mainly magnitudes of A and Young's modulus E) are strongly dependent on the temperature, and these materials become stronger as the temperature decreases. Figure 4.13a shows the settlement-time curves at the center of the footing for the three loading cases considered, and Figure 4.13b shows the corresponding settlement rate-time curves. Decrease in the settlement rate with increasing time can be seen from Figure 4.13b.

A more common structure-frozen soil interaction problem encountered in practice was simulated next, this being the interaction of a vertically loaded cylindrical footing with frozen soil, schematically depicted in Figure 4.14. Such interaction problems are commonly encountered in pier-type foundations for pipe-line installations, electrical transmission towers, water towers, etc.. The footing dimensions

and soil properties were selected to simulate a field problem. The cylindrical footing had a radius a of one metre and was assumed to be concrete with $E = 4 \times 10^4$ MPa and $\nu = 0.3$. The frozen soil was assumed to be the sand given by equation (4.6) with $E = 6000$ MPa and $\nu = 0.47$. Three values of buried depth d were considered, denoted by the d/a ratios of 0 (foundation placed on the surface of the soil), 1, and 2. Both the depth and the radius of the soil domain were taken as 81 times the footing radius. The r-z plane was discretized by a mesh of 380 four node finite elements and 424 nodes. Each footing was analyzed under the action of two equal load increments of 345.6 kN applied 20 days apart, as well as under the sum of the two load increments (ie. 691.2 kN) applied as a single load step.

The results of the numerical simulations are shown in Figure 4.15, where the vertical displacement at the center of the footing bottom is plotted against time, for all loading cases and footing embedments considered. The response for the two-step load is similar to that seen in the pressuremeter tests earlier. Figure 4.15 shows that the footings subjected to the two load steps undergo a larger creep settlement than the corresponding footings subjected to the sum of the two load steps as a single load step. Another observation arising from Figure 4.15 is the decrease in settlement and rate of settlement as the depth of embedment increases. This indicates that the deeper the footing, the lesser is the creep settlement. As a quantitative example for the decrease in settlement rate with time, it was seen from the numerical results that the settlement rates of the footing on the surface under a single load step at 200, 300 and 400 days, respectively, were 0.0294, 0.0223 and 0.0184 mm/day.

The code was next used to simulate the creep settlement of a cylindrical concrete footing of radius 1 m, and embedded to a depth of 2 m in different types of frozen soils at $-10°$C, the creep properties of which are given in Table 2.1 (after Klein 1979). The concrete was assumed to have elastic constants as $E = 3.5 \times 10^7$ kPa and $\nu = 0.30$. For all frozen soils in Table 2.1, it was assumed that $E = 25$ GPa and $\nu = 0.49$. The value of E was estimated using the data given by Andersland and Anderson (1978) for frozen sands. The analyses were performed under a vertical load of 23562 kN, and by using the same mesh as used in the earlier example (ref. to Figure 4.14). The results of the simulations for five types of frozen soils are

shown in Figure 4.16, where the settlement of the footing is shown against time. Figure 4.16 indicates the highly non-linear nature of the creep phenomenon. Creep settlement manifests as a result of the combination of magnitudes of parameters used. Settlement of Emscher-Marl attenuates rapidly, due partly to the comparatively low value of C, while Bat-Baioss clay and Karlshruher sand show much lower rates of attenuation, due in part to the comparatively high values A for these two frozen soils.

4.2.3 Laterally Loaded Rigid Cores in Ice

Penetration of laterally loaded rigid cores in ice plates is investigated in this subsection, by using the secondary stage power law model ($C = 1$ in equations 3.10, 3.14) in plane strain finite element analyses. One purpose of computational analyses of laterally loaded rigid cores in ice is the possible use of these results to interpret the movement of laterally loaded piles in ice (or frozen soils), a problem that will be discussed in greater detail in Chapter 5. Thus, analyses in this section would be used to build relationships between the force applied on the rigid core and the steady lateral penetration rate generated by it. Plane strain conditions may be assumed to approximately exist in a laterally loaded pile-ice system, at locations sufficiently distant from the ends of the pile such that end effects are not appreciable, and in situations where the piles deform with large radii of curvature. These analyses are based on the fact that ice is known to display prolonged stages of secondary creep under moderate loading intensities (Glen 1955), following a relatively short primary creep period. Above observation had also been noted by Domaschuk et al. (1989), during tests conducted by Kenyon on laterally loaded steel rods embedded in ice; their experimental results are as shown in Figure 4.17 (after Domaschuk et al. 1989).

The results of Domaschuk et al. (1989) in Figure 4.17 were obtained by embedding steel rods of diameter 76 mm in ice (at $-2°C$) to a length of 610 mm, and by applying two equal lateral loads on the protruding ends of the rods at the top and bottom of the ice mass. However, it was not possible to directly evaluate the creep parameters (A, B) or elasticity constants of the ice using those test results. Two

qualitative properties of ice evident from the experimental results in Figure 4.17 are that: (*i*). the rods attained a constant rate of penetration, and (*ii*). an appreciable instantaneous deflection (about 2 mm) occurred. Observation (*i*) above indicates that the creep of ice had taken place at an almost constant strain rate during the time span considered, a situation that can be conveniently described by an equation of the type (3.14) with $C = 1$, and (*ii*) indicates that the Young's modulus (E) of the ice probably had a low value. Thus $E = 500$ MPa was selected for the numerical simulations along with a Poisson's ratio (ν) of 0.47 to represent approximately total elastic incompressibility of ice.

Values suggested in the literature for A and B of ice vary over a considerable range, depending on pressure, temperature, texture, fabric, grain boundary structure, etc. (see §1.2, Hooke 1981). Thus determination of an exact value of B for ice used in the above tests was difficult. However, since a value of B in the vicinity of 3 seemed reasonable, $B = 3.17$ proposed by Glen (1955) was selected, and A was evaluated by an indirect (numerical) method using some of the above test results and the selected value of B, as described below.

A rigid circular core of diameter 76 mm was considered to be embedded in an ice plate under plane strain conditions. The configuration had symmetry about the loading axis, and thus the area of half the plane domain considered for the finite element discretization was approximately 1500×600 mm, with unit thickness in the third dimension. A total of 158, eight node finite elements were used in the mesh, with four Gauss points per element to maintain stress history. The finite element mesh is shown schematically in Figure 4.18, and the core was assumed to be fully bonded to the ice. (The mesh was prepared in such a way that the same mesh could be later used for simulations with separation between ice and core at the back of the core). A lateral load (P) of 114 N/mm was applied on the core, and its penetration into ice was simulated by the computer code for a set of values of A ranging from 0.0035 to 0.0250 $(\text{mm}^2/\text{N})^B$ and $B = 3.17$. The applied load was equivalent to one of the four load cases used in the tests (34.8 kN at each end of rod), and the initial value of A (0.0035) was obtained at $-2°$C by graphically interpolating the values of A given by Glen (1955) for different temperatures. Each simulation resulted in a

constant penetration rate of the core after a brief period of primary creep, similar to the behaviour seen in above tests. By plotting penetration-rate vs. parameter A, which resulted in a straight line, the value of A corresponding to the experimental rate (Figure 4.17) of 0.018 mm/hour was estimated as 0.0214 $(\text{mm}^2/\text{N})^B$.

With the above A and B values, simulations were performed using the same mesh for the remaining three loading cases considered in the tests, these being 40.6, 46.5, and 52.3 kN at each end of the rod (Domaschuk et al. 1989), or equivalently, 133.12, 152.46, and 171.48 N per unit depth in third dimension, for plane strain simulations. Numerical results from these simulations are shown in Figures 4.19a and 4.19b. Figure 4.19a shows the initial response, and Figure 4.19b shows the response predicted over a considerable period of time. Penetration rates evaluated from Figure 4.19b (by computing the slopes of the lines) are shown in Figure 4.20, along with the test results (from Figure 4.17) for comparison. For $P = 114$ N/mm, the numerical and test results coincide due to the above evaluation procedure, but the remaining loading cases provide a measure of the accuracy of prediction. From Figure 4.20, a fairly good comparison is seen for $P = 133.12$ and 152.46 N/mm, where the numerical values underestimate the test results by 10% and 15%, respectively. This indicates that the constitutive assumptions can be regarded valid for the relevant stress range and time span. But for $P = 171.48$ N/mm, the deviation is 29%. These comparisons can be affected by the following factors: (a). Different A and B values may prevail at higher loads (stresses). (b). Possible separation between ice and back of the core. (c). Inaccuracy of the value of E. (d). Use of small displacement formulation to model comparatively large penetrations.

Due to (d), the response curves may be inaccurate as time increases. However, the effect on rates would be negligible since the latter were computed from the initial parts of the response curves. Influence of (c) was found to be minimal, as simulations performed for different E values (150–9000 MPa) with all other conditions identical yielded almost identical penetration rates. Effect of (b) was investigated by modifying the mesh such that half the circumferential length of the core at its back was completely detached from the ice. Penetration rates predicted for this mesh with same parameters as earlier are also shown on Figure 4.20, for

P = 152.46 and 171.48 N/mm, and these overestimate the test values by about 100%. (Sample results for this unbonded core problem are compared with the fully bonded case in Figure 4.21). Thus the penetration rate for a separated core is more than twice that of a fully bonded core, and the test values for higher loads are between these two extremes. It is indeed possible that separation may occur over an area less than half the circumferential length, and a thorough study of this effect requires a more elaborate model involving bond elements and material parameters to simulate the bond between the core and the ice. However, lack of accurate data precludes the validity of such a study at this stage. The possibility of (a) is real (Hooke 1981), but a comprehensive parametric study using different combinations of A and B values were not undertaken here, mainly due to limitations of time.

By using the least squares method to fit the numerical results for the fully bonded circular core (Figure 4.20) to a power relationship, the following equivalent non-linear dashpot model can be proposed for the circular core-ice system with full bond:

$$\dot{d} = (0.51737 \times 10^{-8}) P^{3.1835} \ , \tag{4.8}$$

where $\dot{d}$ is the penetration rate in units of (mm/hour), and P the applied load in units of (N/mm). A similar set of simulations using a square-shaped core with circumferential length equal to that of the circular core (i.e. each side 59.69 mm) was conducted using the same creep and elasticity parameters as earlier. The finite element mesh used for the study is as shown in Figure 4.22. The predicted penetration behaviour in this case are as shown in Figures 4.23a and 4.23b, and the penetration rates of the square core are compared with those of the circular core in Figure 4.24, which indicates that a square core would show a lesser penetration rate than a circular core, at a given load and under the dimensions considered. The equivalent dashpot model for the square core-ice system with full bond is:

$$\dot{d} = (0.3457 \times 10^{-8}) P^{3.2256} \ , \tag{4.9}$$

where all notations are as earlier. By using equations (4.8) or (4.9), simple beam elements on non-linear dashpot mechanisms can be formulated, which can then be

used for analyses of pile-ice systems. These latter developments are discussed in §5.2.

An alternate study was conducted by evaluating parameter A in such a way that the predicted rate of penetration would exactly match the highest observed test rate, instead of the lowest test rate as done earlier. The computational procedure was identical to above, and the value of A thus computed was 0.0305 $(\text{mm}^2/\text{N})^B$. Using this value of A along with all other parameters as earlier, a series of plane strain simulations were performed, and the resulting steady rates of penetrations of the core are as shown in Figure 4.25, where test data (Domaschuk et al. 1989) are also shown for comparison. The equivalent dashpot model based on this investigation is:

$$\dot{d} = (0.8338 \times 10^{-8}) P^{3.1567} \ , \tag{4.10}$$

where all notations are as earlier. As can be seen from Figure 4.25, this effort does not improve the agreement between the predicted and observed penetration rates, as compared to that in Figure 4.20. The reasons for the deviations of the predicted results are as discussed earlier.

Figure 4.26 shows the profile of σ_{xx} (normal stress parallel to the load axis) along a line parallel to and 7.41 mm away from the axis of loading, at times $t = 0$ (initial elastic stage) and $t = 166$ hours, for the case of $P = 133.12$ N/mm. The stress profiles are shown for the ice domain in front of the core only, and the plot was obtained by averaging the stress values available at Gauss points. Figure 4.26 indicates that the redistribution of σ_{xx} at some locations along the line considered amounted to 35% of the magnitude at $t = 0$. At locations further away from the loading axis, larger percentage variations (in the range of 100%) occurred in the magnitude of σ_{xx}. Similar behaviour was observed in the case of σ_{yy} also.

The code ITFECC-A was next used to simulate an example of creep movement of a group of cores (consisting of two cores) in ice, under lateral loads. The purpose of this investigation was to demonstrate the influence of the core spacing on the interaction between the two cores. In field situations, this type of situation arises

in the case of pile groups. The schematic diagram for the FE simulations here is shown in Figure 4.27, where the two square cores, each of cross-sectional dimensions 400×400 mm^2, are located with a clear distance of d between one another. The core dimensions were selected to be typical of a field situation. Material parameters for ice were selected as $A = 0.0214$ (mm/N)^B (hr)$^{-C}$ and $B = 3.17$, as earlier. Simulations were carried out for different magnitudes of d, and for each d, a selected set of loads given by $P = 300$, 450, 600, and 800 N/mm were applied, in turn, on the core at the left in Figure 4.27. The d values were 400, 800, and 2000 mm. For comparison purposes, a single core was also simulated under the same set of loads, a case that corresponded to $d \rightarrow \infty$. Due to the symmetry about the loading axis, half the actual domain was considered, with a length of 11.6 m and a breadth of 3.9 m, and the FE mesh consisted of 108, 8-node elements and 481 nodes. In all cases, it was assumed that a perfect bond exists at the core-ice interface. During the simulations, the lateral displacement of the loaded core was noted with elapsed time.

Sample displacement vs. time curves obtained from the above simulations are shown in Figure 4.28. The rates of displacements computed from all simulations (by evaluating the slopes of the displacement-time plots) are as shown in Figure 4.29. As expected, Figures 4.29 and 4.28 show that the influence of the unloaded core on the displacement (or displacement rate) of the loaded core diminishes as the spacing between the two cores increase. It shows that for larger spacings (ie. $d = 2$ m), the behaviour of the core group approaches the limiting case of a single core. Additional simulations by applying the load on the core at the right in Figure 4.27 showed that reciprocity existed in these problems, i.e. the lateral movements of the unloaded core and the loaded core were unaffected by the location of the loaded core, as long as the symmetry of the mesh discretization and complete bond between the cores and the ice were assumed.

4.2.4 Penetration Tests on Frozen Soils

The computer code ITFECC-A was used to model several structure-frozen soil/ ice interaction examples encountered in field testing of frozen ground. These situations were the simulations of static penetration tests (SPT) and penetration-rate controlled tests in frozen soils, using three types of indenter shapes. One shape used was a cone (Figure 4.30), identical to the indenter used in the standard electric penetrometer for soil investigations (de Ruiter 1971). Alternative simulations were conducted with a cylindrical indenter (disk type indenter) of diameter 35.6 mm, and a semi-spherical indenter of the same diameter. Each of these indenter tips were assumed to be fixed to a shaft of diameter 35.6 mm, as usually is the case in a soil-penetrometer. Similar type of field tests had been carried out by Ladanyi (1976) on frozen soils, with the objective of using the results of static and penetration-rate controlled penetrometer tests to predict the behaviour of foundation elements on frozen soil. Numerical analyses such as the present study can be used to develop sets of curves relating penetration, penetration-rate and resistance, which may later be useful for interpretation of creep properties in the field. These simulations are also important in situations where stresses generated around an indenter need to be studied, as experienced in several field applications, e.g. in ice breaking in arctic waters. The penetration-rate controlled loading are also encountered in the field, e.g. in the case of an ice sheet over a water body pressing against a pier.

The frozen soils selected for this analysis are frozen Ottawa sand, Emscher-Marl, and Bat-Baioss clay. The creep properties for these soils are as given in Table 2.1 (after Klein 1979). The E values were approximately estimated (using data of Andersland and Anderson 1978) as 25 GPa for all soils except Bat-Baioss clay, which was estimated to have $E = 2$ GPa, and $\nu = 0.49$ was used for all soils to represent elastic incompressibility. The frozen soil domain considered for the axisymmetric finite element simulation had a radius 16.9 times the radius of the penetrometer shaft, and a depth of 39.3 times the latter. The finite element mesh for the conical and disk indenter problems consisted of 280 elements and 315 nodes, while that for the spherical indenter problem consisted of 207 elements and 235 nodes.

At the commencement of the analyses, both the conical and semi-spherical indenters were assumed to be already embedded in the frozen ground up to the level where the shaft assumed the cylindrical shape with diameter 35.6 mm, while the disk indenter was assumed to rest on the frozen ground surface (not embedded). Also, slip between the indenters and the soil was not modelled, nor was the stress singularity at the tip of the conical indenter. Due to these reasons, certain discrepencies may exist between the numerical results obtained here and the actual field observations.

In the first type of tests simulated, a single-stage load of 18 kN was applied on the conical indenter placed on the three soils. The penetration-time behaviour obtained from the simulations is plotted in Figure 4.31. The results show that the penetration and the rate of penetration are largest for Bat-Baioss clay. Within the time span considered, Ottawa sand undergoes the least penetration and Emscher-Marl undergoes an amount larger than the latter; however, the rate of penetration in Ottawa sand is higher than that in Emscher-Marl, and thus Ottawa sand would show a larger penetration than Emscher-Marl in the long term. Ottawa sand and Emscher-Marl attenuates much faster than Bat-Baioss clay. Figure 4.32 shows the penetration with time in Ottawa sand for the three different indenter shapes, subjected to the same load. The disk indenter shows a penetration and a rate of penetration much larger than the other two indenters, while the other two shapes (semi-sphere and cone) show responses close to one another. The conical indenter shows the least penetration. A primary creep response can be noticed for all indenter shapes. The conical and semi-spherical indenters have identical contact surface areas of 19.91 cm^2, and the disk indenter half of that (9.95 cm^2). Thus the disk indenter shows the largest settlement probably due to its least contact area. The cone and semi-sphere, although having the same contact area, show responses slightly different from one another probably because of the difference in shape. It is noted that these results are obtained under the assumption of perfect bond between the indenter and the frozen medium.

The second type of simulations considered were penetration-rate controlled problems. The indenters were subjected to imposed penetration rates and the re-

sistance offered by the frozen medium was evaluated. The frozen soils, the indenter shapes and the finite element meshes used were the same as earlier. Simulations were done using a low penetration rate of 4 cm/day, and two higher rates of 10.2 cm/hr. and 38 cm/hr.. The latter two rates were the same as two of the rates selected by Ladanyi (1976) for his rate-controlled tests on permafrost, and the slower rate (4 cm/day) was a value suggested by Huneault and Ladanyi (1987). For the numerical simulations, constant time intervals were used throughout the analysis history, these being 0.001 hrs. for 4 cm/day, 2.0×10^{-5} hrs. for 10.2 cm/hr. and 5.0×10^{-6} hrs. for 38 cm/hr..

The resistance-penetration curves for the conical indenter in frozen Ottawa sand for the three penetration rates are as given in Figure 4.33, which, as expected, show an increased resistance for higher rates of penetration. A drop in the rate of increase of resistance is seen for all penetration rates with increasing penetration. The resistance encountered for the lowest rate of penetration (4 cm/day) shows a tendency to stabilize as penetration increases. This stabilizing tendency might be encountered for the higher rates of penetration after a much larger penetration had occurred, but the numerical analysis here do not hold for such large deformations; therefore such phenomena were not investigated. The resistance-penetration curves for the three indenters subjected to a penetration rate of 4 cm/day in frozen Ottawa sand are given in Figure 4.34; according to these results, the disk indenter encounters the least resistance, followed by the sphere, and the cone, respectively in the order of increasing resistance. As mentioned earlier, slip between the indenter surface and the frozen medium was not modelled in the analyses here.

It is somewhat difficult to directly compare these numerical results with the test results obtained by Ladanyi (1976) due to some basic differences. Ladanyi (1976) obtained an average resistance for each penetration rate used (which ranged from 38 to 152 cm/hour), and the resistance was somewhat erratic due to the presence of varves; he achieved penetrations up to approx. 60 cm, and reported an increased resistance with increasing penetration rate. The latter property is observed from the numerical results (Figure 4.33), but the presence of inhomogeneities or layers etc. was not modelled in the simulations here. In addition, large depths of pene-

tration cannot be modelled using the small displacement theory used here. Thus the numerical scheme would yield reasonable results for small depths of penetration only, and thorough studies of the penetration phenomena can be made for low rates of penetration.

4.3 Analyses Using Fish's Unified Creep Model

Computer code ITFECC-A is capable of analyzing interaction problems using the generalized version of Fish's unified creep model (see §3.5). The validity of the generalization process applied to the uniaxial model of Fish is evident from Figure 3.10. In the ensuing subsections, the generalized creep model of Fish is applied to solve several example problems involving the deformation of frozen soils and ice. These examples are more oriented towards demonstrating the ability of the creep model of Fish to simulate various stages of creep, including the tertiary (accelerating) creep stage which the power law model discussed previously cannot simulate. Emphasis is placed on the general trends of creep deformation that the model can simulate, and parallels are drawn with creep behaviour of frozen media as observed by experimentalists.

Test data from uniaxial creep compressive tests on samples of the relevant frozen material are the most convenient means of deriving appropriate creep parameters for the model. Results of this type of tests are available in the literature, for ice (e.g. Mellor and Cole 1982, Jacka 1984) and frozen soils (e.g. Yuanlin and Carbee 1983). Appropriate parameters for different frozen materials can be derived based on some of these data, but each set of parameters would be applicable within the relevant stress and temperature ranges. Derivation of creep parameters is further discussed in §4.3.1.

4.3.1 Uniaxial Creep Tests on Ice

Jacka (1984) published experimental data obtained from a series of uniaxial creep tests on polycrystalline ice samples. He selected four temperatures (-5, -10.6, -17.8, and $-32.5°C$) at each of which, ice samples were subjected to uniaxial creep

under different magnitudes of constant applied stress. Strain and time were recorded in each test, and strain rates were calculated from raw test data. The summary of data at minimum strain rate is given in Table 2 of Jacka (1984). It can be seen from his data that some tests (under low applied stresses) have not reached the minimum creep strain rate during the testing period. Data from tests where a minimum creep strain rate has been recorded can be used to evaluate the appropriate parameters (see equation 3.27) for the creep model of Fish (1984).

The method of least squares was used to fit selected sets of data of Jacka (1984) to relations given in equation (3.27). It was noted that, at a given temperature, if all available data (i.e. data under all the stress magnitudes considered) were used, the fit to equations (3.27) was poor. This indicated clearly that such fits can be reasonable only within selected ranges in the magnitude of stress. Therefore, by selecting an appropriate range of stress under each temperature (the reported time to minimum strain rate can also be used as a criterion here), reasonably good least squares fits of Jacka's (1984) data to relations in equations (3.27) were obtained. Sample creep parameters A_1, η, C_o, and μ obtained in this manner for the four temperatures are shown in Table 4.1. When the parameters in Table 4.1 were re-substituted in relations of equation (3.27) and used to predict the relevant test data (from Table 2 of Jacka, 1984), the maximum deviation between a predicted and an observed value (of either minimum strain rate or time to minimum strain rate) was less than 16%.

In order to demonstrate the use of the generalized model to predict uniaxial test data, code ITFECC-A was used to re-simulate the uniaxial tests using axisymmetric finite element analyses. The creep parameters shown in Table 4.1 for $-5°C$, along with a value of $\delta = 0.5$, were used to model ice. This value of δ is close to 0.47 suggested by Fish (1987) for ice. The same thin rod structure used for results presented in Figure 3.10 earlier (i.e. length = 60 mm; radius = 0.2 mm; modelled by a column made of 3, 8-node axisymmetric elements stacked upon one another) was considered, with values of Young's modulus (E) = 8000 MPa (Sego and Morgenstern 1983) and Poisson's ratio (ν) =0. The results predicted by finite element analyses are compared in Figure 4.35 with the experimental results of Jacka (1984)

for four load cases. Jacka (1984) presented his results by using octahedral shear stress and octahedral shear strain values (he multiplied uniaxial stress by $\sqrt{2}/3$ to obtain octahedral shear stress, and uniaxial strain by $1/\sqrt{2}$ to obtain octahedral shear strain); therefore the vertical strain rates predicted by the code were converted appropriately to octahedral shear strain rates, and are shown in Figure 4.35. The agreement between the predicted and experimental observations is reasonable, except that the predictions noticeably overestimate the observed values in the primary creep stage for lower stress magnitudes (1.0 and 1.3 bar).

Figure 4.36 presents comparison of predicted strain rates with some of the experimental curves obtained by Jacka (1984) at lower temperatures. Predictions in Figure 4.36 were obtained by using the appropriate parameters for the respective temperatures, shown in Table 4.1. The agreement between predicted and observed values in Figure 4.36 is reasonable. Comparisons in Figures 4.35 and 4.36 indicate the ability of the generalized creep model to reasonably re-simulate uniaxial creep test data and to display characteristics of the entire creep curve, including the decelerating and accelerating creep stages.

Some general characteristics of the influence of temperature on the creep parameters of Fish's model can be noted from Table 4.1. Among the trends notable are the increase in the magnitude of A_1 and the decrease in the magnitude of C_o, as the temperature decreases. These trends generally reflect the facts that, under a given stress, time to minimum strain rate increases as the temperature falls, with a simultaneous decrease in the magnitude of the minimum strain rate; in other words, failure is predicted to occur quicker when temperature rises. However, it is noted that Table 4.1 cannot be used to conduct a very precise evaluation of the temperature effect on the parameters, since different stress ranges have been considered at different temperatures (ref. Columns 1 & 2 of Table 4.1).

4.3.2 Pressuremeter Tests on Frozen Ground

The generalized creep model given by equation (3.28) was next used to simulate the response of an icy frozen soil in a pressuremeter test. As considered earlier

(§4.2.1), it is reasonable to assume plane strain conditions over a cross-sectional plane at or near the center of the probe due to the large length/radius ratio of the pressuremeter probe. Thus, a pressuremeter test in frozen soil was simulated under conditions of plane strain axisymmetry.

Yuanlin and Carbee (1983) reported results of uniaxial creep tests on remolded, saturated frozen Fairbanks silt; of these, results obtained at $-5°C$ were quoted by Fish (1984) for use in his model. Using a least squares fitting of these uniaxial test data (at $-5°C$), to the relations given in equations (3.27), the following numerical values were obtained for the various parameters:

$$\begin{aligned} A_1 &= 151.83 \left(\frac{N^2}{mm}\right)^{\eta} hr \\ \eta &= 6.256 \\ C_o &= 0.00055 \left(\frac{mm^2}{N}\right)^{\mu} hr^{-1} \\ \mu &= 6.158 \end{aligned} \tag{4.11}$$

In addition to above, $\delta = 0.47$, an average value applicable to ice (Fish 1987), was selected as applicable to the icy frozen silt considered here. A Young's modulus (E) of 8 GPa and a Poisson's ratio (ν) of 0.47 (to signify elastic incompressibility) were used. A Poisson's ratio very close to 0.5 was not used since, due to numerical complications, this particular finite element behaved very stiffly at such values.

The configuration of the pressuremeter test considered is similar to that shown in Figure 4.1, and a horizontal plane at the center of the pressuremeter probe was considered for FE simulations. The diameter of the bore-hole is 76 mm and the outer boundary of the frozen domain is at a radius of 1038 mm. The radius of the bore-hole corresponds to the diameter of the OYO elastmeter 100 pressuremeter probe (Kjartanson 1986). The pressure (q) applied on the wall of the bore-hole was considered in multiples of 1 MPa, in order to demonstrate the behaviour of the frozen media predicted by the generalized model given by equation (3.28). The frozen domain was discretized by 100 elements of equal size along a radial line, with three nodes per each element. Numerical integration of order two was used in the

radial direction and stresses needed for the incremental analysis were maintained at two Gauss points in each element.

The results of the numerical analysis of the pressuremeter test for a range of loads (q =1, 1.5, 2, and 3 MPa) are as shown in Figure 4.37, where the radial displacement of the bore-hole wall is plotted with time. As seen from Figure 4.37, for all load cases considered, the response of the frozen medium remained within the primary (or attenuating) creep range during the time interval considered. For $q = 1$ MPa, the response did not enter the tertiary stage but remained in the primary stage for a very long time period such as two years. This shows that the model can be used to simulate situations of attenuating creep (where failure does not occur) for practical purposes.

The pressuremeter test was simulated under a load of 3 MPa by varying the magnitude of A_1 in equation (4.11). A decrease in the magnitude of A_1 can be caused, for example, by a rise in the temperature (see §4.3.1, Table 4.1). In Figure 4.38, the results of simulations carried out for three magnitudes of A_1 ($A_1 = 151.83$, 15.18 and 3.79 $(\mathrm{N/mm^2})^{\eta}\mathrm{hr}$), with all other parameters held identical to those in equation (4.11) are shown. Figure 4.38 shows that the creep displacement decreases with decreasing magnitude of A_1 at a given time, while the creep curve approaches failure point (by flattening) faster for lower magnitudes of A_1. Thus the curve for $A_1 = 3.79$ $(\mathrm{N/mm^2})^{\eta}\mathrm{hr}$ shows the tendency to reach the inflexion point earliest of the three magnitudes of A_1. Figure 4.39 shows the displacement curve for $A_1 = 0.75$ $(\mathrm{N/mm^2})^{\eta}\mathrm{hr}$ with all other parameters held identical to earlier; it clearly shows a tertiary creep stage following the primary creep stage and the inflexion point. A scrutiny of the numerical results showed that the displacement rate accelerated after approximately 200 hours. Note that Figure 4.39 is presented for a fairly large displacement range for the purpose of clarifying the behaviour predicted by the creep model in this instance.

Figure 4.40a shows the distribution of the radial stress (σ_{rr}) at different time histories, along with the analytical elastic stress distribution obtained by plane strain analysis, for the material described by the parameters given by equation

(4.11) and subjected to a pressure of 1 MPa. Away from the bore-hole wall, the creep process has caused the radial stress to acquire magnitudes of more than 10 times the corresponding magnitudes derived from linear elastic analysis. There is a rapid variation in magnitude of σ_{rr} in the far field during the first few hours, and the stress distribution throughout the domain apparently stabilizes after approximately 1500 hours. A stabilized stress distribution is indicated by the closeness of the stress profiles at $t = 1634$ and $t = 3634$ hrs.. The tangential stress ($\sigma_{\theta\theta}$) at different times for the same example are shown in Figure 4.40b, along with the corresponding analytical solution. Here, redistribution of the stress (change in magnitude relative to the initial linear elastic stress) takes place throughout the domain, and the stress near the bore-hole wall changes rapidly during the first few minutes. The entire tangential stress distribution turns compressive later in the creep process, and apparently stabilizes after a long period of time similar to the case of the radial stress. Stress curves for other cases where the response attenuated showed similar trends and are thus not shown here. For higher loads, it took longer to reach the stabilized stress state than in the case of lower loads. It is noted that the stress behaviour depends on the particular magnitudes of material parameters used in the model. In cases where the tertiary creep behaviour was predicted, it was not possible to determine the long-term stress behaviour as the material displayed large deformations with increasing time. Characteristics seen from the Figures 4.40a and 4.40b are that the creep model considered here causes a considerable amount of stress redistribution, and that, for attenuating responses, the stress distribution apparently stabilizes towards a profile which is quite different from the linear elastic stress distribution. In contrast, the generalized power law creep model (§4.2.1) would cause a comparatively less amount of stress redistribution (relative to the corresponding linear elastic stress state) near the center of the pressuremeter probe, for low magnitudes of the power term of stress used in the model. The radial stress profiles predicted in a similar pressuremeter simulation using the power law model are as shown in Figure 4.40c.

In Fish's model, failure is basically governed by the time t_m to minimum creep strain rate; in the uniaxial case, it is easily seen that this occurs at $t = t_m$ (Figure

2.2). However it is difficult to make a prediction regarding the failure time in a multi-dimensional case such as the examples considered here, by using a simple analytical method. In some pressuremeter examples presented here, the failure can be witnessed in a global sense. In such cases, it is reasonable to expect that a considerable portion of the domain should enter tertiary creep stage for the bore-hole wall to show an accelerating creep displacement. Different failure times t_m would be in effect at different points in the domain depending on the magnitude of the equivalent stress existing at that point and time, and the appearance of tertiary creep in the domain would be a result of the cumulative effect of these individual states of creep deformation.

The existence of different creep stages at different locations in the domain is demonstrated by Figures 4.41a and 4.41b. Figure 4.41a shows the radial strain rate with time at radial distances (d) of 1.91, 21.91 and 141.9 mm from the bore-hole wall, and Figure 4.41b shows the tangential strain rate with time at the same locations, for the simulation shown in Figure 4.39 (i.e. for $A_1 = 0.75$ $(\mathrm{N/mm^2})^n\mathrm{hr}$ and remaining parameters as in equation 4.11, and a load of 3 MPa). Figure 4.41a shows that the radial strain rate accelerates after about 150 hours at $d = 1.91$ mm and 200 hours at $d = 21.91$ mm, but does not enter the accelerating stage until after 450 hours at $d = 141.9$ mm. In Figure 4.41b, tangential strain rate shows a trend approximately similar to that of the radial strain rate. It is notable that although the radial strain rate had entered tertiary creep stage close to the bore-hole wall at 150 hours, the global response shown in Figure 4.39 does not reflect this behaviour until approximately 200 hours had elapsed.

An interesting similarity can be seen between the first two curves in Figures 4.41 and the strain rate-time curves in Figure 1.7. Curves in Figure 1.7 show the variation of the circumferential strain rate at the bore-hole wall with time, obtained from a series of actual pressuremeter tests conducted on ice at $-2°\mathrm{C}$ by Shields et al. (1989). From Figure 1.7, failure point in the curve for 2.5 MPa can be noticed at approximately 125 hours and the minimum strain rate (at the wall) is approximately 0.06 hour^{-1}. From the computational results in Figure 4.41b, where 3 MPa and creep parameters in equation (4.11) with the exception of $A_1 = 0.75$ $(\mathrm{N/mm^2})^n\mathrm{hr}$

were used, a point 1.91 mm away from the wall is seen to fail at approximately 160 hours and the minimum strain rate is 0.3×10^{-3} hour^{-1}. Unfortunately, no direct comparison with the test data in Figure 1.7 can be made since uniaxial test data necessary to evaluate the parameters in equation (3.27) for the ice used in the tests by Shields et al. (1989) are not available. However, similarity between the responses observed from actual tests and those predicted by numerical simulations indicate the suitability of the generalized model (equation 3.28) to represent the constitutive behaviour of frozen media experiencing accelerating creep.

4.3.3 Laterally Loaded Rigid Cores in Frozen Ground

A problem similar to the laterally loaded rigid core in ice considered earlier under the power law (§4.2.3) was simulated using Fish's generalized model. This example was analyzed under plane strain conditions. The finite element mesh used was identical to that given in Figure 4.18. The core had a diameter of 76 mm, was assumed to be completely bonded to the embedding frozen medium at all times, and was forced to move under the action of three lateral loads (P) of magnitude 228, 343 and 456 N/mm, applied in turn. The configuration had symmetry about the loading axis, and thus the area of half the plane domain considered for the finite element discretization was approximately 1500×600 mm, with unit thickness in the third dimension. A total of 158, eight node finite elements were used in the mesh, with four Gauss points per element to maintain stress history. As noted while discussing the power law model in §4.2.3, results of this type of simulation can be used later to develop a model of a beam on a non-linear dashpot mechanism, which in turn will serve as a simplified pile model to analyze problems of laterally loaded piles in permafrost. Also, similar analyses can be used to study stress distribution in ice sheets pressing against pier-type structures.

The results of the above simulations are presented in Figure 4.42, which shows the lateral displacement of the rigid core with time under the three loads of 228, 343 and 456 N/mm. The frozen medium was characterized by $A_1 = 3.79$ (N/mm^2)^{n}hr with all other parameters as given in equation (4.11), along with $\delta = 0.47$, $E = 8000$ MPa and $\nu = 0.49$. For the plane strain finite element, it was possible to use $\nu = 0.49$

without encountering any significant numerical complication. It can be seen (Figure 4.42) that the response becomes larger with increasing load, and for the case of 456 N/mm, the material in front of the core fails by entering the tertiary creep stage. The global response is in the attenuating creep stage under 228 N/mm, while it displays almost a steady state (straight line) for 343 N, indicating that the global response has entered a transition stage in between the primary and tertiary creep stages.

Figure 4.43 shows the profile of σ_{xx} (normal stress of the frozen material parallel to the loading axis) at $t = 0$ and $t = 255$ hours, for the case of P = 343 N/mm, along a line parallel to and 7.41 mm away from the loading axis; the stress profiles are shown for the frozen domain in front of the core only, and the plot was obtained by averaging the stress values available at Gauss points. As seen from Figure 4.43, the percentage of stress redistribution with time amounts to about 70% at some locations along the line. However, at locations further away from the loading axis, redistribution yielded variations exceeding 100% of the magnitude of the elastic stress. Stress σ_{yy} (normal stress perpendicular to the loading axis) experienced similar amounts of redistribution with time, but the stress profiles were somewhat irregular, and are not shown here.

4.3.4 Plate Load Tests on Frozen Ground

A plate load test on frozen ground was considered for simulation using the generalized model of Fish, using axisymmetric analyses. The configuration of the plate load test is shown in Figure 4.44. The finite element discretization of the r-z plane was done using 118, eight node finite elements, with four Gauss points per each element to maintain the stress history. The steel plate had a diameter of 300 mm, a thickness of 50 mm, a Young's modulus of 2×10^5 MPa and a Poisson's ratio of 0.3. Outer radius of the frozen domain was 4.5 times the plate radius, and the depth of the frozen domain was 11 times the plate radius.

Simulations were carried out for three uniform loading intensities (p) applied on the plate, these being 0.88, 1.76 and 2.64 MPa. The frozen material was character-

ized by parameters in equation (4.11) with the exception of $A_1 = 3.79\ (\mathrm{N/mm^2})^n\mathrm{hr}$, and by $\delta = 0.47$, $E = 8000$ MPa and $\nu = 0.49$. The axisymmetric finite element used here did not encounter numerical complications for $\nu = 0.49$. The results are shown in Figure 4.45, where the vertical settlement at the center of the plate are plotted against time. The global response (settlement at the center of plate) under the largest load of 2.64 MPa displays failure or tertiary creep behaviour, while those under the two lower loads display attenuating behaviour. These results confirm the ability of the generalized model given by equation (3.28) to represent attenuating as well as accelerating global responses in multi-axial stress situations.

Figure 4.46 shows the distribution of the vertical normal stress (σ_{zz}) along a line parallel to and 18.75 mm away from the axis of axisymmetry, at times $t = 0$ and $t = 146$ hours, for the case of 2.64 MPa applied on the plate. Redistribution of stress during this time amounts to 100% of the elastic stress values at some locations along the line considered. Note that the stress profiles are based on stresses at element boundaries, which were obtained by averaging available stress values at Gauss points. Similar redistribution behaviour was seen at other points in the frozen domain, and in the case of other stress quantities.

4.4 Analyses Using Domaschuk's Model

Computer code ILFENP was used to analyze some examples involving deformation of frozen sands. The accuracy of the algorithms in the code were verified earlier (see §3.6.3). The model was described previously in §2.4 and §3.2.3, and numerical values for various parameters involved were derived by Rahman (1988) for the particular frozen sand (at $-3°$C) used in the experimental program. The relevant parameters are not yet available for other frozen materials. Thus, computational analyses described in the ensuing sub-sections will be limited to the set of parameters evaluated by Rahman (1988).

4.4.1 Pressuremeter Tests on Frozen Sand

Pressuremeter tests, similar in configuration to that shown in Figure 4.1, were

simulated by using the model of Domaschuk (§2.4, §3.2.3) to represent the creep of the frozen sand. Rahman (1988) evaluated the parameters involved in this model given by equations (3.33)–(3.36), basing all computations on the kN-m-hr system of units. Thus the equations (3.33) and (3.34), for the particular sand, can be written as (Rahman 1988, Domaschuk et al. 1991):

$$K_c = 10250 \left(1 + 1.756 \times 10^{-2} \exp\{-0.0045t\}\, \sigma_m\right)^2 , \qquad (4.12a)$$

and

$$G_c = \left(3 \times 10^{-5}\, \sigma_m^{-0.205}\, t^{0.147} + 1 \times 10^{-5}\, t^{0.23}\, \frac{S_d}{\sigma_m}\right)^{-1} , \qquad (4.12b)$$

where σ_m and S_d are, respectively, the current volumetric mean stress (kPa) and current resultant deviatoric stress (kPa), defined by equation (3.35), and t is the elapsed time (hours) from the instance of application of the load. Assuming that equations (4.12) represent the constitutive behaviour of the frozen sand under consideration, a pressuremeter test similar to the Test 1 depicted in Figure 4.1 was simulated for two different applied loads by using axisymmetric FE analyses.

A pressuremeter probe of length 0.39 m was assumed to be placed in the borehole of radius 0.038 m, and centered at a depth of 0.55 m below the surface of the frozen sand. The outer radius of the frozen sand domain was assumed at a radius of 0.965 m. The total depth of the frozen sand domain was 1.8 m. The r-z plane was discretized using a mesh of 491 nodes and 111, 8-node axisymmetric elements. Two applied loads, given by probe pressures of 880 kPa and 1770 kPa, were considered in turn. For the load incrementing algorithm in code ILFENP, a total of 100 load increments was used for each analysis (i.e. the load was divided into 100 parts of equal size in each case), and stresses were maintained at 4 Gauss points in each element. As required due to the nature of the constitutive model, a separate analysis was performed for each time instant considered under each load case.

The results of the analyses for each of the applied probe pressures (880 and 1770 kPa) at elapsed times (t) of 10, 24, 48, 96, 192, 288, 480, and 960 hours, are as shown in Figure 4.47, where the radial displacement at the center of the probe is shown against time. Figure 4.47 shows that the qualitative behaviour of the model

is satisfactory, since increasing creep deformations are predicted with increasing time and load. However, these predictions do not agree with the test observations of Lach (1989) for the relevant pressuremeter test (Test 1) considered in §4.2.1. Therefore, no attempt is made here to compare the predictions with test results.

The analyses for the applied probe pressure of 880 kPa was repeated by using a plane strain axisymmetric mesh, in order to verify the equivalence of predictability of the 8-node Serendipity axisymmetric element and the 2-node plane strain axisymmetric element. The latter mesh was assumed to represent the horizontal plane intersecting the mid-depth of the probe, and the resulting line-domain was discretized by using 100, 2-node plane strain axisymmetric elements of equal radial length. Stresses were maintained at a single Gauss point in each element. The results predicted by these analyses overestimated the previous predictions obtained using the fully axisymmetric mesh by 6% to 7%. This deviation is acceptable due to differences in mesh discretization in the radial direction in the two cases, and differences in the existing stress state as assumed for the two types of elements. Thus it can be reasonably assumed that the results in Figure 4.47 are computationally accurate predictions under the constitutive model of equation (4.12) and (3.36).

4.4.2 A Plate Load Test on Frozen Sands

A plate load test on frozen sand, similar to that depicted in Figure 4.44, was simulated using the constitutive model in equations (4.12) and (3.36). The dimensions of the plate and the finite element discretization of the domain were identical to those described in §4.3.3. The steel plate was assumed to have a Young's modulus of 2×10^8 kPa and a Poisson's ratio of 0.3, which were equivalent to an elastic bulk modulus of 1.6667×10^8 kPa and an elastic shear modulus of 7.6923×10^7 kPa. Because of the presence of the steel plate, this example directly involved interaction of an elastic structure with a frozen soil. For the purpose of modelling non-creeping structural domains, the same element subroutines for creeping media in ILFENP could be used, by using an input of $t = 0$, regardless of the time of solution under consideration (Appendix D). In the case of $t = 0$, the parameter K_o in equation (3.33) represented the elastic bulk modulus, and equation (3.34) was replaced with

an elastic shear modulus of constant magnitude.

The analysis was conducted for a uniform pressure of 880 kPa applied on the plate, and the predicted settlement at the center of the plate at different times are shown in Figure 4.48. The times selected for the FE analyses were identical to those in the previous pressuremeter tests (§4.4.1), and the load was incremented in 100 equal parts as earlier. The results in Figure 4.48 show increasing settlement with time, as should be expected qualitatively. However, as before, no comparisons are made with available test results (Lach 1989).

Table 4.1: Creep parameters for Fish's (1984) model based on data of Jacka (1984) for ice

Temp. °C	Applicable stress range		A_1 $(\text{MPa})^{\eta}\text{hr}$	η	C_o $(\text{MPa})^{-\mu}\text{hr}^{-1}$	μ
	τ_0 bar Jacka 1984	Equiv. uniaxial stress, σ MPa				
−5.0	1.0–3.0	0.209–0.628	3.148	4.183	6.774×10^{-11}	3.412
−10.6	2.0–6.0	0.419–1.256	26.30	3.420	1.877×10^{-11}	3.051
−17.8	3.0–8.0	0.628–1.675	104.49	2.428	4.814×10^{-12}	2.960
−32.5	3.6–10.0	0.754–2.094	492.71	2.503	1.073×10^{-12}	2.653

Note: Jacka (1984) gave τ_0 as the octahedral shear stress in bars (1 bar = 0.098692 MPa).

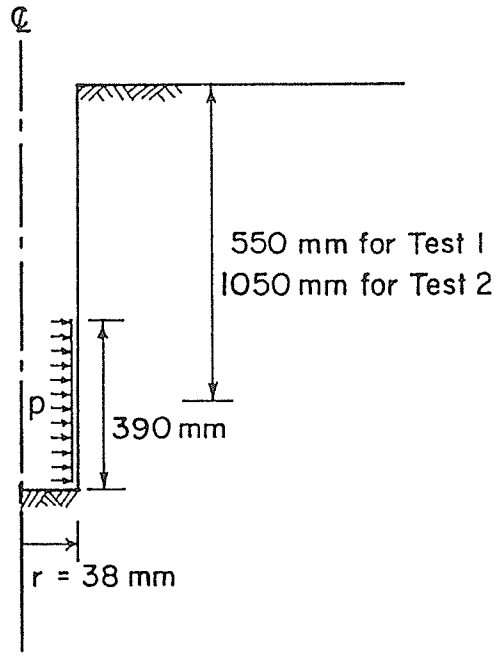

Figure 4.1. Configuration of pressuremeter tests.

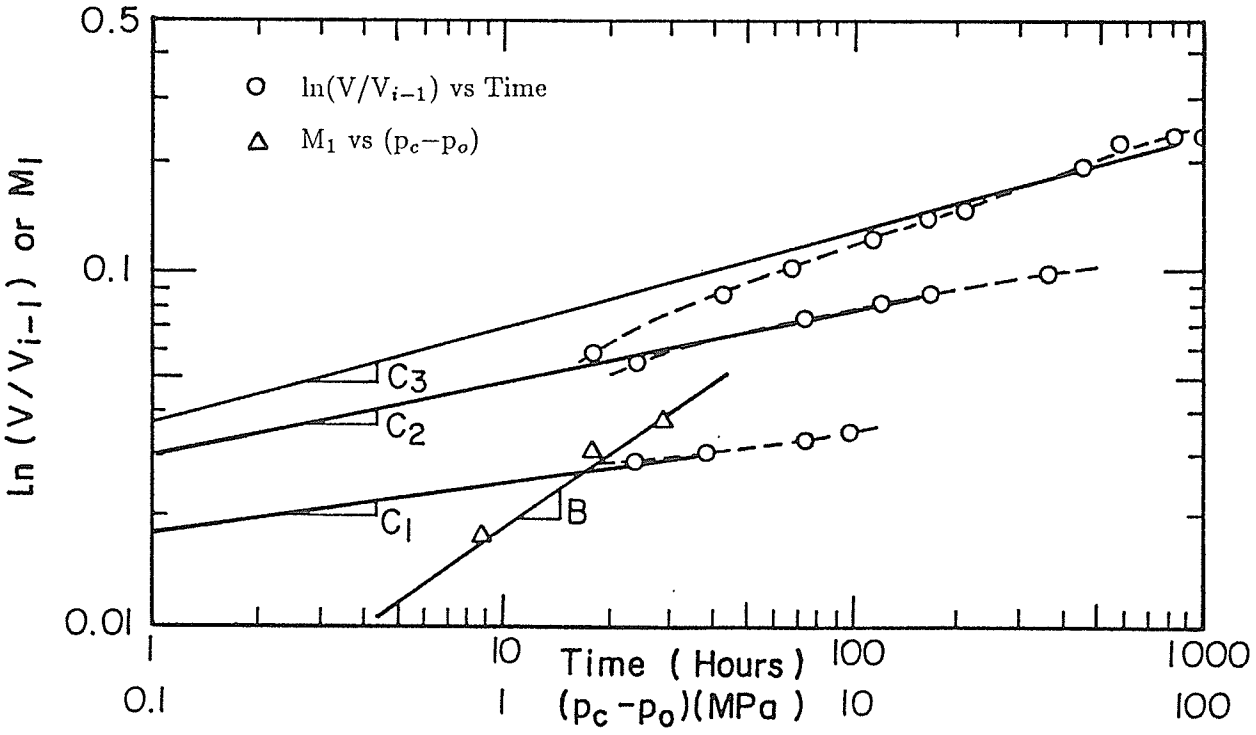

Figure 4.2. Evaluation of creep parameters.

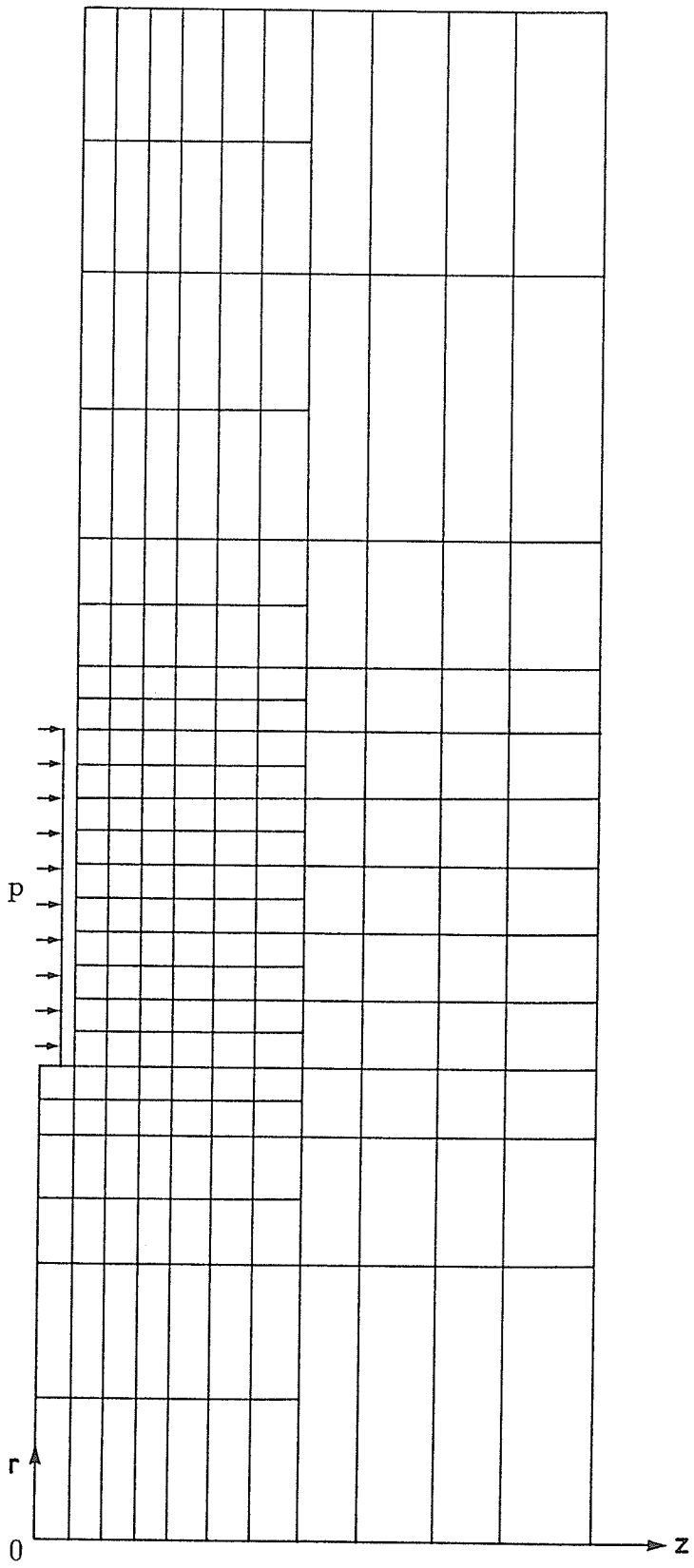

Figure 4.3. Axisymmetric finite element mesh for pressuremeter test simulation.

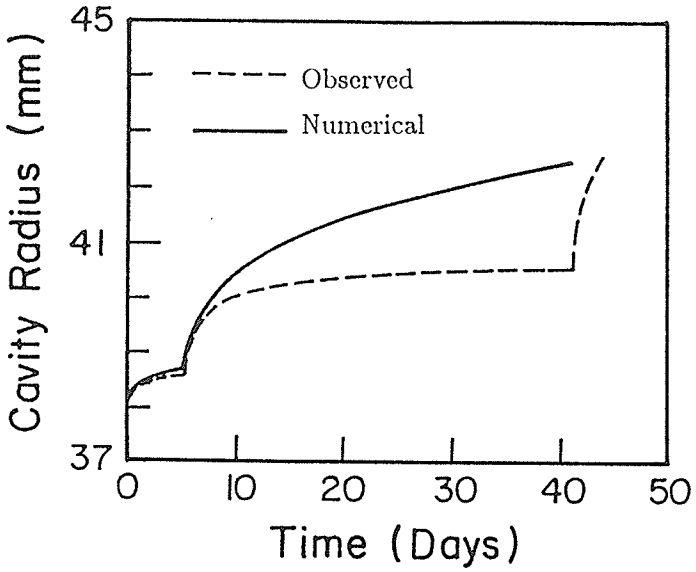

Figure 4.4. Comparison of observed data and numerical results using Power Law Ext. I for test 1.

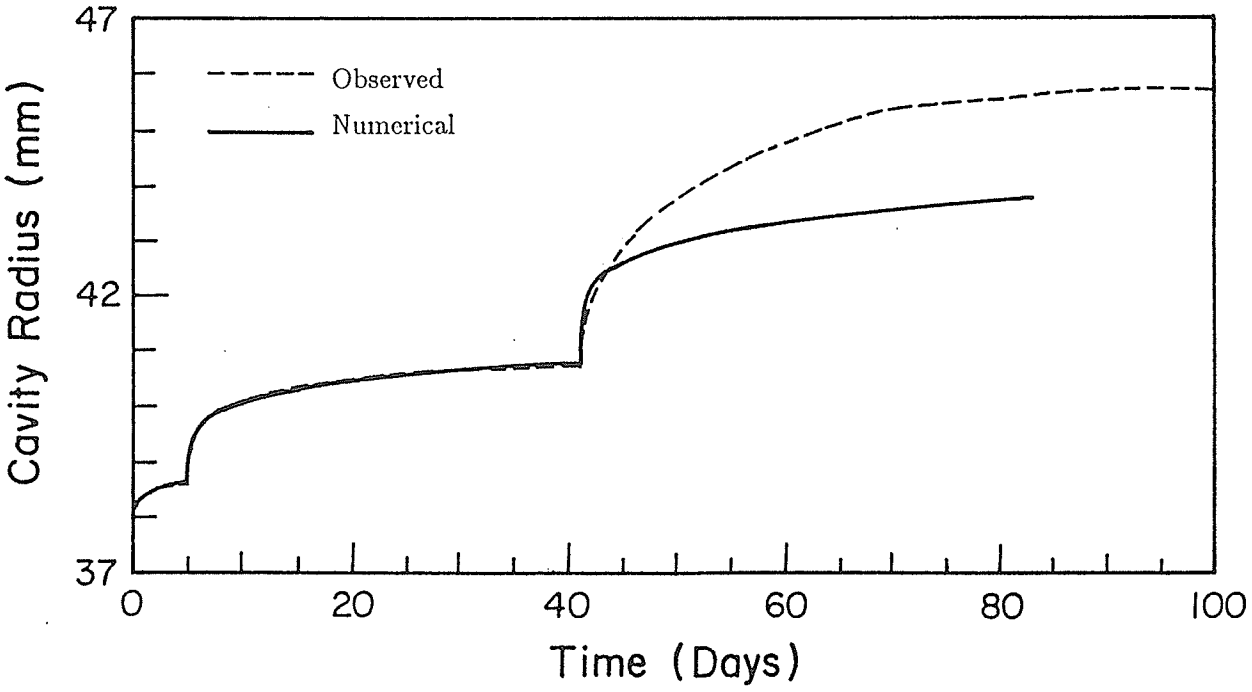

Figure 4.5. Comparison of observed data and numerical results using Power Law Ext. II with averaged creep parameters for test 1.

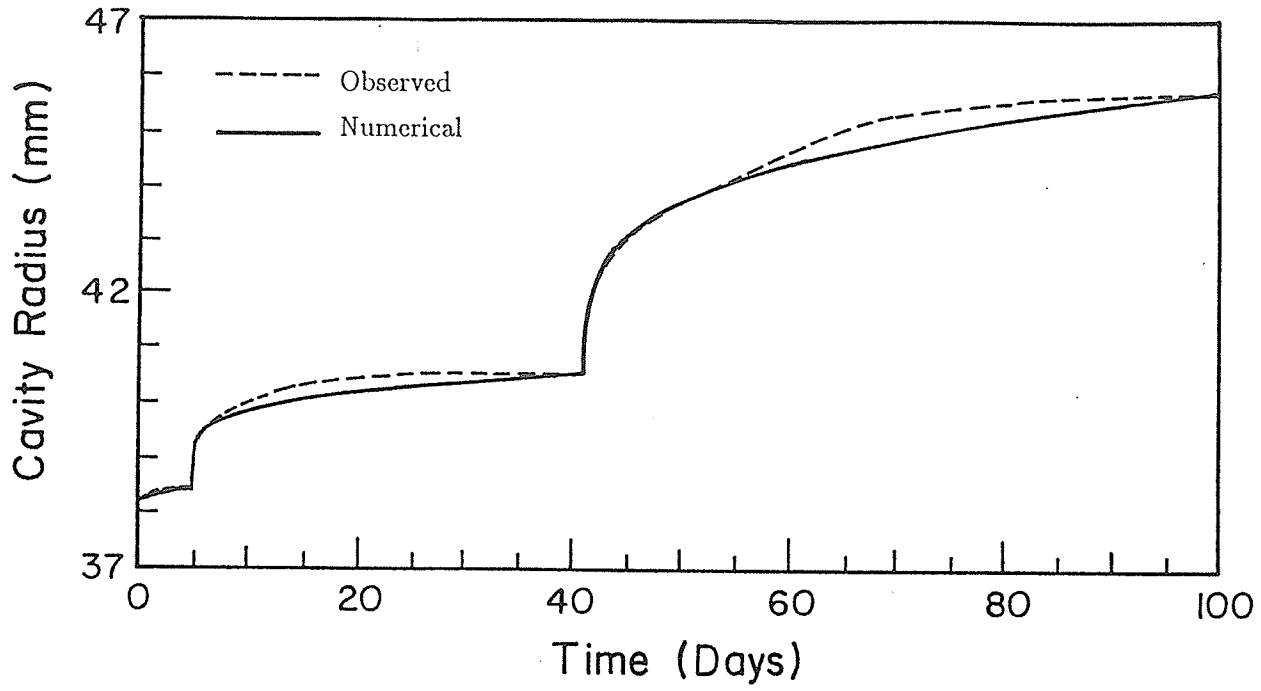

Figure 4.6. Comparison of observed data and numerical results using Power Law Ext. II with individual creep parameters for test 1.

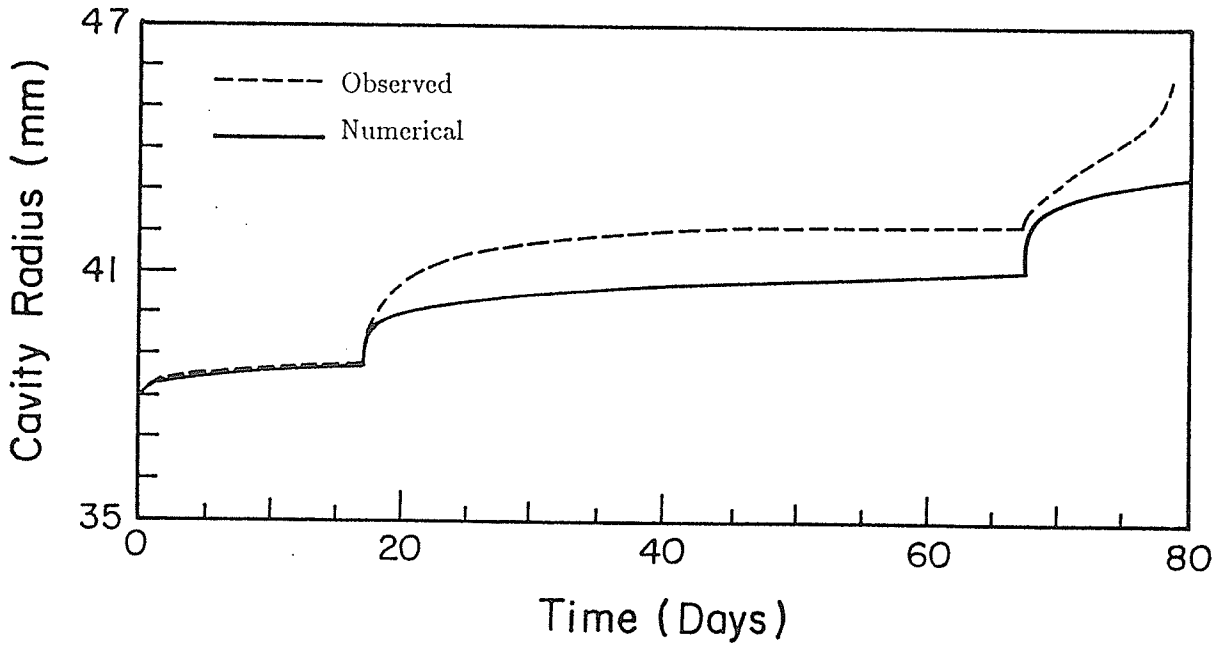

Figure 4.7. Comparison of observed data and numerical results using Power Law Ext. II for test 2, and averaged creep parameters from test 1.

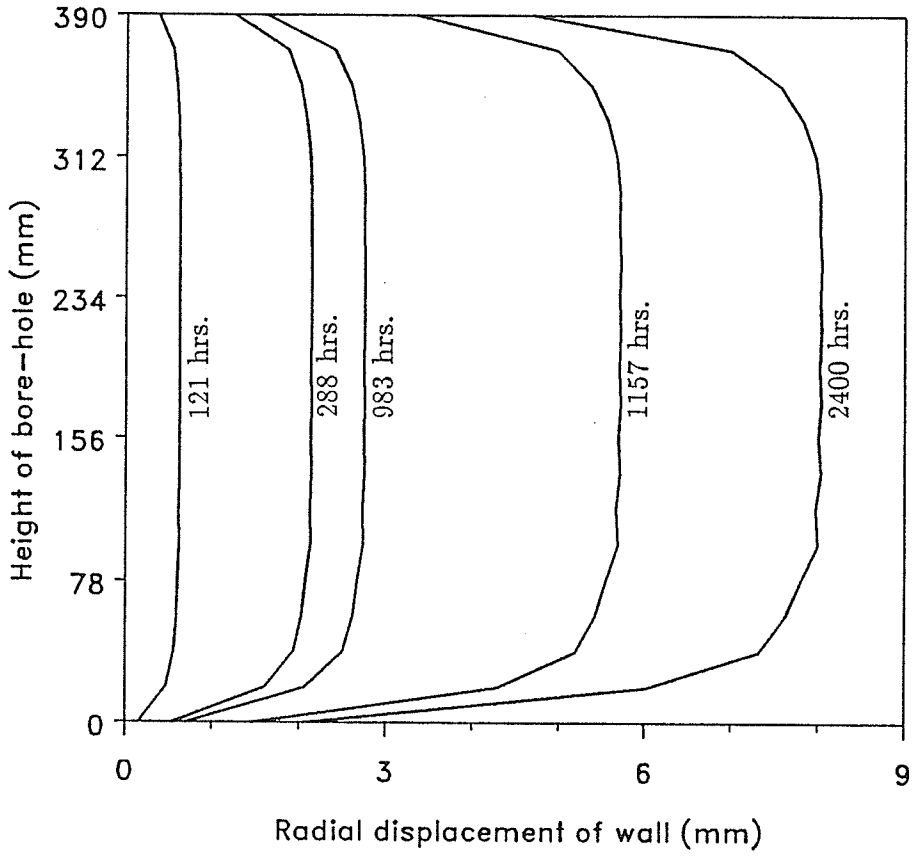

Figure 4.8. Predicted displacement profiles for pressuremeter test 1.

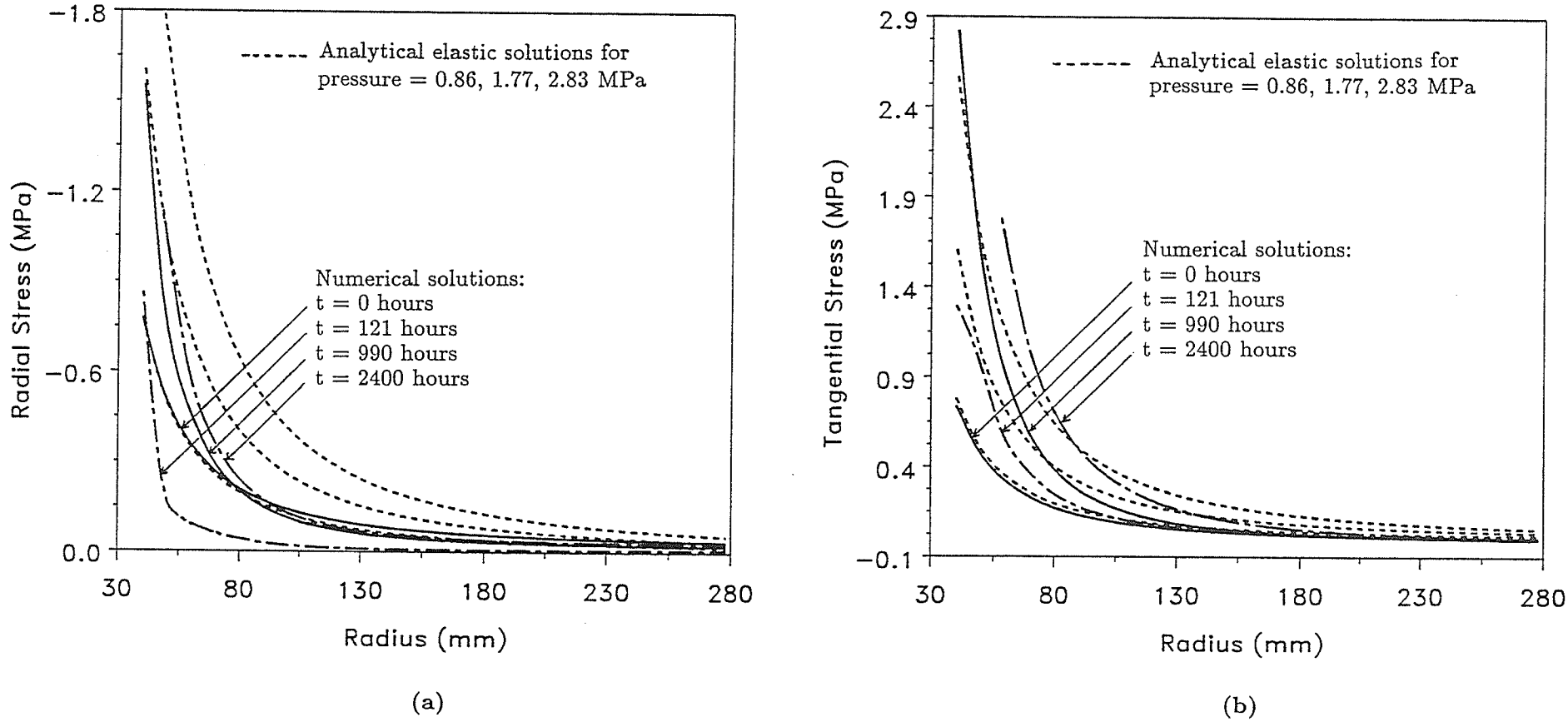

Figure 4.9. Stress distributions along a radial line at centre of the probe. (a). Radial stress (σ_{rr}), and (b). Tangential stress ($\sigma_{\theta\theta}$).

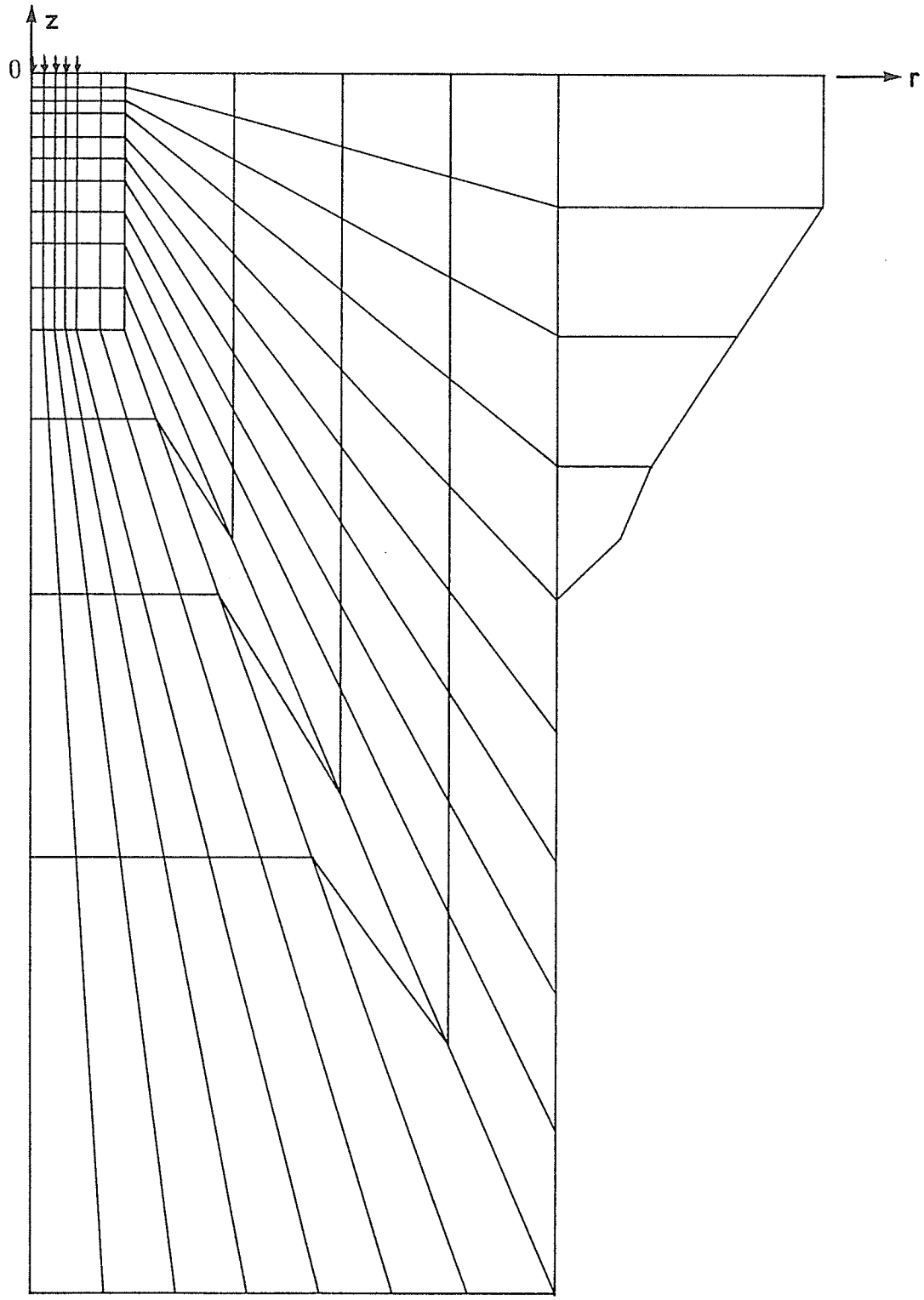

Figure 4.10. Axisymmetric finite element mesh for flexible footing on frozen soil.

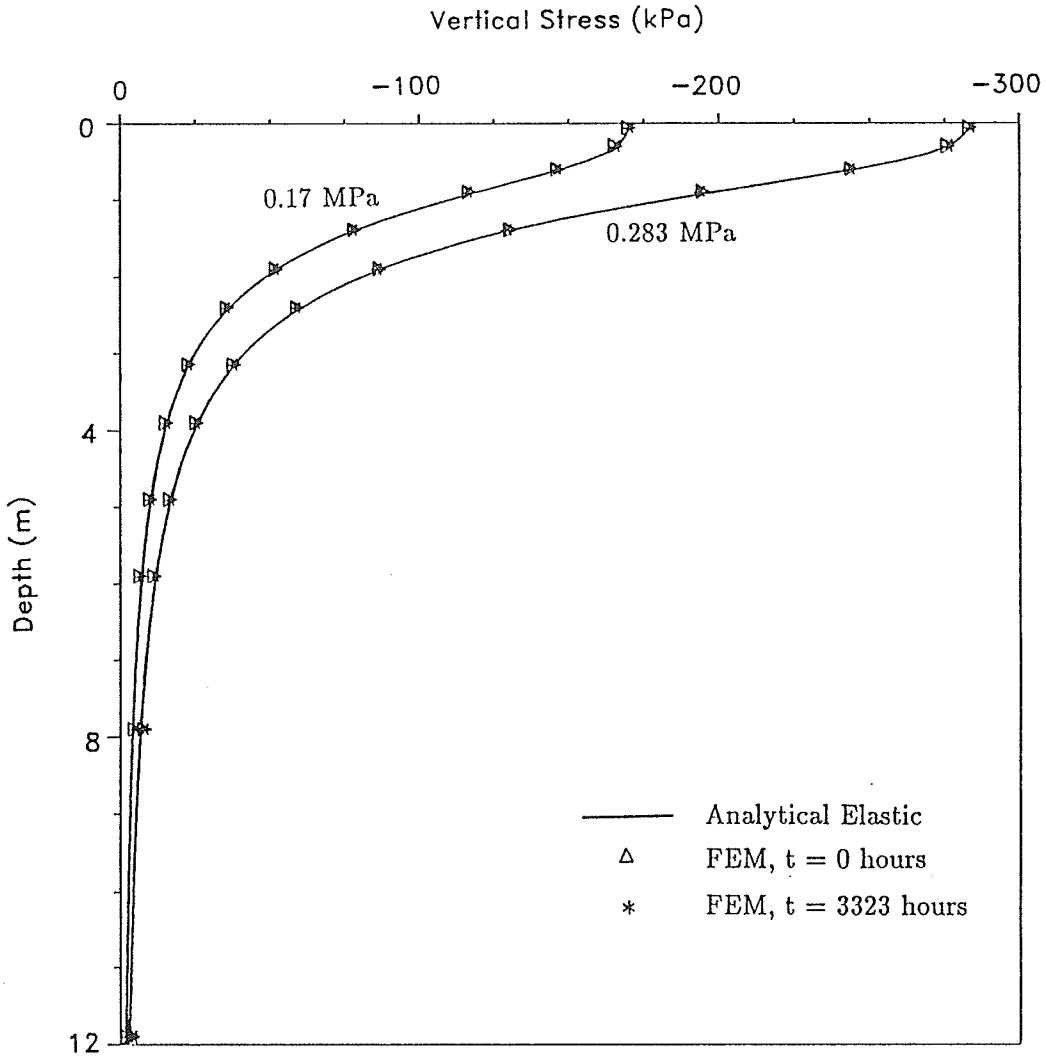

Figure 4.11. Vertical stress (σ_{zz}) distribution for a perfectly flexible circular footing.

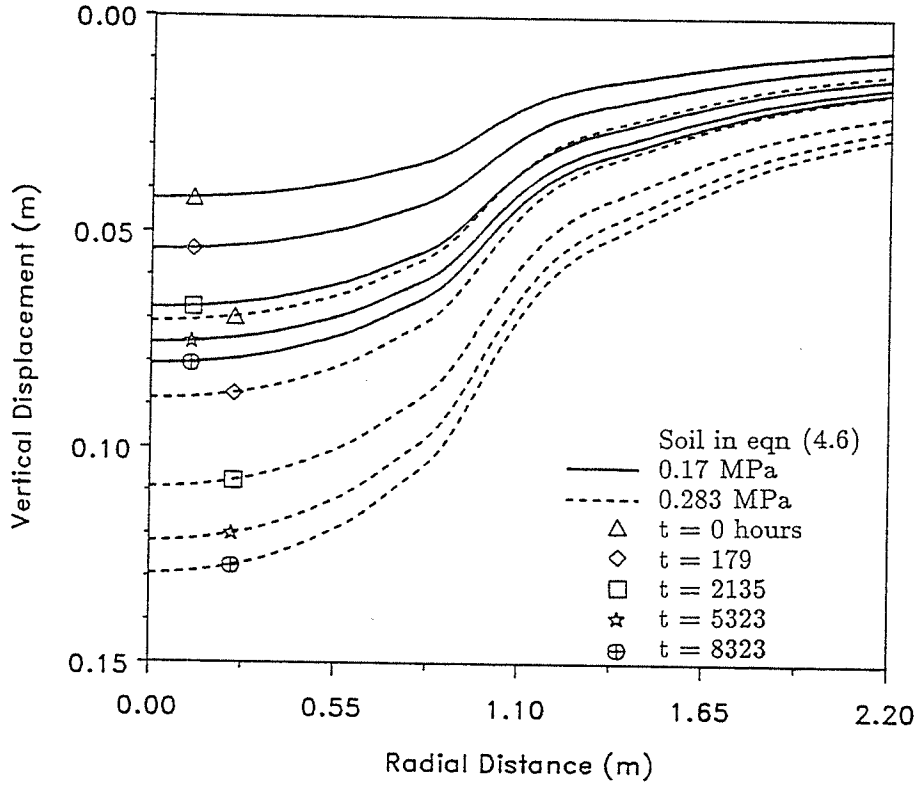

(a)

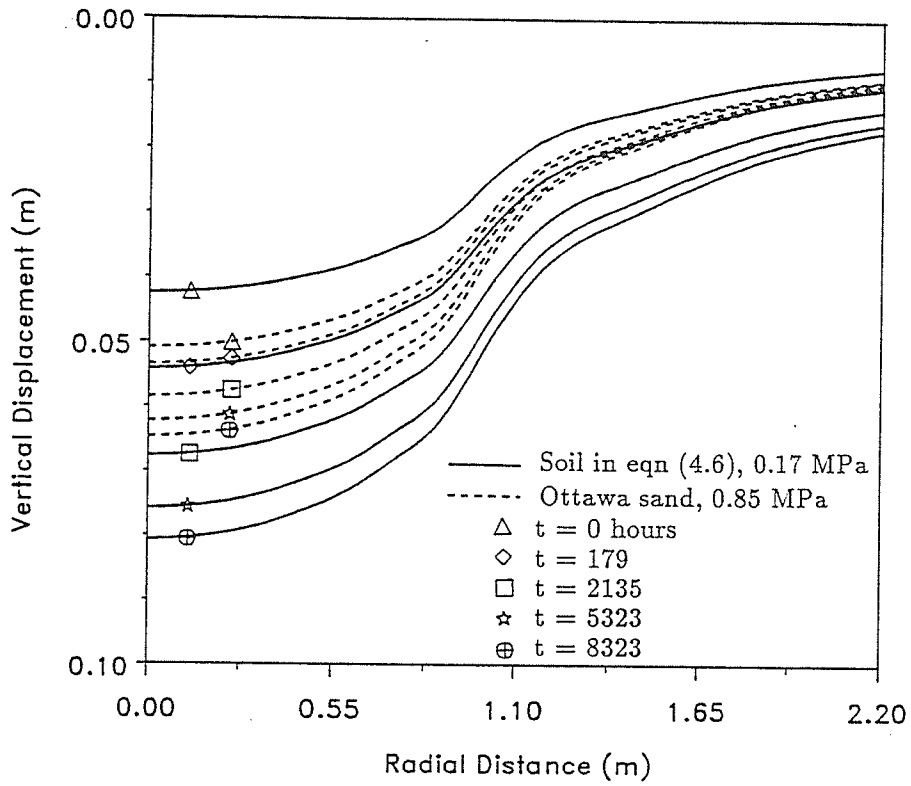

(b)

Figure 4.12. Surface settlement profiles for a perfectly flexible circular footing: (a). under different loads. (b). for different soils.

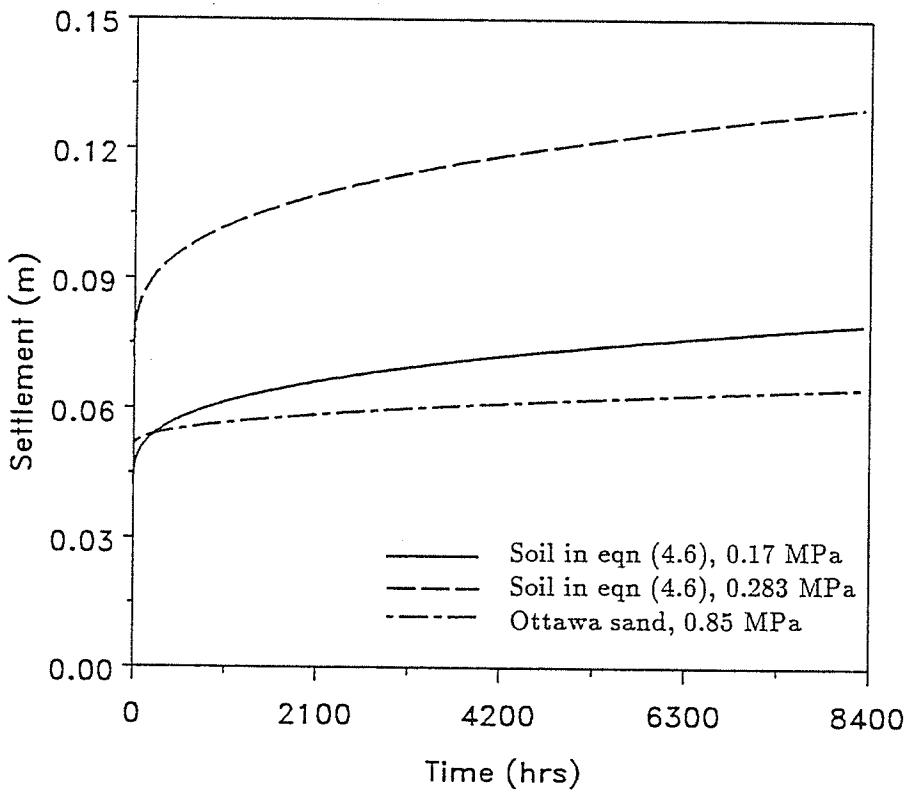

(a)

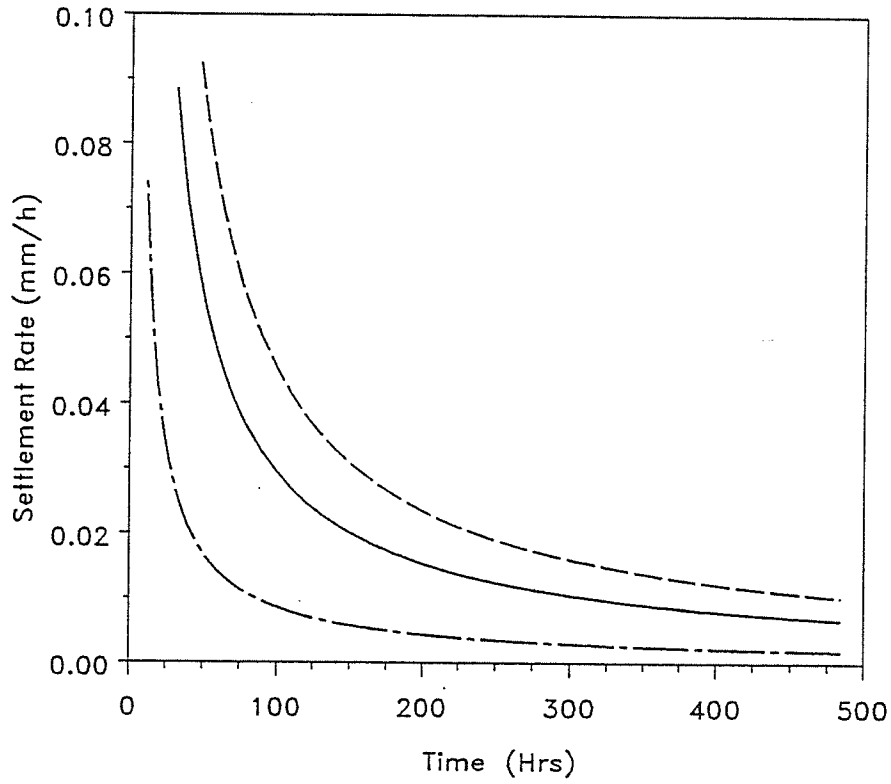

(b)

Figure 4.13. (a). Settlement at center of circular flexible footings. (b). Rate of settlement at center of circular flexible footings.

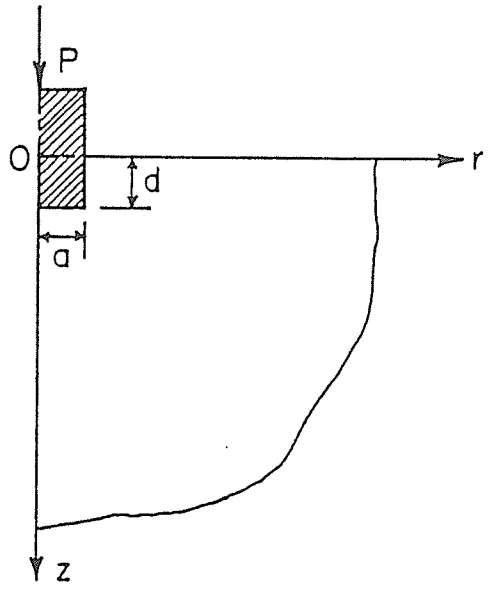

Figure 4.14. Cylindrical footing on frozen soil.

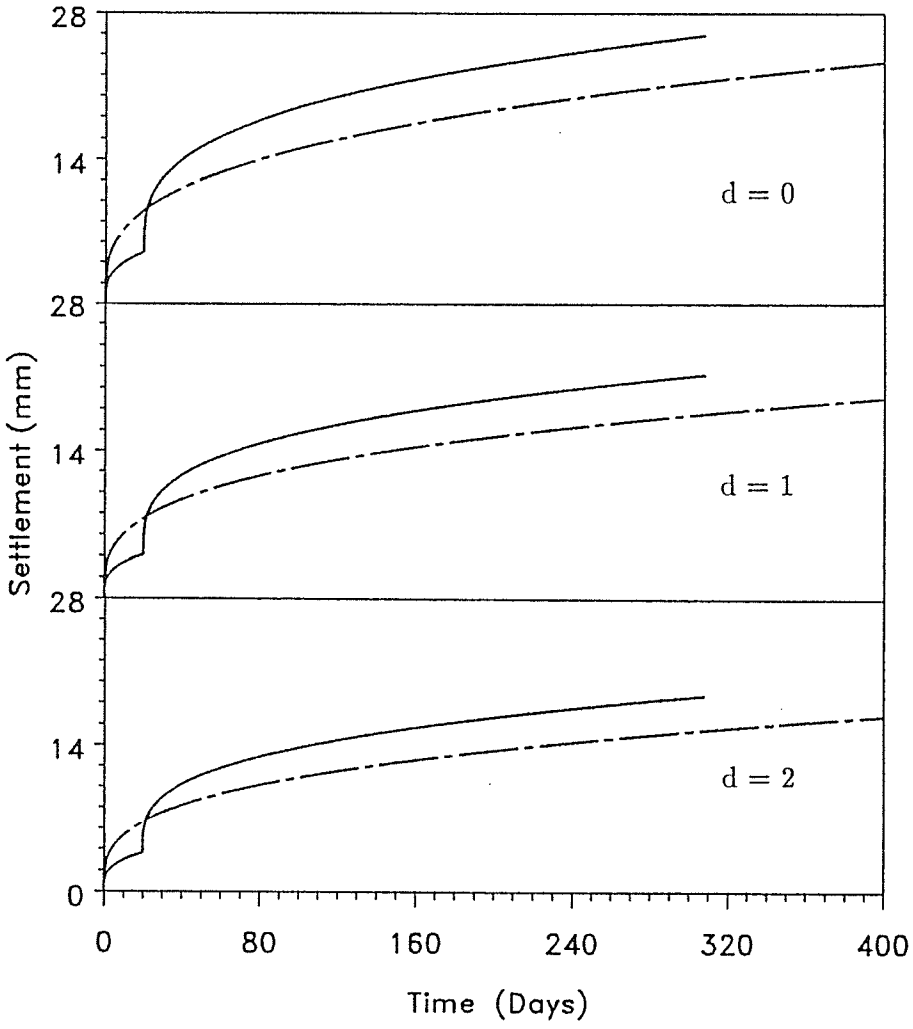

Figure 4.15. Settlement of cylindrical footings on frozen soil.

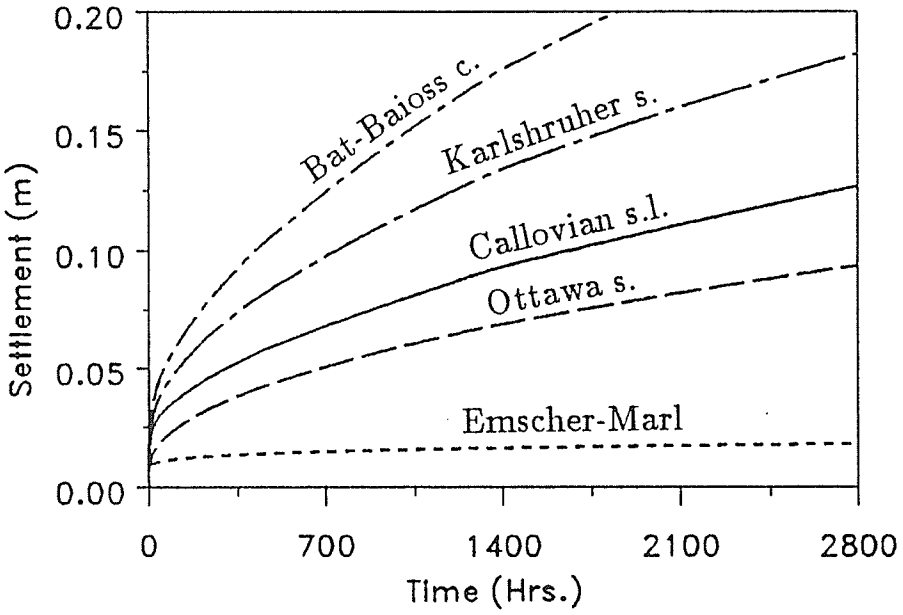

Figure 4.16. Creep settlement of footings embedded in different frozen soils.

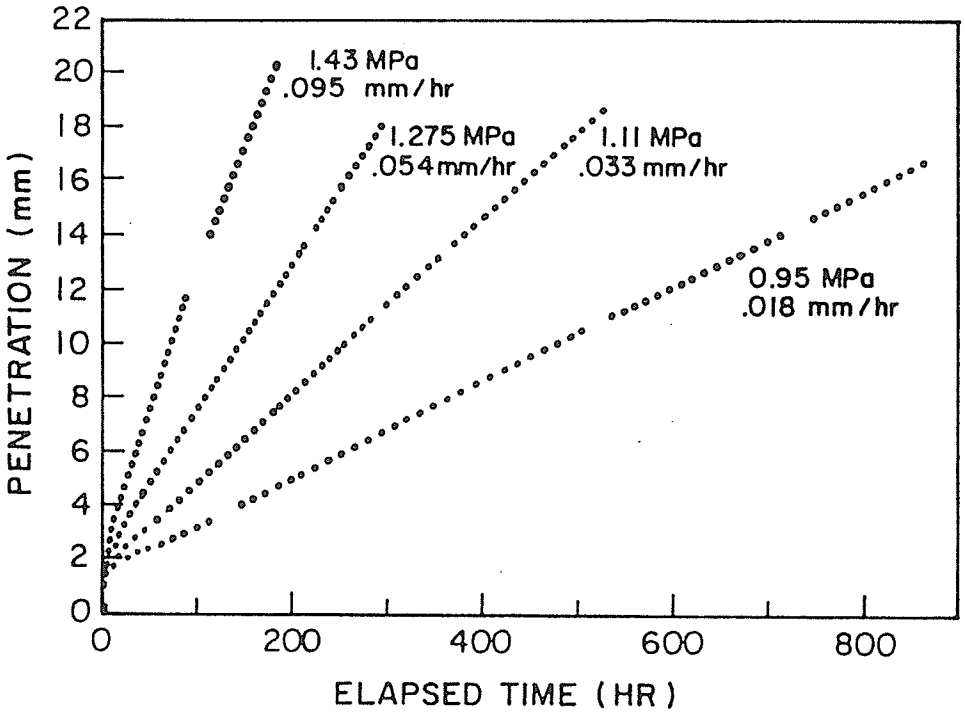

Figure 4.17. Penetration of steel rods in ice (after Domaschuk, Shields and Kenyon, 1989).

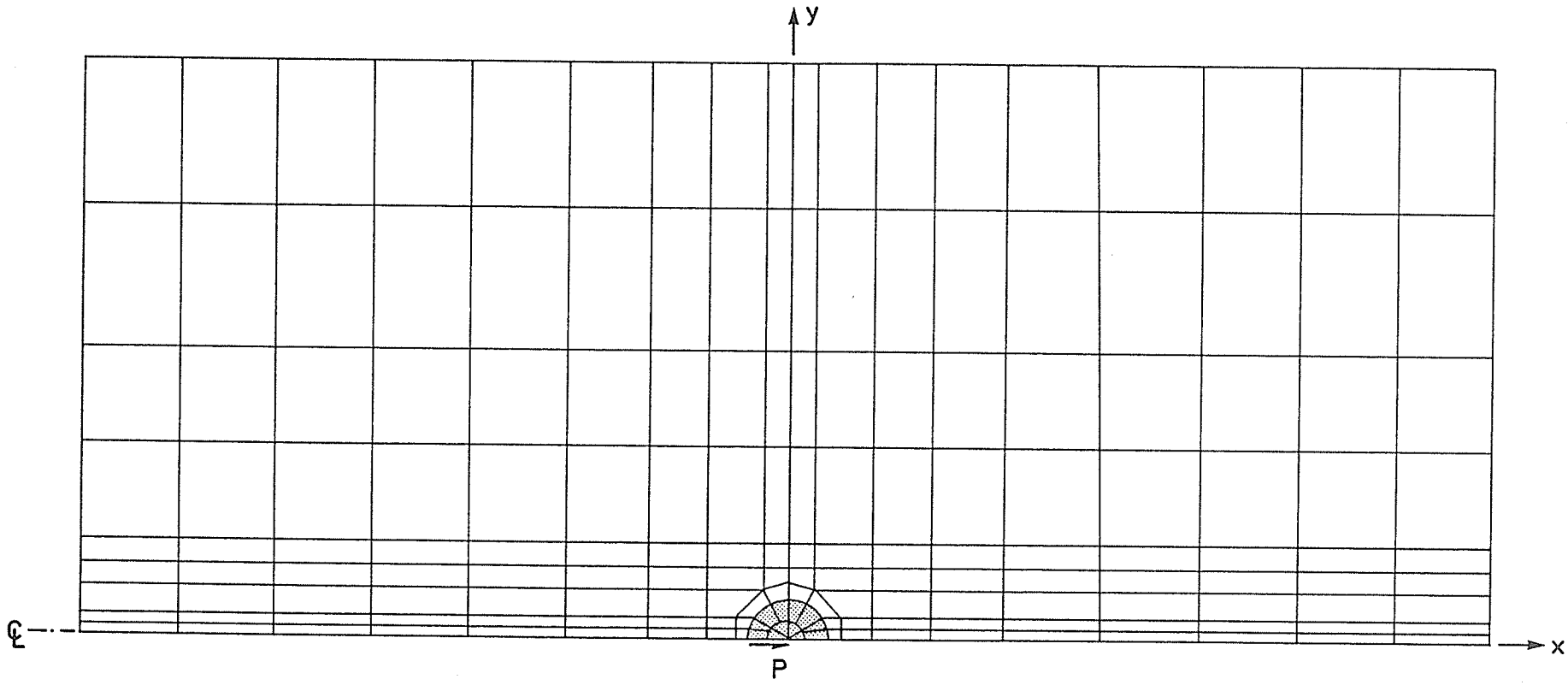

Figure 4.18. Finite element mesh for laterally loaded circular core in ice.

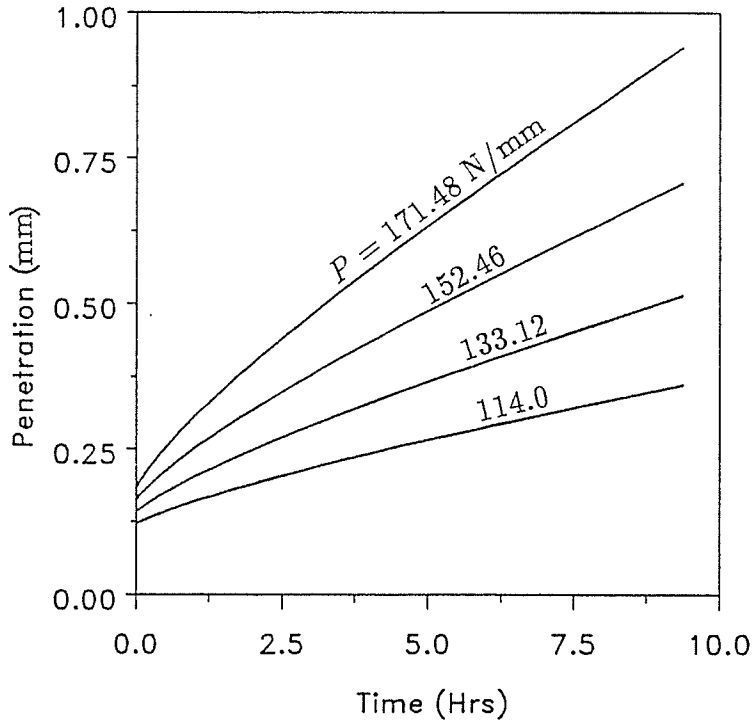

Figure 4.19(a). Initial lateral displacement behaviour of circular core in ice, under power law model.

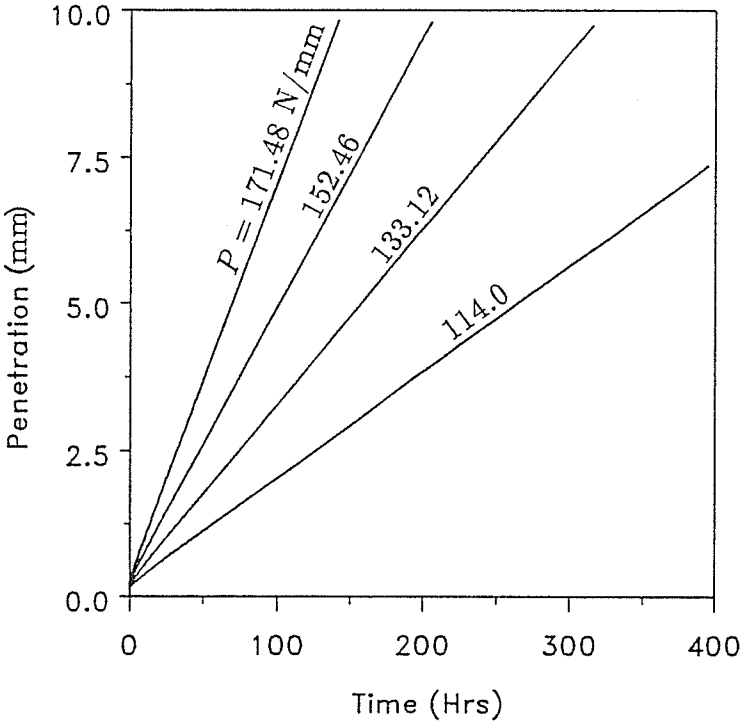

Figure 4.19(b). Lateral displacement of circular core in ice, under power law model.

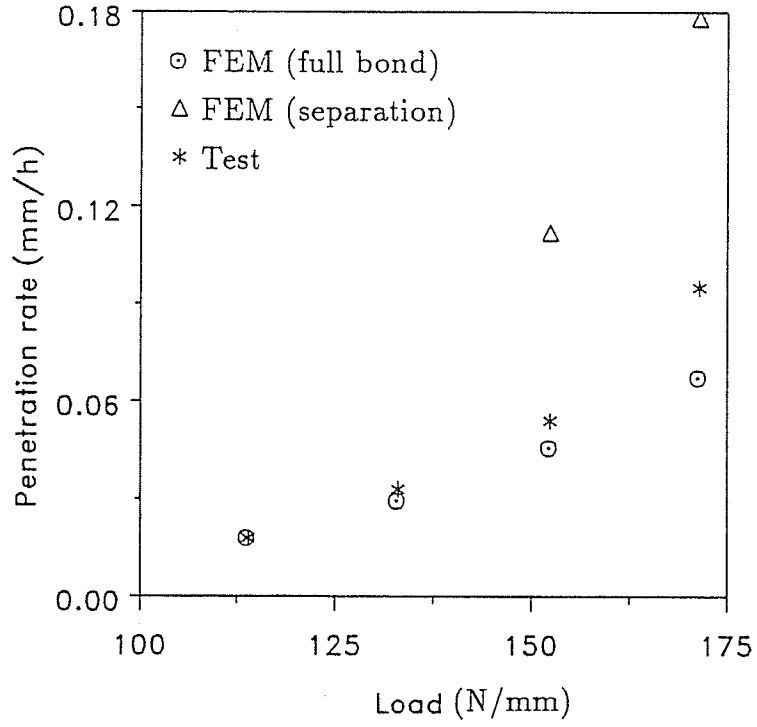

Figure 4.20. Penetration rates of circular rigid core in ice.

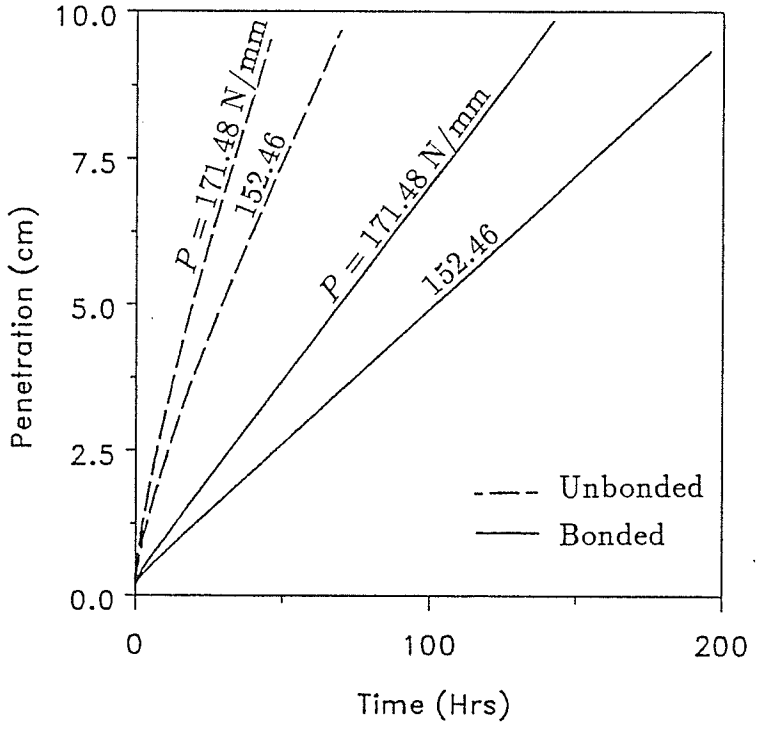

Figure 4.21. Lateral displacement of bonded and unbonded circular cores in ice, under power law model.

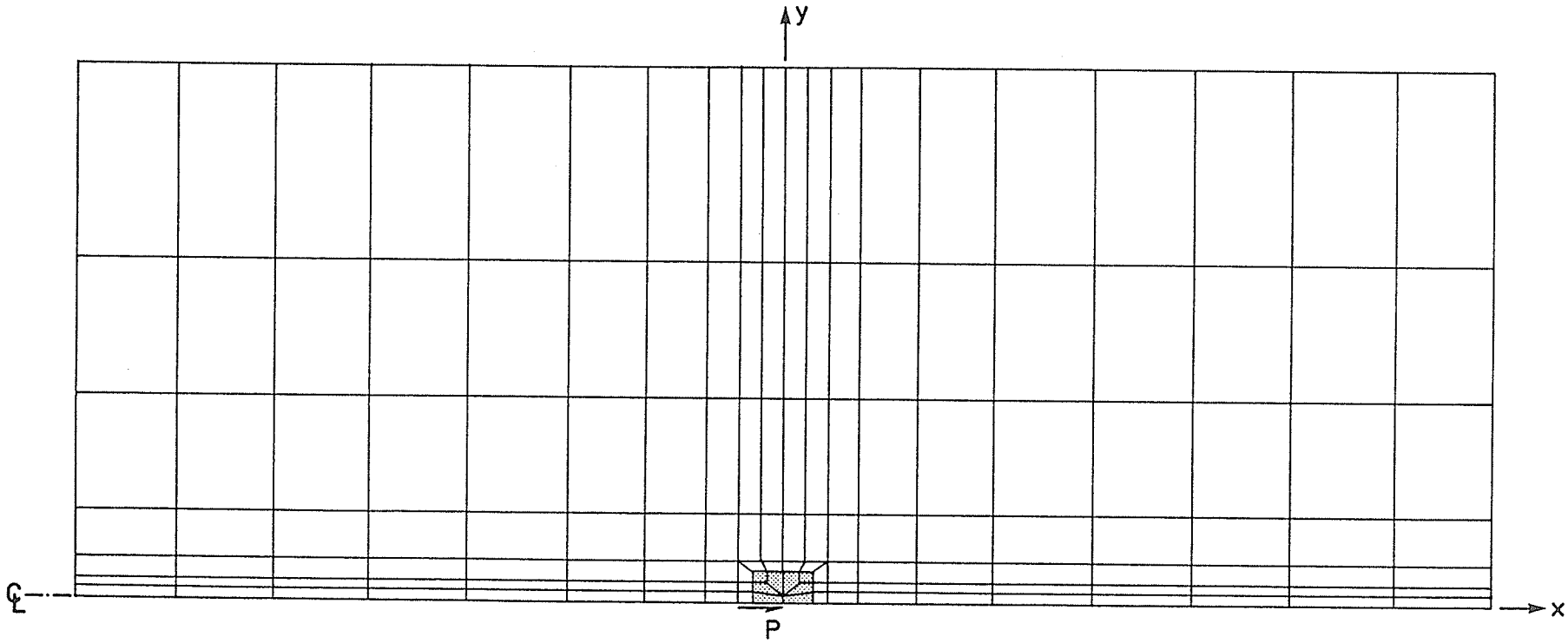

Figure 4.22. Finite element mesh for laterally loaded square core in ice.

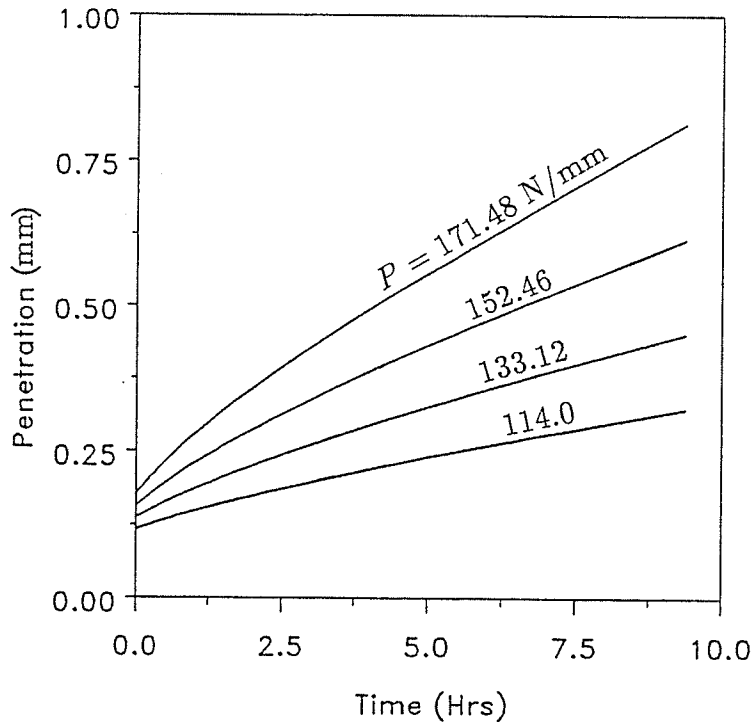

Figure 4.23(a). Initial lateral displacement behaviour of square core in ice, under power law model.

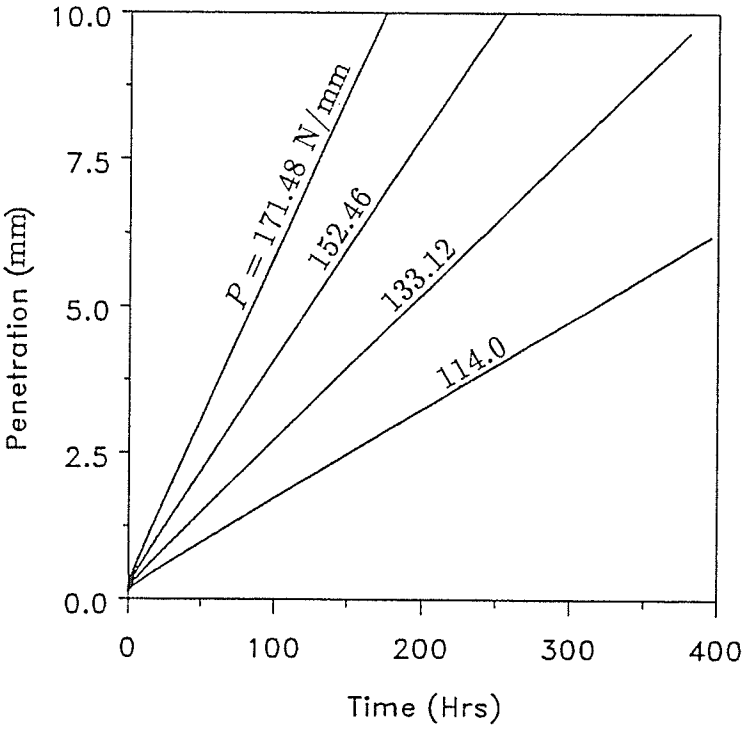

Figure 4.23(b). Lateral displacement of square core in ice, under power law model.

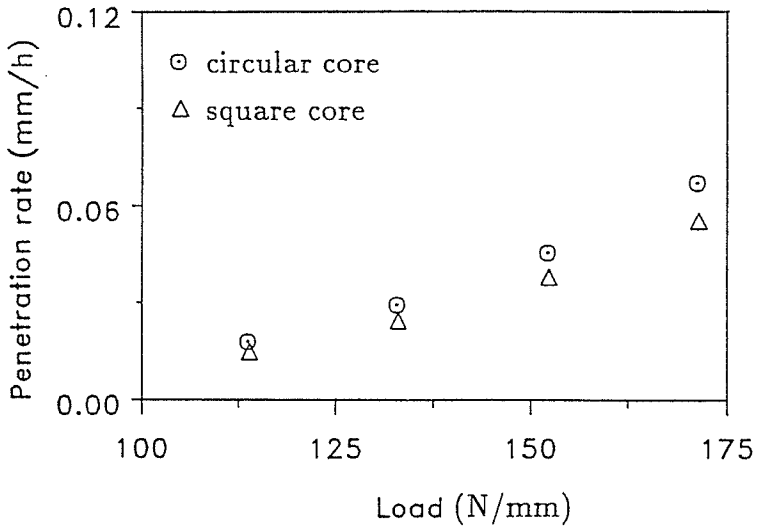

Figure 4.24. Predicted penetration rates of circular and square rigid cores in ice, under power law model.

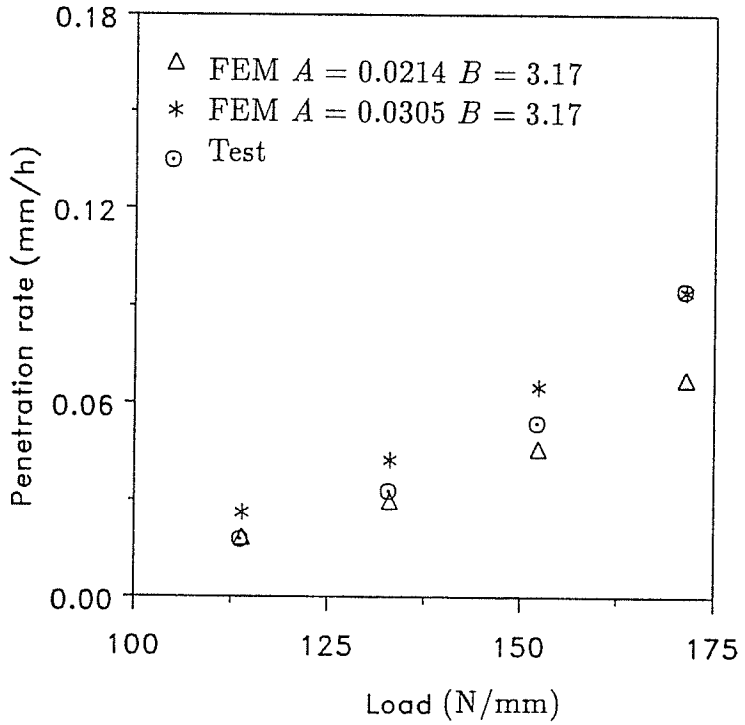

Figure 4.25. Penetration rates of circular rigid core in ice.

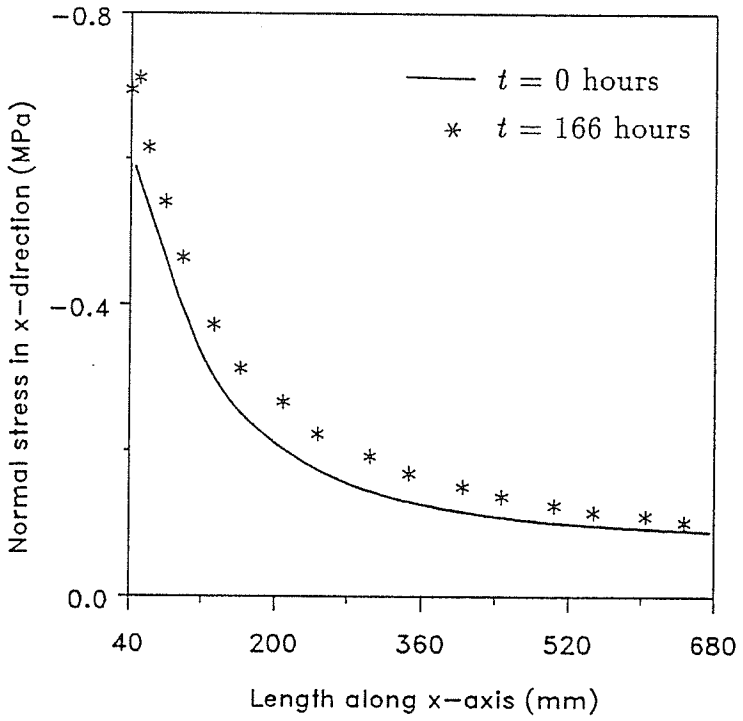

Figure 4.26. Normal stress distribution in front of a laterally loaded circular rigid core in ice, under power law model. ($P = 133.12$ N).

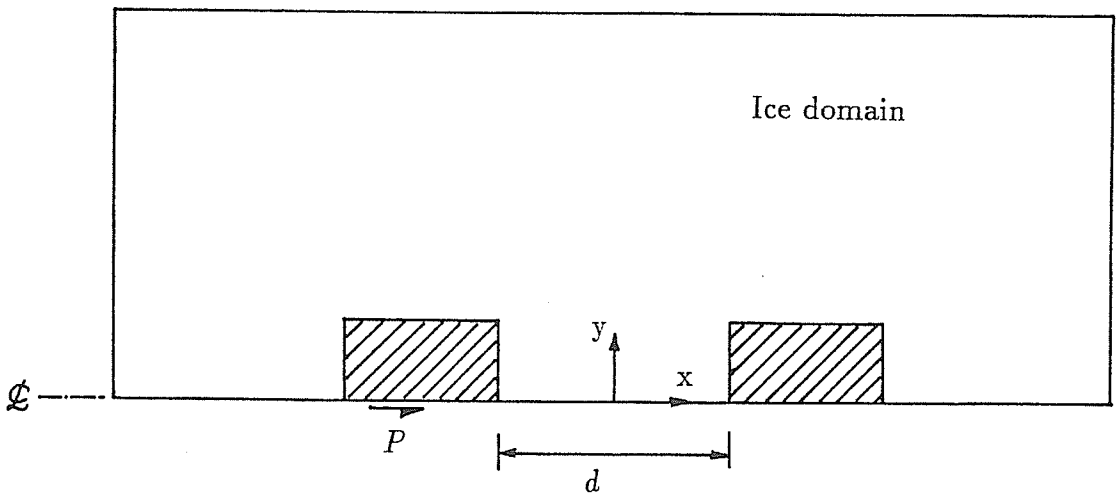

Figure 4.27. Configuration of group of square cores in ice.

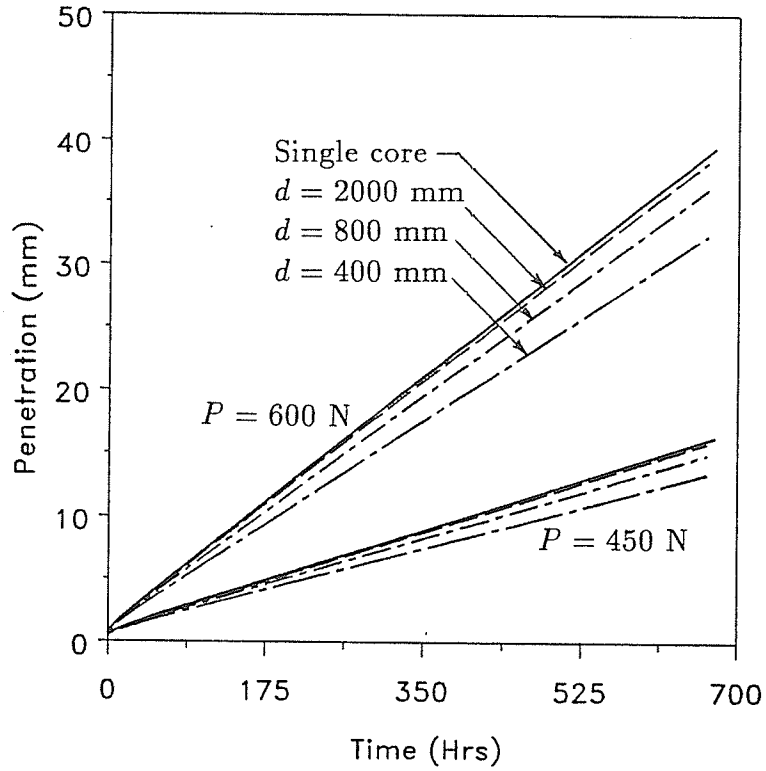

Figure 4.28. Lateral movement of the loaded core in a group of two square cores for different spacing between cores.

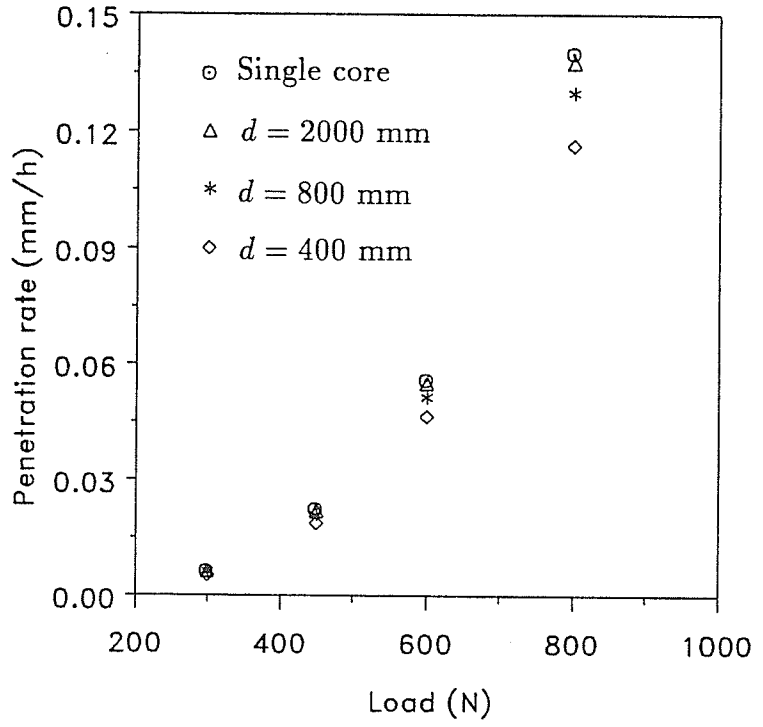

Figure 4.29. Penetration rates of the loaded core in a group of two square cores for different spacing between cores.

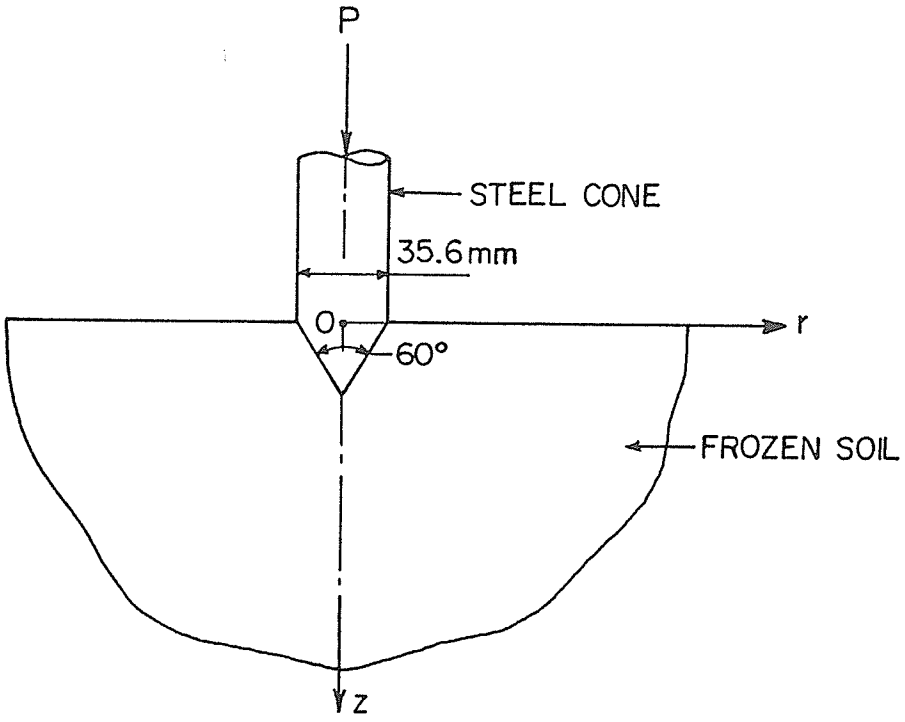

Figure 4.30. Configuration of conical indenter in frozen soil.

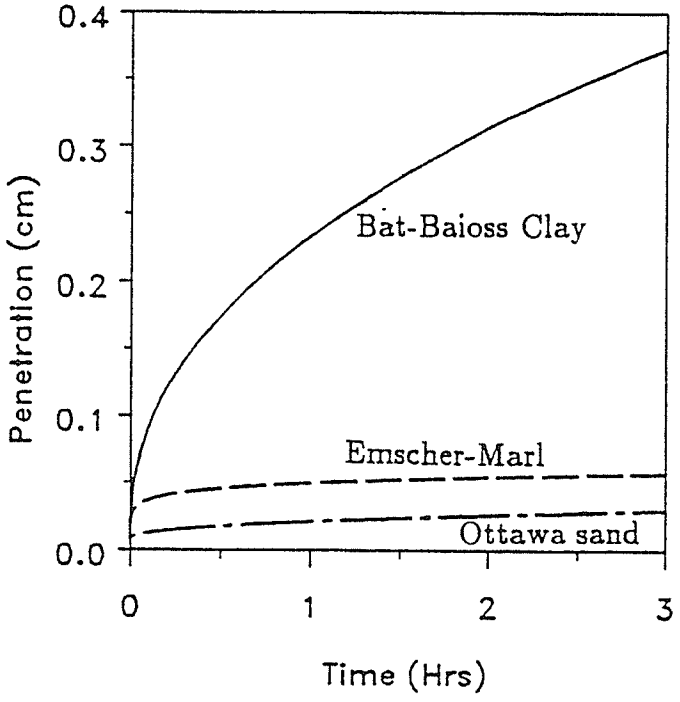

Figure 4.31. Predicted settlement of conical indenter under static load in different frozen soils.

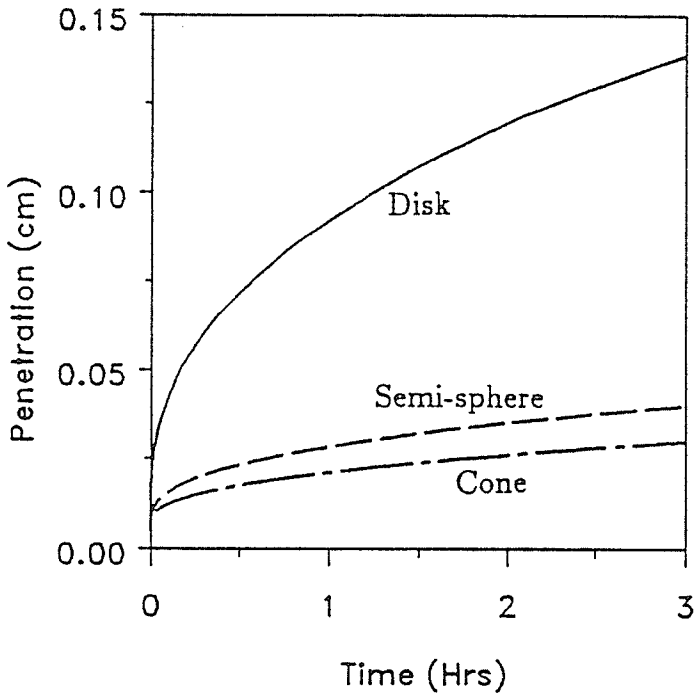

Figure 4.32. Predicted settlement of conical, semi-spherical, and disk indenters under static load in frozen Ottawa sand.

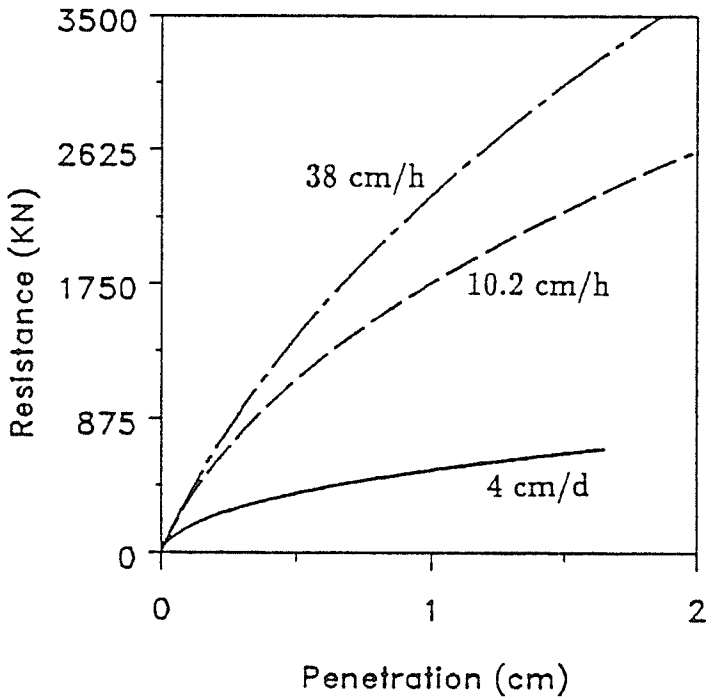

Figure 4.33. Predicted resistance to conical indenter in frozen Ottawa sand at different penetration rates.

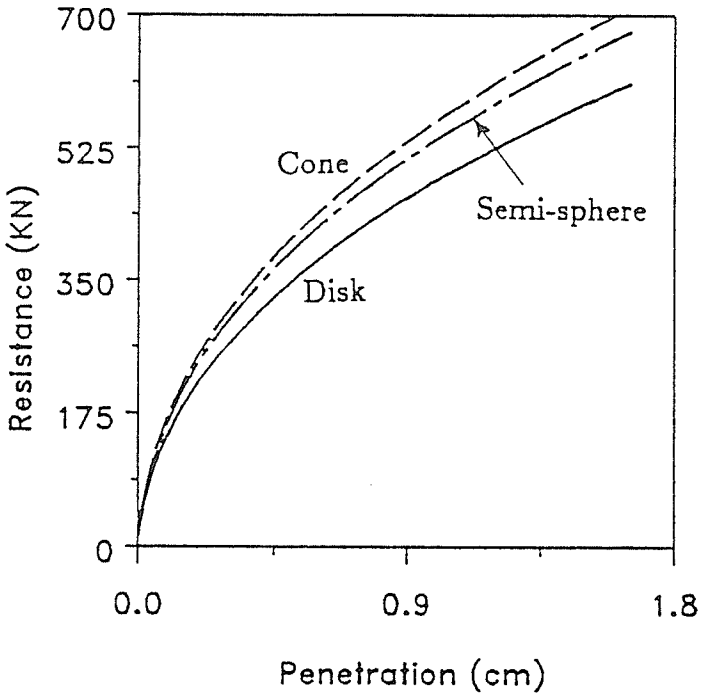

Figure 4.34. Predicted resistance to conical, semi-spherical, and disk indenters in frozen Ottawa sand at a penetration rate of 4 cm/day.

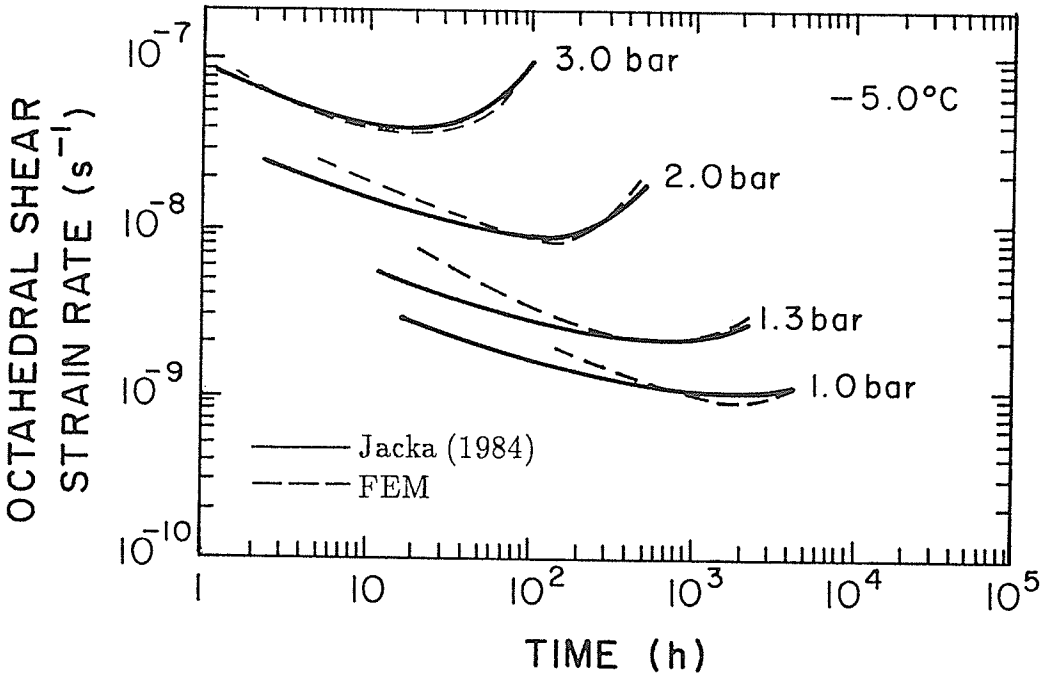

Figure 4.35. Comparison of numerical results with some experimental results of Jacka (1984) for ice at −5°C.

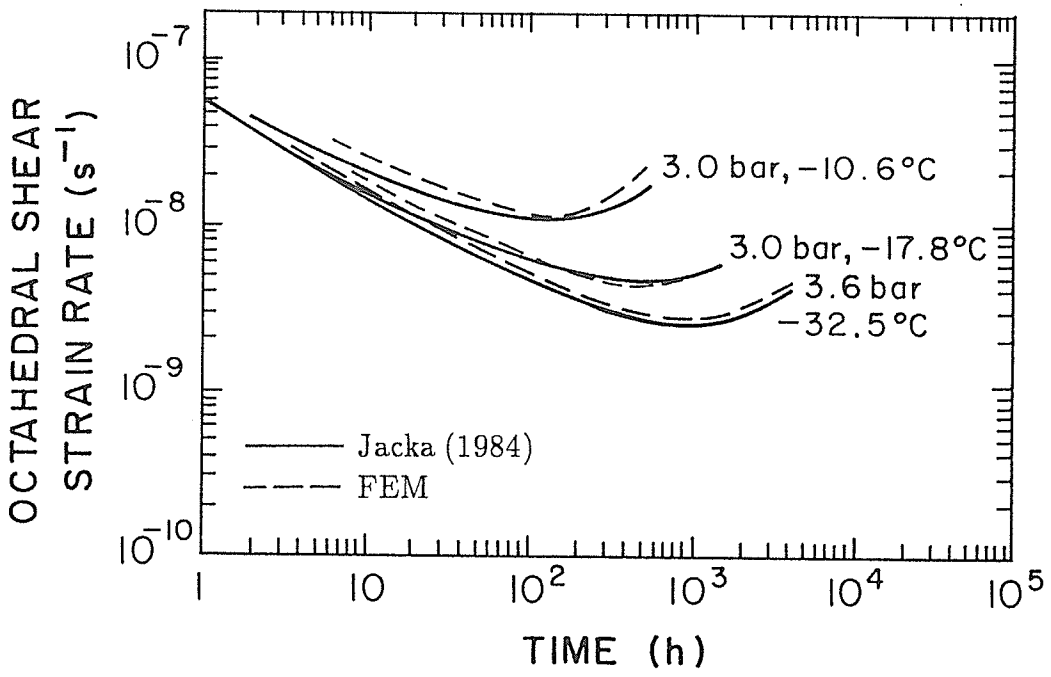

Figure 4.36. Comparison of numerical results with some experimental results of Jacka (1984) for ice at several temperatures.

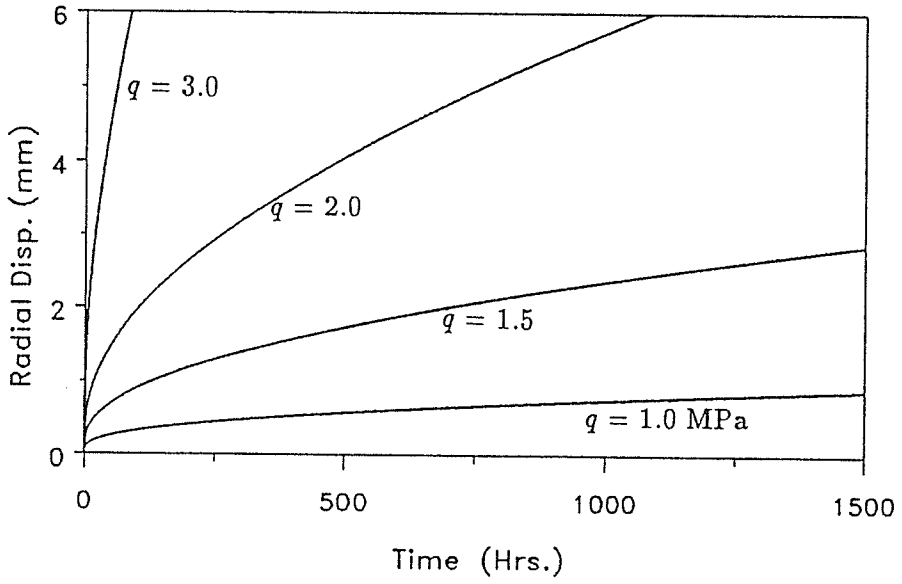

Figure 4.37. Predicted radial displacement of bore hole wall for different loads under Fish's model.

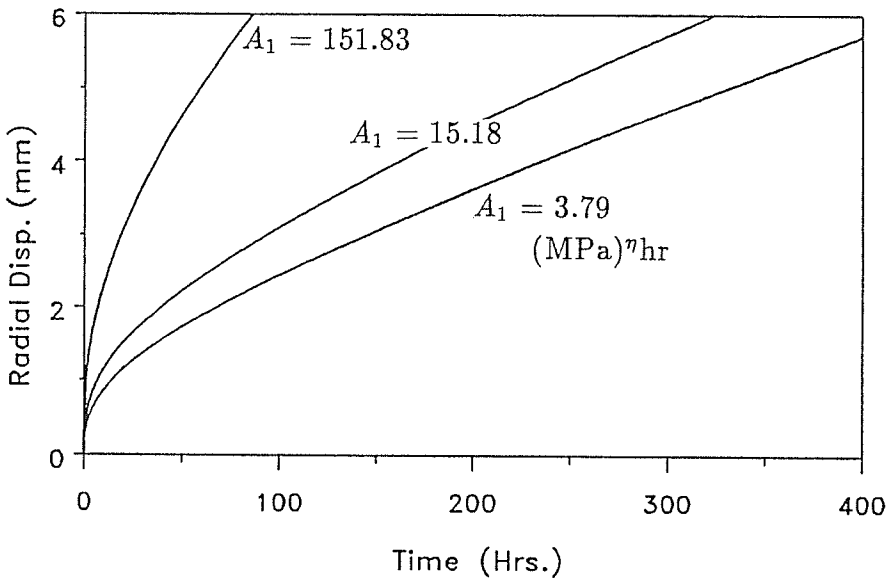

Figure 4.38. Predicted radial displacement of bore hole wall for different creep parameters under Fish's model.

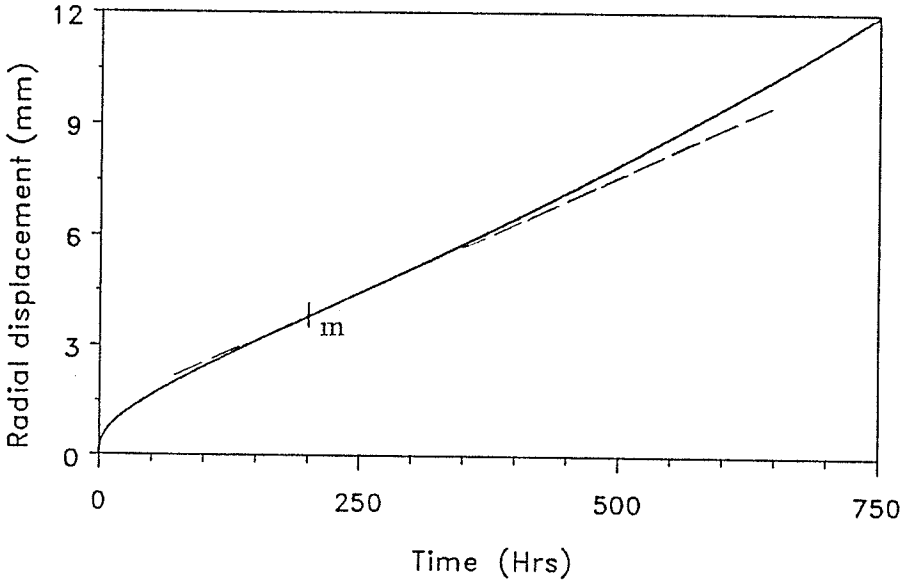

Figure 4.39. Predicted radial displacement of bore hole wall for an applied pressure of 3 MPa under Fish's model (creep parameters in eqn. (4.11) except for $A_1 = 0.75$ (MPa)$^\eta$hr)

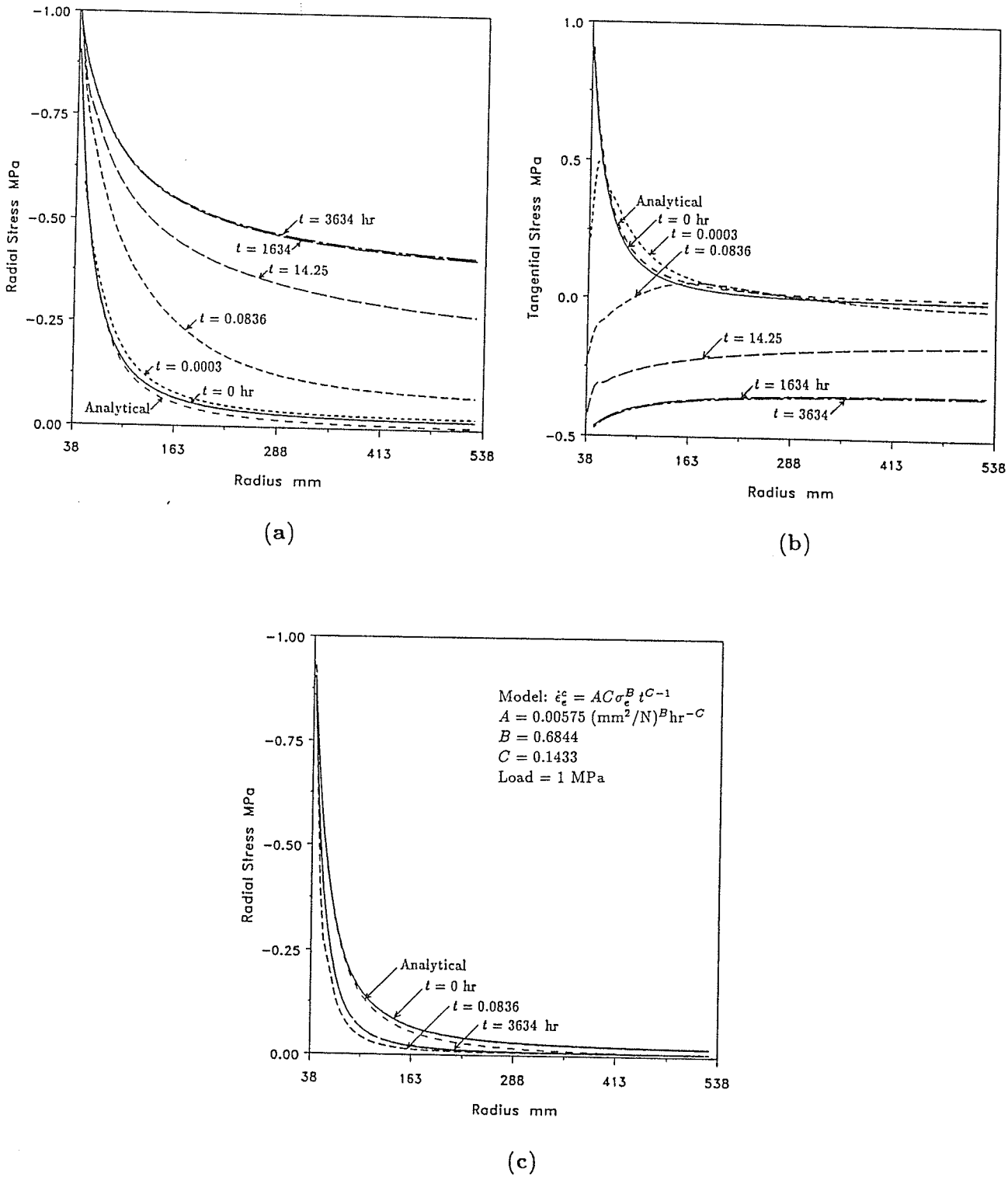

Figure 4.40. Stress distributions at different times for pressuremeter problem: (a). σ_{rr} predicted by Fish's model, (b). $\sigma_{\theta\theta}$ predicted by Fish's model, (c). σ_{rr} predicted by the power law model with selected parameters.

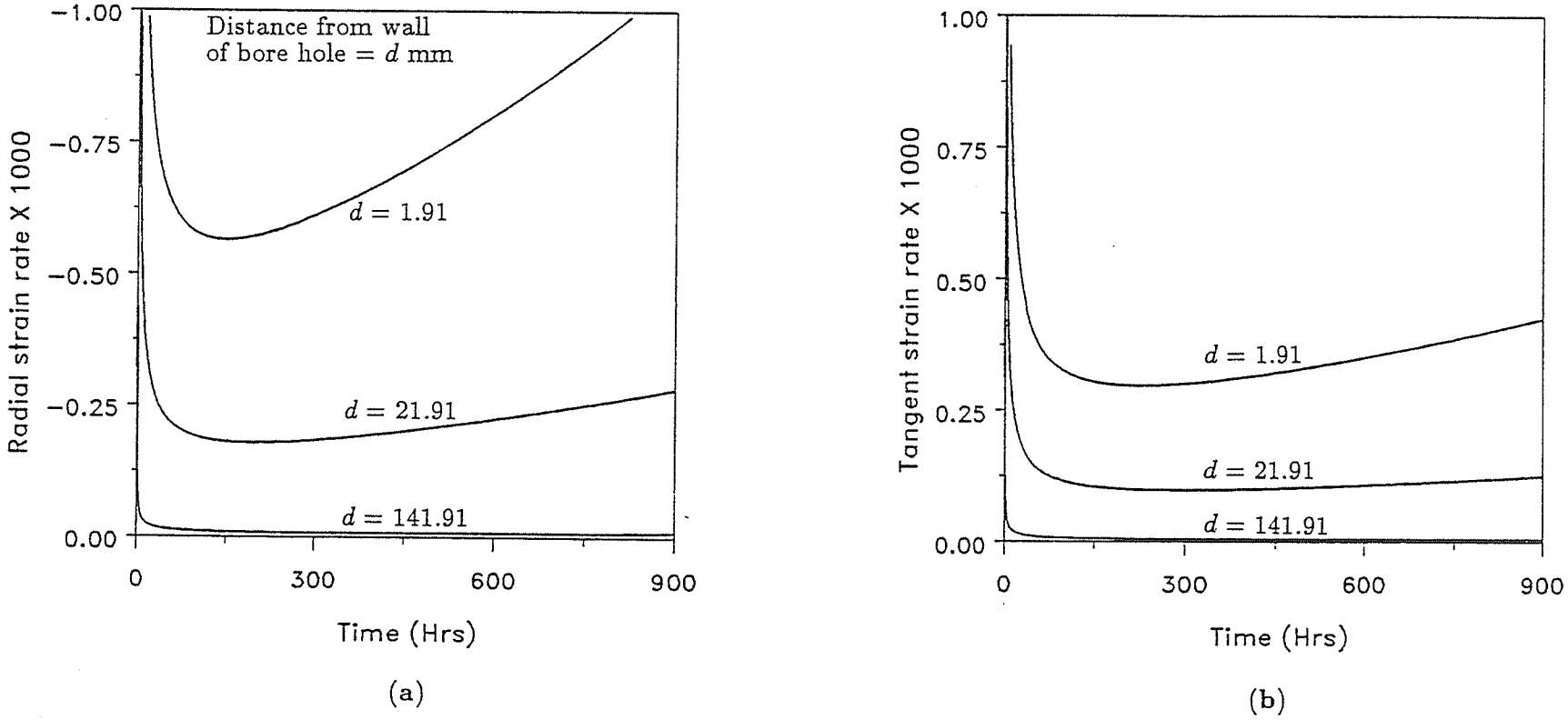

Figure 4.41. Strain rates at different locations for pressuremeter problem in figure 4.39: (a). radial strain rate, (b). tangential strain rate.

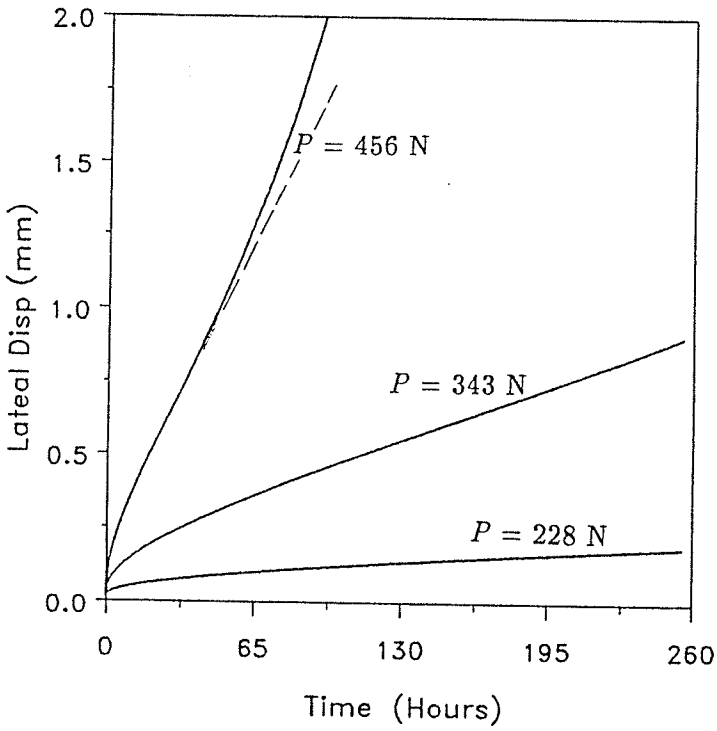

Figure 4.42. Predicted lateral displacement of a rigid circular core in frozen ground for different loads (using Fish's model).

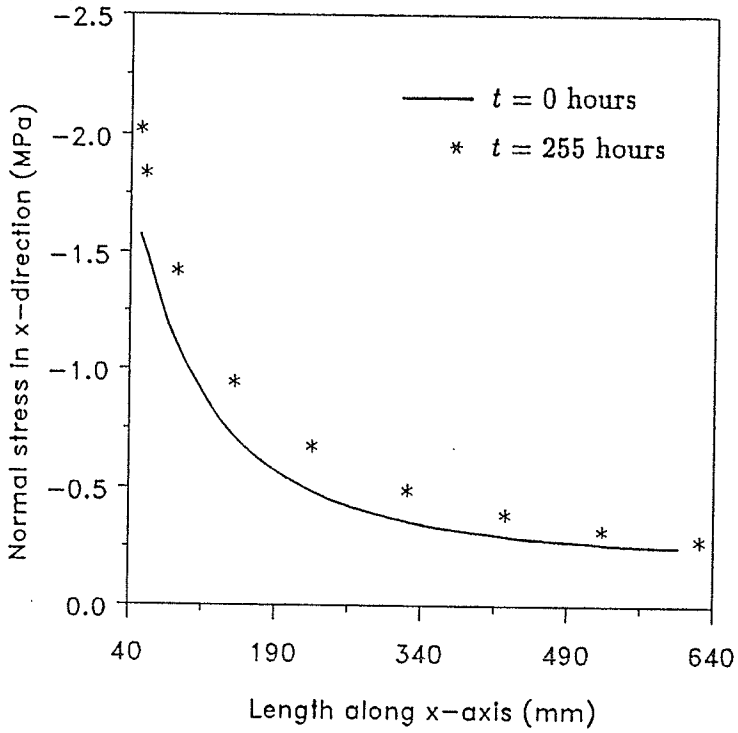

Figure 4.43. Normal stress (σ_{xx}) distribution in front of a laterally loaded rigid circular core in frozen ground (using Fish's model).

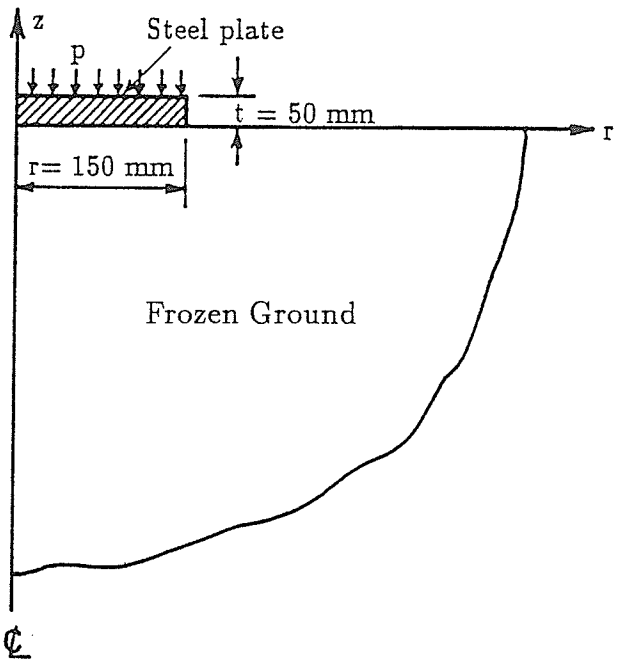

Figure 4.44. Configuration of plate load test.

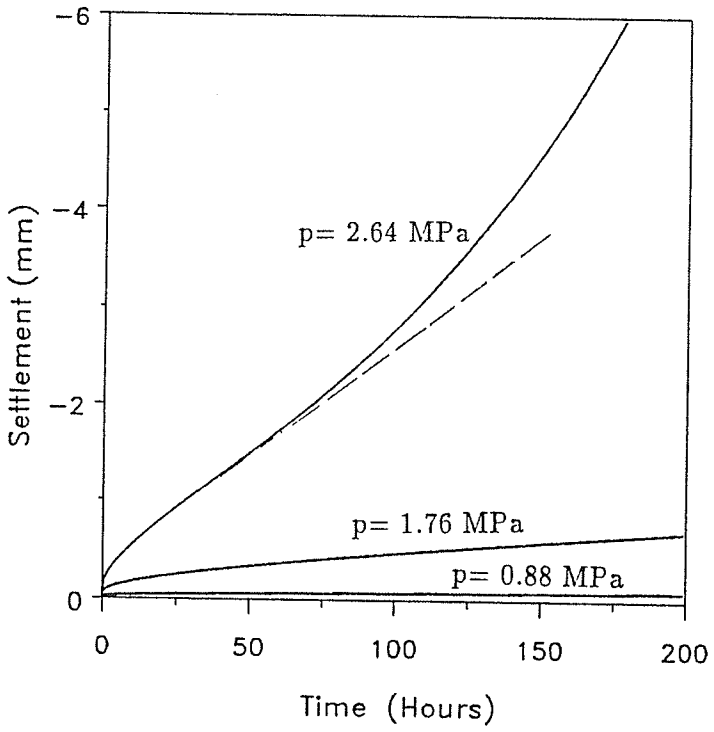

Figure 4.45. Predicted settlement at the center of a plate on frozen ground for different loads (using Fish's model).

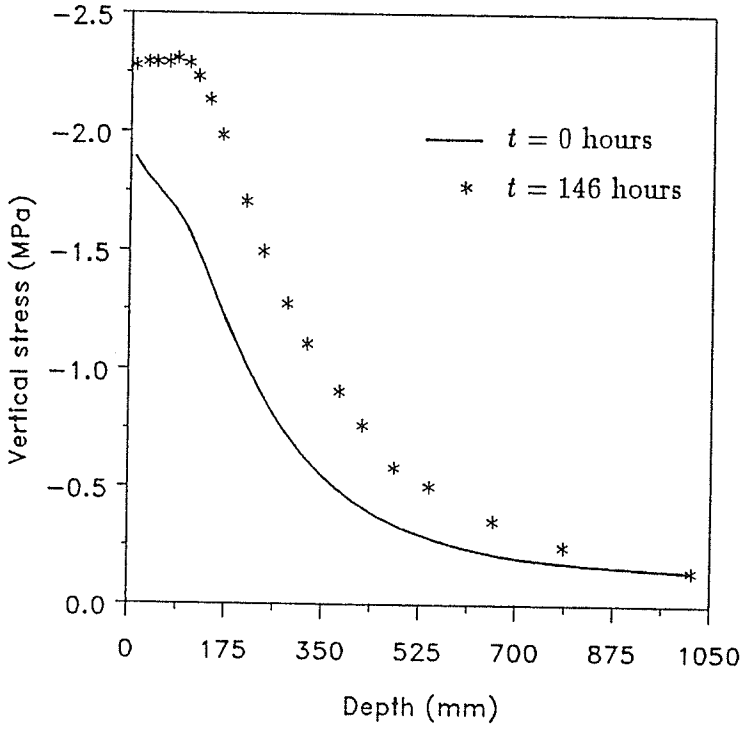

Figure 4.46. Vertical stress (σ_{zz}) distribution along a vertical line close to the symmetry axis under the plate (using Fish's model).

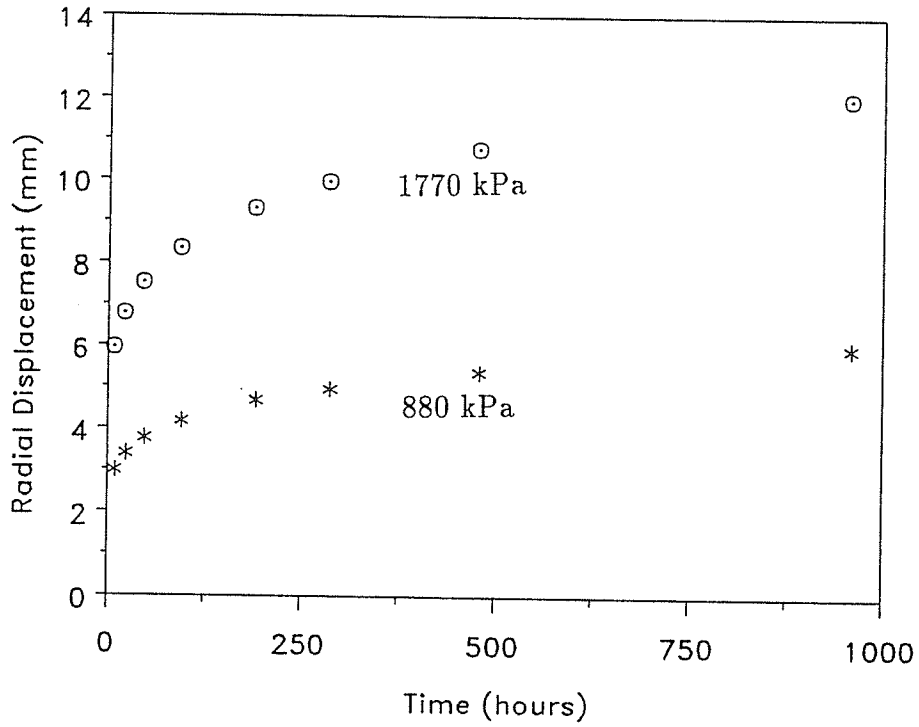

Figure 4.47. Predicted radial displacement at centre of pressuremeter probe under Domaschuk's model.

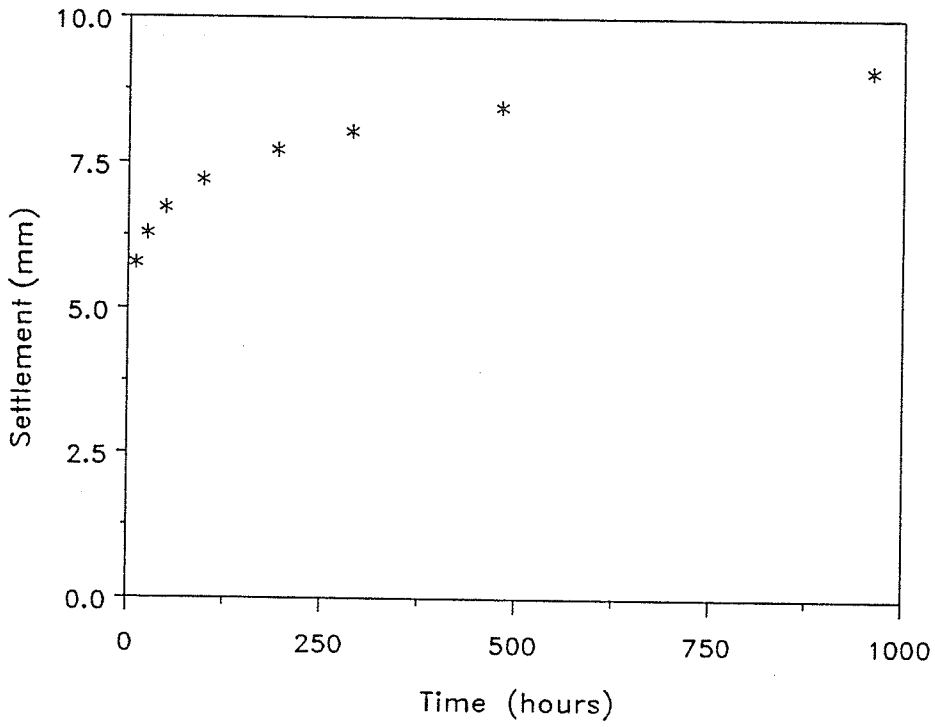

Figure 4.48. Predicted vertical settlement at centre of plate under Domaschuk's model.

Chapter 5

ANALYSES OF LATERALLY LOADED PILES IN ICE/FROZEN SOILS

5.1 General

In permafrost areas, piles are widely used to support structures ranging from large, heavy, heated buildings to single microwave communication towers located at remote sites (Johnston 1981). Because of the frequent use of pile foundations, prediction of creep deformations in pile-permafrost /ice interaction problems has gained much importance. Axially loaded piles can be conveniently analyzed using the FEM under an axisymmetric treatment, similar to several cases discussed earlier in Chapter 4. In cases where adfreeze strength plays a major role in such structures, an appropriate interface element capable of modelling the adfreeze/bond strength of frozen soil/ice to pile can be incorporated; the development of such an interface element is discussed later in Chapter 6. In laterally loaded piles, the load resisting mechanisms are different from those in axially loaded piles. Such lateral loads on pile foundations may be generated due to many sources, for example, by the design load transfer mechanism in pile supported structures such as buildings and bridge abutments, by wind loads on all pile supported structures, by cable tensile loads on pile supported tower structures, by lateral ice pressures (e.g. due to a floating ice sheet) or earth pressures on structures supported by piles, etc. In the present Chapter, computational analyses of laterally loaded piles in ice/permafrost are treated at length.

In the case of rigid piles embedded in soil media, analysis of the interaction problem is performed using concepts of active and passive lateral earth pressures conventionally employed in soil mechanics. When the pile is flexible, many additional parameters like flexibility of the pile, stiffness of the surrounding medium, effective embedment length, etc., acquire a greater degree of importance (Poulos and Davis 1980). Analytical and numerical studies on piles embedded in linear elastic media and subjected to general dynamic loads have been conducted to eval-

uate the influence of different parameters on pile displacements (Rajapakse and Shah 1987). When the pile is embedded in a frozen medium and subjected to a static (or quasi-static) lateral load, the deformation will vary with time due to creep of the medium, and the relevant interaction problem should be analyzed using a time-incrementing numerical scheme. Numerical methods are pertinent due to the redistributing nature of the lateral reactions of the surrounding medium.

Nixon (1984), and Neukirchner and Nixon (1987), suggested that laterally loaded piles in permafrost be modelled as beams on a non-linear dashpot system governed by a creep model of the type of secondary stage power law. Foriero and Ladanyi (1990) analyzed the problem using an explicit time incrementing FE program, and by modelling the laterally loaded pile as a beam supported by a spring-dashpot system. In the ensuing §5.2, the development of a simple pile element to model laterally loaded piles in permafrost/ice will be discussed. The approach followed here differs from that of Foriero and Ladanyi (1990) in many respects, as will be discussed later. The iterative, time-incrementing FE code developed here will be verified for accuracy, and analyses of several pile-ice/frozen soil interaction problems will be presented. In §5.3, pile-ice/ frozen soil interaction problems will be analyzed using completely three-dimensional analyses with continuum elements, and in §5.4, predicted results from the two approaches would be compared. The merits of the particular approach followed to develop the non-linear dashpot relationship and the elastic spring constant (for the simple pile model) will be discussed.

5.2 Development of a Simple Pile Element

In this section, a computationally simple pile element is developed to model laterally loaded piles in ice/ permafrost. The development of the relevant iterative, time-incrementing finite element code, and the performance of the pile element in FE analyses is discussed thereafter.

5.2.1 Basis for Development of the Pile Element

It is known that ice, in many circumstances, deforms continuously under load

and displays secondary creep characteristics. Thus, it is analytically convenient and physically reasonable, to model the creep deformation of frozen icy soils using a secondary or steady creep rate relationship (Nixon 1984). Therefore, it is possible to represent ice or icy permafrost by a system of non-linear dashpots (Nixon 1984, Neukirchner and Nixon 1987) where the displacement rate $\dot{u}$ is related to applied load as,

$$\dot{u} = I_1 a \bar{B} p^b \ , \tag{5.1}$$

where a is the half width or radius of the loaded area, $\bar{B}$ and b are creep parameters from uniaxial tests on ice (or permafrost), p is the horizontal stress on the loaded area, and I_1 is an influence factor dependent on b and geometry of the loaded area. Quantity p can also be referred to as the reactive stress generated by the frozen medium. Equation (5.1) represents a viscous fluid, which will not show any instantaneous deformation upon loading. An alternative model would be to couple a spring element in series to the dashpot element of equation (5.1), and the resulting system would indicate an instantaneous displacement followed by the continuous rate of displacement described by equation (5.1). The reaction p would undergo redistribution from its initial elastic state towards a steady-state distribution in the long term.

It is possible to hypothesize attenuating creep behaviour instead of equation (5.1), given by,

$$\dot{u}(t) = C_1 \, p^b \, t^{C_2} \ , \qquad C_2 < 0 \ , \tag{5.2}$$

where t is the current time and C_1, b, C_2 are parameters. For $C_2 = 0$, equations (5.2) and (5.1) are equivalent. Foriero and Ladanyi (1990) used a dashpot relationship of the above type in their FE analysis of laterally loaded piles using a similar spring-dashpot system. This relationship, however, was developed using an analytical, plane strain elastic solution given by Baguelin et al. (1977) for a laterally loaded disk in an infinite soil. Foriero and Ladanyi (1990) used the analytical expressions for elastic stress distributions to represent creep stress distributions. As can be seen from the numerical results presented in Figure 4.26, the redistributed stresses have magnitudes different from the initial elastic stresses (although this difference is not dramatic), and consequently, an approximation had been introduced into the

analysis of Foriero and Ladnayi (1990). Additionally, they consider that the lateral creep movement of the core is governed by stresses at the point where the axis of lateral load intersects the core-permafrost interface at the fore. This in general is not true, since the displacement of the core depends on the stress distribution along the entire cicumference of the interface rather than on stresses at a single point on the interface.

In the approach followed here, the pile is modelled as a beam supported by a spring-dashpot system, as shown in Figure 5.1. The load-deformation relations for the spring-dashpot system are developed based on the results of a series of plane strain FE analyses of laterally loaded rigid cores in ice, as described previously in §4.2.3. The plane strain analyses were conducted using a secondary stage power law creep model to characterize ice. As an example, equation (4.8) can be used to characterize the equivalent dashpot in the case of a circular pile here, and equation (4.9) can be used to characterize the same for a square pile. The particular numerical values of coefficients and exponents in equations (4.8) and (4.9) would depend on the creep parameters of the ice (or permafrost), magnitudes of applied loads, shape of the core, and the state of the bond between the core and ice (fully bonded or separated over a part of the interface). The coefficient of the Winkler medium k_w (the spring constant of the equivalent spring element of the spring-dashpot system) can be obtained by evaluating the ratio of the load (Force/Length) applied on the rigid core and the instantaneous lateral displacement. Since linear elasticity was considered in the continuum models in Chapters 3 and 4, this spring constant will not depend on the magnitude of the load, but only on the E and ν of the frozen medium, shape of the core, and state of the bond at the interface. The pertinent assumption made in this approach is that the state of deformation in each horizontal plane intersecting the pile can be approximated by a state of plane strain deformation. This assumption is reasonable when the pile deforms with large radii of curvature.

According to the classical beam theory, the governing equation of equilibrium

for a prismatic beam on a Winkler medium is given by,

$$EI\,\frac{\partial^4 w}{\partial x^4} + R(x) = 0\ , \tag{5.3}$$

where w is the total lateral deflection at a point on the beam designated by coordinate x, E the Young's modulus, I the second moment of area of the cross-section, and $R(x)$ the lateral ice reaction in units of (Force/Length). Ice reaction on the pile is given by,

$$R(x,t) = k_w\,(w - w_c)\ , \tag{5.4}$$

where R is the lateral ice reaction defined earlier, w the total lateral displacement and w_c the lateral creep displacement at the point under consideration, and k_w the elastic Winkler (spring) coefficient in units of (Force/Length^2). Creep displacement is described by,

$$\dot{w}_c = \frac{dw_c}{dt} = C_1\,R^b\ , \tag{5.5}$$

where superposed dot denotes time derivative, C_1 and b are parameters (for eg., from equations 4.8 or 4.9), and all other notations are as defined earlier.

The above equations (5.3)–(5.5) can be converted to a form suitable for implementation in a time-incrementing FE code. The pile can then be discretized into several elements, and analyzed using the code, where at each time step, equation (5.5) is used to evaluate the creep displacements at each node by using the prevailing values of ice/ permafrost reactions. Development of the relevant iterative, time-incrementing FE algorithm is described below.

5.2.2 Finite Element Algorithm for Pile Element

The complete problem is posed as follows:

$$EI\,\frac{\partial^4 w}{\partial x^4} + k_w(w - w_c) = 0\ , \qquad 0 < x < l\ , \tag{5.6a}$$

$$EI\,\frac{\partial^2 w}{\partial x^2} - \bar{M} = 0 \quad \text{or} \quad w = \bar{w} \quad \text{at} \quad x = 0, l\ , \tag{5.6b}$$

$$\frac{\partial}{\partial x}\left(EI\,\frac{\partial^2 w}{\partial x^2}\right) + \bar{V} = 0 \quad \text{or} \quad \frac{\partial w}{\partial x} = \bar{\alpha} \quad \text{at} \quad x = 0, l\ , \tag{5.6c}$$

where $\bar{M}$, $\bar{V}$, $\bar{w}$, $\bar{\alpha}$ denote, respectively, a specified moment, shear force, displacement, and rotation. Assuming that the choice of w is so restricted as to satisfy forced boundary conditions $w = \bar{w}$ and $w' = \bar{\alpha}$, the Galerkin's equation in weak form of equations (5.6) can be written, for cases where natural boundary conditions exist, as:

$$G(v,w) = \int_0^l \left\{ EI\,\frac{\partial^4 w}{\partial x^4} + k_w(w - w_c) \right\} v\,dx + \left\{ EI\,\frac{\partial^2 w}{\partial x^2} - \bar{M} \right\} v_1 \Big|_0^l + \left\{ \frac{\partial}{\partial x}\left(EI\,\frac{\partial^2 w}{\partial x^2} \right) + \bar{V} \right\} v_2 \Big|_0^l = 0 \qquad (5.7)$$

where v, v_1, v_2 are appropriately selected values. The first term on the right hand side of equation (5.7) can be rearranged through integration by parts as:

$$\int_0^l v\left(EI\,\frac{\partial^4 w}{\partial x^4} \right) dx = \int_0^l \frac{\partial^2 v}{\partial x^2}\, EI \frac{\partial^2 w}{\partial x^2}\, dx - \frac{\partial v}{\partial x}\, EI \frac{\partial^2 w}{\partial x^2} \Big|_0^l + v\, EI\, \frac{\partial^3 w}{\partial x^3} \Big|_0^l . \qquad (5.8)$$

By selecting $v_1 = \frac{\partial v}{\partial x}$ and $v_2 = -v$, equations (5.7) and (5.8) result in the following weak form Galerkin's equation:

$$G(v,w) = \int_0^l \left(\frac{\partial^2 v}{\partial x^2}\, EI \frac{\partial^2 w}{\partial x^2} \right) dx + k_w \int_0^l v(w - w_c)\, dx - \bar{M} \frac{\partial v}{\partial x} \Big|_0^l - \bar{V} v \Big|_0^l = 0 \ . \qquad (5.9)$$

The last two terms of equation (5.9) can be referred to as 'boundary terms', and v can selected such that v, $\frac{\partial v}{\partial x}$ at the respective boundaries are unity. In cases where forced boundary conditions prevail at the ends, the weak form of the governing equations is:

$$\int_0^l \left(\frac{\partial^2 v}{\partial x^2}\, EI \frac{\partial^2 w}{\partial x^2} \right) dx + k_w \int_0^l v(w - w_c)\, dx - \frac{\partial v}{\partial x}\, EI \frac{\partial^2 w}{\partial x^2} \Big|_0^l + v\, EI \frac{\partial^3 w}{\partial x^3} \Big|_0^l , \qquad (5.10)$$

where last two (boundary) terms can be forced to vanish by selecting v, $\frac{\partial v}{\partial x}$ as zero at the boundaries; such choice is possible since the equation need not be solved at the boundaries. In either case (equations 5.9 or 5.10), v need to be selected in the form of a vector $\mathbf{v}$, and the number of elements v_j $(j = 1, 2 \ldots m)$ in this vector is equal to the number of unknowns only. Thus the following usual selections are made:

$$w = [N]\mathbf{q} \qquad \text{and} \qquad \mathbf{v} = [N]^T , \qquad (5.11)$$

where $[N]^T$ is a shape function vector, and $\mathbf{q}$ is the vector of nodal variables. Now the weak form expression of the boundary value problem can be written as:

$$G(v,w) = \int_0^l \left\{ \frac{\partial^2 [N]^T}{\partial x^2} EI \frac{\partial^2 [N]}{\partial x^2} \mathbf{q} + k_w [N]^T \left([N]\mathbf{q} - w_c \right) \right\} dx + \mathbf{F} = \mathbf{0} \ , \quad (5.12)$$

where $\mathbf{F}$ denotes forces prevailing at the boundaries of the system. Let Figure 5.2 depict a beam finite element of length l, representing a discrete part of a beam on a spring-dashpot system; the first local node of the element is at a distance x_1 from the origin of the global coordinate system. With reference to Figure 5.2, it is possible to select the following expressions (Desai 1979), such that compatibility is maintained with respect to all requirements mentioned earlier:

$$\mathbf{q} = \langle w_1, \ \alpha_1, \ w_2, \ \alpha_2 \rangle \ , \quad (5.13a)$$

$$s = (x - x_1)/l \ , \quad (5.13b)$$

$$[N] = \langle (1 - 3s^2 + 2s^3), \ \ ls(1 - 2s + s^2), \ \ s^2(3 - 2s), \ \ ls^2(s - 1) \rangle \ , \quad (5.13c)$$

where the nodal variables w_i, α_i denote, respectively, the lateral displacement and rotation at the ith local node, x is the global coordinate measure, and s denotes a relative coordinate.

Assembly of equation (5.12) for all the finite elements representing the beam can be written as:

$$\sum_e \int_0^1 \{ [B]^T EI [B] + k_w [N]^T [N] \} l \, ds \, \mathbf{q} - \sum_e \int_0^1 k_w [N]^T w_c l \, ds + \sum_e \mathbf{F}_e = \mathbf{0} \ , \quad (5.14)$$

where $\sum$ denotes summation over all elements, a subscript e denotes an elemental quantity, and

$$[B] = \frac{\partial^2 [N]}{\partial x^2} = \frac{1}{l^2} \frac{\partial^2 [N]}{\partial s^2} \ . \quad (5.15)$$

Based on the equations (5.14) and (5.5), an iterative, time-incrementing finite element algorithm can be developed as outlined hereafter.

Assuming that the solutions are known at a time t_k, equation (5.14) can be written for this time instant as:

$$\boldsymbol{\chi}_k = \sum_e \int_0^1 \{[B]^T EI[B] + k_w[N]^T[N]\} l\, ds\, \mathbf{q}_k - \sum_e \int_0^1 k_w[N]^T w_{c,k} l\, ds + \sum_e \mathbf{F}_{e,k} = \mathbf{0}\ , \tag{5.16}$$

where a subscript k denotes that the relevant quantity is considered at time t_k. Equation (5.4) can be rewritten as,

$$R_k(s) = k_w\{w_k - w_{c,k}\} = k_w\{[N]\mathbf{q}_k - w_{c,k}\}\ , \tag{5.17}$$

where $R_k(s)$ denotes the lateral ice (permafrost) reaction in units of (Force/Length) at the location s. Let the time be incremented by the next time interval to $t_{k+1} = t_k + \Delta t_k$. An iterative process can be followed to evaluate the incremental corrections of nodal variables and soil reactions at the time t_{k+1}. Thus equation (5.16) can be rewritten for the nth iteration for the present time step as,

$$\boldsymbol{\chi}^n_{k+1} = \sum_e \int_0^1 \{[B]^T EI[B]\} l\, ds\, \mathbf{q}^n_{k+1} + \sum_e \int_0^1 [N]^T R^n_{k+1}(s)\, l\, ds + \sum_e \mathbf{F}_{e,k+1} \neq \mathbf{0}\ , \tag{5.18}$$

where a superscript n denotes that the relevant quantity is considered at the nth iteration, and the unequal sign is used to denote that exact equilibrium had not been reached yet. At a given location s inside the element, the difference between the soil reaction at this iterative cycle and that at time t_k can be written as:

$$\psi^n_{k+1} = R^n_{k+1} - R_k - k_w[N]\{\mathbf{q}^n_{k+1} - \mathbf{q}_k\} + k_w\, \Delta t_k\, \dot{w}_c(R^n_{k+\theta}) \neq 0\ , \tag{5.19}$$

where the following relations had been used:

$$w^n_{c,k+1} - w_{c,k} = \dot{w}_c(R^n_{k+\theta}) \cdot \Delta t_k\ , \tag{5.20a}$$

and

$$R^n_{k+\theta} = (1-\theta)R_k + \theta R^n_{k+1}\ , \qquad 0 < \theta < 1\ . \tag{5.20b}$$

In above, the nature of the iterative scheme can be categorized according to the value of θ used (as in equation 3.45 earlier), and a general form of the creep displacement rate $\dot{w}_c$ given earlier by equation (5.2) can be written as,

$$\dot{w}_c(s,t) = C_1\{R(s,t)\}^b\, t^{C_2} \ , \qquad C_2 \leq 0 \ , \tag{5.21}$$

where C_1, C_2, b are parameters, and $C_2 = 0$ for steady state creep deformations. Applying curtailed Taylor expansion on equation (5.19), the following expression is obtained:

$$\psi_{k+1}^{n+1} = \psi_{k+1}^{n} + \Delta R_{k+1}^{n} - k_w[N]\,\Delta q_{k+1}^{n} + k_w\,\Delta t_k\;\theta\;\frac{\partial \dot{w}_c}{\partial R_{k+\theta}^{n}}\;\Delta R_{k+1}^{n} = 0 \ . \tag{5.22}$$

Equation (5.22) is set equal to zero assuming that equilibrium had been exactly satisfied at this $(n+1)$th iteration. In view of equations (5.19) and (5.22), the iterative correction of soil reaction at location s can be written as,

$$\Delta R_{k+1}^{n} = \bar{D}\left[k_w[N]\,\delta \mathbf{q}_{k+1}^{n} - (R_{k+1}^{n} - R_k) - k_w\,\Delta t_k\,\dot{w}_c(R_{k+\theta}^{n})\right] \ , \tag{5.23a}$$

where

$$\bar{D} = \left[1 + k_w\,\Delta t_k\;\theta\;\frac{\partial \dot{w}_c}{\partial R_{k+\theta}^{n}}\;\right]^{-1} \ , \tag{5.23b}$$

and

$$\delta \mathbf{q}_{k+1}^{n} = \mathbf{q}_{k+1}^{n} + \Delta \mathbf{q}_{k+1}^{n} - \mathbf{q}_k \ . \tag{5.23c}$$

Curtailed Taylor expansion of equation (5.18) yields:

$$\boldsymbol{\chi}_{k+1}^{n+1} = \boldsymbol{\chi}_{k+1}^{n} + \sum_e \int_0^1 \{[B]^T EI[B]\} l\, ds\, \Delta \mathbf{q}_{k+1}^{n} + \sum_e \int_0^1 [N]^T\, \Delta R_{k+1}^{n}\, l\, ds = \mathbf{0} \ . \tag{5.24}$$

Due to the assembly process, it is possible to replace the sum of the integrated elemental quantities by a single global integral, ie.,

$$\sum_e \int_0^1 \{\quad\}\, l\, ds \equiv \int_L \{\quad\}\, dL \ , \tag{5.25}$$

where L denotes the total length of the pile. In view of equations (5.18), (5.23a) and (5.25), equation (5.24) can be written as:

$$\chi_{k+1}^{n+1} = \int_L \{[B]^T EI[B]\} dL\, \Delta \mathbf{q}_{k+1}^n + \int_L [N]^T \bar{D} \{k_w [N] \delta q_{k+1}^n - (R_{k+1}^n - R_k) - k_w\, \Delta t_k\, \dot{w}_c(R_{k+\theta}^n)\}\, dL + \int_L \{[B]^T EI[B]\}\, dL\, \mathbf{q}_{k+1}^n + \int_L [N]^T \{R(L)\}_{k+\theta}^n\, dL + \mathbf{F}_{k+1} = \mathbf{0}\ . \tag{5.26}$$

By substracting equation (5.16), in view of equation (5.17), from equation (5.26), the following expression is finally obtained:

$$\int_L \{[B]^T EI[B] + [N]^T \bar{D}\, k_w [N]\} dL\, \delta \mathbf{q}_{k+1}^n + \int_L [N]^T \{1 - \bar{D}\}(R_{k+1}^n - R_k)\, dL - \int_L [N]^T \bar{D}\, k_w\, \Delta t_k\, \dot{w}_c(R_{k+\theta}^n)\, dL + \Delta \mathbf{F}_{k+1} = \mathbf{0}\ . \tag{5.27}$$

At each iterative cycle, equation (5.27) is solved for the incremental nodal variable vector $\delta \mathbf{q}$, and equation (5.23a) thereafter yields the iterative correction of soil (ice) reaction at given locations. The iterations are started with $R_{k+1}^0 = R_k$ and $\mathbf{q}_{k+1}^0 = \mathbf{q}_k$. At the end of each iterative cycle, the solutions can be updated as:

$$\mathbf{q}_{k+1}^{n+1} = \mathbf{q}_k + \delta \mathbf{q}_{k+1}^n \qquad \text{and} \qquad R_{k+1}^{n+1} = R_{k+1}^n + \Delta R_{k+1}^n\ . \tag{5.28}$$

If convergence has occurred at the above $(n+1)$ th iteration, we set $\mathbf{q}_{k+1} = \mathbf{q}_{k+1}^{n+1}$ and $R_{k+1} = R_{k+1}^{n+1}$, and proceed to the next time step; otherwise iteration is continued. At convergence, the element end forces $\mathbf{f}_{e,k+1}$ for each element (ie. shear forces and bending moments) can be calculated using:

$$\mathbf{f}_{e,k+1} = \int_l \{[B]^T EI[B]\}\, dl\, \mathbf{q}_{k+1} + \int_l [N]^T R_{k+1}(l)\, dl\ . \tag{5.29}$$

The finite element code was developed using the above pertinent equations (5.27) and (5.23a). As can be seen from the above, the algorithm requires that the current total deformations (lateral displacements and rotations) at nodal points

and current soil (ice) reactions at Gauss points within each element be maintained explicitly. The solution process is initiated by obtaining the instantaneous elastic deformations and soil (ice) reaction distribution, by solving equations (5.16) and (5.17) at $t = 0$ (with no creep deformations). These solutions are then used to obtain the incremental deformation and reaction vectors during the first time interval Δt_0, by solving equations (5.27) and (5.23a) through the iterative procedure given above. For the iterative scheme, the following convergence criterion is used:

$$\|\Delta \mathbf{q}_k^n\| \quad < \quad 0.01 \times \|\Delta \mathbf{q}_k^{n-1}\| \ , \tag{5.30}$$

where $\|\mathbf{x}\|$ denotes the Euclidean norm of the relevant vectorial quantity $\mathbf{x}$. The solution process is repeated for each time interval, until the analysis is terminated at a pre-specified time.

5.2.3 On the Finite Element Code for Pile Element

A finite element code was developed by incorporating the iterative, time incremental algorithm for a laterally loaded pile outlined in §5.2.2. This code is named **FEPILE-I**, and its general features are very similar to those of the codes developed earlier for continuum analyses (see §3.5). Figures 3.1 and 3.2 apply to code FEPILE-I also. The main program section and element subroutines perform tasks identical to those detailed in §3.5. The code has two element subroutines, one for a beam on a spring-dashpot system as considered in §5.2.2 above, and another for an elastic beam element on a spring system (Winkler medium) which can be used to model either non-embedded portions of a pile or portions of a pile embedded in elastic media. This enables the use of the code to analyze laterally loaded piles in layered media (for example, when part of a pile is embedded in unfrozen soil underlying the frozen layer). The execution of the code is controlled by the use of Macro commands, identical to the process described earlier in §3.5. Further details about the code FEPILE-I are given in Appendix F, and by Puswewala and Rajapakse (1991a).

It is possible to develop an alternative finite element code by introducing a slight variation to the iterative, time incremental algorithm outlined in §5.2.2. In

this alternative algorithm, the current total deformation vector and the current creep displacement vector are maintained explicitly, and soil (ice) reactions are evaluated whenever necessary by using equation (5.17). This algorithm is briefly outlined in Appendix F, and a FE code named **FEPILE-II** was developed using it. This alternative code was useful for verifying results obtained from code FEPILE-I.

5.2.4 Verification of Code

The code **FEPILE-I** was verified for accuracy and reliability by simulating several examples. In the first instance, the tests of Domaschuk et al. (1989) were re-simulated using the pile element. In these tests, steel bars of length 610 mm and diameter 76 mm were embedded in ice and subjected to different lateral loads by applying two equal loads at the the top and bottom of the bars (Domaschuk et al. 1989). These same examples were analyzed in Chapter 4 earlier (§4.2.3), using plane strain analyses of laterally loaded rigid cores in ice to approximate the test conditions. (See §4.2.3 for properties of ice and interface bond conditions used). The dashpot relationship evaluated from plane strain analyses is given by equation (4.8), and the value of k_w was obtained by dividing the applied load by the corresponding initial elastic displacement. Thus, following values were used for the pile analyses here:

$$\begin{aligned} & k_w = 946 \ \text{N/mm}^2 \ , \qquad b = 3.1835 \\ & C_1 = 0.5174 \times 10^{-8} \ \text{ for } R \text{ in N/mm and } \dot{w}_c \text{ in mm/hour} \\ & C_2 = 0.0 \ , \qquad EI = 3.2 \times 10^{11} \ \text{N mm}^2 \end{aligned} \tag{5.31}$$

Note that the values of C_1, b, and $C_2 = 0$, are directly given by equation (4.8). Young's modulus of steel was assumed as 2×10^5 MPa. Four loading cases were considered, where a load of 34.8, 40.65, 47.1, and 52.3 kN were applied at each end of the bar, respectively (Domaschuk et al. 1989). The pile was simulated using 13 finite elements of equal length, with two Gauss points for each element. Solutions were not very sensitive to time discretization, since results obtained by using 7200 time increments (starting with an interval of 10^{-5} hours and gradually increasing it to a maximum of 0.06 hours over a time history of 176 hours) were almost identical

with those obtained using approximately 500 time increments (starting with an interval of 10^{-2} hours and gradually increasing it to a maximum of 0.1 hours over a time history of 176 hours).

The results obtained from code FEPILE-I are shown in Figure 5.3a, where the displacement at the top of the rod is plotted against time for each of the loading cases. The rates of displacement predicted by the code for each loading case are given in Figure 5.3b, along with the corresponding rates predicted by plane strain analyses performed in §4.2.3. It can be seen that the rates predicted by the two approaches (pile element and plane strain analyses) agree closely. The ability of the code to reproduce the rates obtained from previous plane strain analyses verifies that the dashpot relationship (equation 4.8, or equivalent equation 5.5) is correctly implemented in the code, and that the time integrating routines function properly.

The code was next used to simulate a pile analysis problem which was analyzed independently by Morin et al. (1991), who used a finite difference scheme for the numerical analysis. For this problem, a fictitious steel pile of length 2.5 m, completely embedded in ice and loaded at the top end with a lateral load of 100 kN, was considered under two different boundary conditions at the bottom. In one case, the lower end of the pile was fully restrained (cantilever pile), and in the other case, the pile was allowed to float freely (unrestrained except for the resistance by ice, similar to the bars used by Domaschuk et al. 1989). The values of different parameters used were as follows:

$$\begin{aligned} & k_w = 2 \times 10^5 \text{ kN/m}^2 \ , \qquad b = 3.864 \\ & C_1 = 0.346 \times 10^{-10} \ \text{ for } R \text{ in kN/m and } \dot{w}_c \text{ in m/year} \\ & C_2 = 0.0 \ , \qquad EI = 8.2 \times 10^4 \text{ kN m}^2 \end{aligned} \tag{5.32}$$

The pile was discretized by 20 elements of equal length with two Gauss points for each element. For the pile with lower end fixed, an initial step of 10^{-4} years was used, which was increased to 0.1 years over a time history of 250 years. For the floating pile, a constant time step of 10^{-4} years was used over a history of 50 days. The comparison between results (pile head displacement) predicted by

code FEPILE-I and those of Morin et al. (1991) is shown in Figure 5.4 for the floating pile, and in Figure 5.5 for the fixed pile. The two predictions are seen to almost coincide in Figures 5.4 and 5.5. In Figure 5.5, with increasing time, the pile head displacement approaches the analytical elastic solution for a free standing (non-embedded) cantilever beam given by,

$$w_L = \frac{PL^3}{3EI} , \tag{5.33}$$

where w_L is the displacement at the free end of the cantilever beam, P the lateral load at the free end, and L the length of the beam. The predicted results were not influenced by an increase of the number of elements (to 60 or 100). Profiles of bending moments, shear forces, and lateral ice reactions predicted by the code would be discussed later in §5.2.5 with regard to several examples of pile analysis, and hence these profiles are not presented at this point. Simulation of above two examples by code FEPILE-II yielded results almost identical to those of code FEPILE-I. This indicated that the algorithms in the two codes are equivalent as expected, and the results of either code are reliable.

Further tests for reliability of algorithms in both codes were conducted by analyzing several cantilever pile problems with $C_1 = 0$ (no creep in the surrounding medium). In these cases, the solutions remained static at the initial elastic values, regardless of the distance advanced along the time axis using time steps. When relatively large values of C_1 were used, the piles showed initial time-dependent deformation and approached the analytical solution of equation (5.33) rapidly; thereafter, the solutions remained static with increasing time. A problem with relatively large C_1 is considered later in §5.2.5. The examples described above were deemed to be sufficient to verify the accuracy and reliability of the code FEPILE-I.

5.2.5 Analyses of Pile-Ice/Permafrost Interaction Problems

An important characteristic of laterally loaded piles is the influence of the restraint condition at the bottom of the pile on the deformed shape of the pile. For piles embedded in elastic media (where no creep is involved), the influence can be

characterized by a non-dimensionalized parameter λl defined as,

$$\lambda l = l \left(\frac{k_w}{4EI} \right)^{\frac{1}{4}} ,$$

where l is the length of the pile, and all other parameters are defined as before. For $\lambda l > 3$, the pile behaves as a flexible pile (Selvadurai 1979) and the influence of the bottom restraint condition on the pile head displacement will be negligible. This effect was investigated by the code FEPILE-I using elastic analysis (creep mode was not invoked) and a pile of length 1030 mm subjected to a lateral load of 34800 N at one end; the other end was free in one case and fully restrained (in both translation and rotation) in the other case. Different values of k_w and EI were considered. The results of the study are shown in Figure 5.6, which confirms that the pile head displacement does not depend on the boundary condition at the far end when $\lambda l > 3$. As would be shown later, approximately similar behaviour is observed in case of very flexible piles in creeping media represented by Maxwell rheological models (Figures 5.12 & 5.13).

A model steel pile (with square cross-section of 59.69×59.69 mm^2 and length of 1030 mm), fully embedded in ice, was considered for simulation by the code FEPILE-I. The length to half-width ratio of the model pile here is ≈ 34, which implies that it can be considered as a long pile. The square rigid core considered in §4.2.3 for plane strain analyses had identical cross-sectional dimensions as the pile considered here. Therefore, the dashpot relationship of equation (4.9) was selected for the analyses here, and the Winkler coefficient k_w was obtained by dividing the applied load by the corresponding initial lateral displacement. Thus the values of different parameters used were:

$$\begin{aligned} & k_w = 630.36 \text{ N/mm}^2 , \qquad b = 3.2256 \\ & C_1 = 0.3457 \times 10^{-8} \text{ for } R \text{ in N/mm and } \dot{w}_c \text{ in mm/hour} \\ & C_2 = 0.0 , \qquad EI = 2.1157 \times 10^{11} \text{ N mm}^2 \end{aligned} \tag{5.34}$$

In above, EI was computed using $E = 2 \times 10^5$ MPa for steel. Figures 5.7a and 5.7b show the pile configurations considered for simulation. Figure 5.7a shows

a pile with lower end fully restrained, and Figure 5.7b shows a pile which floats in ice. Each pile configuration was considered under loads of 23300, 34800, and 40650 N, respectively, applied laterally at the top. The pile length was divided into 50 finite elements of equal length, and an iterative scheme with $\theta = 0.5$ was used for the analyses. The lateral pile head displacement predicted by the code FEPILE-I for the six cases are as shown in Figure 5.8. As can be seen from Figure 5.8, the floating piles show almost constant rates of pile head displacement after a brief initial period of decelerating displacement, while the fixed piles show attenuation of the pile head displacement towards the analytical elastic solution for a free-standing cantilever (equation 5.33). The steady displacement rates of floating piles are in agreement with the steady-state dashpot relationship used to characterize creep of ice ($C_2 = 0$ in equation 5.21). In cantilever piles, the attenuating behaviour of the pile head displacement is caused by the combination of the fixed boundary condition at the bottom of the pile and the Maxwell rheological model assumed to represent the creep of ice. Physically, the lateral ice reaction relaxes with time while an increasing proportion of the applied load is resisted by the deformation of the pile itself. Therefore, the theoretical upper bound of this type of fixed piles is given by equation (5.33), which holds for a free cantilever (not embedded in a medium). This behaviour is further demonstrated in Figure 5.9, where the cantilever pile of Figure 5.7a was analyzed for two different values of C_1, while all other parameters and the applied load (= 34800 N) were held constant. In one case, parameters given by equation (5.34) were used (thus $C_1 = 3.457 \times 10^{-9}$), and in the other case, a larger C_1 ($= 3.457 \times 10^{-5}$) was used while keeping all other parameters identical to those in equation (5.34). Figure 5.9 shows that both piles approach the solution of 59.75 mm given by equation (5.33), but with different rates, and that the larger value of C_1 implies that the particular ice offers little physical resistance to pile deformation, and the viscosity of the surrounding ice, modelled as a Maxwell (fluid) medium, is relatively low.

It should be mentioned that in usual field conditions, a more realistic assumption is a pile floating in the surrounding medium. Unless the pile tip is driven well into a hard material such as bedrock, the assumption of full restraint at the

bottom of the pile (against rotation and translation) cannot be made for analytical purposes. In permafrost or ice, such anchoring in bedrock is very rare, and piles almost always exist as floating piles.

The detailed numerical results for the fixed pile (Figure 5.7a) with parameters of equation (5.34) and lateral load of 34800 N applied at the pile head are shown in Figures 5.10a–d. Figure 5.10a shows the deformed shapes of the pile at different times, and the pile is seen to approach the deformed shape of a free cantilever beam (no embedding media) in the long-term. Figure 5.10b shows the bending moment profiles along the pile at different times, and Figure 5.10c shows shear force profiles. With increasing time, bending moment and shear force profiles approach those for a free cantilever beam. Figure 5.10d shows the redistribution of ice reaction with time; ice reaction throughout the length of the pile tends towards zero (vanishes) in the long-term, thus enabling the pile to behave as if the surrounding medium did not exist at large elapsed times.

Numerical results for the floating pile (Figure 5.7b) with parameters of equation (5.34) and lateral load of 34800 N applied at the pile head are shown in Figures 5.11a–d. Figure 5.11a shows the deformed shapes of the pile at different times. Figure 5.11b shows the bending moment profiles along the pile at different times, and Figure 5.11c shows shear force profiles. Figure 5.11d shows the redistribution of ice reaction with time. The bending moment, shear force and ice reaction profiles all approach steady state distributions in the long-term. This is a direct consequence of the steady state dashpot relationship used and freedom of the pile to float in the ice with no forced restraints.

Similar analyses were considered for a more flexible pile, by selecting $E = 10^4$ MPa for the pile material (This value is representative of the longitudinal E value of some types of hard wood). Pile dimensions were as earlier, the lateral load applied at the pile head was 34800 N, and all parameters were as given in equation (5.34). The pile was analyzed for the fully restrained and free boundary conditions, respectively, at the bottom end of the pile. The deformed shapes of cantilever pile (Figure 5.7a) at different times are shown in Figure 5.12, and those of floating pile

are shown in Figure 5.13. The increased flexibility of the pile (lower EI) here causes it to deform with relatively smaller radii of curvature as compared to the deformed shapes presented in Figures 5.10a and 5.11a for the stiffer pile ($E = 2 \times 10^5$ MPa). Comparison of deformed pile shapes in Figures 5.12 and 5.13 show that the influence of the bottom boundary condition on the deformed shapes of very flexible piles is negligible, under small displacement displacement considerations. This behaviour is somewhat similar to that seen in elastic analysis (ref. Figure 5.6).

Figures 5.14a–c show the profiles of bending moment, shear force, and ice reaction, respectively, at different times for the case of the floating pile considered above ($E = 10^4$ MPa). These profiles have different shapes as compared to the corresponding profiles for the stiffer pile (with $E = 2 \times 10^5$) shown in Figures 5.11b–d. As expected, profiles of ice reaction, bending moment, and shear force approach steady state solutions in the long-term, due to reasons mentioned earlier.

5.3 Three-Dimensional Analyses Using Continuum Elements

The problem of laterally loaded piles can be alternatively solved using three dimensional analyses. As compared to the simple pile element considered in §5.2 earlier, three dimensional analyses have an advantage in that it is not necessary to perform additional numerical analyses (eg: plane strain analyses of §4.2.3) to develop dashpot relationships. This type of continuum analyses needs the material parameters for the pile element and surrounding medium, and no additional relationships. Thus, three dimensional continuum analyses have advantages in cases where, for example, the stress distribution in permafrost needs to be investigated, or models like Fish's model are to be employed. Among the disadvantages, are the large number of degrees of freedom involved in a realistic three dimensional mesh, and the consequent requirement of considerable computer resources. In this section a general discussion of the three dimensional analyses of laterally loaded piles in ice/ permafrost will be presented.

The computer code ITFECC-A, described in §3.5 and §3.6.1, has the capability to perform three dimensional creep analyses using either 8 node brick elements or 20

node higher order elements; either the power law or Fish's model can be used as the creep model. Using the code ITFECC-A in elastic mode, a series of elastic analyses of a cantilever beam, discretized by three dimensional elements, was conducted to compare the performance of the 20 node higher order element (with numerical integration of order two in each of the three directions) and that of the 8 node brick element (under the same order of numerical integration). It should be noted here that the use of a single Gauss point for the 8 node brick element gives rise to singularity in the stiffness matrices. For the investigation, a steel cantilever beam ($E = 2 \times 10^5$ MPa; $\nu = 0.3$) of length 1030 mm and of cross-sectional dimensions 57.69×57.69 mm^2 was analyzed for elastic response under a lateral load of 34800 N applied at the free end. Due to the symmetry of the problem about the axis of loading, half of the beam cross sectional area was considered for analysis here. The length of the beam was discretized by six, 20-node elements of equal depth, stacked one upon another (total 117 nodes). This mesh yielded a value of 67.44 mm for the lateral displacement of the free end of the beam, as compared to the analytical result of 68.66 mm (equation 5.33); the deviation was -1.78%. When the same beam was discretized by 12, 20-node elements of equal depth stacked one upon another (total 225 nodes), the predicted result was 99.01% of the analytical result. When the depths of elements were varied in the latter mesh to obtain a finer mesh close to the loading point, the predicted result deteriorated slightly, to 98.39% of the analytical result. The same mesh domain was discretized using 24, 8-node brick elements of equal depth stacked upon one another (total 100 nodes), and the predicted result was 74.55% of the analytical result. When the element depths were varied in the latter mesh to obtain a finer division close to the loading point, the result again deteriorated to 60.3% of the analytical result.

The above elastic analyses clearly demonstrated the superiority of the 20-node element over the 8-node element, and hence it is reasonable to expect that the performance of the 20-node element in creep analysis would also be much better than that of the 8-node element. Further, it was seen that a uniform mesh discretization along the depth of the pile tends to yield a better result as compared to that given by an uneven discretization.

Based on the above observations, a three-dimensional mesh was prepared to simulate laterally loaded model piles embedded in a frozen medium, using 20-node three dimensional continuum elements and a uniform discretization along the length of the pile. The mesh contained 2093 nodes and 198 elements, and is as shown in Figure 5.15. Due to the symmetry of the problem about the plane containing the axis of the lateral load and the axis of the pile, only half of the actual domain was considered for discretization (as shown in Figure 5.15). The model pile had a length of 1030 mm and a square cross section of 59.69×59.69 mm^2. Thus the pile was equivalent to that considered using the code FEPILE-I in §5.2.5, and its cross section was identical to the dimensions of the laterally loaded square core considered in §4.2.3 (with reference to equation 4.9). The pile was unrestrained and allowed to float in the surrounding medium under a lateral load applied at the top. The domain shown in Figure 5.15 has a length of 3180 mm, a breadth of 380 mm, and a depth of 1030 mm. The nodes on the three far boundaries of the brick shaped domain were completely restrained, while the upper and lower faces of the domain were allowed to be free. The near face of the domain (containing the loading axis and the center-line of the pile) was restrained in the direction perpendicular to the loading direction (i.e. the symmetry consideration). All analyses were performed assuming the power law creep model.

Material properties for ice and pile were selected as identical to those in §4.2.3 (ref. equation 4.9), i.e.

$$\begin{aligned} &E_p = 2 \times 10^5 \text{ MPa} \;\; ; \qquad \nu_p = 0.3 \\ &E_s = 500 \text{ MPa} \;\; ; \qquad \nu_s = 0.47 \\ &A = 0.0214 \left(\frac{\text{mm}^2}{\text{N}}\right)^B \text{hr}^{-C} \;\; ; \quad B = 3.17 \;\; ; \quad C = 0 \end{aligned} \tag{5.35}$$

where subscript p denotes quantities for pile material, subscript s denotes quantities for frozen medium, and A, B, C are creep parameters for the power law model. Ice is assumed to undergo steady state creep. Initial test problems for three dimensional analyses were conducted using a lateral load of 34800 N at the top of the pile applied in the direction of x-axis, and the material properties in equation (5.35). The computer memory requirement for creep analysis using the mesh in Figure 5.15 was

about 8 megabytes. All problems were analyzed on SUN4/280 computers (AMD-HAL 5870 mainframe could not allocate the required memory). Time discretization was done using an initial time step of 0.01 hours which was gradually increased to 4.5 hours over a time span of 756 hours (using a toal of 450 time steps). The lateral displacement of the pile head predicted by two different time incremental schemes (described later) are shown in Figure 5.16, where the two sets of results almost coincide. In one scheme, $\theta = 0.5$ with no iterations was used, while in the other, $\theta = 1.0$ with iteration until convergence (according to criterion in equation 3.53) was used. The non-iterative solution process required approximately 50 CPU hours. The iterative process, for each time increment, consumed approximately double the CPU time requirement of the non-iterative scheme. (The observation that the two incremental schemes yielded almost coincident results was also noted during a previous set of analyses of a laterally loaded pile in ice, performed using a mesh of 552 nodes and 362, 8-node brick elements).

In order to verify whether the results obtained using mesh in Figure 5.15 were converged and were not dependent on mesh discretization, the identical problem was analyzed using a finer mesh. This new mesh consisted of 3213 nodes and 312, 20-node elements. As earlier, half the actual domain was considered for analyses, and had a length of 4040 mm, a breadth of 430 mm, and a height of 1030 mm. Boundary conditions, loads and material parameters were similar to earlier case. Simulations using the finer mesh required 13 megabytes of memory, and the same non-iterative time incremental scheme with $\theta = 0.5$ as used for the earlier mesh now consumed approximately 105 CPU hours. The results predicted by this simulation are also plotted on Figure 5.16 for comparison, and it can be seen that there is close agreement between the results obtained using the two meshes.

Based on the above comparisons, it was decided that the mesh in Figure 5.15 is sufficient for subsequent 3-dimensional analyses of laterally loaded piles in ice, and that the non-iterative time incrementing scheme yielded acceptable results. The paramount reasons for reaching these decisions were the considerations regarding the amount of computer resources needed (CPU time and computer memory) and the available time. The mesh in Figure 5.15 was thereafter used to analyze a

series of floating pile problems in ice, using a non-iterative time scheme with $\theta = 0.5$. These results are presented in the next section (§5.4), and compared with the corresponding results obtained using the simple pile element (code FEPILE-I).

5.4 Comparison of Results Using Continuum and Pile Elements

Equations (5.35) and (5.34) describe material parameters for identical laterally loaded pile problems, with respect to the approach of continuum analysis (§5.3) and that of a beam supported by a spring-dashpot system (§5.2), respectively. A floating model pile of length 1030 mm and cross section 59.69×59.69 mm^2 was analyzed using the code ITFECC-A, mesh in Figure 5.15 (see §5.3), material parameters in equation (5.35), and three different lateral loads of 23300, 34800 and 40650 N, respectively, applied at the top end. A non-iterative time incrementing scheme with $\theta = 0.5$ was used for all examples, and the time discretization started with a step of 0.01 hours which was gradually increased to 10 hours over a time history of approximately 4000 hours (a total of 860 time steps). Each simulation consumed approximately 90 CPU hours in SUN4/280 computers, and was performed using the facility in ITFECC-A to terminate analysis at intermediate stages in order to resume it later. The lateral pile head displacements predicted by the code ITFECC-A for these 3-dimensional analyses are presented in Figure 5.17. The identical laterally loaded pile problems were analyzed by using the simple pile element (using code FEPILE-I) earlier in §5.2, and the results were presented in Figure 5.8. The results for the floating piles shown in Figure 5.8 are replotted in Figure 5.17 for the purpose of comparison with the predictions made using continuum elements. A close agreement between the two sets of results can be seen in Figure 5.17. Figure 5.18 shows the deformed shapes at different times of the floating pile under a load of 34800 N, as predicted by the two approaches. A good agreement can be seen in Figure 5.18 between the results predicted by three dimensional analyses (by ITFECC-A) and pile analyses (by FEPILE-I).

In order to investigate whether results predicted by the two approaches show similar agreement for piles of greater flexibility than above, those analyses were repeated for piles with lower E_p values. The two additional cases considered were

$E_p = 10^4$ MPa and $E_p = 3.5 \times 10^3$ MPa, values which characterize wooden piles. The lateral load applied at the top of the pile was 34800 N in each case. Material parameters for ice were unchanged from equations (5.35) and (5.34). The simulations were performed exactly as earlier, using code ITFECC-A and mesh in Figure 5.15 for three dimensional analyses, and code FEPILE-I and a mesh of 50 finite elements for analysis using the pile element, but by changing the E_p value appropriately. The lateral pile head displacements predicted by the two approaches for the E_p values of 2×10^5, 10^4 and 3.5×10^3 MPa, and under the lateral load of 34800 N, are shown in Figure 5.19. The predictions by the two approaches compare closely in Figure 5.19. Deformed shapes at different times for the pile with $E_p = 10^4$, predicted by the two codes, are shown in Figure 5.20, where a good comparison is again evident. The CPU time requirements for examples here were similar to those in corresponding examples earlier.

The comparisons in Figures 5.17–5.20 show a remarkably good agreement between the results predicted by three dimensional analyses and the analyses using the simple pile element developed in §5.2. This confirms that results predicted by the simple pile element developed here can be reproduced by a rigorous analysis of the same problem using three dimensional continuum elements. The difference of computer resources required by each approach is vast, since each curve corresponding to three dimensional analyses in Figures 5.17 and 5.19 was plotted after 90 hours of CPU time using about 8 megabytes, whereas each curve corresponding to the simple pile element of code FEPILE-I was obtained using approximately 10 CPU minutes and less than 2 kilobytes of memory. However, it should be remembered that the analysis using the simple pile element requires the appropriate relationships for the dashpot and spring mechanisms, which were developed after performing a series of plane strain analyses using a particular set of material properties for ice. These dashpot relationships can be developed most conveniently for steady creep, whereas for primary and tertiary creep situations, the process will be more complicated. No such additional effort is required for analyses using three dimensional continuum elements, and many alternative creep models can be used to represent the surrounding medium. Also, the stress field generated in the surround-

ing medium can be studied in the latter case. However, unless an extremely fine mesh is used, the 3-dimensional continuum analyses will not yield reliable results for bending moments and shear forces along the pile length. Such fine 3-D meshes would be computationally prohibitive, unless access to super-computers is available. For cases where 3-dimensional analyses of laterally loaded piles are preferable (e.g. when Fish's model represents the creep behaviour of permafrost), an alternate possibility is to develop an ordinary beam element that can be coupled to the surrounding 3-dimensional continuum elements.

An important aspect of the good agreement of the results from the two approaches shown in Figures 5.17–5.20 is the cross-verification of the different types of finite elements and creep formulations developed in this dissertation. More specifically, these results confirm the validity of the plane strain continuum elements, 3-dimensional continuum elements, and simple pile elements on a spring-dashpot system, all considered under the power law creep model. It also confirms the correspondence of incremental schemes of codes ITFECC-A and FEPILE-I. It should be noted that all analyses were based on the assumption that isothermal conditions prevailed along the length of the pile. For non-isothermal conditions, appropriate different values of creep parameters should be used along of the pile length, or a thermorheological theory should be used.

It is noted that several other methods have been proposed to evaluate an appropriate Winkler coefficient for the surrounding medium (Frank 1984, Foriero and Ladanyi 1990). Of these, Frank (1984) proposed an empirical rule given by $(k_w/2a) \approx 1.3E_s$, where $2a$ is the projected length (or diameter) of the pile cross-section.

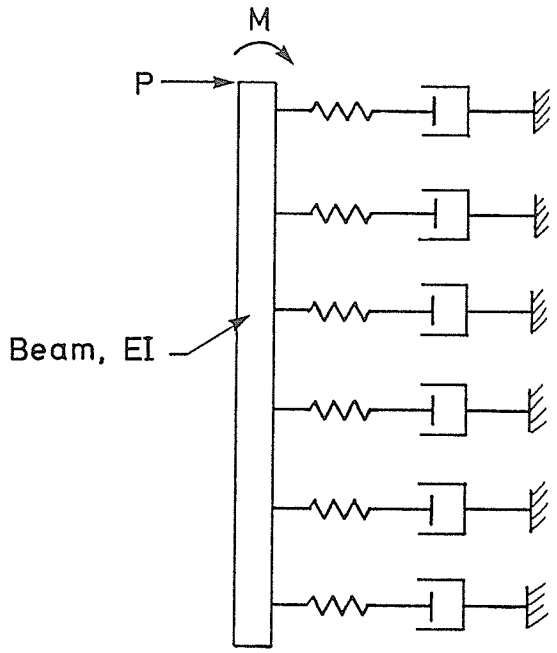

Figure 5.1. Beam (pile) on spring-dashpot system.

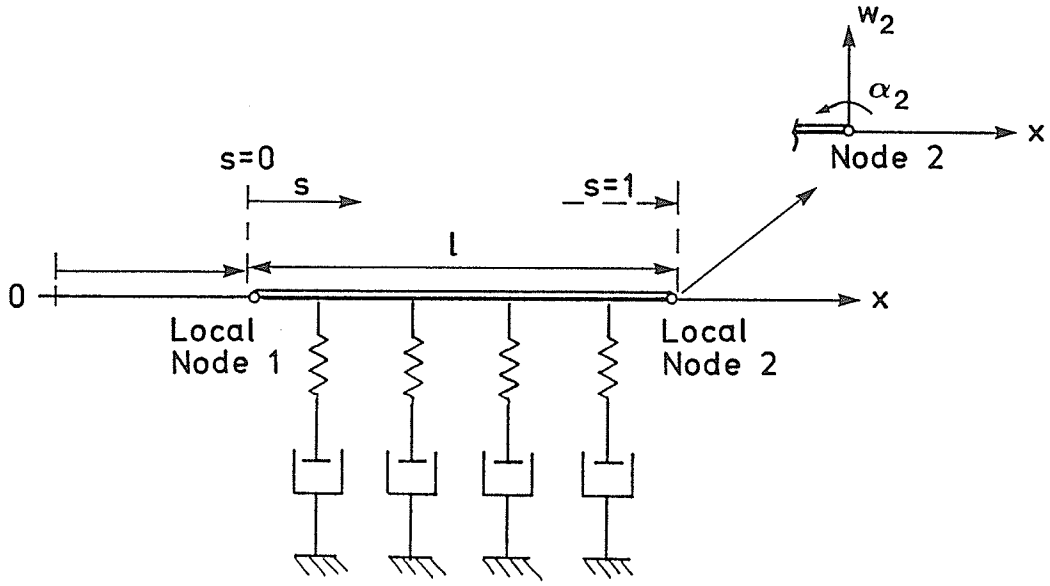

Figure 5.2. A discrete finite element representing part of a beam on a spring-dashpot system.

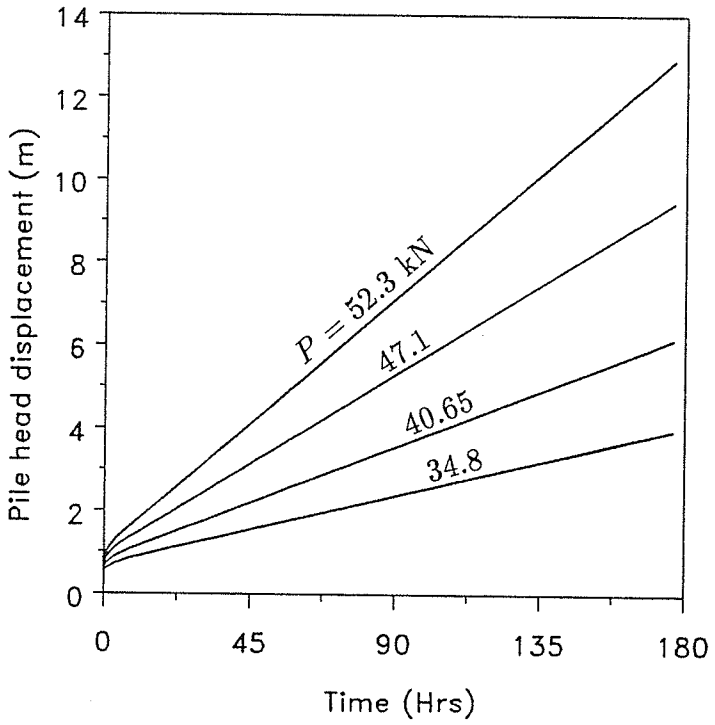

Figure 5.3a. Predicted displacement of laterally loaded bars in ice.

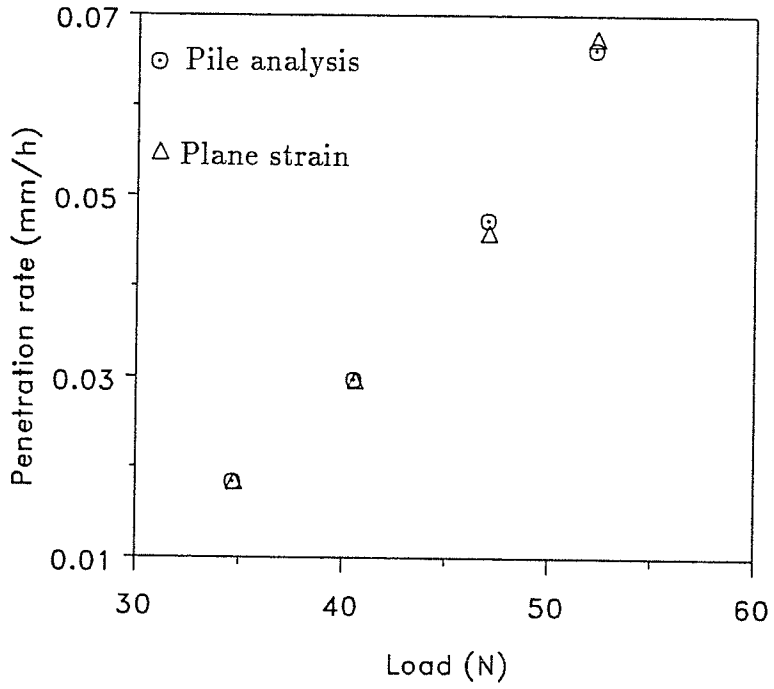

Figure 5.3b. Comparison of rates of displacement predicted using pile analysis and plane strain analysis.

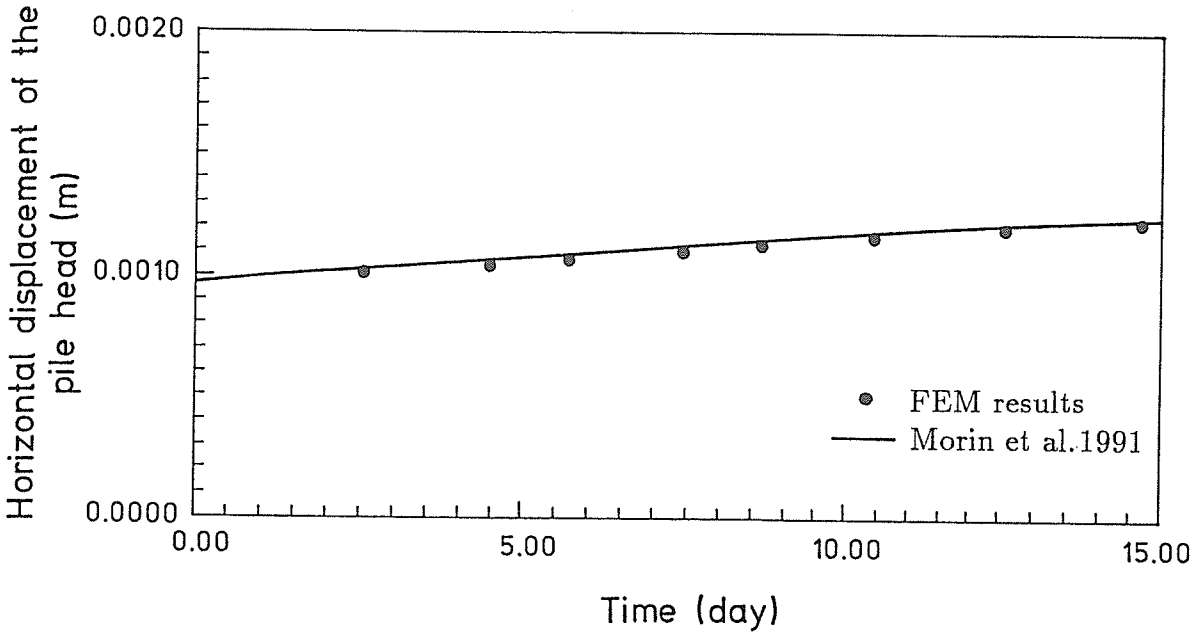

Figure 5.4. Comparison of predicted results for floating pile.

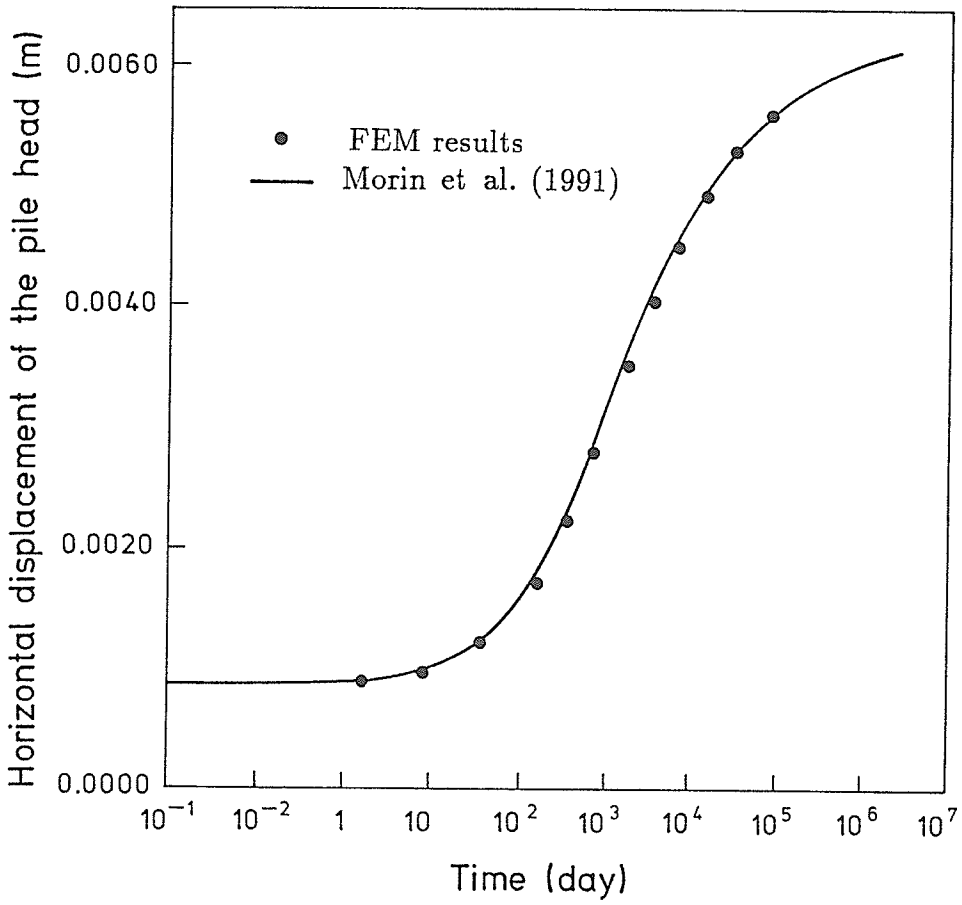

Figure 5.5. Comparison of predicted results for fixed (cantilever) pile.

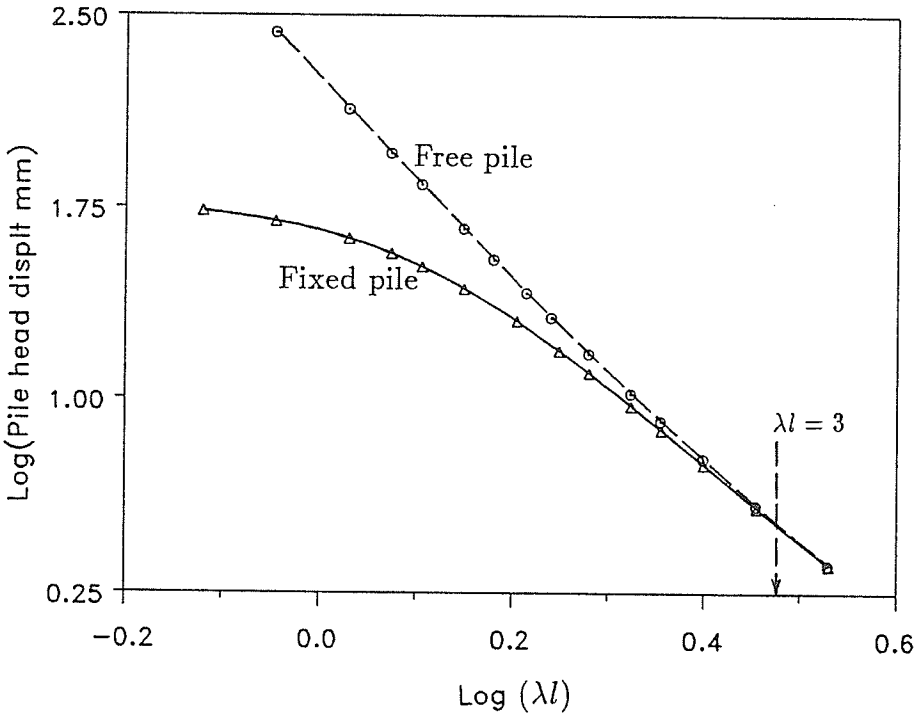

Figure 5.6. Variation of elastic displacement at pile head with λl.

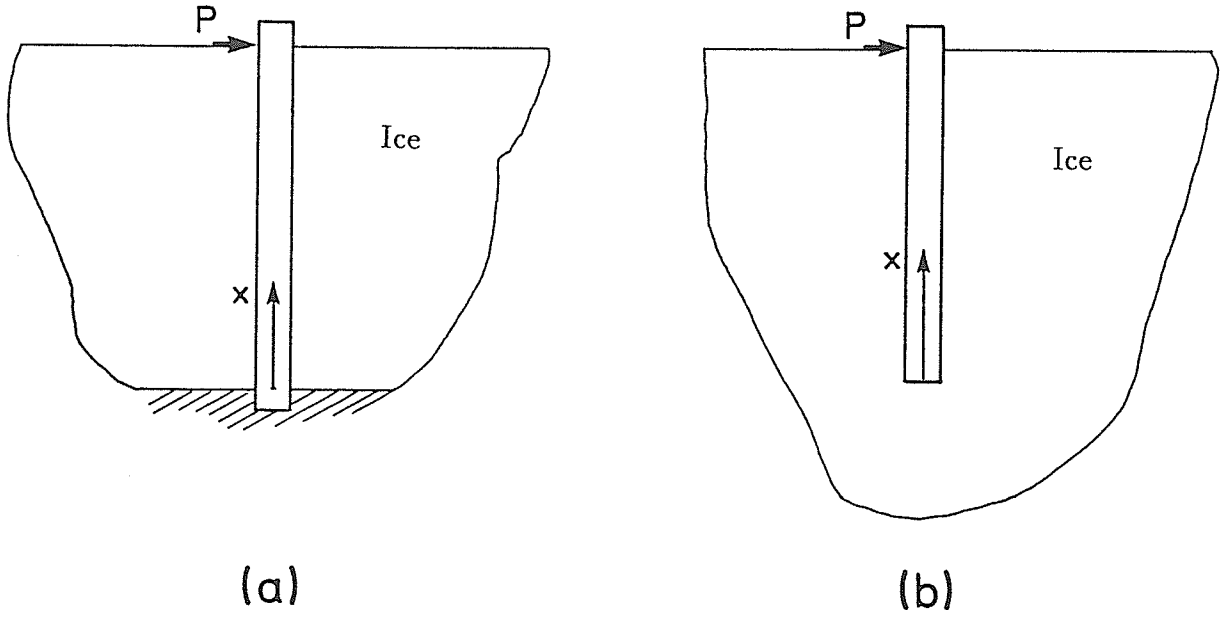

Figure 5.7. Laterally loaded piles in ice: (a). Fixed pile, (b). Floating pile.

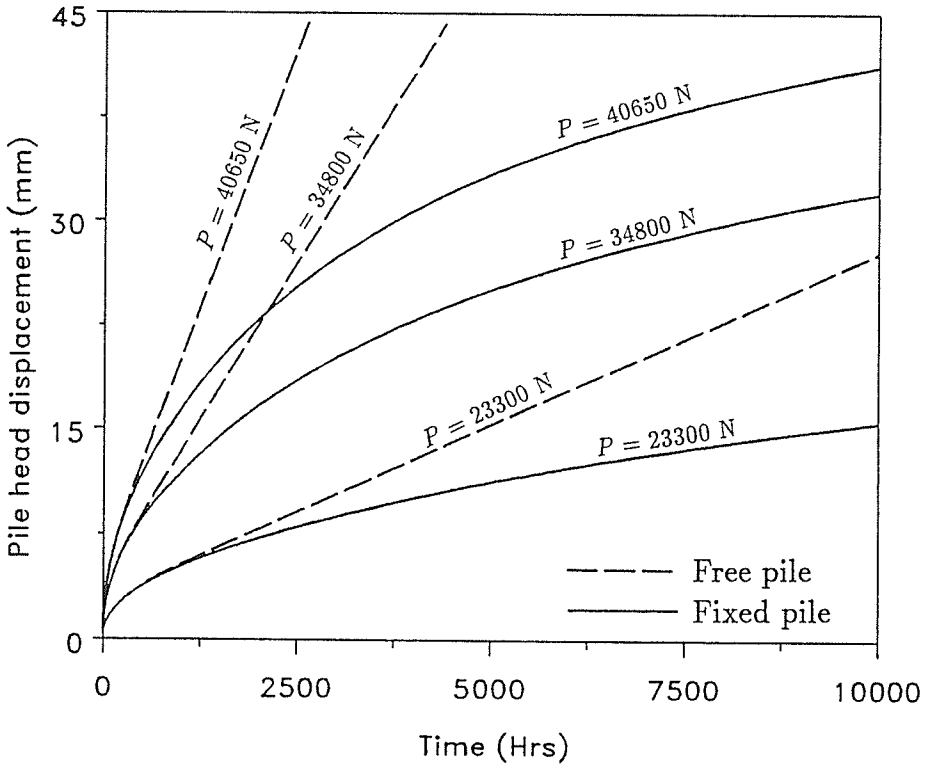

Figure 5.8. Lateral pile head displacements for fixed (cantilever) and free (floating) piles under different loads.

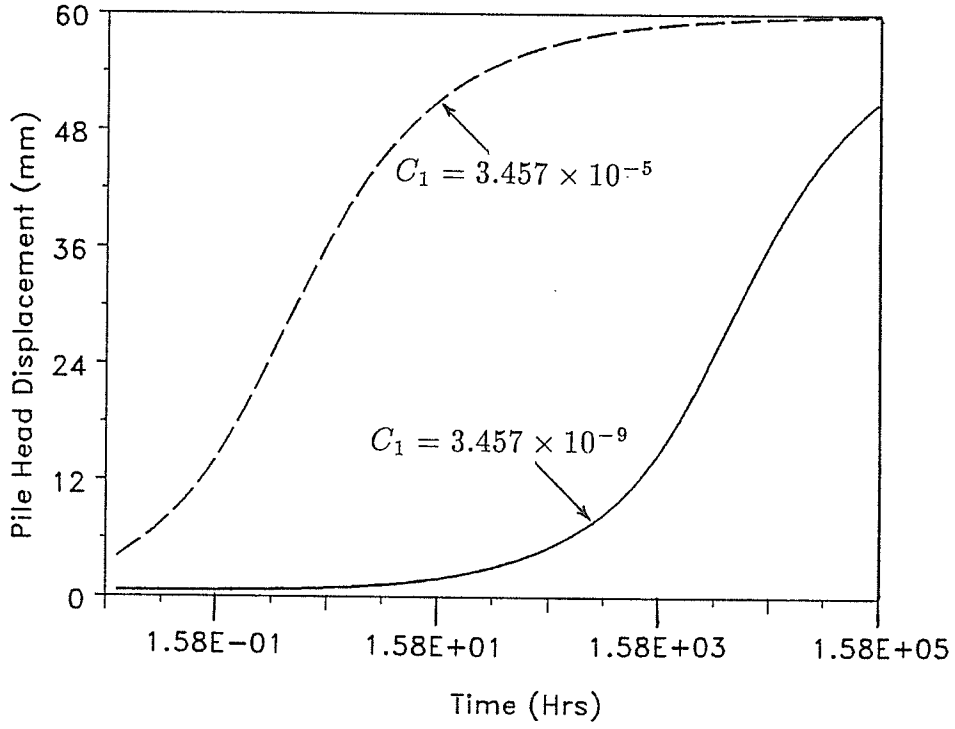

Figure 5.9. Lateral pile-head displacement of a fixed pile for two values of C_1.

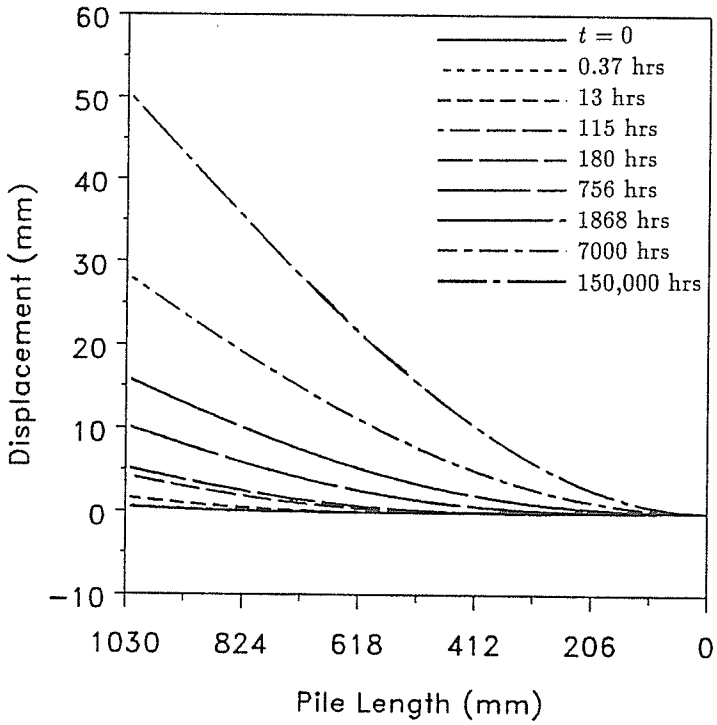

Figure 5.10a. Displacement profiles of a fixed pile with $E = 200$ GPa.

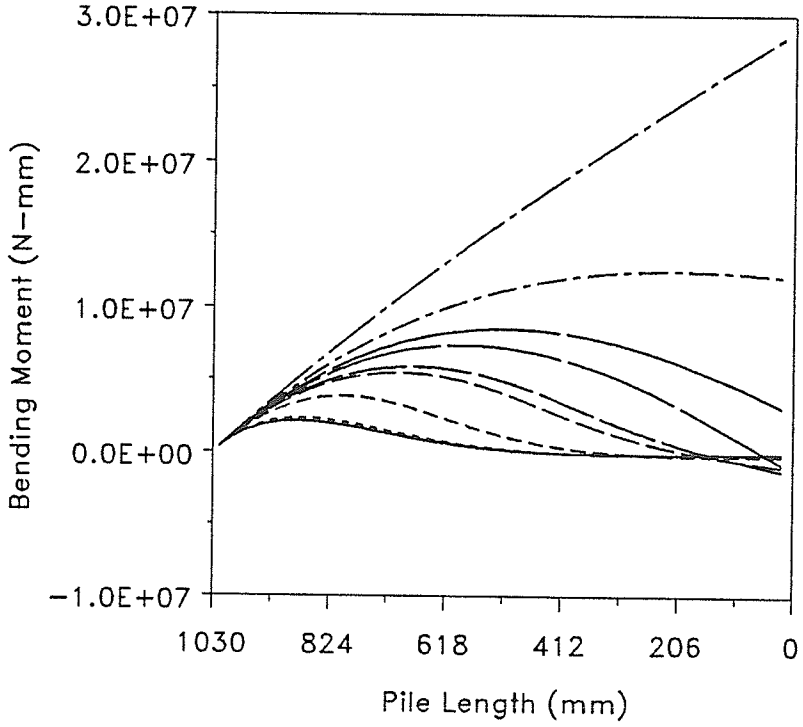

Figure 5.10b. Bending moment profiles of a fixed pile with $E = 200$ GPa.

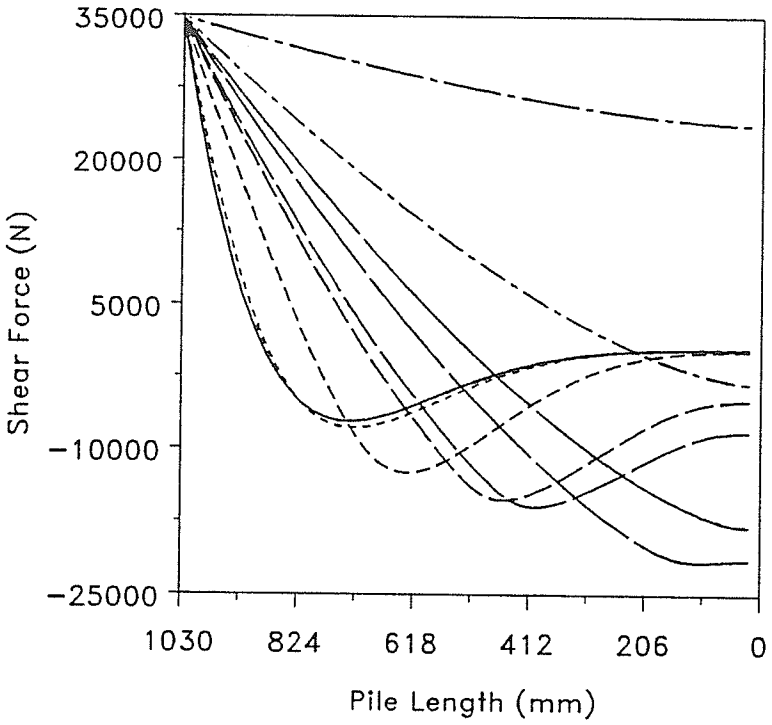

Figure 5.10c. Shear force profiles of a fixed pile with $E = 200$ GPa.

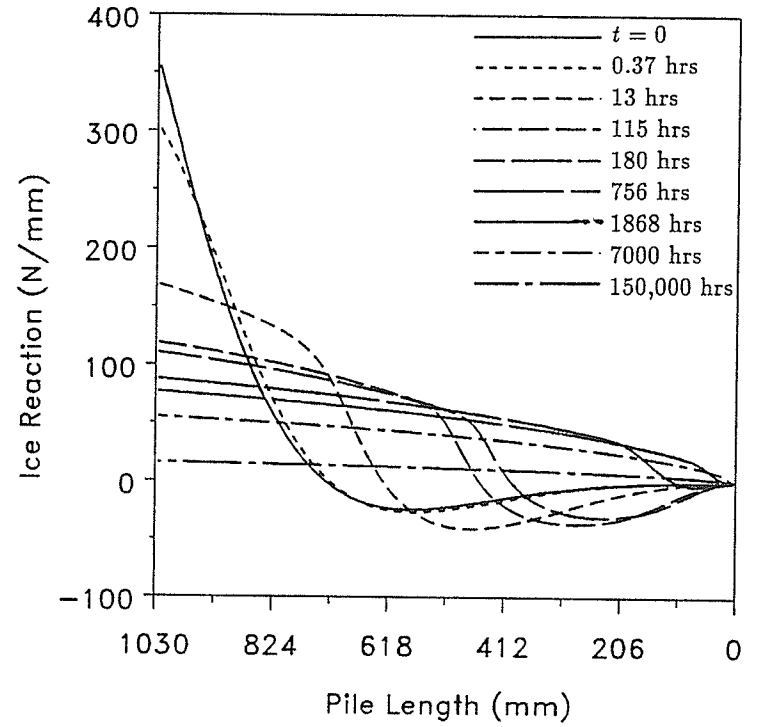

Figure 5.10d. Lateral ice reaction on a fixed pile with $E = 200$ GPa.

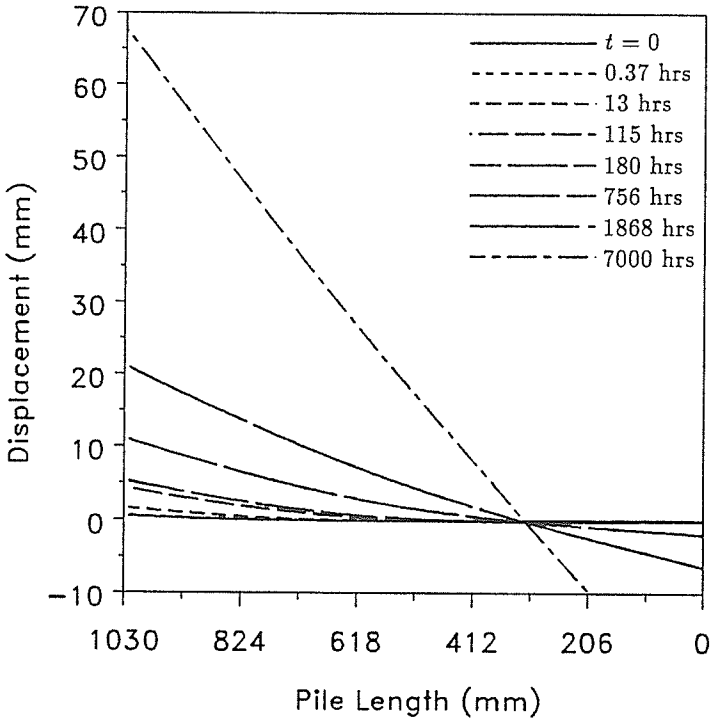

Figure 5.11a. Displacement profiles of a floating pile with $E = 200$ GPa.

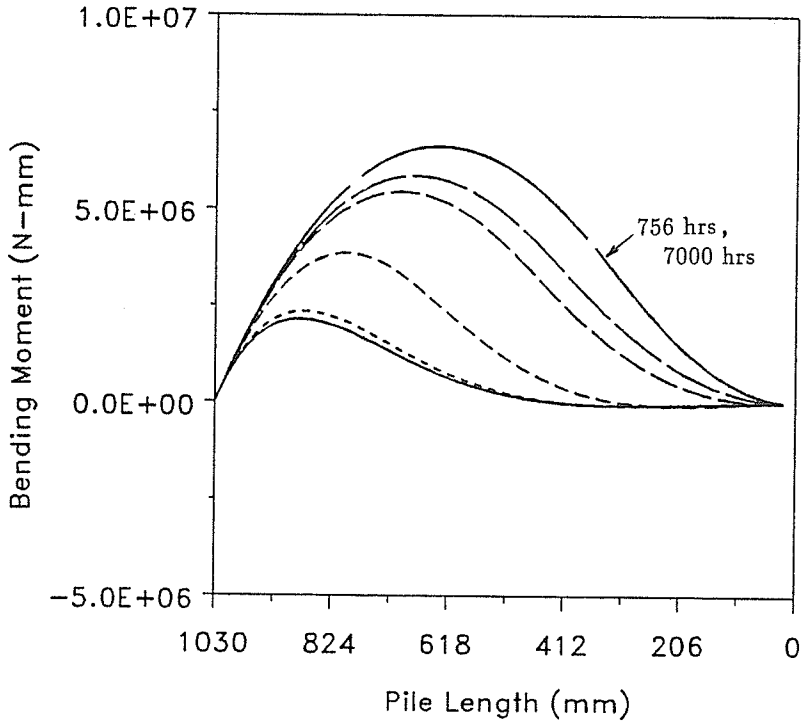

Figure 5.11b. Bending moment profiles of a floating pile with $E = 200$ GPa.

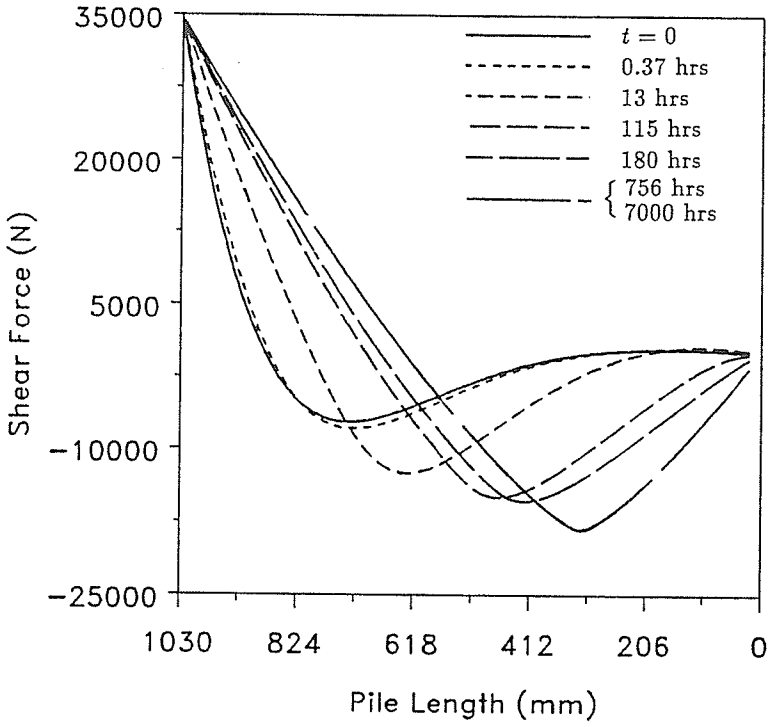

Figure 5.11c. Shear force profiles of a floating pile with $E = 200$ GPa.

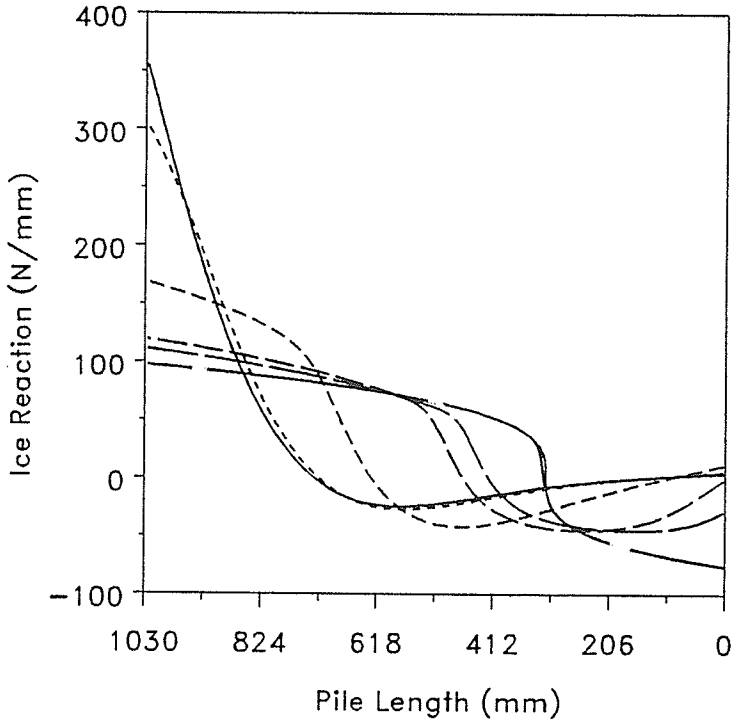

Figure 5.11d. Lateral ice reaction on a floating pile with $E = 200$ GPa.

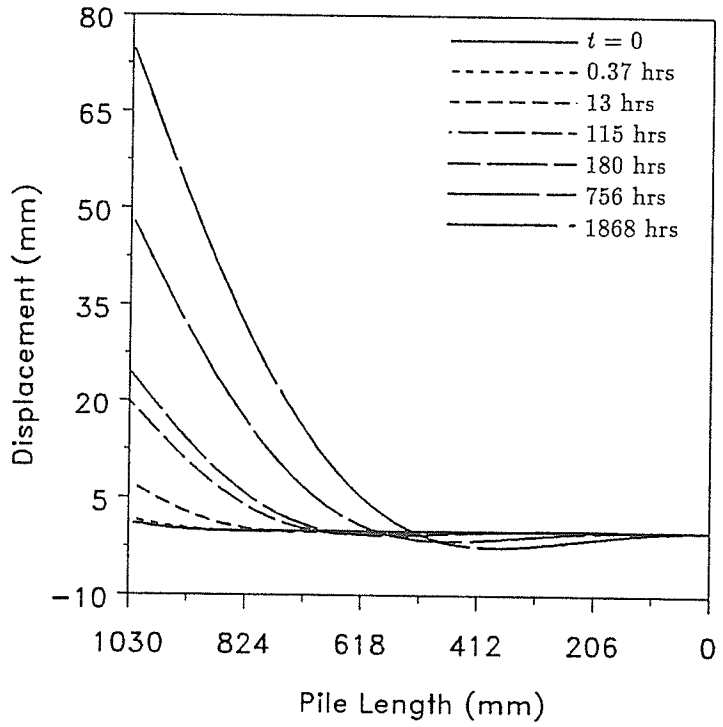

Figure 5.12. Displacement profiles of a fixed pile with $E = 10$ GPa.

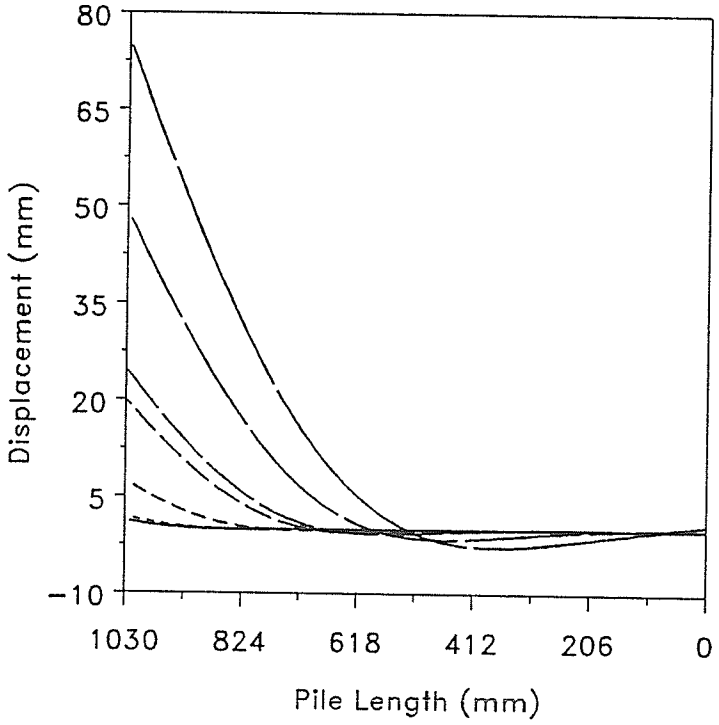

Figure 5.13. Displacement profiles of a floating pile with $E = 10$ GPa.

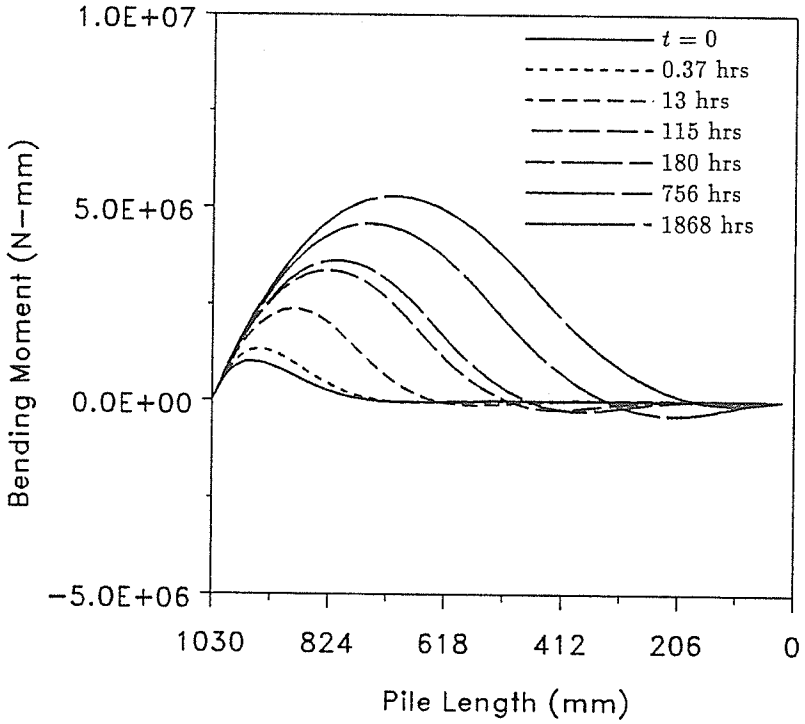

Figure 5.14a. Bending moment profiles of a floating pile with $E = 10$ GPa.

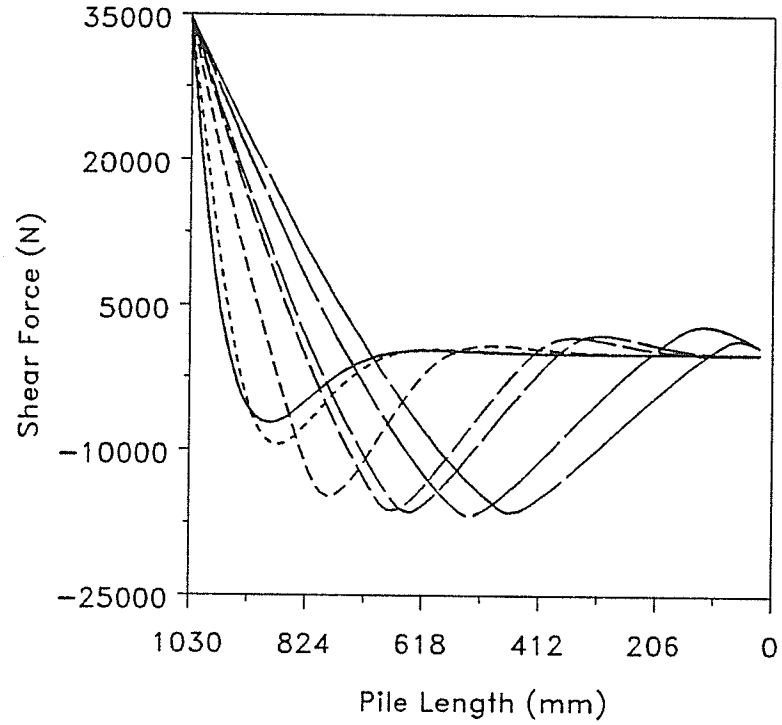

Figure 5.14b. Shear force profiles of a floating pile with $E = 10$ GPa.

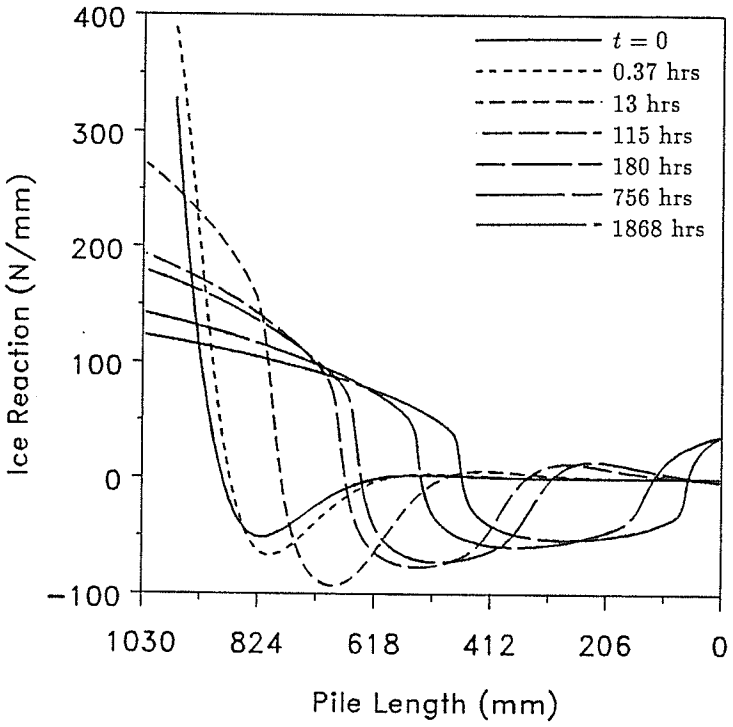

Figure 5.14c. Lateral ice reaction on a floating pile with $E = 10$ GPa.

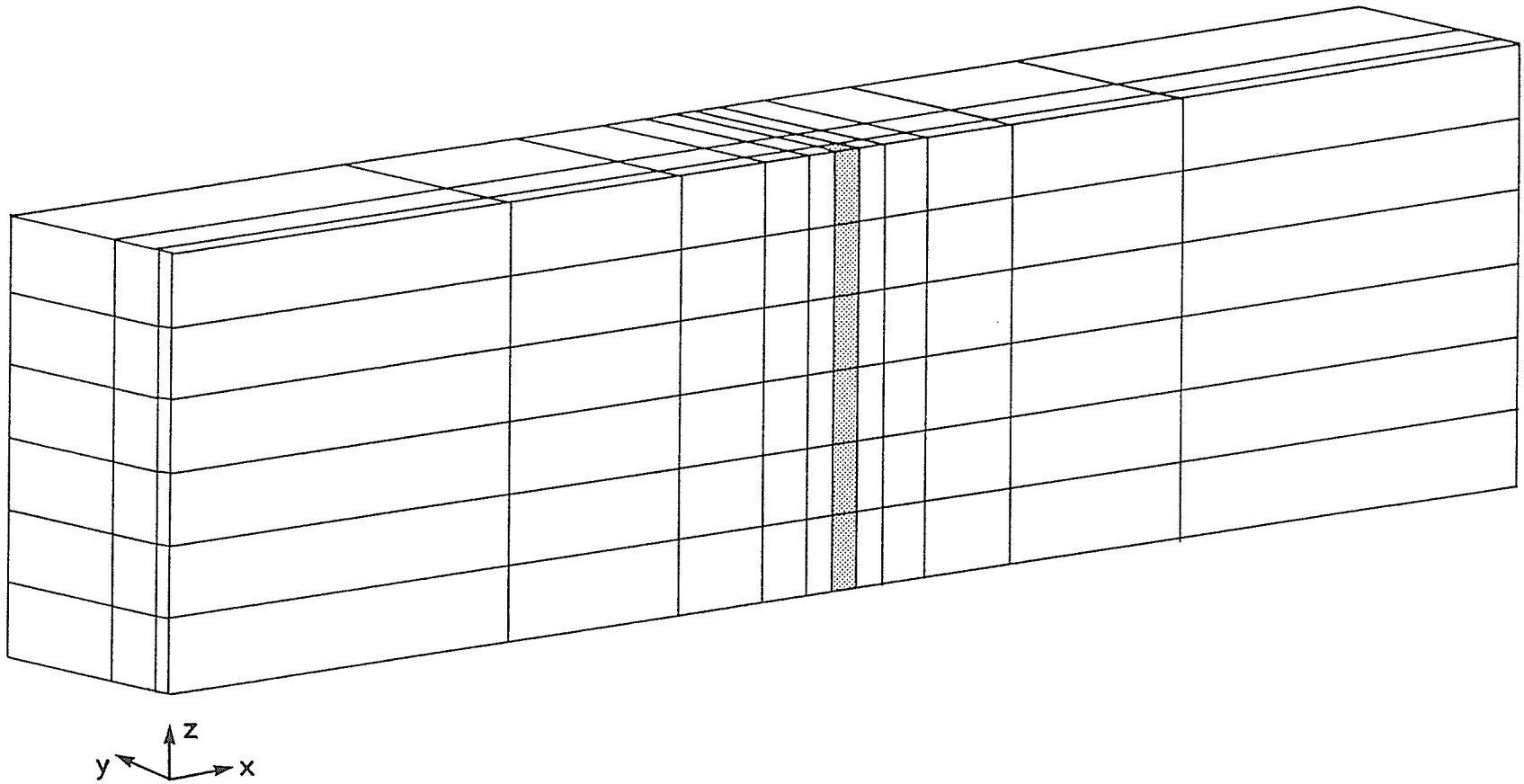

Figure 5.15. 3-D mesh for FE analysis of laterally loaded pile.

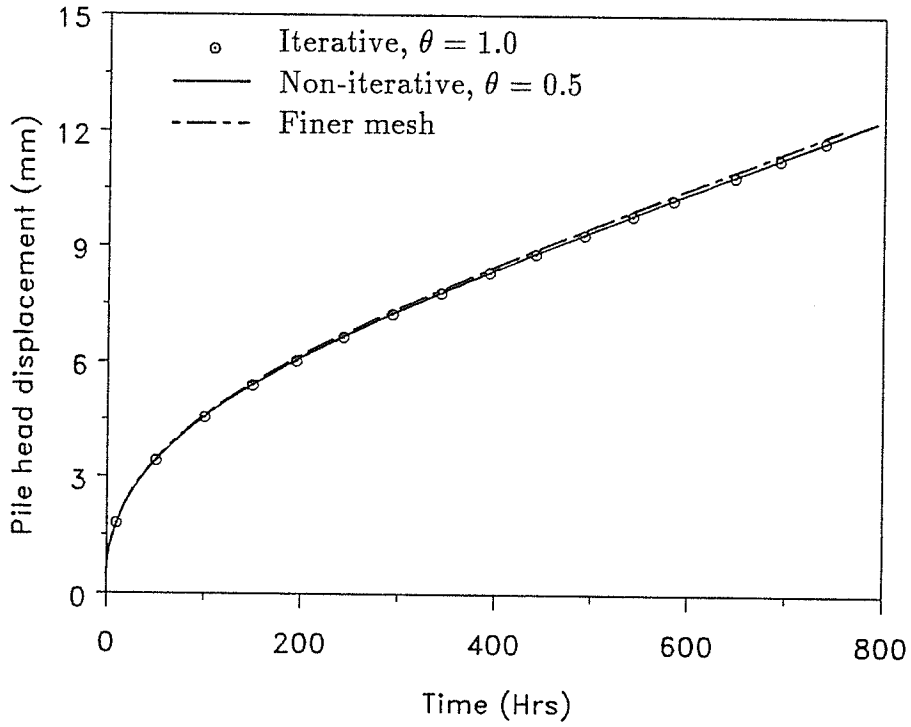

Figure 5.16. Comparison of results from 3-D FE analysis of laterally loaded piles.

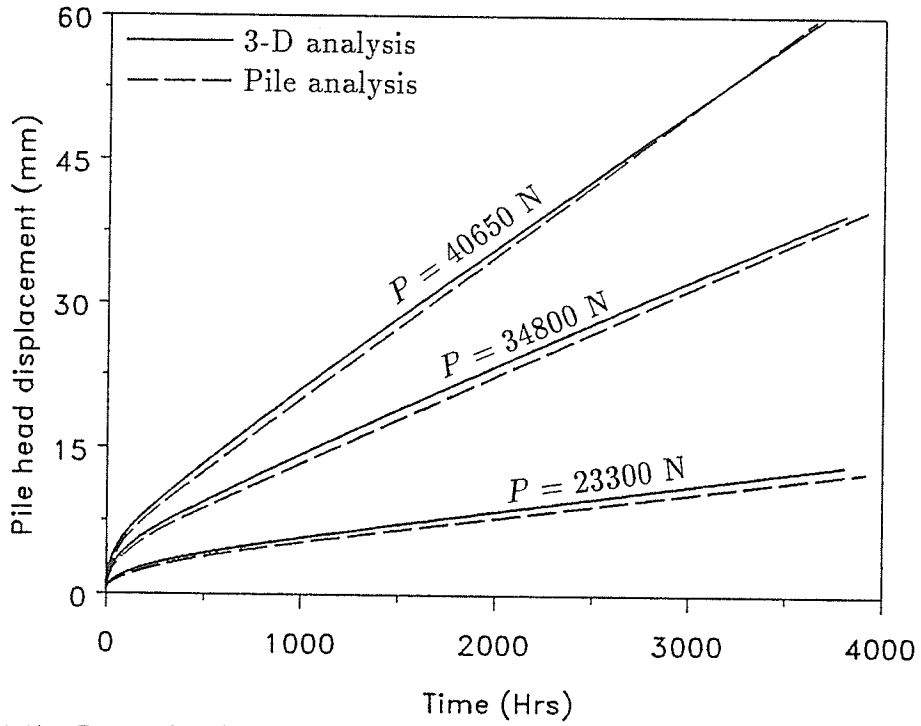

Figure 5.17. Lateral pile head displacement of a floating pile (E_p = 200 GPa) under different loads; Comparison of results using 3-D analysis and pile analysis.

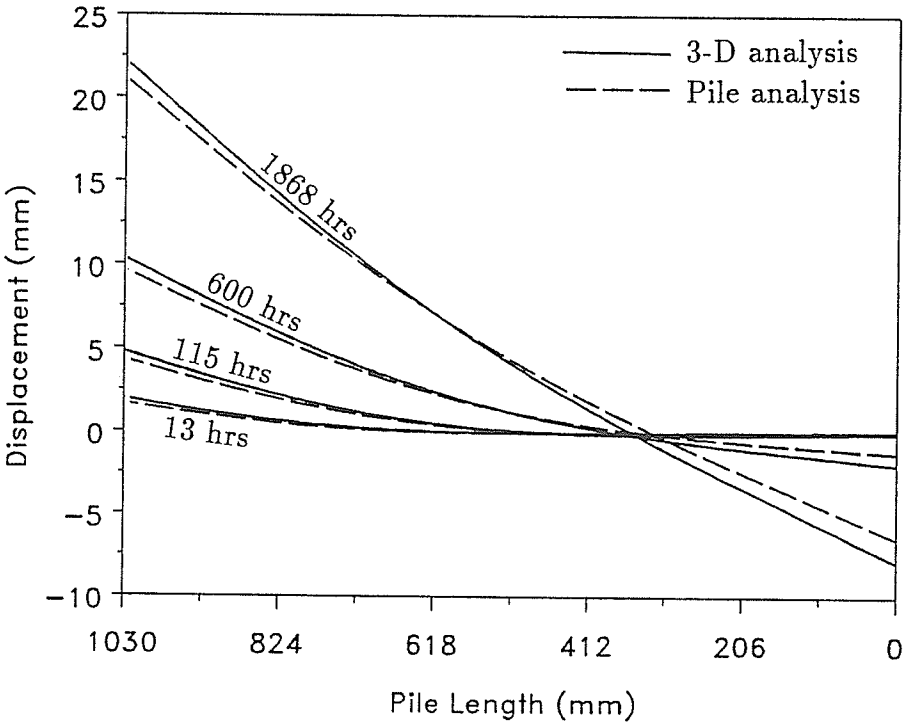

Figure 5.18. Displacement profiles of a floating pile (E_p = 200 GPa) under a lateral load of 34800 N; Comparison of results using 3-D analysis and pile analysis.

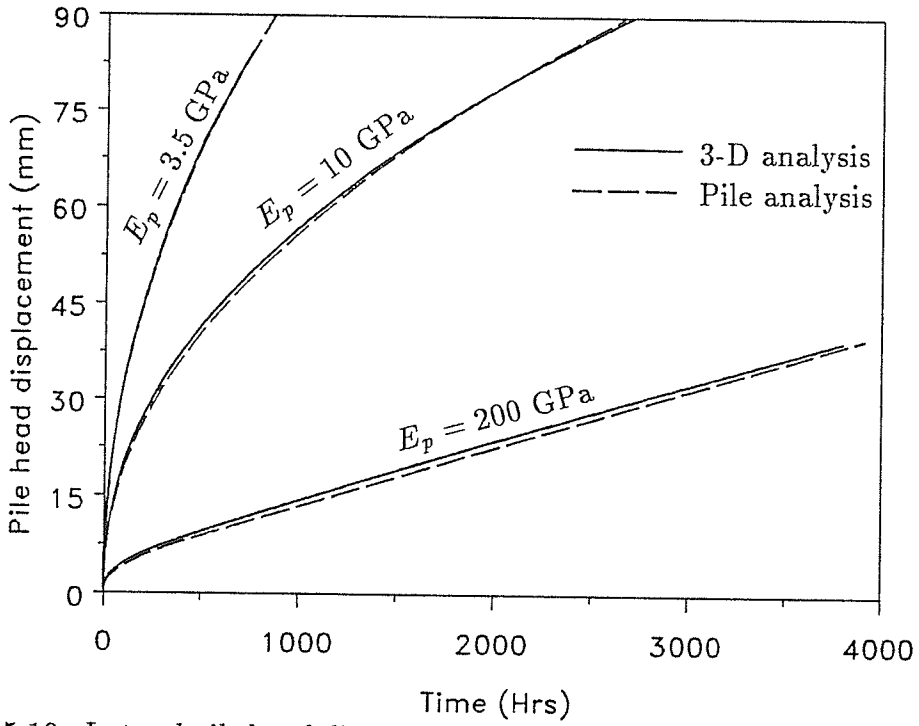

Figure 5.19. Lateral pile head displacement of floating piles with different E_p (under lateral loads of 34800 N); Comparison of results using 3-D analysis and pile analysis.

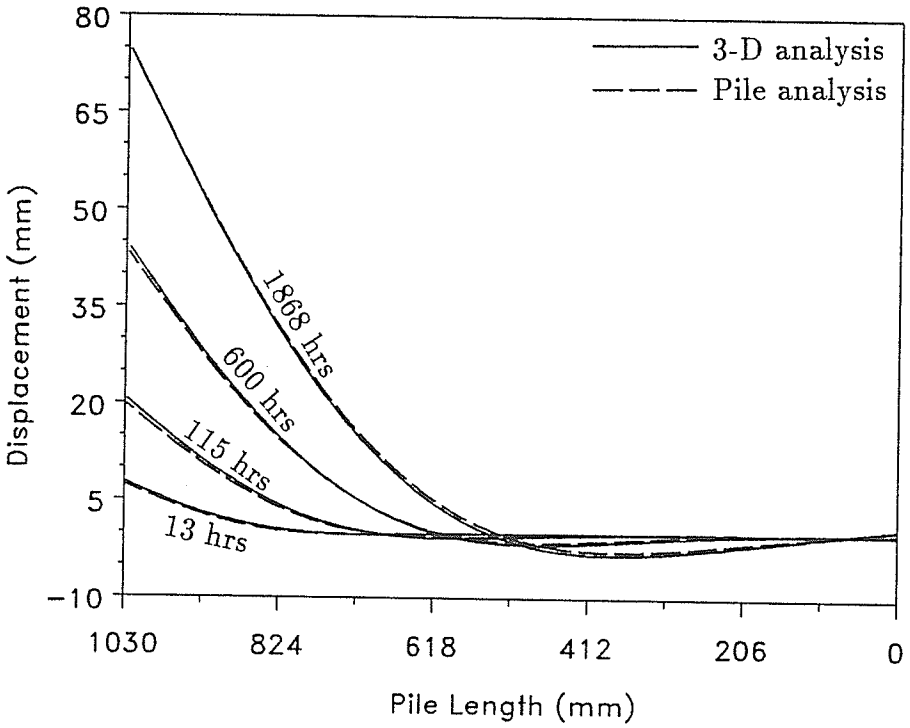

Figure 5.20. Displacement profiles of a floating pile ($E_p = 10$ GPa) under a lateral load of 34800 N; Comparison of results using 3-D analysis and pile analysis.

Chapter 6

NUMERICAL MODELLING OF ADFREEZE/BOND STRENGTH

6.1 General

The adfreeze/bond strength of frozen soils/ice to a foundation element plays an important role in certain classes of structure-frozen media interaction problems. Foremost among these problems are axially loaded piles in icy frozen soils and ice. The general background and experimental observations on the adfreeze strength phenomena in frozen soils and ice were briefly outlined in §2.6 earlier. In this Chapter, a finite element will be developed to represent the general observed behaviour of adfreeze/ bond strength at the interface of frozen soils/ice and the structure. This adfreeze/ bond strength finite element is included in the element library of the computer code ITFECC-A (ref. Chapter 3). It can be incorporated in any two dimensional or axisymmetric finite element mesh, and used to simulate interface behaviour between two different materials according to the interface constitutive assumption described later in §6.2. All developments in this Chapter are made within the limits of the small displacement theory.

Based on the observed interface behaviour involving piles in frozen soils/ ice, a general expression of the following type can be proposed to characterize the steady state creep behaviour at the pile-soil interface (Johnston and Ladanyi 1972, Parameswaran 1979, Soo 1983):

$$\frac{\dot{u}_a}{r} = \bar{A}\,\tau^{\bar{b}}\ , \tag{6.1}$$

where pile displacement rate $\dot{u}_a$ is normalized by the pile radius r, τ is the shear stress at the interface, and $\bar{A}$, $\bar{b}$ are parameters. Equation (6.1) conforms to a power-law type expression, and applies in a direction parallel to the bond interface. However, a more complete constitutive relationship needs to be hypothesized in order to develop an adfreeze/ bond strength element for use in conjunction with different continuum elements developed earlier (see Chapter 3). This relationship should account for the instantaneous response of the interface, followed by the sub-

sequent creep response, and should include the description of the material behaviour along the interface as well as that normal to the interface.

Previous numerical work had been conducted to develop finite elements to model joints and interfaces. Most of these interface elements were proposed for situations where creep is not involved, and in many instances for the purpose of modelling rock joints. Different types of finite elements proposed for interface behaviour include standard finite elements with small thickness (Pande and Sharma 1979), linkage elements which connect the opposite nodes (sometimes known as stick/slip elements and Lagrange elements), finite elements with finite thickness but specifically modified to represent relative motion on the interface (Ghaboussi et al. 1973), and interface/ joint elements of zero thickness (Goodman et al. 1968, Soo 1983, Gens et al. 1988). Out of the latter cases, Gens et al. (1988) formulated a family of zero-thickness finite elements to model interface behaviour using an elasto-plastic constitutive assumption, and Soo (1983) a 4-node adfreeze/bond element of zero thickness to simulate creep behaviour at the interface; Soo's (1983) adfreeze element was developed by modifying the previous joint elements introduced by Goodman et al. (1968) and Ghaboussi et al. (1973).

In the remainder of this Chapter, development of an appropriate adfreeze/ bond strength interface element for creep analysis will be described, by modifying the ideas of Soo (1983) and Gens et al. (1988). This element will then be incorporated in an iterative, time incremental finite element algorithm. Several numerical examples to demonstrate the general behaviour of this interface element will also be presented.

6.2 Material Model for Adfreeze/Bond Strength Element

The material model for the adfreeze element is hypothesized on a basis similar to that of Soo (1983). Since a zero thickness is assumed for the interface element, the constitutive model involves a stress-relative displacement relationship rather than the usual stress-strain relationship in continuum elements. The relative displacement at a given location on the interface is defined as the difference in displacement undergone by two corresponding points on the two surfaces of the interface which

initially had identical coordinates. The material model adopted is described below.

Stress-relative displacement relationship normal to the bond interface is expressed as,

$$\sigma_n = C_n\, d_n \qquad \text{if} \qquad d_n \leq d_{nf}\ , \tag{6.2a}$$

$$\sigma_n = 0 \qquad \text{if} \qquad d_n > d_{nf}\ , \tag{6.2b}$$

where σ_n is the stress normal to bond interface, d_n is the relative displacement in a direction normal to bond interface, d_{nf} is the maximum normal relative displacement that can be sustained, and C_n is a bond modulus for normal stress-relative displacement relations in units of (Force/ Length^2/ Length). When the condition given by equation (6.2b) occurs with separation between the two surfaces of the interface, debonding is said to occur, and the element would be deemed to have vanished. Overlapping of the two surfaces may be predicted during the analysis. If this is the case, it can be remedied by using an artificially high value of C_n or by restraining the normal movement of the two surfaces at the interface by specifying boundary conditions in the local direction normal to the bond interface.

Stress-relative displacement relationship parallel to the bond interface is expressed as,

$$\sigma_s = C_s\,(d_s - d_s^c) \qquad \text{if} \qquad |\sigma_s| \leq \sigma_{sf}\ , \tag{6.3a}$$

$$\sigma_s = \sigma_{pf} \qquad \text{if} \qquad |\sigma_s| \quad \text{exceeded} \quad \sigma_{sf}\ , \tag{6.3b}$$

where σ_s is the shear stress on the bond interface (stress parallel to the interface), d_s is the total relative displacement parallel to the bond interface, d_s^c the creep relative displacement parallel to the bond interface, C_s a bond modulus for the adfreeze strength in units of (Force/ Length^2/ Length), σ_{sf} the failure bond stress (above which the interface stress cannot increase), and σ_{pf} is the post-failure stress (the residual bond stress after $|\sigma_s|$ has exceeded σ_{sf}). For cases of clean shearing (after reaching the peak bond stress), σ_{pf} can be specified as zero. The creep relative displacement above is defined as the difference in creep displacements undergone by two corresponding points on the two surfaces of the interface which initially had

identical coordinates. Numerical values for bond modulii C_s and C_n are available in the literature (Alwahhab 1983, Soo 1983).

The constitutive relationship in equation (6.3a) is analogous to that in equation (3.37) postulated for continuum elements. Therefore, the rheological model assumed for the bond behaviour along the interface is once again characterized by a Maxwell model where a linear elastic spring element is coupled in series with a non-linear dashpot, and thus the total displacement parallel to the interface consists of an elastic and a creep portion. The relevant dashpot (viscous) relationship can in general be given as,

$$\dot{d}_s^c = H\,\sigma_s^h\,t^g\ , \qquad g \leq 0\ , \tag{6.4}$$

where $\dot{d}_s^c$ is the time rate of the creep relative displacement along the bond interface, σ_s is the adfreeze bond stress defined earlier, t is the elapsed time, and H, h, g are parameters to be evaluated by experiments. The value of $g = 0$ signifies a steady-state creep deformation at the interface, and for $g < 0$, the behaviour is of attenuating type. The parameters H and h are temperature dependent, and some appropriate numerical values for these parameters under steady state situations ($g = 0$) are available in the literature (e.g. Alwahhab 1983, Soo 1983). Equation (6.4) is a power-law type expression, but the element developed (see §6.3) using the above model can be used along with continuum elements conforming to any time incremental creep model.

6.3 Formulation of Interface Element for Adfreeze/Bond Strength

The interface element for adfreeze/bond strength developed here has the following features:

i. Iso-parametric formulation.

ii. Four/six node element.

iii. Zero thickness.

iv. Constitutive behaviour defined as a stress-relative displacement relationship.

The typical interface element in local coordinate system designated by (s, n)

is shown in Figure 6.1. As shown in the figure, the element has local node numbers 1,2,3 on one surface and local node numbers 4,5,6 on the other surface. The mid-plane points, designated by i, j, k, are as shown in Figure 6.1. The relative displacements in the interface are evaluated at these mid-plane points, and are accepted to be equal to the difference between the displacements of the two adjacent nodes. Thus for example, relative displacement in a given direction at mid-plane point i is the difference of displacements in that direction at nodes 4 and 1. For the four node interface element, local nodes 3 and 6, and the mid-plane point k, would vanish in Figure 6.1.

The interpolation of coordinates and displacements in the local coordinate s parallel to the interface is achieved by standard one-dimensional shape functions N_l (see Appendix G). For the 6-node element, $[N]$ is 1×3 row matrix representing the quadratic shape functions, while for the 4-node element, $[N]$ is a 1×2 matrix representing linear shape functions. No interpolation is considered in the local normal (n) direction. Thus the interpolation of global coordinates r or displacements u, respectively, can be achieved by,

$$r = [N(s)]r_l \ , \qquad \text{and} \qquad u = [N(s)]u_l \ , \tag{6.5}$$

where subscript l denotes a relevant quantity at a particular local node number l, and the expansion of l takes place on either of the two surfaces (either l= 1,2,3 or l= 4,5,6).

The orientation of the local coordinate system with respect to the global coordinate frame is of importance, and is signified by the angle ϑ as depicted in Figure 6.2. It is convenient to define the following transformation matrix at this point:

$$[G] = \begin{bmatrix} \cos\vartheta & \sin\vartheta \\ -\sin\vartheta & \cos\vartheta \end{bmatrix} \ . \tag{6.6}$$

Matrix $[G]$ maps vectors in the global coordinate frame to the local coordinate system. A notation $[G]_l$ would denote that the matrix $[G]$ is being considered at a point l.

The stress-relative displacement relationships of equations (6.2) and (6.3) can

be written in matrix notation, for a given point on the mid-plane, as,

$$\boldsymbol{\sigma} = [C]\,\mathbf{d} - C_s\,\mathbf{d}^c \ , \tag{6.7}$$

where,

$$\boldsymbol{\sigma} = \left\{ \begin{array}{c} \sigma_s \\ \sigma_n \end{array} \right\} \ ; \quad [C] = \left[\begin{array}{cc} C_s & 0 \\ 0 & C_n \end{array} \right] \ ; \quad \mathbf{d} = \left\{ \begin{array}{c} d_s \\ d_n \end{array} \right\} \ ; \quad \mathbf{d}^c = \left\{ \begin{array}{c} d_s^c \\ 0 \end{array} \right\} \ . \tag{6.8}$$

In above, $\boldsymbol{\sigma}$, $\mathbf{d}$, $\mathbf{d}^c$ are defined in the local coordinate system (s, n), $\mathbf{d}^c$ is the vector of creep relative displacements, $\boldsymbol{\sigma}$ the stress vector, $\mathbf{d}$ the vector of relative displacements, and all other notations are as before. The local relative displacements $\mathbf{d}$ at the mid-plane of an element are related to the global nodal displacement vector $\mathbf{a}$ of the element by a geometry matrix $[M]$ defined as:

$$\mathbf{d} = [M]\,\mathbf{a} \ . \tag{6.9}$$

The geometry matrix $[M]$ is given for a joint element with m nodes on each surface of the interface (a total of $2m$ nodes for the entire element) as,

$$[M] = \langle\ -[M]_1,\ -[M]_2,\ \ldots - [M]_m,\ [M]_1,\ [M]_2,\ \ldots [M]_m\ \rangle \ , \tag{6.10}$$

where

$$[M]_l = N_l\,[G]_l \ , \tag{6.11}$$

where $[M]$ is a 2×12 matrix for a 6-node element, or a 2×8 matrix for a 4-node element. For the above formulations, it was assumed that the relative displacements are obtained by substracting the displacements at the nodes identified with smaller (local) numbers from those at the corresponding nodes identified with larger number (for example, in Figure 6.1, substract displacements at local node 1 from those at node 4, etc.). Detailed derivation of equations (6.10) and (6.11) for the 6-node element is given in Appendix G.

The virtual work principle can be employed to develop the finite element algorithm for the above interface element. The elemental equilibrium equations arising from the interface elements are assembled into the global system of equations containing the contribution from the rest of the domain (i.e. from continuum elements).

Assume that a set of compatible virtual nodal displacements $\Delta\mathbf{r}$ is applied to the material domain, which generates a virtual relative displacement field $\Delta\mathbf{d}_v$ at the mid-plane of the interface. In view of equation (6.9), the vectors $\Delta\mathbf{d}_v$ and $\Delta\mathbf{r}$ are related to each other by,

$$\Delta\mathbf{d}_v = [M]\,\Delta\mathbf{r}\ . \tag{6.12}$$

Assuming that each adfreeze element was in equilibrium under a stress field $\boldsymbol{\sigma}$ at its mid-plane and an equivalent set of nodal loads denoted by $\mathbf{P}_e$, the internal virtual work due to the virtual displacement field would be:

$$W_I = \sum_e \int_{A_e} \Delta\mathbf{d}_v^T\,\boldsymbol{\sigma}\,dA_e\ , \tag{6.13}$$

where A_e denotes surface area of each interface element, and $\sum$ denotes the summation over all adfreeze elements. Equivalent external work will be given as,

$$W_E = \sum_e \Delta\mathbf{r}^T\,\mathbf{P}_e\ . \tag{6.14}$$

By the application of the principle of virtual work ($W_I = W_E$), and in view of equations (6.12), (6.9) and (6.7), above equations (6.13) and (6.14) yield the following equilibrium equation for the entire interface region:

$$\sum_e \int_{A_e} [M]^T[C][M]\mathbf{a}\,dA_e - \sum_e C_s \int_{A_e} [M]^T\,\mathbf{d}^c\,dA_e - \sum_e \mathbf{P}_e = \mathbf{0}\ , \tag{6.15}$$

The summation sign $\sum$ and subscript e can be dropped from the equilibrium equation (6.15) without loss of generality, and the resulting equation can be written at a time t_k as,

$$\int_A [M]^T[C][M]\mathbf{a}_k\,dA - C_s \int_A [M]^T\,\mathbf{d}_k^c\,dA - \mathbf{P}_k = \mathbf{0}\ , \tag{6.16}$$

or equivalently (in view of equations 6.7 and 6.9) as,

$$\chi_k = \int_A [M]^T\,\boldsymbol{\sigma}_k\,dA - \mathbf{P}_k = \mathbf{0}\ , \tag{6.17}$$

where subscript k denotes that the relevant quantity is being considered at time t_k. Assuming that the solutions $(\mathbf{a}_k, \boldsymbol{\sigma}_k)$ at time t_k are known, an iterative creep algorithm can be used to solve for the unknowns at time t_{k+1}, ie. $t_{k+1} = t_k + \Delta t_k$. As in §3.4 earlier, Newton-Raphson iterative procedure is applied to obtain solutions at time t_{k+1}. At the nth iteration at t_{k+1}, at which the solutions may not have converged yet, equation (6.17) may be written as,

$$\boldsymbol{\chi}^n_{k+1} \;=\; \int_A [M]^T \boldsymbol{\sigma}^n_{k+1}\, dA \;-\; \mathbf{P}_{k+1} \;\neq\; \mathbf{0}, \tag{6.18}$$

where the unequal sign is used since $\boldsymbol{\sigma}^n_{k+1}$ is not a converged solution, and superscript n denotes the nth iterative cycle. In view of equations (6.7) and (6.9), the difference between the stresses at this iterative cycle and the previous time t_k can be written as,

$$\boldsymbol{\psi}^n_{k+1} \;=\; \boldsymbol{\sigma}^n_{k+1} - \boldsymbol{\sigma}_k - [C]\,[M]\,\{\mathbf{a}^n_{k+1} - \mathbf{a}_k\} + C_s\,\Delta t_k\,\boldsymbol{\alpha}(\boldsymbol{\sigma}^n_{k+\theta}) \;\neq\; \mathbf{0}, \tag{6.19}$$

where, the unequal sign is used for same reasons as earlier, $\boldsymbol{\alpha}$ denotes the vector of rate of creep relative displacements defined by the time derivatives of equations $(6.8)_4$ and (6.4), which can be rewritten as,

$$\boldsymbol{\alpha} = \dot{\mathbf{d}}^c\,(\boldsymbol{\sigma}, t)\;, \tag{6.20}$$

and

$$\mathbf{d}^c_{k+1} - \mathbf{d}^c_k = \Delta t_k \cdot \boldsymbol{\alpha}(\boldsymbol{\sigma}^n_{k+\theta})\;, \tag{6.21a}$$

where

$$\boldsymbol{\sigma}^n_{k+\theta} \;=\; (1-\theta)\,\boldsymbol{\sigma}_k + \theta\,\boldsymbol{\sigma}^n_{k+1}\;, \qquad (0 \le \theta \le 1)\;. \tag{6.21b}$$

As earlier (see §3.4), use of $\theta = 1,\ 1/2$ or 0 in above results in, respectively, a fully implicit iterative, an implicit-explicit (where iterations may or may not be incorporated), or a fully explicit, numerical scheme. Curtailed Taylor expansion of equations (6.18) and (6.19) yield the following expressions, respectively, which are assumed to have converged at the present $(n+1$ th) iteration:

$$\boldsymbol{\chi}^{n+1}_{k+1} \;=\; \boldsymbol{\chi}^n_{k+1} \;+\; \int_A [M]^T\,\Delta\boldsymbol{\sigma}^n_{k+1}\, dA\;, \tag{6.22}$$

$$\psi_{k+1}^{n+1} \;=\; \psi_{k+1}^{n} \;+\; \Delta\boldsymbol{\sigma}_{k+1}^{n} - [C]\,[M]\,\Delta\mathbf{a}_{k+1}^{n} + C_s\,\Delta t_k\,[S]^n\,\theta\,\Delta\boldsymbol{\sigma}_{k+1}^{n}\;, \qquad (6.23)$$

where,

$$[S]^n \;=\; \left(\frac{\partial\boldsymbol{\alpha}}{\partial\boldsymbol{\sigma}}\right)_{k+\theta}^{n}\;.$$

By substituting equations (6.18) and (6.19) in equations (6.22) and (6.23), the following equations are finally obtained to solve for the iterative corrections of stresses $\Delta\boldsymbol{\sigma}_{k+1}^{n}$ and displacements $\Delta\mathbf{a}_{k+1}^{n}$:

$$\Delta\boldsymbol{\sigma}_{k+1}^{n} = [\bar{C}]^n\Big[[M](\Delta\mathbf{a}_{k+1}^{n}+\mathbf{a}_{k+1}^{n}-\mathbf{a}_k)-[C]^{-1}(\boldsymbol{\sigma}_{k+1}^{n}-\boldsymbol{\sigma}_k)-[C]^{-1}\,C_s\,\Delta t_k\,\boldsymbol{\alpha}(\boldsymbol{\sigma}_{k+\theta}^{n})\Big], \qquad (6.24)$$

and,

$$\int_A [M]^T[\bar{C}]^n[M]\,\Delta\mathbf{a}_{k+1}^{n}\,dA = \int_A [M]^T[\bar{C}]^n[C]^{-1}\Big\{(\boldsymbol{\sigma}_{k+1}^{n}-\boldsymbol{\sigma}_k) + C_s\Delta t_k\,\boldsymbol{\alpha}(\boldsymbol{\sigma}_{k+\theta}^{n})\Big\}\,dA$$
$$- \int_A [M]^T[\bar{C}]^n[M](\mathbf{a}_{k+1}^{n}-\mathbf{a}_k) - \int_A [M]^T\boldsymbol{\sigma}_{k+1}^{n}\,dA + \mathbf{P}_{k+1}\;, \qquad (6.25)$$

where matrix $[\bar{C}]^n$ is given by,

$$[\bar{C}]^n \;=\; [C]\Big[[I] + C_s\,\Delta t_k[S]^n\theta\Big]^{-1}\;, \qquad (6.26)$$

where $[I]$ is the identity matrix. The process of updating the solutions is identical to that given by equation (3.52), and the solution procedure is exactly as described in §3.4 following the equation (3.52). It was necessary for the solution procedure here to be identical to that described under the time incremental solution scheme for continuum elements described earlier (§3.4, Chapter 3), since these adfreeze elements were developed to model the interface between two continuum domains. This interface element is suitable for incorporation in any 2-dimensional FE mesh that can be handled by the code ITFECC-A. The integral over the interface area A (see equation 6.25) was arranged appropriately so that the same element subroutine can be used for plane stress/strain as well as axisymmetric analyses (this is achieved by specifying a control parameter in element properties).

An additional subroutine was attached to the element subroutine to check for the various limiting conditions in the material model. Once limiting stresses are

reached, the stresses generated in excess of these limiting values are redistributed to the relevant nodes. In case of debonding at the interface, the relevant element is made to vanish by employing a null local stiffness matrix. Explicit forms of different matrices and expressions encountered above can be found in Appendix G.

6.4 Demonstration Problems Using Adfreeze/Bond Element

In order to demonstrate the validity of the numerical implementation of the constitutive relations given by equations (6.4), (6.7) and (6.8), a problem was simulated where a steel rod of circular cross-section was pulled out of a cylinder of frozen sand in which it was embedded. This was similar to a problem considered by Soo (1983) as far as the material properties and problem configuration were concerned, although weighting functions to account for different creep properties of frozen soils in tension and compression, as used by Soo (1983), were not used here. The configuration of the problem is as shown in Figure 6.3. The frozen soil cylinder had a diameter of 6 inches, and a height of 6 inches. The steel rod had a diameter of 0.625 inches, and was embedded along the central axis of the cylinder, so that the problem had axial symmetry. A load of 250 lbs was applied downwards at the bottom of the rod, pulling the latter out of the frozen soil cylinder which was restrained against vertical movement over its bottom surface. The problem domain was discretized by using 32 axisymmetric elements (8 nodes per element) to model ice, 8 axisymmetric elements to model the steel rod, and 8 adfreeze elements (6-nodes per element) to model the interface between the ice and steel rod. (The mesh used was similar to that shown in Figure 6.6, which is actually applicable to another problem discussed later in this section). Assuming that the problem was considered at a temperature of $-10°$C, the following material properties were selected based on the information of Alwahhab (1983) and Soo (1983):
For bond interface (adfreeze elements):

$$\begin{aligned} &C_s = C_n = 0.334 \times 10^6 \text{ lb/in}^2\text{/in}, \\ &H = 0.77085 \times 10^{-8} \text{ for } \sigma_s \text{ in psi and } \dot{d}_s^c \text{ in inch/hour}, \\ &h = 2.75, \qquad g = 0 \text{ (steady creep)}. \end{aligned} \tag{6.27a}$$

For frozen soil (power law creep):

$$
\begin{aligned}
&E = 0.88 \times 10^6 \text{ psi} , \qquad \nu = 0.47 , \\
&A = 0.10527 \times 10^{-6} \ (1/\text{psi})^B \, \text{hr}^{-C} , \\
&B = 1.61 , \qquad C = 0.26 .
\end{aligned}
\tag{6.27b}
$$

For steel rod :

$$
E = 0.3 \times 10^8 \text{ psi} , \qquad \nu = 0.25 . \tag{6.27c}
$$

In above, parameters for adfreeze elements are as defined in equations (6.4), (6.7) and (6.8), A, B, and C are the usual parameters for the power law creep model used for the frozen soil, and E and ν denote the Young's modulus and Poisson's ratio, respectively, of the relevant material. In addition to values in equations (6.27a), a relatively higher magnitude of 100 psi was used for σ_{sf} and σ_{pf}.

The problem was simulated using the code ITFECC-A under an iterative scheme with $\theta = 1.0$. The initial time step of 0.01 hours was gradually increased to the range of 1 hour as the analyses progressed. For the purpose of evaluation of stiffness and stresses, 4 Gauss points were used for 8-node axisymmetric elements and 3 Gauss points for the adfreeze elements. The vertical displacement at two initially coincident points **I** and **J** on the two surfaces at the interface are presented in Figure 6.4; point **I** is located at the uppermost end of the steel rod at the interface, while point **J** is located on the frozen soil domain (at the interface), and had coordinates identical to those of point **I** in the undeformed stage. Separation of the points **I** and **J** on the two surfaces as time increases is clearly visible in Figure 6.4. Also, the displacement of the steel rod takes place at a steady rate, as governed by $g = 0$ in equation (6.27a).

The profiles of adfreeze (or bond, shear) stress σ_s along the interface at different times are as shown in Figure 6.5. With increasing time, the adfreeze stress attains a uniform, steady-state value of 21.22 psi throughout the interface, which is in equilibrium with the applied load of 250 lbs. The steady relative displacement rate

of 3.43178×10^{-5} in/hr can be computed from equation (6.4) by using the values of $\sigma_s = 21.22$ psi, and H, h and $g = 0$ as given by equation (6.27a). The steady relative displacement rate predicted by the FE analysis is 3.41322×10^{-5} in/hr, as computed by evaluating the slope of the relative displacement vs. time curve for the steel rod based on Figure 6.4. These two values for the displacement rate of the steel rod agrees closely, with a deviation of only -0.54%. For cases where adfreeze creep behaviour dominates at the interface, the subroutine of the adfreeze element is verified by the close agreement between the values predicted by simulation of rod movement and by the creep relation used for the interface.

A hypothetical example similar to above was considered next. The problem configuration was similar to that in Figure 6.3, but the dimensions of the frozen soil cylinder was considered as 150 mm in diameter and 50 mm in height, and the steel rod had a diameter of 10 mm. The finite element mesh used for the problem is shown in Figure 6.6, where 20 axisymmetric (8-node) elements, 5 adfreeze (6-node) elements, and a total of 110 nodes were used. Following hypothetical material parameters were assumed for the problem:
For bond interface (adfreeze elements):

$$\begin{aligned} &C_s = 91.0 \ \text{MPa} , \qquad C_n = 900.0 \ \text{MPa}, \\ &H = 5.75 \times 10^{-3} \ \text{ for } \sigma_s \text{ in MPa and } \dot{d}_s^c \text{ in mm/hour} , \\ &h = 2.14 , \qquad g = 0 \ \text{(steady creep)} , \\ &\sigma_{sf} = \sigma_{pf} = 10 \ \text{MPa} . \end{aligned} \tag{6.28a}$$

For frozen soil (power law creep):

$$\begin{aligned} &E = 6000 \ \text{MPa} , \qquad \nu = 0.47 , \\ &A = 5.75 \times 10^{-3} \ \ (\text{MPa})^{-B} \, \text{hr}^{-C} , \\ &B = 0.684 , \qquad C = 0.143 . \end{aligned} \tag{6.28b}$$

For steel rod :

$$E = 2 \times 10^5 \ \text{MPa} , \qquad \nu = 0.30 . \tag{6.28c}$$

The problem was simulated for a vertical load of 3000 N applied vertically downwards at the bottom of the rod. A time incremental scheme identical to that for the earlier case was used. The results for the vertical displacement at the points **I** and **J** (see Figure 6.6) are as shown in Figure 6.7. These results show that the steel rod undergoes vertical displacement at a steady rate after a relatively short initial period of decelerating (primary) displacement, while the adjoining frozen soil experiences attenuating creep. The profiles for the bond stress σ_s at different times are shown in Figure 6.8, where it can be seen that σ_s approaches a uniform, steady state value of 1.9098 MPa with time, as required by equilibrium considerations.

The identical problem was simulated using three additional loads of magnitudes 2750, 3750, and 4500 N. The predicted results for the relative vertical displacement for the steel rod (differences of displacement at points **I** and **J**) under all four load cases considered here are as shown in Figure 6.9. In all load cases, the bond stress σ_s at the interface approached the uniform value governed by the equilibrium of the rod. The steady rate of displacement ($\dot{\gamma}$) computed by evaluating the slope of each line in Figure 6.9 was fitted to the corresponding adfreeze stress value (σ_s), using a least squares fit. The resulting relationship can be given as,

$$\dot{\gamma} = 5.5496 \times 10^{-3} \, (\sigma_s)^{2.1744} \; . \tag{6.29}$$

In above, $\dot{\gamma}$ is in mm/hr, and σ_s is in MPa. Once again, it can be seen that the coefficient and the exponent in the relationship of equation (6.29) agree reasonably with H and h, respectively, of equation (6.28a), as should be the case for situations where adfreeze creep behaviour dominates the relative movement at the interface; minor deviations should be expected since the predicted relationship in equation (6.29) is obtained after involving elastic deformations etc. at the interface, whereas equation (6.4) is expressed exclusively for relative creep displacements. The demonstration problems above clearly show the capability of the adfreeze/bond element developed here to model the general behaviour observed at structure-frozen soil/ice interfaces.

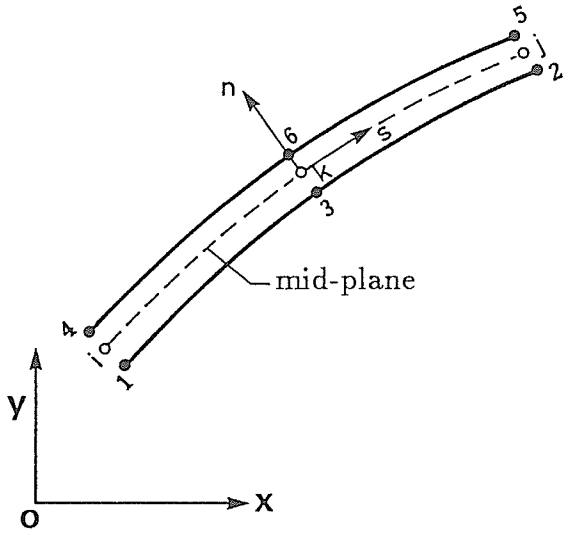

Figure 6.1. A typical interface element to represent adfreeze/bond behaviour.

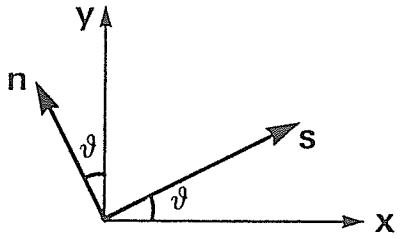

Figure 6.2. Orientation of local and global coordinate systems.

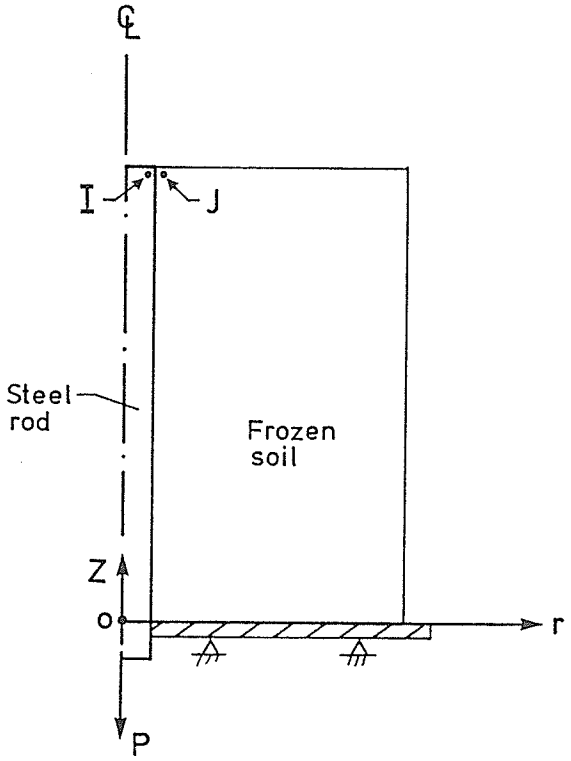

Figure 6.3. Configuration of problem where an embedded steel rod is pulled out of a frozen soil cylinder.

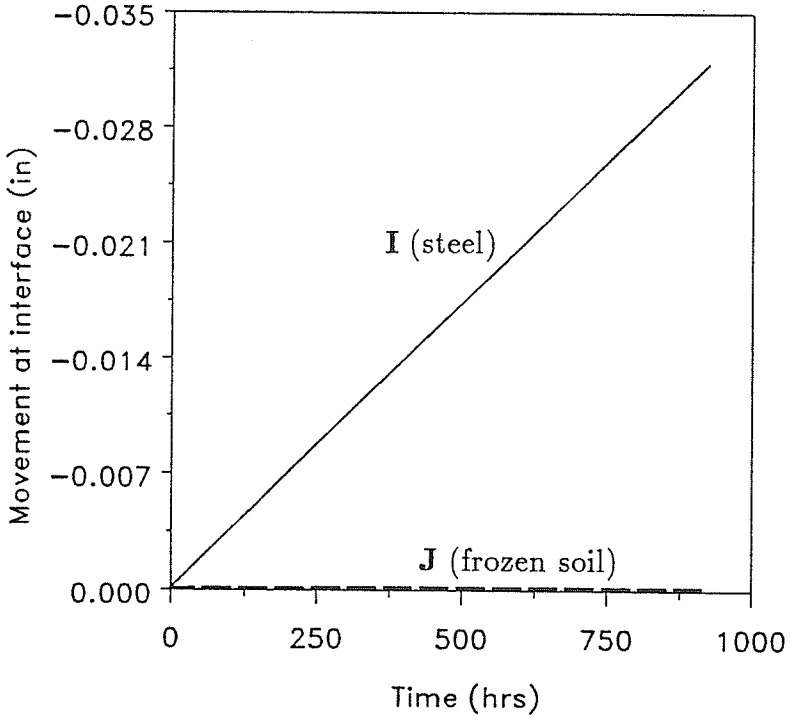

Figure 6.4. Separation of originally corresponding points **I** on steel surface and **J** on frozen soil surface, for the problem in Figure 6.3.

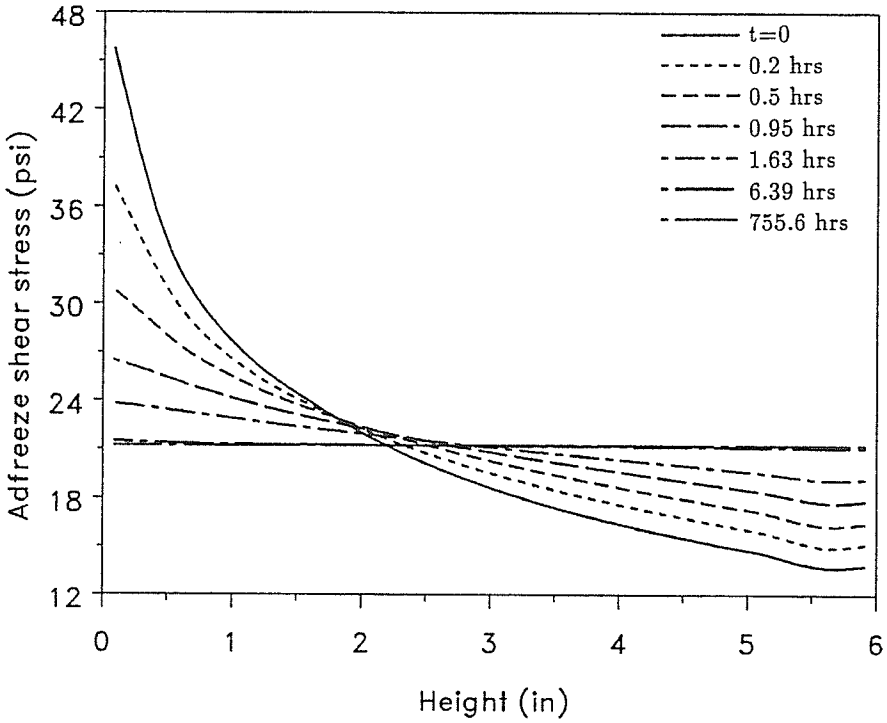

Figure 6.5. Adfreeze shear stress profiles along the interface at different times, for the problem in Figure 6.3.

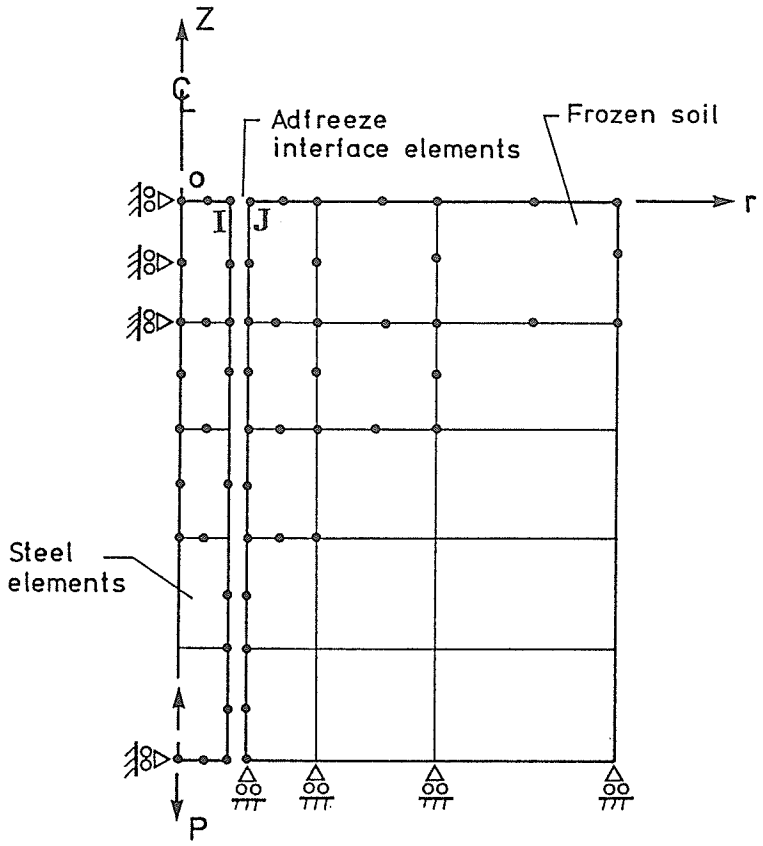

Figure 6.6. Finite element discretization of the pull-out problem configuration.

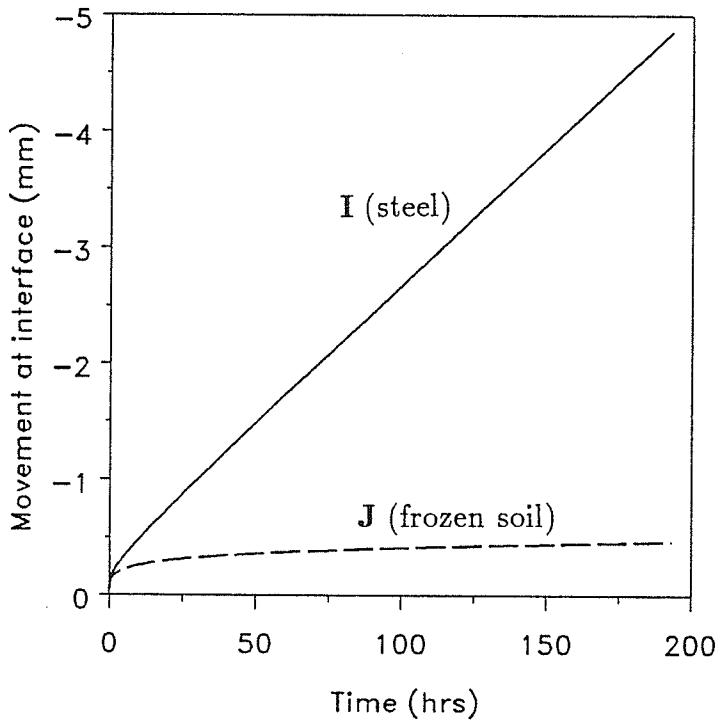

Figure 6.7. Separation of originally corresponding points **I** on steel surface and **J** on frozen soil surface, for the problem in Figure 6.6.

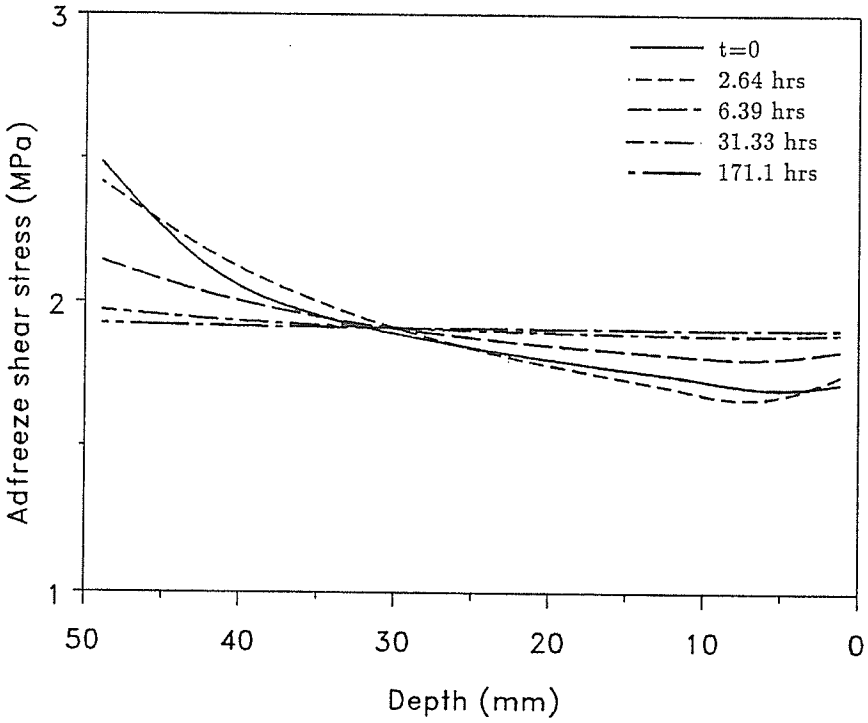

Figure 6.8. Adfreeze shear stress profiles along the interface at different times, for the problem in Figure 6.6.

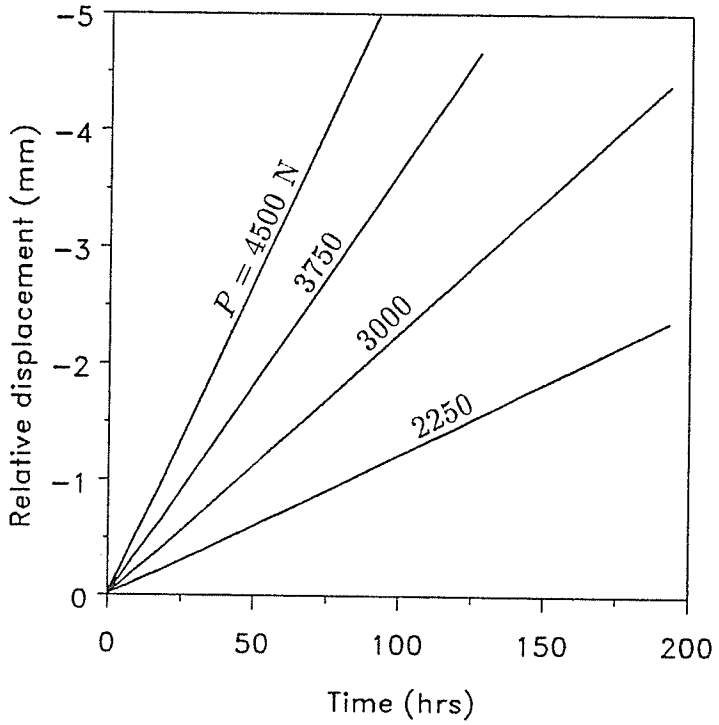

Figure 6.9. Relative vertical displacement at interface for different loads, for the problem in Figure 6.6.

Chapter 7

SUMMARY AND CONCLUSIONS

7.1 Summary

Three creep models reported in the literature, namely the Power Law (time hardening) creep model, Fish's unified creep model, and Domaschuk's incremental creep model, were selected for numerical implementation using the finite element method. Generalization of the power law and Fish's model to multi-axial stress and strain situations was performed under the assumptions of incompressibility and isotropy of the material. The model of Domaschuk had already been proposed for multi-axial situations and for isotropic, but compressible, materials.

Appropriate finite element codes were developed for the implementation of the selected creep models, by employing iterative solution schemes to solve the non-linear boundary value problems associated with the structure-frozen media interaction. The power law creep model and Fish's unified creep model were implemented in the computer code ITFECC-A, developed by using an iterative, time incrementing finite element algorithm. Code ITFECC-A is capable of analyzing structure-frozen media interaction problems under conditions of plane stress/strain, plane strain axisymmetry, axisymmetry, three dimensional analysis, and situations involving adfreeze/ bond behaviour at the structure-frozen media interface. One dimensional examples could also be analyzed, mainly for verification purposes. Code ITFECC-A included capability to analyze problems using a particular extension of the power law creep model (Power Law Extension II) to cover multiple-step loads. A similar but smaller code, named ITFECC-B, was developed to incorporate an alternative extension of the power law creep model (Power Law Extension I). The constitutive concept in codes ITFECC-A and ITFECC-B is equivalent to a non-linear Maxwell viscoelastic model, where total deformation can be decomposed into an elastic and viscous (creep) part. The viscous part is governed by the selected creep model (power law or Fish's model) and the elastic part by isotropic linear elasticity.

An iterative, load incrementing finite element algorithm was used to develop the computer code ILFENP, where Domaschuk's creep model was implemented. The algorithm of this code is applicable for any constitutive model based on the concept of hypoelasticity.

A computer code named FEPILE-I was developed using an iterative, time incremental finite element algorithm, for the purpose of modelling laterally loaded piles in ice/ permafrost; this pile element was developed as a beam on a distributed spring-dashpot mechanism (equivalent to a Maxwell viscoelastic model with a non-linear dashpot). For purposes of verification of the latter code, a fifth code FEPILE-II was developed by employing a slight variation in the numerical algorithm used for evaluating the lateral ice/ permafrost reaction on the pile.

All computer codes were developed using the concept of 'program modules', whereby certain modules could be changed whenever necessary without much effect on the rest of the code. Options were included to select iterative or non-iterative solution schemes, to change the boundary conditions during the analysis of a given problem, and to stop and resume the analysis later by using tape or disk mounts. Execution of each code was controlled by a sequence of Macro commands, which would determine, for example, the desired time discretizations, output of results, etc. The codes consisted of a main program section and a library of appropriate element subroutines, with each routine suitable for modelling a particular type of domain (i.e. creep or linear elastic elements for 1-D, 2-D and 3-D analysis, adfreeze elements, pile elements, etc.).

The accuracy and reliability of all codes were investigated by analyzing many verification examples using different types of elements and creep models incorporated therein, and by comparing the predicted results with those obtained by using closed-form analytical expressions or independent numerical means. The time/load discretization necessary for accuracy, reliability of time incremental codes for analysis over long periods of time, and ability to model transient stress behaviour, etc. were investigated.

Computer codes ITFECC-A and ITFECC-B were used to analyze multiple-step load pressuremeter tests on a frozen soil by using the Power Law Extensions I and II under axisymmetric conditions, and the predictions were compared with the available test results. Numerical results for deformations and stresses were presented. Code ITFECC-A was used to simulate steady creep of laterally loaded rigid cores in ice by using the power law model in plane strain analyses, and the predicted results were compared with available test results on laterally loaded steel rods in ice. The relations derived on the basis of above analyses were used to develop non-linear dashpot relationships and linear elastic Winkler coefficients for the spring-dashpot mechanism used for laterally loaded piles in the code FEPILE-I. The latter code was used to analyze laterally loaded piles in ice/ permafrost, and the predicted behaviour of cantilever piles and free-floating piles were presented in detail. The results obtained from code FEPILE-I for laterally loaded floating piles were compared with results obtained by independent analyses of the identical problems using three dimensional continuum elements (under the power law model) available in code ITFECC-A. Predicted interaction between a pair of laterally loaded rigid cores in ice was investigated by using the power law model. Code ITFECC-A and the power law model were employed to predict creep movements of various footing foundations on different types of frozen soils, by using axisymmetric analyses; similar analyses were performed to model static penetration tests as well as rate-controlled penetration tests on frozen soils, by using different indenter shapes.

The generalized, unified creep model of Fish, incorporated in the code ITFECC-A, was used to resimulate selected uniaxial creep tests on ice reported in the literature, and to analyze pressuremeter tests on frozen media. Quantitative and qualitative comparisons were drawn between the predicted behaviour and reported test results. Further analyses of interaction problems involving frozen ground were performed using the model, these being plane strain analyses of laterally loaded, embedded, rigid cores, and axisymmetric analyses of plate load tests. Characteristics observed from the numerical predictions were discussed.

Code ILFENP was used to investigate the qualitative behaviour of the model

of Domaschuk in simulating creep of a frozen sand; for this purpose, pressuremeter tests and a plate load test on a selected frozen sand was modelled under axisymmetric conditions.

A special finite element of zero thickness was developed to model adfreeze/bond strength characteristics at the structure - frozen soil/ ice interface. The performance of this element was illustrated by using the code ITFECC-A to simulate few examples where adfreeze phenomenon was involved.

The computer codes developed for this research constitute powerful and versatile tools applicable in analyses of a wide variety of structure-frozen soil/ice interaction problems encountered in engineering practice. Estimates of deformations predicted by the codes would be valuable for the design of structures on frozen media, provided the creep characteristics of the base conform to the particular creep model selected, and the material parameters are accurately evaluated. The applicability of the codes had been substantially broadened by allowing for incorporation of additional creep models, as and when such need arises.

7.2 Conclusions

The objectives of the research, as outlined in §1.4, were accomplished satisfactorily. Based on the results of the research, the following conclusions can be itemized:

(a) Finite element computer codes incorporating rheological constitutive equations provide a flexible and versatile means of solving structure-frozen soil/ice interaction problems in which creep is prevalent.

(b) The power law creep model can be used to predict instances of structure-permafrost interaction where primary, attenuating, or secondary creep is involved. Fish's creep model is capable of modelling interaction problems which involve failure through accelerating creep, while Domaschuk's model simulates instances of attenuating creep which include a volumetric creep component.

(c) As seen from analyses of pressuremeter tests, the phenomenological assumption of initializing the time variable in the power law model to zero at each instance of application of a distinct step load tended to yield satisfactory agreement between numerical and experimental results.

(d) Applying appropriate codes to the problem of a laterally loaded pile indicated that modelling the permafrost or ice as a spring-dashpot system provided good agreement between numerical and experimental data when the model was calibrated using experimental data.

(e) Use of the pile element on a spring-dashpot system to model laterally loaded piles in permafrost results in vast savings of computer resources such as time and memory, as compared to the rigorous analyses of these problems using three-dimensional continuum elements.

7.3 Recommendations for Further Study

Recommendations for further study may be proposed on two fronts, i.e. (1) further numerical work on this topic (outlined in §7.3.1 below), and (2) experimental work that may be undertaken to evaluate the validity of numerical models used here (briefly mentioned in §7.3.2 below).

7.3.1 Further Numerical Studies

Incorporation of other creep models in the codes can be conveniently accomplished. For continuum elements, additional components of the total deformation, such as delayed elasticity and plasticity, can be considered. As an example, incorporation of the Kelvin-Voigt rheological model in the numerical scheme may be used to extend the codes to cases where delayed elasticity effects are considered. Different creep properties in tension and compression can be incorporated, provided reliable test data exists, and material damage can be accounted for by including damage parameters. The algorithm developed for the pile element can be modified to include a non-linear Winkler coefficient, which may, for example, be expressed as a function of lateral displacement. Finally, the codes may be extended to geometrically non-linear cases where large deformations and strains are encountered.

7.3.2 Note on Experimental Work

It would be interesting to compare the predictability of the models considered in the present study, by using the different models to simulate creep in one material. This comparison, specially between the power law model and Fish's model, can be made most conveniently in the case of a material in the primary creep stage. For this, material samples should be subjected to constant (compressive) stress creep tests under isothermal conditions, and the axial deformation should be recorded with time. The exact procedure for these tests was outlined by Jacka (1984). Tests should be continued until accelerating creep is noticed. From the raw data, strain rates can be calculated, and therefore the magnitudes of minimum strain rates and times to minimum strain rate may be evaluated under each stress and temperature.

These data can be used to evaluate parameters for Fish's model (see §4.3.1), but the parameter δ should be evaluated as recommended by Fish (1987). The stress-strain-time data from the same tests, but within the primary creep stage, can be used to evaluate the creep parameters for the power law model, by using the method of least squares (with three variables) to fit the data to the power law model in equation (3.11). The subsequent comparison between the two models can be made in the primary creep stage only, since the power law model is not applicable to tertiary creep.

The experimental program necessary to evaluate parameters for Domaschuk's model is outlined by Domaschuk et al. (1991), Rahman (1988) and briefly in Chapter 2. Triaxial creep tests are necessary in this case, since the model is based on volumetric creep deformations. Therefore, for the same material above, a separate set of experiments are required to evaluate this model. If these parameters are evaluated, primary creep predicted by this model can be compared with that predicted by the two earlier models.

REFERENCES

Alwahhab, R.M. (1983). *Bond And Slip Of Steel Bars In Frozen Sand*, Ph.D. dissertation, Michigan State University.

Andersland, O.B., and Akili, W. (1967). "Stress effects on creep rates of a frozen clay soil", *Geotechnique*, Vol. 17, 27-39.

Andersland, O.B., and Alnouri, I. (1970). "Time-dependent stress behaviour of frozen soils", *J. Soil Mech. Foun. Div., ASCE*, Vol. 96, SM4, 1249-1269.

Andersland, O.B., and Anderson, D.M. (1978). *Geotechnical Engineering for Cold Regions*, McGraw-Hill Co., New York, N.Y.

Andersland, O.B., and Douglas, A.G. (1970). "Soil deformation rates and activation energies", *Geotechnique*, Vol. 20, 1-16.

Ashby, M.F., and Duval, P. (1985). "The creep of polycrystalline ice", *Cold Reg. Sci. Tech.*, Vol. 11, 285-300.

Assur, A. (1980). "Some promising trends in ice mechanics", in *Physics and Mechanics of Ice*, IUTAM symposium, P. Tryde (Ed.), Springer-Verlag, Berlin, 1-15.

Baguelin, F., Frank, R., and Said, Y.H. (1977). "Theoretical study of lateral reaction mechanism of piles", Geotechnique, Vol. 27, No.3, 405-434.

Bragg, A.R., and Andersland, O.B. (1982). "Strain dependence of Poisson's ratio for frozen sand", *Proc. 4th Can. Permafrost Conf.*, 365-373.

Chamberlain, E., Groves, C., and Pertham, R. (1972). "The mechanical behaviour of frozen earth materials under high pressure triaxial conditions", *Geotechnique*, Vol. 22, No.3, 469-483.

Chehayeb, F.S., Ting, S.-K., Sunder, S.S., and Connor, J.J. (1987). "Sea-ice indentation in creeping mode", *J. Engrg. Mech., ASCE*, Vol. 113, No.7, 965-983.

Christensen, R.M. (1971). *Theory Of Viscoelasticity - An Introduction*, Academic Press Inc., New York, N.Y.

Czurda, K.A. (1983). "Freezing effects on soils: comprehensive summary of ISGF 82", *Cold Reg. Sci. Tech.*, Vol. 8, 93-107.

de Ruiter, J. (1971). "Electric penetrometer for site investigations", *J. Soil Mech. Found. Div., ASCE*, Vol. 97, SM2, 457–472.

Desai, C.S. (1979). *Elementary Finite Element Method*, Prentice-Hall Inc., Engle-

wood Cliffs, N.J.

Domaschuk, L., Knuttson, L., Shields, D.H., and Rahman, M.G. (1985). "Creep of frozen sand under isotropic and deviatoric components of stress", *J. of Energy Resources Tech.*, Vol. 107, 199-203.

Domaschuk, L., Shields, D.H., and Kenyon, R. (1989). "Penetration of spheres and rods into ice",*POAC speciality Conf.*, June 1989, Lulea, Sweden.

Domaschuk, L., Shields, D.H., and Rahman, M.G. (1991). "A model for attenuating creep of frozen sand", *Cold Reg. Sci Tech.*, Vol 19, No.2, 145-161.

Domaschuk, L., and Wade, N.H., (1969). "A study of bulk and shear modulii of sand", *Soil Mech. Found. Div., ASCE*, Vol. 101, GT7, 601-614.

Dorn, J.E. (1954). "Some fundamental experiments on high tempe- rature creep", *J. Mech. Phys. Solids*, Vol. 3, 85-116.

Eckardt, H. (1979). "Creep behaviour of frozen soils in uniaxial compression tests", *Engrg. Geology*, Vol. 13, 185-195.

Emery, J.J., and Mirza, F.A. (1980). "Finite element method simulation of large ice mass flow behaviour", in *Physics and Mechanics of Ice*, IUTAM symposium, P. Tryde (Ed.), Springer-Verlag, Berlin, 83-91.

Fish, A.M. (1980). "Kinetic nature of the long term strength of frozen soils", pre-prints of *2nd Int. Sym. on Ground Freezing*, Trondheim, Norway, 95-108.

Fish, A.M. (1981). "Deformation and failure of frozen soils and ice at constant and steadily increasing stresses", *Proc. 4th Can. Permafrost Conf.*, 419-428.

Fish, A.M. (1984). "Thermodynamic model of creep at constant stress and constant strain rate", *Cold Reg. Sci. Tech.*, Vol. 9, 143-161.

Fish, A.M. (1987). "Shape of creep curves in frozen soil and polycrystalline ice", *Can. Geotech. J.*, Vol. 24, 623-629.

Fish, A.M., and Sayles, S.H. (1981). "Acoustic emissions during creep of frozen soils", *Acoustic Emissions in Geot. Eng. Practices*, V.P. Drnevich and R.E. Gray (Eds.), ASTM STP 750, 194-206.

Foriero, A., and Ladanyi, B. (1990). "Finite element simulation of behaviour of laterally loaded piles in permafrost", *J. Geotech. Engrg., ASCE*, Vol. 116, No.1, 1-14.

Frank, R. (1984). "Etudes théoriques de fondations profondes et d'essais en place

par autoforage dans les LPC et résultats pratiques (1972-1983)", *Rapport de recherche LPC No. 128*, Laboratoire Central des Ponts et Chaussées, Paris, p. 61.

Frederking, R.M.W. (1979). "Laboratory tests on downdrag loads developed by floating ice covers on vertical piles", *Proc. POAC 79*, The Norwegian Inst. of Tech., Trondheim, Norway, Vol. II, 1097-1110.

Frenkel, J.I. (1947). *Kinetic Theory Of Liquids*, Clarendon Press, Oxford, U.K.

Frivik, P.E., Janbu, N., Seatersdal, R., and Finborud, L.I. (Eds.) (1980). *Ground Freezing 1980. Developments In Geotechnical Engineering, Vol.28*, Elsevier Scientific Pub. Co., Netherlands.

Gardner, A.R., Jones, R.H., and Harris, J.H. (1984). "A new creep equation for frozen soils and ice", *Cold Reg. Sci. Tech.*, Vol. 9, 271-275.

Gens, A., Carol, I., and Alonso, I.I. (1988). "An interface element formulation for the analysis of soil-reinforcement interaction", *Comput. and Geotech.*, Vol. 7, 133-151.

Ghaboussi, J., Wilson, E.L., and Isenberg, J. (1973). "Finite element for rock joints and interfaces", *J. Soil Mech. Found. Div., ASCE*, Vol. 99, SM10, 833-848.

Glasstone, S., Laidler, K., and Eyring, H. (1941). *The Theory of Rate Processes*, McGraw-Hill Co. Inc., NY.

Glen, J.W. (1955). "The creep of polycrystalline ice", *Proc. Roy. Soc. of London*, Ser. A, Vol. 228, 519-538.

Gold, L.W. (1966). "Dependence of crack formation on crystallographic orientation of ice", *Can. J. Phys.*, Vol. 44, 2757-2764.

Gold, L.W. (1970). "Process of failure in ice", *Can. Geotech. J.*, Vol. 7, No.4, 405-413.

Gold, L.W. (1977). "Engineering properties of freshwater ice", *J. Glaciology*, Vol. 19, No.8, 197-211.

Gold, L.W., and Sinha, N.K. (1980). "The rheological behaviour of ice at small strains", in *Physics and Mechanics of Ice*, IUTAM symposium, P. Tryde (Ed.), Springer-Verlag, Berlin, 116-128.

Goodman, R.E., Taylor, R.L., and Brekke, T.L. (1968). "A model for mechanics of jointed rock", *J. Soil Mech. Found. Div., ASCE*, Vol. 94, SM3, 637-659.

Goughnour, R.R., and Andersland, O.B. (1968). "Mechanical properties of a sand-ice system", *J. Soil Mech. Found. Div., ASCE*, Vol. 94, SM4, 923-949.

Greenbaum, G.A., and Rubinstein, M.F. (1968). "Creep analysis of axisymmetric bodies using finite elements", *Nuc. Eng. Des.*, Vol. 7, 379–397.

Hill, R. (1950). *The Mathematical Theory Of Plasticity*, Clarendon Press, Oxford, U.K.

Hooke, R.L. (1981). "Flow law for polycrystalline ice in glaciers: comparison of theoretical predictions, laboratory data, and field measurements", *Review of Geophysics and Space Physics*, Vol. 9, No.4, 664-672.

Hughes, T.J.R., and Taylor, R.L. (1978). "Unconditionally stable algorithms for quasi-static elasto/visco-plastic finite element analysis", *Comp. Stuct.*, Vol. 8, 169-173.

Hult, J.A.H. (1966). *Creep In Engineering Structures*, Blaisdel Pub. Co., Waltham, Mass.

Huneault, P., and Ladanyi, B. (1987). "Resistance of frozen ground to steady cone or pile penetration", *Proc. 6th Offshore Mech. and Arctic Eng. Symp.*, IV, Houston, 125–132.

Jacka, T.H. (1984). "The time and strain required for development of minimum strain rates in ice", *Cold Reg. Sci. Tech.*, Vol. 8, No.3, 261–268.

Jessberger, H.L. (Ed.) (1978). *Ground Freezing. Developments In Geotechnical Engineering, Vol.26*, Elservier Scientific Pub. Co., Netherlands.

Jessberger, H.L. (1980)a. "A state-of-the-art report. Ground freezing: Mechanical properties, processes and design", in *Ground Freezing 1980. Developments In Geotechnical Engineering, Vol.28*, P.E. Frivik et al. (Eds.), Elservier Scientific Pub. Co., Netherlands, 5-30.

Jessberger, H.L. (1980)b. "Theory and application of ground freezing in civil engineering", *Cold Reg. Sci. Tech.*, Vol. 3, No.1, 3-28.

Johnston, G.H. (1981). *Permafrost: Engineering Design And Construction*, National Research Council of Canada, John Wiley and Sons, Toronto.

Johnston, G.H., and Ladanyi, B. (1972). "Field tests of grouted rod anchors in permafrost", *Can. Geotech. J.*, Vol. 9, 176–194.

Jumikis, A.R. (1966). *Thermal Soil Mechanics*, Rutgers University Press, New

Brunswick, N.J.

Kamb, B. (1972). "Experimental recrystallization of ice under stress", in *Flow And Fracture Of Rocks, Geophys. Monogr. Ser.*, Vol. 16, H.C. Heard et al. (Eds.), AGU, Washington, D.C., 211-241.

Kanok-Nukulchai, W. (1984). *FEAP84 - Finite Element Analysis Program : User's handbook*, Asian Institute of Technology, Thailand.

Klein, J. (1979). "The application of finite elements to creep problems in ground freezing", *Proc. 3rd Int. Conf. Num. Meth. Geomech.*, Aachen, Germany, 493–502.

Klein, J., and Jessberger, H.L. (1979). "Creep stress analysis of frozen soils under multiaxial states of stress", *Eng. Geology*, Vol. 13, 353–365.

Kjartanson, B.H. (1986). *Pressuremeter Creep Testing In Laboratory Ice*, Ph.D. dissertation, University of Manitoba.

Kjartanson, B.H., Shields, B.H., Domaschuk, L., and Man, C.-S. (1988). "The creep of ice measured with the pressuremeter", *Can. Geotech. J.*, Vol. 25, 250–261.

Lach, P.R. (1989). *Creep Analysis Of Plate-Load And Pressuremeter Tests On Frozen Sand*, M.Sc. Thesis, University of Manitoba.

Ladanyi, B. (1972). "An engineering theory of creep of frozen soils", *Can. Geotech. J.*, Vol. 9, 63–80.

Ladanyi, B. (1976). "Use of static penetration test in frozen soil", *Can. Geotech. J.*, Vol. 13, 95–110.

Ladanyi, B., and Johnston, G.H. (1973). "Evaluation of in-situ creep properties of frozen soils with the pressuremeter", *Proc. 2nd Int. Conf. Permafrost*, 310-318.

Le Gac, H., and Duval, P. (1980). "Constitutive relations for the non-elastic deformation of polycrystalline ice", in *Physics and Mechanics of Ice*, IUTAM symposium, P. Tryde (Ed.), Springer-Verlag, Berlin, 51-59.

Lunardini, V.J. (1981). *Heat Transfer In Cold Climates*, Van Nostrand Reinhold Co., New York, N.Y.

Man, C.-S., Shields, D.H., Kjartanson, B., and Sun, Q.-X. (1985). "Creep of ice as a fluid of complexity 2: the pressuremeter problem", *Proc. 10th Can.*

Cong. Appl. Mech., A347-A348.

McTigue, D.F., Passman, S.L., and Jones, S.J. (1985). "Normal stress effects in the creep of ice", *J. of Glaciology*, Vol. 31, No.108, 120-126.

Mellor, M. (1980). "Mechanical properties of ice", in *Physics and Mechanics of Ice*, IUTAM symposium, P. Tryde (Ed.), Springer-Verlag, Berlin, 217-245.

Mellor, M., and Cole, D.M. (1982). "Deformation and failure of ice under constant stress or constant strain rate", *Cold Reg. Sci. Tech.*, Vol. 5, No.3, 201-219.

Mellor, M., and Cole, D.M. (1983). "Stress/strain/time relations for ice under uniaxial compression", *Cold Reg. Sci. Tech.*, Vol. 6, No.3, 207-230.

Mellor, M., and Testa, R. (1969). "Effect of temperature on creep of ice", *J. Glaciology*, Vol. 8, 131-145.

Mitchell, J.K., Campanella, R.G., and Singh, A. (1968). "Soil creep as a rate process", *J. Soil Mech. Found. Div., ASCE*, Vol. 94, SM1, 231-253.

Morgenstern, N.R., Roggensack, W.D., and Weaver, J.S. (1980). "The behaviour of friction piles in ice and ice-rich soils", Can. Geotech. J., Vol. 17, 405-415.

Morland, L.W. (1979). "Constitutive laws for ice", *Cold. Reg. Sci. Tech.*, Vol. 1, No.2, 101-108.

Morland, L.W., and Spring, U. (1981). "Viscoelastic fluid relation for the deformation of ice", *Cold Reg. Sci. Tech.*, Vol. 4, No.3, 255-268.

Morin, P., Shields, D.H., Kenyon, R., Domaschuk, L., and Frank, R. (1991). "Predicting creep displacements of laterally loaded piles in ice and ice-rich materials", *Proc. 1st Int. Offshore and Polar Engrg. Conf. (ISOPE-91)*, Edinburgh, Scotland, (August 1991).

Murat, J.R., Ladanyi, B., and Huneault, P. (1989). "In situ determination of creep properties of sea ice with the pressuremeter", *Can. Geotech. J.*, Vol. 26, 575-594.

Neukirchner, R.J., and Nixon, J.F. (1987). "Behaviour of laterally loaded piles in permafrost", *J. Geotech. Engrg., ASCE*, Vol. 113, No.1, 1-14.

Nixon, J.F. (1984). "Laterally loaded piles in permafrost", *Can. Geotech. J.*, Vol. 21, 431-438.

Nixon, J.F., and McRoberts, E.C. (1973). "A study of some factors affecting the thawing of frozen soils", *Can. Geotech. J.*, Vol. 10, 439-452.

Nixon, J.F., and McRoberts, E.C. (1976). "A design approach for pile foundations in permafrost", *Can. Geotech. J.*, Vol. 13, 40-57.

Norton, F.H. (1929). *Creep of steel at high temperatures*, McGraw-Hill Book Co., New York, N.Y.

Nye, J.F. (1956). "The distribution of stress and velocity in glaciers and ice sheets", *Proc. Roy. Soc. Lon.*, Vol. 239, Ser. A, 113-133.

Odquist, F.K.G. (1966). *Mathematical Theory of Creep and Creep Rupture*, Clarendon Press, Oxford, U.K.

Owen, D.R.J., and Hinton, E. (1980). *Finite Elements In Plasticity: Theory And Practice*, Pineridge Press Ltd., Swansea, U.K.

Pande, G.N., and Sharma, K.G. (1979). "On joint/ interface elements and associate problems of numerical ill-condition", Int. J. Numer. Meth. Engrg., Vol. 14, 293-300.

Parameswaran, V.R. (1978). "Adfreeze strength of frozen sand to model piles", *Can. Geotech. J.*, Vol. 15, No.4, 494-500.

Parameswaran, V.R. (1979). "Creep of model piles in frozen soil", *Can. Geotech. J.*, Vol. 16, No.1, 69-77.

Parameswaran, V.R. (1981). "Adfreeze strength of model piles in ice", *Can. Geotec. J.*, Vol. 18, No.1, 8-16.

Penner, E. (1970). "Frost heaving forces in Leda clay", *Can. Geotech J.*, Vol. 7, 8-16.

Poulos, H.G., and Davis, E.H. (1980). *Pile Foundation Analysis and Design*, Wiley, New York, N.Y.

Puswewala, U.G.A., and Rajapakse, R.K.N.D. (1991)a. *FEPILE-I: Finite element code for laterally loaded piles in permafrost*, User manual for FEPILE-I, Dept. of Civil Engrg., Univ. of Manitoba.

Puswewala, U.G.A., and Rajapakse, R.K.N.D. (1991)b. *ILFENP: Finite element code for non-linear elasticity*, User manual for ILFENP, Dept. of Civil Engrg., Univ. of Manitoba.

Puswewala, U.G.A., and Rajapakse, R.K.N.D. (1991)c. *ITFECC-A: Finite element code for structure-frozen media interaction*, User manual for ITFECC-A, Dept. of Civil Engrg., Univ. of Manitoba.

Rahman, M.G. (1988). *The Creep Of Frozen Sands*, Ph.D. dissertation, University of Manitoba.

Rajapakse, R.K.N.D., and Shah, A.H. (1989). "Impedance curves for an elastic pile", *Soil Dyn. Earthq. Engrg.*, Vol. 8, No.3, 145-152.

Rowley, R.K., Watson, G.H., and Ladanyi, B. (1973). "Vertical and lateral pile load tests in permafrost", *Proc. 2nd Int. Conf. Permafrost*, 712-721.

Rivlin, R.S., and Ericksen, J.L. (1955). "Stress-deformation relations for isotropic materials", J. Rational Mech. Anal., Vol. 4, 323-425.

Sanger, F.J., and Kaplar, C.W. (1963). "Plastic deformation of frozen soils", *Proc. 1st Int. Conf. Permafrost*, 305-315.

Sayles, F.H. (1968). "Creep of frozen sands", *US Army CRREL Tech. Rep. 190*, Hanover, N.H.

Sayles, F.H. (1973). "Triaxial and creep tests on frozen Ottawa sand", *Proc. 2nd Int. Conf. on Permafrost*, 384-391.

Sayles, F.H., and Haynes, D. (1974). "Creep of frozen silt and clay", *US Army CRREL Tech. Note 252*, Hanover, N.H.

Sego, D.C., and Morgenstern, N.R. (1983). "Deformation of ice under low stresses", *Can. Geotech. J.*, Vol. 20, 587-602.

Selvadurai, A.P.S. (1979). *Elastic Analysis Of Soil-Foundation Interaction. Developments In Geotechnical Engineering, Vol.17*, Elservier Scientific Pub. Co., Netherlands.

Shields, D.H., Domaschuk, L., Azizi, F., and Kjartanson, B. (1989). "Primary creep parameters as measured in-situ", *Cold Reg. Sci. Tech.*, Vol. 16, 281-290.

Sinha, N.K. (1977). "Effective elasticity of ice", *Workshop on the mechanical properties of ice*, January 1977, Calgary, Alt.

Sinha, N.K. (1983). "Creep model for monotonically increasing stress", *Cold Reg. Sci. Tech.*, Vol. 8, 25-33.

Soo, S. (1983). *Studies Of Plane And Reinforced Frozen Soil Structures*, Ph.D. dissertation, Michigan State University.

Soo, S., Wen, K., and Andersland, O.B. (1987). "Finite element method for analysis of frozen earth structures", *Cold Reg. Sci. Tech.*, Vol. 15, 121-129.

Sun, Q.-X., (1987). *On Two Special Rivlin-Ericksen Fluid Models Generalizing*

Glen's Law For Polycrystalline Ice, Ph.D. dissertation, University of Manitoba.

Szyszkowski, W., and Glockner, P.G. (1985). "Modelling of time-dependent behaviour of ice", *Cold Reg. Sci. Tech.*, Vol. 11, 3-21.

Terzaghi, K., and Peck, R.B. (1948). *Soil Mechanics In Engineering Practice*, John Wiley & Sons Inc., New York, N.Y.

Thimus, Jean-Francois (1988). *Caracteristiques Physiques, Mecaniques et Rheologiques D'un Sol Argileux Lors De Sa Congelation*, Thesis presented for the Degree of Doctor of Applied Sciences, Universite Catholique De Louvain, Belgium, Chap. 5.

Thimus, Jean-Francois (1990). Personal communications.

Timoshenko, S., and Goodier, J.N. (1951). *Theory Of Elasticity*, 2nd Ed., McGraw-Hill Co., New York, N.Y.

Ting, J.M. (1983). "Tertiary creep model for frozen sands", *J. Geotec. Engrg., ASCE*, Vol. 109, No.7, 932-945.

Traetterberg, A., Gold, L.W., and Frederking, R.M. (1975). "The strain rate and temperature dependence of Young's Modulus of ice", Proc. 3rd Int. Sym. on Ice Problems, IAHR, Hanover, N.H., 479-486.

Truesdell, C. (1955). "Hypo-elasticity", *J. Rational Mech. Anal.*, Vol. 4, No.1, 83-133.

Tsytovich, N.A. (1975). *The Mechanics Of Frozen Ground*, McGraw-Hill Co., New York, N.Y.

Tsytovich, N.A., and Sumgin, M.I. (1959). "Fundamentals of the Mechanics of Frozen Soils", *SIPRE Transl. 19*, Hanover, N.H.

Valliappan, P. (1974). *Nonlinear Stress-Deformation Analysis Of Lake Agassiz Clays Using Finite Element Method*, Ph.D. dissertation, University of Manitoba.

Vyalov, S.S. (1963). "Rheology of frozen soils", *Proc. 1st Int. Conf. Permafrost*, 332-339.

Vyalov, S.S. (1965)a. "Rheological properties and bearing capacity of frozen soils", *CRREL Tech. Transl. 74*, Hanover, N.H.

Vyalov, S.S. (1965)b. "Strength and creep of frozen soils and calculations of ice-soil

retaining structures", *CRREL Tech. Transl. 76*, Hanover, N.H.

Vyalov, S.S. (1973). "Long-term rupture of frozen soils as a thermally activated process", *Proc. 2nd Int. Conf. on Permafrost* (USSR contribution), 222-228.

Williams, H.T. (1984). "Single integral representation in ice mechanics", *Cold Reg. Sci. Tech.*, Vol. 9, 89-95.

Yin, J. (1990). *Constitutive Modelling Of Time-Dependent Stress-Strain Behaviour Of Soils*, Ph.D. dissertation, University of Manitoba.

Yong, R.N., and Osler, J.C. (1971). "Heave and heaving pressures in frozen soils", *Can. Geotech. J.*, Vol. 8, 272-282.

Yuanlin, Z., and Carbee, D.L. (1983). "Creep behaviour of frozen silt under constant uniaxial stress", *Proc. 4th Int. Conf. Permafrost*, Fairbanks, 1507-1512.

Yuanlin, Z., and Carbee, D.L. (1984). "Uniaxial compressive strength of frozen silt under constant deformation rates", *Cold Reg. Sci. Tech.*, Vol. 9, 3-15.

Zienkiewicz, O.C. (1977). *The Finite Element Method*, 3rd Ed., McGraw-Hill Co., Maidenhead, Berkshire, U.K.

Zienkiewicz, O.C., and Cormeau, F.C. (1974). "Visco-plasticity - Plasticity and creep in elastic solids - A unified numerical approach", *Int. J. Num. Meth. Engrg.*, Vol. 8, 821-845.

APPENDIX A

Finite Element Implementation Under Isotropic Linear Elasticity And Power Law Creep Model

(I). Plane Strain Analysis

Plane Strain General Formulations:

The two dimensional coordinate system is denoted by x_1 and x_2. The direction normal to x_1-x_2 plane is denoted by x_3.

$$\boldsymbol{\sigma} = \langle\ \sigma_{11},\ \sigma_{22},\ \sigma_{12}\ \rangle^T\ , \quad \text{and} \quad \sigma_{33} = \nu(\sigma_{11} + \sigma_{22}) \tag{A.I.1}$$

$$\boldsymbol{\epsilon} = \langle\ \epsilon_{11},\ \epsilon_{22},\ \gamma_{12}\ \rangle^T\ , \quad \text{where} \quad \gamma_{12} = 2\epsilon_{12} \tag{A.I.2}$$

$$[D] = \frac{E(1-\nu)}{(1+\nu)(1-2\nu)} \begin{bmatrix} 1 & \frac{\nu}{(1-\nu)} & 0 \\ \frac{\nu}{(1-\nu)} & 1 & 0 \\ 0 & 0 & \frac{(1-2\nu)}{2(1-\nu)} \end{bmatrix} \tag{A.I.3}$$

$$\mathbf{u} = \langle\ u_1,\ u_2\ \rangle^T \tag{A.I.4}$$

where $\mathbf{u}$ is the displacement at any point (x_1,x_2) in an element. Let the element have m nodes, and let the vector of nodal displacements for the element be denoted by $\mathbf{a}^e$. Then,

$$\mathbf{u} = [N]\,\mathbf{a}^e = \Big[[I]N_1,\ [I]N_2,\ [I]N_3,\ \ldots [I]N_m\Big]\,\mathbf{a}^e \tag{A.I.5}$$

where N_i is the 2-D shape function associated with the ith node (see Zienkiewicz 1977), $[I]$ is the (2×2) identity matrix, $[N]$ is a (2×2m) matrix, and $\mathbf{a}^e$ is a vector of 2m components.

$$\boldsymbol{\epsilon} = [L]\,\mathbf{u}\ , \qquad \text{where} \qquad [L] = \begin{bmatrix} \frac{\partial}{\partial x_1} & 0 \\ 0 & \frac{\partial}{\partial x_2} \\ \frac{\partial}{\partial x_2} & \frac{\partial}{\partial x_1} \end{bmatrix} \tag{A.I.6}$$

$$\boldsymbol{\epsilon} = [B]\,\mathbf{a}^e = \Big[[B_1],\ [B_2],\ [B_3],\ \ldots [B_m]\Big]\,\mathbf{a}^e\ , \qquad \text{where} \quad [B_i] = [L]\,[I]\,N_i \tag{A.I.7}$$

Thus $[B]$ is a (3×2m) matrix made of m number of (3×2) matrices $[B_i]$, defined for the ith node.

Plane Strain Formulations For Creep Analysis With Power Law:

$$\sigma_e = \left[\sigma_{11}^2 + \sigma_{22}^2 - \sigma_{11}\sigma_{22} + \nu(\nu-1)(\sigma_{11}^2 + \sigma_{22}^2 + 2\sigma_{11}\sigma_{22}) + 3\sigma_{12}^2\right]^{\frac{1}{2}} \qquad (A.I.8)$$

Define following:

$$\Phi = \left[(2-\nu)\sigma_{11} - (1+\nu)\sigma_{22}\right] \; ; \quad \Psi = \left[(2-\nu)\sigma_{22} - (1+\nu)\sigma_{11}\right] \qquad (A.I.9a)$$

$$\Omega = \left[2(\nu^2 - \nu + 1)\sigma_{11} + (2\nu^2 - 2\nu - 1)\sigma_{22}\right] \qquad (A.I.9b)$$

$$\Gamma = \left[2(\nu^2 - \nu + 1)\sigma_{22} + (2\nu^2 - 2\nu - 1)\sigma_{11}\right] \qquad (A.I.9c)$$

$$X_1 = AC\sigma_e^{B-1}\, t^{C-1} \; ; \quad X_2 = \frac{(B-1)}{4\sigma_e^2} \; ; \quad X_3 = \frac{3}{2}AC(B-1)\sigma_e^{B-3}\, t^{C-1} \qquad (A.I.9d)$$

$$\nu_1 = \frac{(2-\nu)}{2} \; ; \quad \nu_2 = \frac{(1+\nu)}{2} \qquad (A.I.9e)$$

The strain rate matrix is (with notations in eqns. A.I.9):

$$\beta = \dot{\epsilon}_{ij}^c = \left\{ \begin{array}{c} \dot{\epsilon}_{11}^c \\ \dot{\epsilon}_{22}^c \\ \dot{\gamma}_{12}^c \end{array} \right\} = \frac{1}{2} X_1 \left\{ \begin{array}{c} \Phi \\ \Psi \\ 6\sigma_{12} \end{array} \right\} \qquad (A.I.10)$$

$[S]^n$ is an unsymmetric matrix of dimensions (3×3), the components of which are (with notations in eqns. A.I.11):

$$S_{11} = \frac{\partial \dot{\epsilon}_{11}^c}{\partial \sigma_{11}} = X_1\left(X_2 \Phi\Omega + \nu_1\right) \qquad (A.I.11)$$

$$S_{12} = \frac{\partial \dot{\epsilon}_{11}^c}{\partial \sigma_{22}} = X_1\left(X_2 \Phi\Gamma - \nu_2\right) \qquad (A.I.12)$$

$$S_{13} = \frac{\partial \dot{\epsilon}_{11}^c}{\partial \sigma_{12}} = X_3 \Phi\sigma_{12} \qquad (A.I.13)$$

$$S_{21} = \frac{\partial \dot{\epsilon}_{22}^c}{\partial \sigma_{11}} = X_1\left(X_2 \Psi\Omega - \nu_2\right) \qquad (A.I.14)$$

$$S_{22} = \frac{\partial \dot{\epsilon}_{22}^c}{\partial \sigma_{22}} = X_1\left(X_2 \Psi\Gamma + \nu_1\right) \qquad (A.I.15)$$

$$S_{23} = \frac{\partial \dot{\epsilon}_{22}^c}{\partial \sigma_{12}} = X_3 \Psi\sigma_{12} \qquad (A.I.16)$$

$$S_{31} = \frac{\partial \dot{\gamma}_{12}^c}{\partial \sigma_{11}} = X_3 \Omega\sigma_{12} \qquad (A.I.17)$$

$$S_{32} = \frac{\partial \dot{\gamma}_{12}^c}{\partial \sigma_{22}} = X_3 \Gamma\sigma_{12} \qquad (A.I.18)$$

$$S_{33} = \frac{\partial \dot{\gamma}_{12}^c}{\partial \sigma_{12}} = 3X_1(12\, X_2 \sigma_{12}\sigma_{12} + 1) \qquad (A.I.19)$$

$[\bar{D}]^n$ is a (3×3) matrix, defined by equation (3.51). Therefore, for an element of m nodes, $[B]^T[\bar{D}]^n[B]$ is a $(2m \times 2m)$ matrix made of m^2 number of $[B_i]^T[\bar{D}]^n[B_j]$ matrices, each of which has dimensions of (2×2).

Plane Strain Formulations For Creep Analysis With Power Law Ext. II:

The equations (A.I.8) to (A.I.19) apply identically for Power Law Extension II, with t in eqns. (A.I.11e) replaced by $(t - t_{i-1})$, where t is the current time, and t_{i-1} is the time at which the ith load step is applied.

Note: Formulations are not derived for Power Law Extension I, under plane strain conditions.

(II). Plane Stress Analysis

Plane Stress General Formulations:

The two dimensional coordinate system is denoted by x_1 and x_2. The direction normal to x_1-x_2 plane is denoted by x_3.

$$\boldsymbol{\sigma} = \langle\ \sigma_{11},\ \sigma_{22},\ \sigma_{12}\ \rangle^T \qquad (A.II.1)$$

$$\boldsymbol{\epsilon} = \langle\ \epsilon_{11},\ \epsilon_{22},\ \gamma_{12}\ \rangle^T\ , \quad \text{where} \quad \gamma_{12} = 2\epsilon_{12}, \quad \text{and} \quad \epsilon_{33} \quad \text{is neglected} \qquad (A.II.2)$$

$$[D] = \frac{E}{(1-\nu^2)} \begin{bmatrix} 1 & \nu & 0 \\ \nu & 1 & 0 \\ 0 & 0 & \frac{(1-\nu)}{2} \end{bmatrix} \qquad (A.II.3)$$

$$\mathbf{u} = \langle\ u_1,\ u_2\ \rangle^T \qquad (A.II.4)$$

where $\mathbf{u}$ is the displacement at any point (x_1,x_2) in an element. Let the element have m nodes. Then equations (A.I.5) to (A.I.7) apply identically to this case also.

Plane Stress Formulations For Creep Analysis With Power Law:

$$\sigma_e = \left[\sigma_{11}^2 + \sigma_{22}^2 - \sigma_{11}\sigma_{22} + 3\sigma_{12}^2\right]^{\frac{1}{2}} \qquad (A.II.5)$$

Define following:

$$\Phi = (2\sigma_{11} - \sigma_{22})\ ; \quad \Psi = (2\sigma_{22} - \sigma_{11}) \qquad (A.II.6a)$$

$$X_1 = AC\sigma_e^{B-1}\, t^{C-1}\ ; \quad X_2 = \frac{(B-1)}{4\sigma_e^2}\ ; \quad X_3 = \frac{3}{2}AC(B-1)\sigma_e^{B-3}\, t^{C-1} \qquad (A.II.6b)$$

The strain rate matrix is (with notations in eqns. A.II.6):

$$\beta = \dot{\epsilon}^c_{ij} = \begin{Bmatrix} \dot{\epsilon}^c_{11} \\ \dot{\epsilon}^c_{22} \\ \dot{\gamma}^c_{12} \end{Bmatrix} = \frac{1}{2} X_1 \begin{Bmatrix} \Phi \\ \Psi \\ 6\sigma_{12} \end{Bmatrix} \qquad (A.II.7)$$

$[S]^n$ is a symmetric matrix of dimensions (3×3); the components of the upper triangle of $[S]^n$ are (with notations in eqns. A.II.6):

$$S_{11} = \frac{\partial \dot{\epsilon}^c_{11}}{\partial \sigma_{11}} = X_1 \left(X_2 \Phi \Phi + 1 \right) \qquad (A.II.8)$$

$$S_{12} = \frac{\partial \dot{\epsilon}^c_{11}}{\partial \sigma_{22}} = X_1 \left(X_2 \Phi \Psi - \frac{1}{2} \right) \qquad (A.II.9)$$

$$S_{13} = \frac{\partial \dot{\epsilon}^c_{11}}{\partial \sigma_{12}} = X_3 \Phi \sigma_{12} \qquad (A.II.10)$$

$$S_{22} = \frac{\partial \dot{\epsilon}^c_{22}}{\partial \sigma_{22}} = X_1 \left(X_2 \Psi \Psi + 1 \right) \qquad (A.II.11)$$

$$S_{23} = \frac{\partial \dot{\epsilon}^c_{22}}{\partial \sigma_{12}} = X_3 \Psi \sigma_{12} \qquad (A.II.12)$$

$$S_{33} = \frac{\partial \dot{\gamma}^c_{12}}{\partial \sigma_{12}} = 3 X_1 (3\, X_2 \sigma_{12} \sigma_{12} + 1) \qquad (A.II.13)$$

$[\bar{D}]^n$ is a (3×3) matrix, defined by equation (3.51). Therefore, for an element of m nodes, $[B]^T[\bar{D}]^n[B]$ is a $(2m \times 2m)$ matrix made of m^2 number of $[B_i]^T[\bar{D}]^n[B_j]$ matrices, each of which has dimensions of (2×2).

Plane Stress Formulations For Creep Analysis With Power Law Ext. II:

The equations (A.II.5) to (A.II.13) apply identically for Power Law Extension II, with t in eqns. (A.II.6b) replaced by $(t - t_{i-1})$, where t is the current time, and t_{i-1} is the time at which the ith load step is applied.

Note: Formulations are not derived for Power Law Extension I, under plane stress conditions.

(III). Axisymmetric Analysis

Axisymmetric General Formulations:

The cylindrical coordinate system is denoted by (r, θ, z). For convenience, coordinate axes r, θ, z are denoted, respectively, by x_1, x_2, x_3. Due to axisymmetry, quantities do not vary with x_2 (ie. θ).

$$\boldsymbol{\sigma} = \langle\, \sigma_{11},\ \sigma_{22},\ \sigma_{33},\ \sigma_{13} \,\rangle^T \qquad (A.III.1)$$

$$\epsilon = \langle\ \epsilon_{11},\ \epsilon_{22},\ \epsilon_{33},\ \gamma_{13}\ \rangle^T\ , \quad \text{where} \quad \gamma_{13} = 2\epsilon_{13} \tag{A.III.2}$$

$$[D] = \frac{E(1-\nu)}{(1+\nu)(1-2\nu)} \begin{bmatrix} 1 & \frac{\nu}{(1-\nu)} & \frac{\nu}{(1-\nu)} & 0 \\ \frac{\nu}{(1-\nu)} & 1 & \frac{\nu}{(1-\nu)} & 0 \\ \frac{\nu}{(1-\nu)} & \frac{\nu}{(1-\nu)} & 1 & 0 \\ 0 & 0 & 0 & \frac{(1-2\nu)}{2(1-\nu)} \end{bmatrix} \tag{A.III.3}$$

$$\mathbf{u} = \langle\ u_1,\ u_3\ \rangle^T \tag{A.III.4}$$

where $\mathbf{u}$ is the displacement at any point (x_1,x_3) in an element. Let the element have m nodes, and let the vector of nodal displacements for the element be denoted by $\mathbf{a}^e$. Then,

$$\mathbf{u} = [N]\,\mathbf{a}^e = \Big[[I]N_1,\ [I]N_2,\ [I]N_3,\ \ldots [I]N_m\Big]\,\mathbf{a}^e \tag{A.III.5}$$

where N_i is the 2-D shape function associated with the ith node (see Zienkiewicz 1977), $[I]$ is the (2×2) identity matrix, $[N]$ is a (2×2m) matrix, and $\mathbf{a}^e$ is a vector of 2m components.

$$\epsilon = [L]\,\mathbf{u}\ , \qquad \text{where} \qquad [L] = \begin{bmatrix} \frac{\partial}{\partial x_1} & 0 \\ \frac{1}{x_1} & 0 \\ 0 & \frac{\partial}{\partial x_3} \\ \frac{\partial}{\partial x_3} & \frac{\partial}{\partial x_1} \end{bmatrix} \tag{A.III.6}$$

$$\epsilon = [B]\,\mathbf{a}^e = \Big[[B_1],\ [B_2],\ [B_3],\ \ldots [B_m]\Big]\,\mathbf{a}^e\ , \qquad \text{where} \quad [B_i] = [L]\,[I]\,N_i \tag{A.III.7}$$

Thus $[B]$ is a (4×2m) matrix made of m number of (4×2) matrices $[B_i]$, defined for the ith node.

Axisymmetric Formulations For Creep Analysis With Power Law:

$$\sigma_e = \left[\sigma_{11}^2 + \sigma_{22}^2 + \sigma_{33}^2 - \sigma_{11}\sigma_{22} - \sigma_{22}\sigma_{33} - \sigma_{33}\sigma_{11} + 3\sigma_{13}^2\right]^{\frac{1}{2}} \tag{A.III.8}$$

Define following:

$$\Phi = \left[2\sigma_{11} - \sigma_{22} - \sigma_{33}\right]\ ; \quad \Psi = \left[2\sigma_{22} - \sigma_{11} - \sigma_{33}\right]\ ; \quad \Omega = \left[2\sigma_{33} - \sigma_{11} - \sigma_{22}\right] \tag{A.III.9a}$$

$$X_1 = AC\sigma_e^{B-1}\,t^{C-1}\ ; \quad X_2 = \frac{(B-1)}{4\sigma_e^2}\ ; \quad X_3 = \frac{3}{2}AC(B-1)\sigma_e^{B-3}\,t^{C-1} \tag{A.III.9b}$$

The strain rate matrix is (with notations in eqns. A.III.9):

$$\beta = \dot{\epsilon}^c_{ij} = \begin{Bmatrix} \dot{\epsilon}^c_{11} \\ \dot{\epsilon}^c_{22} \\ \dot{\epsilon}^c_{33} \\ \dot{\gamma}^c_{13} \end{Bmatrix} = \frac{1}{2} X_1 \begin{Bmatrix} \Phi \\ \Psi \\ \Omega \\ 6\sigma_{13} \end{Bmatrix} \qquad (A.III.10)$$

$[S]^n$ is a symmetric matrix of dimensions (4×4); the components of the upper triangle of $[S]^n$ are (with notations in eqns. A.III.9):

$$S_{11} = \frac{\partial \dot{\epsilon}^c_{11}}{\partial \sigma_{11}} = X_1 \left(X_2 \Phi\Phi + 1 \right) \qquad (A.III.11)$$

$$S_{12} = \frac{\partial \dot{\epsilon}^c_{11}}{\partial \sigma_{22}} = X_1 \left(X_2 \Phi\Psi - \frac{1}{2} \right) \qquad (A.III.12)$$

$$S_{13} = \frac{\partial \dot{\epsilon}^c_{11}}{\partial \sigma_{33}} = X_1 \left(X_2 \Phi\Omega - \frac{1}{2} \right) \qquad (A.III.13)$$

$$S_{14} = \frac{\partial \dot{\epsilon}^c_{11}}{\partial \sigma_{13}} = X_3 \Phi \sigma_{13} \qquad (A.III.14)$$

$$S_{22} = \frac{\partial \dot{\epsilon}^c_{22}}{\partial \sigma_{22}} = X_1 \left(X_2 \Psi\Psi + 1 \right) \qquad (A.III.15)$$

$$S_{23} = \frac{\partial \dot{\epsilon}^c_{22}}{\partial \sigma_{33}} = X_1 \left(X_2 \Psi\Omega - \frac{1}{2} \right) \qquad (A.III.16)$$

$$S_{24} = \frac{\partial \dot{\epsilon}^c_{22}}{\partial \sigma_{13}} = X_3 \Psi \sigma_{13} \qquad (A.III.17)$$

$$S_{33} = \frac{\partial \dot{\epsilon}^c_{33}}{\partial \sigma_{33}} = X_1 \left(X_2 \Omega\Omega + 1 \right) \qquad (A.III.18)$$

$$S_{34} = \frac{\partial \dot{\epsilon}^c_{33}}{\partial \sigma_{13}} = X_3 \Omega \sigma_{13} \qquad (A.III.19)$$

$$S_{44} = \frac{\partial \dot{\gamma}^c_{13}}{\partial \sigma_{13}} = 3X_1 (12\, X_2 \sigma_{13}\sigma_{13} + 1) \qquad (A.III.20)$$

$[\bar{D}]^n$ is a (4×4) matrix, defined by equation (3.51). Therefore, for an element of m nodes, $[B]^T[\bar{D}]^n[B]$ is a $(2m \times 2m)$ matrix made of m^2 number of $[B_i]^T[\bar{D}]^n[B_j]$ matrices, each of which has dimensions of (2×2). In evaluating the stiffness integral, $[B]^T[\bar{D}]^n[B]$ should be multiplied by the appropriate term $2\pi x_1$.

Axisymmetric Formulations For Creep Analysis With Power Law Ext. II:

The equations (A.III.8) to (A.III.20) apply identically for Power Law Extension II, with t in eqns. (A.III.9b) replaced by $(t - t_{i-1})$, where t is the current time, and t_{i-1} is the time at which the ith load step is applied.

Axisymmetric Formulations For Creep Analysis With Power Law Ext. I:

Formulations are given for the case of 2 load steps only. Equations (A.III.8) to (A.III.20) describe the first load step. Let σ_{1e} be the equivalent stress at the end of the duration of the first load step, and let $\sigma_e = \sigma_{2e}$ be the current equivalent stress. Stress σ_e is given by eqn. (A.III.8). Define following:

$$\Phi = \left[2\sigma_{11} - \sigma_{22} - \sigma_{33}\right] \; ; \quad \Psi = \left[2\sigma_{22} - \sigma_{11} - \sigma_{33}\right] \; ; \quad \Omega = \left[2\sigma_{33} - \sigma_{11} - \sigma_{22}\right] \tag{A.III.21a}$$

$$X_1 = \frac{1}{2} AC \left[\sigma_{1e}^{\frac{B}{C}} t_1 + \sigma_e^{\frac{B}{C}} (t - t_1)\right]^{C-1} \sigma_e^{\frac{B}{C}-1} \tag{A.III.21b}$$

$$X_2 = \frac{1}{2}(C-1)\left[\sigma_{1e}^{\frac{B}{C}} t_1 + \sigma_e^{\frac{B}{C}} (t - t_1)\right]^{-1} \sigma_e^{\frac{B}{C}-2} (t - t_1) + \frac{1}{2}\left(\frac{B}{C} - 1\right)\sigma_e^{-2} \tag{A.III.21c}$$

The strain rate matrix is (with notations in eqns. A.III.21):

$$\beta = \dot{\epsilon}_{ij}^c = \begin{Bmatrix} \dot{\epsilon}_{11}^c \\ \dot{\epsilon}_{22}^c \\ \dot{\epsilon}_{33}^c \\ \dot{\gamma}_{13}^c \end{Bmatrix} = X_1 \begin{Bmatrix} \Phi \\ \Psi \\ \Omega \\ 6\sigma_{13} \end{Bmatrix} \tag{A.III.22}$$

$[S]^n$ is a symmetric matrix of dimensions (4×4); the components of the upper triangle of $[S]^n$ are (with notations in eqns. A.III.21):

$$S_{11} = \frac{\partial \dot{\epsilon}_{11}^c}{\partial \sigma_{11}} = X_1 \left(X_2 \Phi\Phi + 2\right) \tag{A.III.23}$$

$$S_{12} = \frac{\partial \dot{\epsilon}_{11}^c}{\partial \sigma_{22}} = X_1 \left(X_2 \Phi\Psi - 1\right) \tag{A.III.24}$$

$$S_{13} = \frac{\partial \dot{\epsilon}_{11}^c}{\partial \sigma_{33}} = X_1 \left(X_2 \Phi\Omega - 1\right) \tag{A.III.25}$$

$$S_{14} = \frac{\partial \dot{\epsilon}_{11}^c}{\partial \sigma_{13}} = X_1 X_2 \Phi 6\sigma_{13} \tag{A.III.26}$$

$$S_{22} = \frac{\partial \dot{\epsilon}_{22}^c}{\partial \sigma_{22}} = X_1 \left(X_2 \Psi\Psi + 2\right) \tag{A.III.27}$$

$$S_{23} = \frac{\partial \dot{\epsilon}_{22}^c}{\partial \sigma_{33}} = X_1 \left(X_2 \Psi\Omega - 1\right) \tag{A.III.28}$$

$$S_{24} = \frac{\partial \dot{\epsilon}_{22}^c}{\partial \sigma_{13}} = X_1 X_2 \Psi 6\sigma_{13} \tag{A.III.29}$$

$$S_{33} = \frac{\partial \dot{\epsilon}_{33}^c}{\partial \sigma_{33}} = X_1 \left(X_2 \Omega\Omega + 2\right) \tag{A.III.30}$$

$$S_{34} = \frac{\partial \dot{\epsilon}_{33}^c}{\partial \sigma_{13}} = X_1 X_2 \Omega 6\sigma_{13} \tag{A.III.31}$$

$$S_{44} = \frac{\partial \dot{\gamma}_{13}^c}{\partial \sigma_{13}} = 6(X_1 X_2\, 6\sigma_{13}\sigma_{13} + 1) \tag{A.III.32}$$

(V). Plane Strain Axisymmetric (P.S.A.) Analysis

P.S.A. General Formulations:

The polar coordinate system is denoted by (r, θ). For convenience, coordinate axes r, θ are denoted, respectively, by x_1, x_2. Due to axisymmetry, quantities do not vary with x_2 (ie. θ). The direction normal to x_1-x_2 plane is denoted by x_3.

$$\boldsymbol{\sigma} = \langle\ \sigma_{11},\ \sigma_{22}\ \rangle^T \quad \text{and} \quad \sigma_{33} = \nu(\sigma_{11} + \sigma_{22}) \tag{A.IV.1}$$

$$\boldsymbol{\epsilon} = \langle\ \epsilon_{11},\ \epsilon_{22}\ \rangle^T \tag{A.IV.2}$$

$$[D] = \frac{E(1-\nu)}{(1+\nu)(1-2\nu)} \begin{bmatrix} 1 & \frac{\nu}{(1-\nu)} \\ \frac{\nu}{(1-\nu)} & 1 \end{bmatrix} \tag{A.IV.3}$$

$$\mathbf{u} = \langle\ u_1\ \rangle \tag{A.IV.4}$$

where $\mathbf{u} = u_1$ is the displacement at any point x_1 in an element. Let the element have m nodes, and let the vector of nodal displacements for the element be denoted by $\mathbf{a}^e$. Then,

$$\mathbf{u} = [N]\,\mathbf{a}^e = \Big[N_1,\ N_2,\ N_3,\ \ldots N_m\Big]\,\mathbf{a}^e \tag{A.IV.5}$$

where N_i is the 1-D shape function associated with the ith node (see Zienkiewicz 1977), $[N]$ is a $(1\times m)$ matrix, and $\mathbf{a}^e$ is a vector of m components.

$$\boldsymbol{\epsilon} = [L]\,\mathbf{u}\ , \qquad \text{where} \qquad [L] = \begin{bmatrix} \frac{\partial}{\partial x_1} \\ \frac{1}{x_1} \end{bmatrix} \tag{A.IV.6}$$

$$\boldsymbol{\epsilon} = [B]\,\mathbf{a}^e = \Big[[B_1],\ [B_2],\ [B_3],\ \ldots [B_m]\Big]\,\mathbf{a}^e\ , \qquad \text{where} \quad [B_i] = [L]\,N_i \tag{A.IV.7}$$

Thus $[B]$ is a $(2\times m)$ matrix made of m number of (2×1) matrices $[B_i]$, defined for the ith node.

P.S.A. Formulations For Creep Analysis With Power Law:

$$\sigma_e = \left[\sigma_{11}^2 + \sigma_{22}^2 - \sigma_{11}\sigma_{22} + \nu(\nu-1)(\sigma_{11}^2 + \sigma_{22}^2 + 2\sigma_{11}\sigma_{22})\right]^{\frac{1}{2}} \tag{A.IV.8}$$

Define following:

$$\Phi = \left[(2-\nu)\sigma_{11} - (1+\nu)\sigma_{22}\right]\ ; \quad \Psi = \left[(2-\nu)\sigma_{22} - (1+\nu)\sigma_{11}\right] \tag{A.IV.9a}$$

$$\Omega = \left[2(\nu^2 - \nu + 1)\sigma_{11} + (2\nu^2 - 2\nu - 1)\sigma_{22}\right] \tag{A.IV.9b}$$

$$\Gamma = \left[2(\nu^2 - \nu + 1)\sigma_{22} + (2\nu^2 - 2\nu - 1)\sigma_{11}\right] \qquad (A.IV.9c)$$

$$X_1 = AC\sigma_e^{B-1}t^{C-1} \; ; \quad X_2 = \frac{(B-1)}{4\sigma_e^2} \; ; \quad \nu_1 = \frac{(2-\nu)}{2} \; ; \quad \nu_2 = \frac{(1+\nu)}{2} \qquad (A.IV.9d)$$

The strain rate matrix is (with notations in eqns. A.IV.9):

$$\beta = \dot{\epsilon}^c_{ij} = \left\{ \begin{array}{c} \dot{\epsilon}^c_{11} \\ \dot{\epsilon}^c_{22} \end{array} \right\} = \frac{1}{2} X_1 \left\{ \begin{array}{c} \Phi \\ \Psi \end{array} \right\} \qquad (A.IV.10)$$

$[S]^n$ is an unsymmetric matrix of dimensions (2×2), the components of which are (with notations in eqns. A.IV.9):

$$S_{11} = \frac{\partial \dot{\epsilon}^c_{11}}{\partial \sigma_{11}} = X_1 \left(X_2 \Phi \Omega + \nu_1\right) \qquad (A.IV.11)$$

$$S_{12} = \frac{\partial \dot{\epsilon}^c_{11}}{\partial \sigma_{22}} = X_1 \left(X_2 \Phi \Gamma - \nu_2\right) \qquad (A.IV.12)$$

$$S_{21} = \frac{\partial \dot{\epsilon}^c_{22}}{\partial \sigma_{11}} = X_1 \left(X_2 \Psi \Omega - \nu_2\right) \qquad (A.IV.13)$$

$$S_{22} = \frac{\partial \dot{\epsilon}^c_{22}}{\partial \sigma_{22}} = X_1 \left(X_2 \Psi \Gamma + \nu_1\right) \qquad (A.IV.14)$$

$[\bar{D}]^n$ is a (2×2) matrix, defined by equation (3.51). Therefore, for an element of m nodes, $[B]^T[\bar{D}]^n[B]$ is a $(m \times m)$ matrix made of m^2 number of $[B_i]^T[\bar{D}]^n[B_j]$ matrices, each of which has dimensions of (1×1). In evaluating the stiffness integral, $[B]^T[\bar{D}]^n[B]$ should be multiplied by the appropriate term $2\pi x_1$.

P.S.A. Formulations For Creep Analysis With Power Law Ext. II:

The equations (A.IV.8) to (A.IV.14) apply identically for Power Law Extension II, with t in eqns. (A.IV.9d) replaced by $(t - t_{i-1})$, where t is the current time, and t_{i-1} is the time at which the ith load step is applied.

Axisymmetric Formulations For Creep Analysis With Power Law Ext. I:

Formulations are given for the case of 2 load steps only. Equations (A.IV.8) to (A.IV.14) describe the first load step. Let σ_{1e} be the equivalent stress at the end of the duration of the first load step, and let $\sigma_e = \sigma_{2e}$ be the current equivalent stress. Stress σ_e is given by eqn. (A.IV.8). Define following:

$$\Phi = \left[(2-\nu)\sigma_{11} - (1+\nu)\sigma_{22}\right] \; ; \quad \Psi = \left[(2-\nu)\sigma_{22} - (1+\nu)\sigma_{11}\right] \qquad (A.IV.15a)$$

$$\Omega = \left[2(\nu^2 - \nu + 1)\sigma_{11} + (2\nu^2 - 2\nu - 1)\sigma_{22}\right] \qquad (A.IV.15b)$$

$$\Gamma = \left[2(\nu^2 - \nu + 1)\sigma_{22} + (2\nu^2 - 2\nu - 1)\sigma_{11}\right] \qquad (A.IV.15c)$$

$$X_1 = \frac{1}{2}AC\left[\sigma_{1e}^{\frac{B}{C}}\, t_1 + \sigma_e^{\frac{B}{C}}\,(t - t_1)\right]^{C-1} \sigma_e^{\frac{B}{C}-1} \qquad (A.IV.15d)$$

$$X_2 = \frac{1}{2}(C-1)\left[\sigma_{1e}^{\frac{B}{C}}\, t_1 + \sigma_e^{\frac{B}{C}}\,(t - t_1)\right]^{-1} \sigma_e^{\frac{B}{C}-2}\,(t - t_1) + \frac{1}{2}\left(\frac{B}{C} - 1\right)\sigma_e^{-2} \qquad (A.IV.15e)$$

The strain rate matrix is (with notations in eqns. A.IV.17):

$$\boldsymbol{\beta} = \dot{\epsilon}_{ij}^c = \left\{ \begin{array}{c} \dot{\epsilon}_{11}^c \\ \dot{\epsilon}_{22}^c \end{array} \right\} = X_1 \left\{ \begin{array}{c} \Phi \\ \Psi \end{array} \right\} \qquad (A.IV.16)$$

$[S]^n$ is an unsymmetric matrix of dimensions (2×2), the components of which are (with notations in eqns. A.IV.15):

$$S_{11} = \frac{\partial \dot{\epsilon}_{11}^c}{\partial \sigma_{11}} = X_1\left(X_2 \Phi \Omega + \nu_1\right) \qquad (A.IV.17)$$

$$S_{12} = \frac{\partial \dot{\epsilon}_{11}^c}{\partial \sigma_{22}} = X_1\left(X_2 \Phi \Gamma - \nu_2\right) \qquad (A.IV.18)$$

$$S_{21} = \frac{\partial \dot{\epsilon}_{22}^c}{\partial \sigma_{11}} = X_1\left(X_2 \Psi \Omega - \nu_2\right) \qquad (A.IV.19)$$

$$S_{22} = \frac{\partial \dot{\epsilon}_{22}^c}{\partial \sigma_{22}} = X_1\left(X_2 \Psi \Gamma + \nu_1\right) \qquad (A.IV.20)$$

(V). Three-Dimensional Analysis

3-D General Formulations:

The orthogonal coordinate system is denoted by x_1, x_2, and x_3.

$$\boldsymbol{\sigma} = \langle\ \sigma_{11},\ \sigma_{22},\ \sigma_{33},\ \sigma_{12},\ \sigma_{23},\ \sigma_{31}\ \rangle^T \qquad (A.V.1)$$

$$\epsilon = \langle\ \epsilon_{11},\ \epsilon_{22},\ \epsilon_{33},\ \gamma_{12},\ \gamma_{23}\ \gamma_{31},\ \rangle^T\ , \quad \text{where} \quad \gamma_{ij} = 2\epsilon_{ij} \qquad (A.V.2)$$

$$[D] = \frac{E(1-\nu)}{(1+\nu)(1-2\nu)} \begin{bmatrix} 1 & \frac{\nu}{(1-\nu)} & \frac{\nu}{(1-\nu)} & 0 & 0 & 0 \\ \frac{\nu}{(1-\nu)} & 1 & \frac{\nu}{(1-\nu)} & 0 & 0 & 0 \\ \frac{\nu}{(1-\nu)} & \frac{\nu}{(1-\nu)} & 1 & 0 & 0 & 0 \\ 0 & 0 & 0 & \frac{(1-2\nu)}{2(1-\nu)} & 0 & 0 \\ 0 & 0 & 0 & 0 & \frac{(1-2\nu)}{2(1-\nu)} & 0 \\ 0 & 0 & 0 & 0 & 0 & \frac{(1-2\nu)}{2(1-\nu)} \end{bmatrix} \qquad (A.V.3)$$

$$\mathbf{u} = \langle\ u_1,\ u_2,\ u_3\ \rangle^T \qquad (A.V.4)$$

where $\mathbf{u}$ is the displacement at any point (x_1, x_2, x_3) in an element. Let the element have m nodes, and let the vector of nodal displacements for the element be denoted by $\mathbf{a}^e$. Then,

$$\mathbf{u} = [N]\,\mathbf{a}^e = \Big[[I]N_1,\ [I]N_2,\ [I]N_3,\ \ldots [I]N_m\Big]\,\mathbf{a}^e \qquad (A.V.5)$$

where N_i is the 3-D shape function associated with the ith node (see Zienkiewicz 1977), $[I]$ is the (3×3) identity matrix, $[N]$ is a $(3\times3m)$ matrix, and $\mathbf{a}^e$ is a vector of $3m$ components.

$$\epsilon = [L]\,\mathbf{u}\ , \qquad \text{where} \qquad [L] = \begin{bmatrix} \frac{\partial}{\partial x_1} & 0 & 0 \\ 0 & \frac{\partial}{\partial x_2} & 0 \\ 0 & 0 & \frac{\partial}{\partial x_3} \\ \frac{\partial}{\partial x_2} & \frac{\partial}{\partial x_1} & 0 \\ 0 & \frac{\partial}{\partial x_3} & \frac{\partial}{\partial x_2} \\ \frac{\partial}{\partial x_3} & 0 & \frac{\partial}{\partial x_1} \end{bmatrix} \qquad (A.V.6)$$

$$\epsilon = [B]\,\mathbf{a}^e = \Big[[B_1],\ [B_2],\ [B_3],\ \ldots [B_m]\Big]\,\mathbf{a}^e\ , \qquad \text{where} \quad [B_i] = [L]\,[I]\,N_i \quad (A.V.7)$$

Thus $[B]$ is a $(6\times3m)$ matrix made of m number of (6×3) matrices $[B_i]$, defined for the ith node.

3-D Formulations For Creep Analysis With Power Law:

$$\sigma_e = \left[\sigma_{11}^2 + \sigma_{22}^2 + \sigma_{33}^2 - \sigma_{11}\sigma_{22} - \sigma_{22}\sigma_{33} - \sigma_{33}\sigma_{11} + 3\sigma_{12}^2 + 3\sigma_{23}^2 + 3\sigma_{31}^2\right]^{\frac{1}{2}} \quad (A.V.8)$$

Define following:

$$\Phi = \left[2\sigma_{11} - \sigma_{22} - \sigma_{33}\right]\ ; \quad \Psi = \left[2\sigma_{22} - \sigma_{11} - \sigma_{33}\right]\ ; \quad \Omega = \left[2\sigma_{33} - \sigma_{11} - \sigma_{22}\right] \quad (A.V.9a)$$

$$X_1 = AC\sigma_e^{B-1}\,t^{C-1}\ ; \quad X_2 = \frac{(B-1)}{4\sigma_e^2}\ ; \quad X_3 = \frac{3}{2}AC(B-1)\sigma_e^{B-3}\,t^{C-1} \quad (A.V.9b)$$

The strain rate matrix is (with notations in eqns. A.V.9):

$$\beta = \dot{\epsilon}_{ij}^c = \begin{Bmatrix} \dot{\epsilon}_{11}^c \\ \dot{\epsilon}_{22}^c \\ \dot{\epsilon}_{33}^c \\ \dot{\gamma}_{12}^c \\ \dot{\gamma}_{23}^c \\ \dot{\gamma}_{31}^c \end{Bmatrix} = \frac{1}{2}X_1 \begin{Bmatrix} \Phi \\ \Psi \\ \Omega \\ 6\sigma_{12} \\ 6\sigma_{23} \\ 6\sigma_{31} \end{Bmatrix} \qquad (A.V.10)$$

$[S]^n$ is a symmetric matrix of dimensions (6×6); the components of the upper triangle of $[S]^n$ are (with notations in eqns. A.V.9):

$$S_{11} = \frac{\partial \dot{\epsilon}^c_{11}}{\partial \sigma_{11}} = X_1 \left(X_2 \Phi \Phi + 1 \right) \qquad (A.V.11)$$

$$S_{12} = \frac{\partial \dot{\epsilon}^c_{11}}{\partial \sigma_{22}} = X_1 \left(X_2 \Phi \Psi - \frac{1}{2} \right) \qquad (A.V.12)$$

$$S_{13} = \frac{\partial \dot{\epsilon}^c_{11}}{\partial \sigma_{33}} = X_1 \left(X_2 \Phi \Omega - \frac{1}{2} \right) \qquad (A.V.13)$$

$$S_{14} = \frac{\partial \dot{\epsilon}^c_{11}}{\partial \sigma_{12}} = X_3 \Phi \sigma_{12} \qquad (A.V.14)$$

$$S_{15} = \frac{\partial \dot{\epsilon}^c_{11}}{\partial \sigma_{23}} = X_3 \Phi \sigma_{23} \qquad (A.V.15)$$

$$S_{16} = \frac{\partial \dot{\epsilon}^c_{11}}{\partial \sigma_{31}} = X_3 \Phi \sigma_{31} \qquad (A.V.16)$$

$$S_{22} = \frac{\partial \dot{\epsilon}^c_{22}}{\partial \sigma_{22}} = X_1 \left(X_2 \Psi \Psi + 1 \right) \qquad (A.V.17)$$

$$S_{23} = \frac{\partial \dot{\epsilon}^c_{22}}{\partial \sigma_{33}} = X_1 \left(X_2 \Psi \Omega - \frac{1}{2} \right) \qquad (A.V.18)$$

$$S_{24} = \frac{\partial \dot{\epsilon}^c_{22}}{\partial \sigma_{12}} = X_3 \Psi \sigma_{12} \qquad (A.V.19)$$

$$S_{25} = \frac{\partial \dot{\epsilon}^c_{22}}{\partial \sigma_{23}} = X_3 \Psi \sigma_{23} \qquad (A.V.20)$$

$$S_{26} = \frac{\partial \dot{\epsilon}^c_{22}}{\partial \sigma_{31}} = X_3 \Psi \sigma_{31} \qquad (A.V.21)$$

$$S_{33} = \frac{\partial \dot{\epsilon}^c_{33}}{\partial \sigma_{33}} = X_1 \left(X_2 \Omega \Omega + 1 \right) \qquad (A.V.22)$$

$$S_{34} = \frac{\partial \dot{\epsilon}^c_{33}}{\partial \sigma_{12}} = X_3 \Omega \sigma_{12} \qquad (A.V.23)$$

$$S_{35} = \frac{\partial \dot{\epsilon}^c_{33}}{\partial \sigma_{23}} = X_3 \Omega \sigma_{23} \qquad (A.V.24)$$

$$S_{36} = \frac{\partial \dot{\epsilon}^c_{33}}{\partial \sigma_{31}} = X_3 \Omega \sigma_{31} \qquad (A.V.25)$$

$$S_{44} = \frac{\partial \dot{\gamma}^c_{12}}{\partial \sigma_{12}} = 3X_1 (12\, X_2 \sigma_{12} \sigma_{12} + 1) \qquad (A.V.26)$$

$$S_{45} = \frac{\partial \dot{\gamma}^c_{12}}{\partial \sigma_{23}} = X_3\, 6 \sigma_{12} \sigma_{23} \qquad (A.V.27)$$

$$S_{46} = \frac{\partial \dot{\gamma}^c_{12}}{\partial \sigma_{31}} = X_3\, 6 \sigma_{12} \sigma_{31} \qquad (A.V.28)$$

$$S_{55} = \frac{\partial \dot{\gamma}^c_{23}}{\partial \sigma_{23}} = 3X_1 (12\, X_2 \sigma_{23} \sigma_{23} + 1) \qquad (A.V.29)$$

$$S_{56} = \frac{\partial \dot{\gamma}^c_{23}}{\partial \sigma_{31}} = X_3\, 6\sigma_{23}\sigma_{31} \qquad (A.V.30)$$

$$S_{66} = \frac{\partial \dot{\gamma}^c_{31}}{\partial \sigma_{31}} = 3X_1(12\, X_2 \sigma_{31}\sigma_{31} + 1) \qquad (A.V.31)$$

$[\bar{D}]^n$ is a (6×6) matrix, defined by equation (3.51). Therefore, for an element of m nodes, $[B]^T[\bar{D}]^n[B]$ is a $(3m \times 3m)$ matrix made of m^2 number of $[B_i]^T[\bar{D}]^n[B_j]$ matrices, each of which has dimensions of (3×3).

3-D Formulations For Creep Analysis With Power Law Ext. II:

The equations (A.V.8) to (A.V.31) apply identically for Power Law Extension II, with t in eqns. (A.V.9b) replaced by $(t - t_{i-1})$, where t is the current time, and t_{i-1} is the time at which the ith load step is applied.

Note: Formulations are not derived for Power Law Extension I, under 3-D conditions.

APPENDIX B

Finite Element Implementation Under Fish's Unified Creep Model

(I). Plane Strain Analysis

Plane Strain General Formulations

The two dimensional coordinate system is denoted by x_1 and x_2. The direction normal to x_1-x_2 plane is denoted by x_3. Equations (A.I.1) to (A.I.7) apply identically here.

Plane Strain Formulations For Creep Analysis With Fish's Model:

$$\sigma_e = \left[\sigma_{11}^2 + \sigma_{22}^2 - \sigma_{11}\sigma_{22} + \nu(\nu-1)(\sigma_{11}^2 + \sigma_{22}^2 + 2\sigma_{11}\sigma_{22}) + 3\sigma_{12}^2\right]^{\frac{1}{2}} \qquad (B.I.1)$$

Define following:

$$\Phi = \left[(2-\nu)\sigma_{11} - (1+\nu)\sigma_{22}\right] \; ; \quad \Psi = \left[(2-\nu)\sigma_{22} - (1+\nu)\sigma_{11}\right] \qquad (B.I.2a)$$

$$\Omega = \left[2(\nu^2 - \nu + 1)\sigma_{11} + (2\nu^2 - 2\nu - 1)\sigma_{22}\right] \qquad (B.I.2b)$$

$$\Gamma = \left[2(\nu^2 - \nu + 1)\sigma_{22} + (2\nu^2 - 2\nu - 1)\sigma_{11}\right] \qquad (B.I.2c)$$

$$X_1 = \frac{1}{2} C \sigma_e^{\mu-1} \exp\{\delta(\bar{t} - \ln \bar{t} - 1)\} \; ; \quad X_2 = \frac{1}{2\sigma_e^2}\{\mu - 1 + \delta\eta(\bar{t} - 1)\} \qquad (B.I.2d)$$

The strain rate matrix is (with notations in eqns. B.I.2):

$$\beta = \dot{\epsilon}_{ij}^c = \begin{Bmatrix} \dot{\epsilon}_{11}^c \\ \dot{\epsilon}_{22}^c \\ \dot{\gamma}_{12}^c \end{Bmatrix} = X_1 \begin{Bmatrix} \Phi \\ \Psi \\ 6\sigma_{12} \end{Bmatrix} \qquad (B.I.3)$$

$[S]^n$ is an unsymmetric matrix of dimensions (3×3), the components of which are (with notations in eqns. B.I.2):

$$S_{11} = \frac{\partial \dot{\epsilon}_{11}^c}{\partial \sigma_{11}} = X_1 \left(X_2 \Phi \Omega + 2 - \nu\right) \qquad (B.I.4)$$

$$S_{12} = \frac{\partial \dot{\epsilon}_{11}^c}{\partial \sigma_{22}} = X_1 \left(X_2 \Phi \Gamma - 1 - \nu\right) \qquad (B.I.5)$$

$$S_{13} = \frac{\partial \dot{\epsilon}_{11}^c}{\partial \sigma_{12}} = X_1 X_2 \Phi \, 6\sigma_{12} \qquad (B.I.6)$$

$$S_{21} = \frac{\partial \dot{\epsilon}^c_{22}}{\partial \sigma_{11}} = X_1 \left(X_2 \Psi \Omega - 1 - \nu \right) \qquad (B.I.7)$$

$$S_{22} = \frac{\partial \dot{\epsilon}^c_{22}}{\partial \sigma_{22}} = X_1 \left(X_2 \Psi \Gamma + 2 - \nu \right) \qquad (B.I.8)$$

$$S_{23} = \frac{\partial \dot{\epsilon}^c_{22}}{\partial \sigma_{12}} = X_1 X_2 \Psi \, 6\sigma_{12} \qquad (B.I.9)$$

$$S_{31} = \frac{\partial \dot{\gamma}^c_{12}}{\partial \sigma_{11}} = X_1 X_2 \Omega \, 6\sigma_{12} \qquad (B.I.10)$$

$$S_{32} = \frac{\partial \dot{\gamma}^c_{12}}{\partial \sigma_{22}} = X_1 X_2 \Gamma \, 6\sigma_{12} \qquad (B.I.11)$$

$$S_{33} = \frac{\partial \dot{\gamma}^c_{12}}{\partial \sigma_{12}} = 6X_1 (6 \, X_2 \sigma_{12} \sigma_{12} + 1) \qquad (B.I.12)$$

$[\bar{D}]^n$ and $[B]^T[\bar{D}]^n[B]$ are as described in Appendix A under plane strain element.

(II). Plane Stress Analysis

Plane Stress General Formulations:

The two dimensional coordinate system is denoted by x_1 and x_2. The direction normal to x_1-x_2 plane is denoted by x_3. Equations (A.II.1)–(A.II.4) and (A.I.5)–(A.I.7) apply identically here.

Plane Stress Formulations For Creep Analysis With Fish's Model:

$$\sigma_e = \left[\sigma_{11}^2 + \sigma_{22}^2 - \sigma_{11}\sigma_{22} + 3\sigma_{12}^2 \right]^{\frac{1}{2}} \qquad (B.II.1)$$

Define following:

$$\Phi = (2\sigma_{11} - \sigma_{22}) \; ; \quad \Psi = (2\sigma_{22} - \sigma_{11}) \qquad (B.II.2a)$$

$$X_1 = \frac{1}{2} C \sigma_e^{\mu - 1} \exp\{\delta(\bar{t} - \ln \bar{t} - 1)\} \; ; \quad X_2 = \frac{1}{2\sigma_e^2} \{\mu - 1 + \delta\eta(\bar{t} - 1)\} \qquad (B.II.2b)$$

The strain rate matrix is (with notations in eqns. B.II.2):

$$\beta = \dot{\epsilon}^c_{ij} = \begin{Bmatrix} \dot{\epsilon}^c_{11} \\ \dot{\epsilon}^c_{22} \\ \dot{\gamma}^c_{12} \end{Bmatrix} = X_1 \begin{Bmatrix} \Phi \\ \Psi \\ 6\sigma_{12} \end{Bmatrix} \qquad (B.II.3)$$

$[S]^n$ is a symmetric matrix of dimensions (3×3); the components of the upper triangle of $[S]^n$ are (with notations in eqns. B.II.2):

$$S_{11} = \frac{\partial \dot{\epsilon}^c_{11}}{\partial \sigma_{11}} = X_1 \left(X_2 \Phi \Phi + 2 \right) \qquad (B.II.4)$$

$$S_{12} = \frac{\partial \dot{\epsilon}^c_{11}}{\partial \sigma_{22}} = X_1 \left(X_2 \Phi \Psi - 1 \right) \qquad (B.II.5)$$

$$S_{13} = \frac{\partial \dot{\epsilon}^c_{11}}{\partial \sigma_{12}} = X_1 X_2 \Phi \, 6\sigma_{12} \qquad (B.II.6)$$

$$S_{22} = \frac{\partial \dot{\epsilon}^c_{22}}{\partial \sigma_{22}} = X_1 \left(X_2 \Psi \Psi + 2 \right) \qquad (B.II.7)$$

$$S_{23} = \frac{\partial \dot{\epsilon}^c_{22}}{\partial \sigma_{12}} = X_1 X_2 \Psi \, 6\sigma_{12} \qquad (B.II.8)$$

$$S_{33} = \frac{\partial \dot{\gamma}^c_{12}}{\partial \sigma_{12}} = 6X_1 (6 \, X_2 \sigma_{12} \sigma_{12} + 1) \qquad (B.II.9)$$

$[\bar{D}]^n$ and $[B]^T[\bar{D}]^n[B]$ are as described in Appendix A under plane stress element.

(III). Axisymmetric Analysis

Axisymmetric General Formulations:

The cylindrical coordinate system is denoted by (r, θ, z). For convenience, coordinate axes r, θ, z are denoted, respectively, by x_1, x_2, x_3. Due to axisymmetry, quantities do not vary with x_2 (ie. θ). Equations (A.III.1) to (A.III.7) apply identically here.

Axisymmetric Formulations For Creep Analysis With Fish's Model:

$$\sigma_e = \left[\sigma_{11}^2 + \sigma_{22}^2 + \sigma_{33}^2 - \sigma_{11}\sigma_{22} - \sigma_{22}\sigma_{33} - \sigma_{33}\sigma_{11} + 3\sigma_{13}^2 \right]^{\frac{1}{2}} \qquad (B.III.1)$$

Define following:

$$\Phi = \left[2\sigma_{11} - \sigma_{22} - \sigma_{33} \right] ; \quad \Psi = \left[2\sigma_{22} - \sigma_{11} - \sigma_{33} \right] ; \quad \Omega = \left[2\sigma_{33} - \sigma_{11} - \sigma_{22} \right] \qquad (B.III.2a)$$

$$X_1 = C\sigma_e^{\mu - 1} \exp\{\delta(\bar{t} - \ln \bar{t} - 1)\} ; \quad X_2 = \frac{1}{4\sigma_e^2} \{ \mu - 1 + \delta\eta(\bar{t} - 1) \} \qquad (B.III.2b)$$

The strain rate matrix is (with notations in eqns. B.III.2):

$$\beta = \dot{\epsilon}^c_{ij} = \begin{Bmatrix} \dot{\epsilon}^c_{11} \\ \dot{\epsilon}^c_{22} \\ \dot{\epsilon}^c_{33} \\ \dot{\gamma}^c_{13} \end{Bmatrix} = \frac{1}{2} X_1 \begin{Bmatrix} \Phi \\ \Psi \\ \Omega \\ 6\sigma_{13} \end{Bmatrix} \qquad (B.III.3)$$

$[S]^n$ is a symmetric matrix of dimensions (4×4); the components of the upper triangle of $[S]^n$ are (with notations in eqns. B.III.2):

$$S_{11} = \frac{\partial \dot{\epsilon}^c_{11}}{\partial \sigma_{11}} = X_1 \left(X_2 \Phi \Phi + 1 \right) \qquad (B.III.4)$$

$$S_{12} = \frac{\partial \dot{\epsilon}^c_{11}}{\partial \sigma_{22}} = X_1 \left(X_2 \Phi \Psi - \frac{1}{2} \right) \qquad (B.III.5)$$

$$S_{13} = \frac{\partial \dot{\epsilon}^c_{11}}{\partial \sigma_{33}} = X_1 \left(X_2 \Phi \Omega - \frac{1}{2} \right) \qquad (B.III.6)$$

$$S_{14} = \frac{\partial \dot{\epsilon}^c_{11}}{\partial \sigma_{13}} = X_1 X_2 \Phi \, 6\sigma_{13} \qquad (B.III.7)$$

$$S_{22} = \frac{\partial \dot{\epsilon}^c_{22}}{\partial \sigma_{22}} = X_1 \left(X_2 \Psi \Psi + 1 \right) \qquad (B.III.8)$$

$$S_{23} = \frac{\partial \dot{\epsilon}^c_{22}}{\partial \sigma_{33}} = X_1 \left(X_2 \Psi \Omega - \frac{1}{2} \right) \qquad (A.III.9)$$

$$S_{24} = \frac{\partial \dot{\epsilon}^c_{22}}{\partial \sigma_{13}} = X_1 X_2 \Psi \, 6\sigma_{13} \qquad (B.III.10)$$

$$S_{33} = \frac{\partial \dot{\epsilon}^c_{33}}{\partial \sigma_{33}} = X_1 \left(X_2 \Omega \Omega + 1 \right) \qquad (B.III.11)$$

$$S_{34} = \frac{\partial \dot{\epsilon}^c_{33}}{\partial \sigma_{13}} = X_1 X_2 \Omega \, 6\sigma_{13} \qquad (B.III.12)$$

$$S_{44} = \frac{\partial \dot{\gamma}^c_{13}}{\partial \sigma_{13}} = 3X_1 (12 \, X_2 \sigma_{13} \sigma_{13} + 1) \qquad (B.III.13)$$

$[\bar{D}]^n$ and $[B]^T[\bar{D}]^n[B]$ are as described in Appendix A under axisymmetric element.

(V). Plane Strain Axisymmetric (P.S.A.) Analysis

P.S.A. General Formulations:

The polar coordinate system is denoted by (r, θ). For convenience, coordinate axes r, θ are denoted, respectively, by x_1, x_2. Due to axisymmetry, quantities do not vary with x_2 (ie. θ). The direction normal to x_1-x_2 plane is denoted by x_3. Equations (A.IV.1) to (A.IV.7) apply identically here.

P.S.A. Formulations For Creep Analysis With Fish's Model:

$$\sigma_e = \left[\sigma_{11}^2 + \sigma_{22}^2 - \sigma_{11}\sigma_{22} + \nu(\nu - 1)(\sigma_{11}^2 + \sigma_{22}^2 + 2\sigma_{11}\sigma_{22}) \right]^{\frac{1}{2}} \qquad (B.IV.1)$$

Define following:

$$\Phi = \left[(2 - \nu)\sigma_{11} - (1 + \nu)\sigma_{22} \right] ; \quad \Psi = \left[(2 - \nu)\sigma_{22} - (1 + \nu)\sigma_{11} \right] \qquad (B.IV.2a)$$

$$\Omega = \left[2(\nu^2 - \nu + 1)\sigma_{11} + (2\nu^2 - 2\nu - 1)\sigma_{22} \right] \qquad (B.IV.2b)$$

$$\Gamma = \left[2(\nu^2 - \nu + 1)\sigma_{22} + (2\nu^2 - 2\nu - 1)\sigma_{11} \right] \qquad (B.IV.2c)$$

$$X_1 = \frac{1}{2}\, C\sigma_e^{\mu-1}\, \exp\{\delta(\bar{t} - \ln \bar{t} - 1)\}\ ; \quad X_2 = \frac{1}{2\sigma_e^2}\{\mu - 1 + \delta\eta(\bar{t} - 1)\} \quad (B.IV.2d)$$

The strain rate matrix is (with notations in eqns. B.IV.2):

$$\beta = \dot{\epsilon}_{ij}^c = \left\{ \begin{array}{c} \dot{\epsilon}_{11}^c \\ \dot{\epsilon}_{22}^c \end{array} \right\} = X_1 \left\{ \begin{array}{c} \Phi \\ \Psi \end{array} \right\} \qquad (B.IV.3)$$

$[S]^n$ is an unsymmetric matrix of dimensions (2×2), the components of which are (with notations in eqns. B.IV.2):

$$S_{11} = \frac{\partial \dot{\epsilon}_{11}^c}{\partial \sigma_{11}} = X_1\,(X_2 \Phi\Omega + 2 - \nu) \qquad (B.IV.4)$$

$$S_{12} = \frac{\partial \dot{\epsilon}_{11}^c}{\partial \sigma_{22}} = X_1\,(X_2 \Phi\Gamma - 1 - \nu) \qquad (B.IV.5)$$

$$S_{21} = \frac{\partial \dot{\epsilon}_{22}^c}{\partial \sigma_{11}} = X_1\,(X_2 \Psi\Omega - 1 - \nu) \qquad (B.IV.6)$$

$$S_{22} = \frac{\partial \dot{\epsilon}_{22}^c}{\partial \sigma_{22}} = X_1\,(X_2 \Psi\Gamma + 2 - \nu) \qquad (B.IV.7)$$

$[\bar{D}]^n$ and $[B]^T[\bar{D}]^n[B]$ are as described in Appendix A, under P.S.A. element.

(V). Three-Dimensional Analysis

3-D General Formulations:

The orthogonal coordinate system is denoted by x_1, x_2, and x_3. Equations (A.V.1) to (A.V.9) apply identically here.

3-D Formulations For Creep Analysis With Fish's Model:

$$\sigma_e = \left[\sigma_{11}^2 + \sigma_{22}^2 + \sigma_{33}^2 - \sigma_{11}\sigma_{22} - \sigma_{22}\sigma_{33} - \sigma_{33}\sigma_{11} + 3\sigma_{12}^2 + 3\sigma_{23}^2 + 3\sigma_{31}^2\right]^{\frac{1}{2}} \quad (B.V.1)$$

Define following:

$$\Phi = \left[2\sigma_{11} - \sigma_{22} - \sigma_{33}\right]\ ; \quad \Psi = \left[2\sigma_{22} - \sigma_{11} - \sigma_{33}\right]\ ; \quad \Omega = \left[2\sigma_{33} - \sigma_{11} - \sigma_{22}\right] \quad (B.V.2a)$$

$$X_1 = C\sigma_e^{\mu-1}\, \exp\{\delta(\bar{t} - \ln \bar{t} - 1)\}\ ; \quad X_2 = \frac{1}{4\sigma_e^2}\{\mu - 1 + \delta\eta(\bar{t} - 1)\} \qquad (B.V.2b)$$

The strain rate matrix is (with notations in eqns. B.V.2):

$$\beta = \dot{\epsilon}_{ij}^c = \left\{ \begin{array}{c} \dot{\epsilon}_{11}^c \\ \dot{\epsilon}_{22}^c \\ \dot{\epsilon}_{33}^c \\ \dot{\gamma}_{12}^c \\ \dot{\gamma}_{23}^c \\ \dot{\gamma}_{31}^c \end{array} \right\} = \frac{1}{2} X_1 \left\{ \begin{array}{c} \Phi \\ \Psi \\ \Omega \\ 6\sigma_{12} \\ 6\sigma_{23} \\ 6\sigma_{31} \end{array} \right\} \qquad (B.V.3)$$

$[S]^n$ is a symmetric matrix of dimensions (6×6); the components of the upper triangle of $[S]^n$ are (with notations in eqns. B.V.2):

$$S_{11} = \frac{\partial \dot{\epsilon}^c_{11}}{\partial \sigma_{11}} = X_1 \left(X_2 \Phi \Phi + 1 \right) \qquad (B.V.3)$$

$$S_{12} = \frac{\partial \dot{\epsilon}^c_{11}}{\partial \sigma_{22}} = X_1 \left(X_2 \Phi \Psi - \frac{1}{2} \right) \qquad (B.V.4)$$

$$S_{13} = \frac{\partial \dot{\epsilon}^c_{11}}{\partial \sigma_{33}} = X_1 \left(X_2 \Phi \Omega - \frac{1}{2} \right) \qquad (B.V.5)$$

$$S_{14} = \frac{\partial \dot{\epsilon}^c_{11}}{\partial \sigma_{12}} = X_1 X_2 \Phi \, 6\sigma_{12} \qquad (B.V.6)$$

$$S_{15} = \frac{\partial \dot{\epsilon}^c_{11}}{\partial \sigma_{23}} = X_1 X_2 \Phi \, 6\sigma_{23} \qquad (B.V.7)$$

$$S_{16} = \frac{\partial \dot{\epsilon}^c_{11}}{\partial \sigma_{31}} = X_1 X_2 \Phi \, 6\sigma_{31} \qquad (B.V.8)$$

$$S_{22} = \frac{\partial \dot{\epsilon}^c_{22}}{\partial \sigma_{22}} = X_1 \left(X_2 \Psi \Psi + 1 \right) \qquad (B.V.9)$$

$$S_{23} = \frac{\partial \dot{\epsilon}^c_{22}}{\partial \sigma_{33}} = X_1 \left(X_2 \Psi \Omega - \frac{1}{2} \right) \qquad (B.V.10)$$

$$S_{24} = \frac{\partial \dot{\epsilon}^c_{22}}{\partial \sigma_{12}} = X_1 X_2 \Psi \, 6\sigma_{12} \qquad (B.V.11)$$

$$S_{25} = \frac{\partial \dot{\epsilon}^c_{22}}{\partial \sigma_{23}} = X_1 X_2 \Psi \, 6\sigma_{23} \qquad (B.V.12)$$

$$S_{26} = \frac{\partial \dot{\epsilon}^c_{22}}{\partial \sigma_{31}} = X_1 X_2 \Psi \, 6\sigma_{31} \qquad (B.V.13)$$

$$S_{33} = \frac{\partial \dot{\epsilon}^c_{33}}{\partial \sigma_{33}} = X_1 \left(X_2 \Omega \Omega + 1 \right) \qquad (B.V.14)$$

$$S_{34} = \frac{\partial \dot{\epsilon}^c_{33}}{\partial \sigma_{12}} = X_1 X_2 \Omega \, 6\sigma_{12} \qquad (B.V.15)$$

$$S_{35} = \frac{\partial \dot{\epsilon}^c_{33}}{\partial \sigma_{23}} = X_1 X_2 \Omega \, 6\sigma_{23} \qquad (B.V.16)$$

$$S_{36} = \frac{\partial \dot{\epsilon}^c_{33}}{\partial \sigma_{31}} = X_1 X_2 \Omega \, 6\sigma_{31} \qquad (B.V.17)$$

$$S_{44} = \frac{\partial \dot{\gamma}^c_{12}}{\partial \sigma_{12}} = 3X_1 (12 \, X_2 \sigma_{12} \sigma_{12} + 1) \qquad (B.V.18)$$

$$S_{45} = \frac{\partial \dot{\gamma}^c_{12}}{\partial \sigma_{23}} = 36 X_1 X - 2 \, \sigma_{12} \sigma_{23} \qquad (B.V.19)$$

$$S_{46} = \frac{\partial \dot{\gamma}^c_{12}}{\partial \sigma_{31}} = 36 X_1 X_2 \, \sigma_{12} \sigma_{31} \qquad (B.V.20)$$

$$S_{55} = \frac{\partial \dot{\gamma}^c_{23}}{\partial \sigma_{23}} = 3X_1 (12 \, X_2 \sigma_{23} \sigma_{23} + 1) \qquad (B.V.21)$$

$$S_{56} = \frac{\partial \dot{\gamma}^c_{23}}{\partial \sigma_{31}} = 36 X_1 X_2 \, \sigma_{23} \sigma_{31} \qquad (B.V.22)$$

$$S_{66} = \frac{\partial \dot{\gamma}^c_{31}}{\partial \sigma_{31}} = 3 X_1 (12 \, X_2 \sigma_{31} \sigma_{31} + 1) \qquad (B.V.23)$$

$[\bar{D}]^n$ and $[B]^T[\bar{D}]^n[B]$ are as described in Appendix A under 3-D element.

APPENDIX C

Finite Element Implementation Of Domaschuk's Creep Model

Let K_c denote the tangent bulk creep function (eqn. 3.33) and G_c the tangent shear creep function (eqn. 3.34). Following quantities are defined:

$$\Phi = K_c + \frac{4G_c}{3} \; ; \qquad \Psi = K_c - \frac{2G_c}{3} \tag{C.1}$$

(I). Plane Strain Analysis

The two dimensional coordinate system is denoted by x_1 and x_2. The direction normal to x_1-x_2 plane is denoted by x_3.

$$d\boldsymbol{\sigma} = \langle\ d\sigma_{11},\ d\sigma_{22},\ d\sigma_{12}\ \rangle^T \ , \quad \text{with} \quad d\sigma_{33} = \Psi(d\epsilon_{11} + d\epsilon_{22}) \tag{C.I.1}$$

$$d\boldsymbol{\epsilon} = \langle\ d\epsilon_{11},\ d\epsilon_{22},\ d\gamma_{12}\ \rangle^T \ , \quad \text{where} \quad d\gamma_{12} = 2d\epsilon_{12} \tag{C.I.2}$$

$$\mathbf{u} = \langle\ u_1,\ u_2\ \rangle^T \tag{C.I.3}$$

$$d\boldsymbol{\sigma} = [\bar{D}]\, d\boldsymbol{\epsilon} \ , \qquad \text{where} \qquad [\bar{D}] = \begin{bmatrix} \Phi & \Psi & 0 \\ \Psi & \Phi & 0 \\ 0 & 0 & 2G_c \end{bmatrix} \tag{C.I.4}$$

Equations (A.I.5)–(A.I.7) apply identically here. $[B]$ is defined in eqn. (A.I.7).

(II). Axisymmetric Analysis

The cylindrical coordinate system is denoted by (r, θ, z). For convenience, coordinate axes r, θ, z are denoted, respectively, by x_1, x_2, x_3. Due to axisymmetry, quantities do not vary with x_2 (ie. θ).

$$d\boldsymbol{\sigma} = \langle\ d\sigma_{11},\ d\sigma_{22},\ d\sigma_{33},\ d\sigma_{13}\ \rangle^T \tag{C.II.1}$$

$$d\boldsymbol{\epsilon} = \langle\ d\epsilon_{11},\ d\epsilon_{22},\ d\epsilon_{33},\ d\gamma_{13}\ \rangle^T \ , \quad \text{where} \quad d\gamma_{13} = 2d\epsilon_{13} \tag{C.II.2}$$

$$\mathbf{u} = \langle\ u_1,\ u_3\ \rangle^T \tag{C.II.3}$$

$$d\boldsymbol{\sigma} = [\bar{D}]\, d\boldsymbol{\epsilon} \ , \qquad \text{where} \qquad [\bar{D}] = \begin{bmatrix} \Phi & \Psi & \Psi & 0 \\ \Psi & \Phi & \Psi & 0 \\ \Psi & \Psi & \Phi & 0 \\ 0 & 0 & 0 & 2G_c \end{bmatrix} \tag{C.II.4}$$

Equations (A.III.5)–(A.III.7) apply identically here. $[B]$ is defined in eqn. (A.III.7). In evaluating the stiffness integral, $[B]^T[\bar{D}][B]$ in eqn. (3.61) should be multiplied by the appropriate term $2\pi x_1$.

(V). Plane Strain Axisymmetric (P.S.A.) Analysis

The polar coordinate system is denoted by (r, θ). For convenience, coordinate axes r, θ are denoted, respectively, by x_1, x_2. Due to axisymmetry, quantities do not vary with x_2 (ie. θ). The direction normal to x_1-x_2 plane is denoted by x_3.

$$d\boldsymbol{\sigma} = \langle\ d\sigma_{11},\ d\sigma_{22}\ \rangle^T \quad \text{and} \quad d\sigma_{33} = \Psi(d\epsilon_{11} + d\epsilon_{22}) \tag{C.III.1}$$

$$d\boldsymbol{\epsilon} = \langle\ d\epsilon_{11},\ d\epsilon_{22}\ \rangle^T \tag{C.III.2}$$

$$\mathbf{u} = \langle\ u_1\ \rangle \tag{C.III.3}$$

$$d\boldsymbol{\sigma} = [\bar{D}]\, d\boldsymbol{\epsilon}\ , \qquad \text{where} \qquad [\bar{D}] = \begin{bmatrix} \Phi & \Psi \\ \Psi & \Phi \end{bmatrix} \tag{C.III.4}$$

Equations (A.IV.5)–(A.IV.7) apply identically here. $[B]$ is defined in eqn. (A.IV.7). In evaluating the stiffness integral, $[B]^T[\bar{D}][B]$ in eqn. (3.61) should be multiplied by the appropriate term $2\pi x_1$.

(IV). Three-Dimensional Analysis

The orthogonal coordinate system is denoted by x_1, x_2, and x_3.

$$d\boldsymbol{\sigma} = \langle\ d\sigma_{11},\ d\sigma_{22},\ d\sigma_{33},\ d\sigma_{12},\ d\sigma_{23},\ d\sigma_{31}\ \rangle^T \tag{C.IV.1}$$

$$d\boldsymbol{\epsilon} = \langle\ d\epsilon_{11},\ d\epsilon_{22},\ d\epsilon_{33},\ d\gamma_{12},\ d\gamma_{23},\ d\gamma_{31}\ \rangle^T\ , \quad \text{where} \quad d\gamma_{ij} = 2d\epsilon_{ij} \tag{C.IV.2}$$

$$\mathbf{u} = \langle\ u_1,\ u_2,\ u_3\ \rangle^T \tag{C.IV.3}$$

$$d\boldsymbol{\sigma} = [\bar{D}]\, d\boldsymbol{\epsilon}\ , \qquad \text{where} \qquad [\bar{D}] = \begin{bmatrix} \Phi & \Psi & \Psi & 0 & 0 & 0 \\ \Psi & \Phi & \Psi & 0 & 0 & 0 \\ \Psi & \Psi & \Phi & 0 & 0 & 0 \\ 0 & 0 & 0 & 2G_c & 0 & 0 \\ 0 & 0 & 0 & 0 & 2G_c & 0 \\ 0 & 0 & 0 & 0 & 0 & 2G_c \end{bmatrix} \tag{C.IV.4}$$

Equations (A.V.5)–(A.V.7) apply identically here. $[B]$ is defined in eqn. (A.V.7).

APPENDIX D

Finite Element Codes For Creep Analysis

(I). Code ITFECC - A

The computer code ITFECC-A employs a "macro-programming language", which permits a sequence of finite element processes specified by the user. The problem size and extent is defined by the input of an initial set of global control parameters. Thereafter, the mesh details (except for boundary conditions) are specified. The macro program mode is activated next, by which boundary condition details and solution process are specified.

See Appendix E for a sample input data file and corresponding output. A brief description of control parameters, macro commands, and element subroutines are provided below; however, for detailed description of features of the code, preparation of input data, and interpretation of output results, **reference should be made to the user manual** for code ITFECC-A.

Global Control Parameters:

NUMNP : No. of nodes.

NUMEL : No. of elements.

NUMMAT : No. of different material sets.

NDM : No. of dimensions for the problem.

NDF : No. of degrees of freedom per node.

NEN : Maximum no. of nodes connected to an element.

NSN : No. of stresses involved in the analysis.

LGS : No. of Gauss points per element for maintaining stress history.

NLD : No. of load steps.

NAD : No. of additional degrees of freedom per element.

ITERC : Iteration indicator.[1] (see Notes on next page)

KAUTO : Automatic time step increase indicator.[2] (see Notes on next page)

NCYCL : Maximum no. of solution cycles for the analysis.

THETA : Value of θ (see eqn. 3.45).

TTIME : Maximum value of elapsed time upto which solution process would be continued.

NAFE : No. of adfreeze elements.

LAGS : No. of integration points ($\leq$ LGS) for adfreeze elements.

Notes:

[1] If ITERC < 0, iteration will be continued until convergence; if ITERC $= 0$, no iterations will be performed; if ITERC $=$ N, (N > 0), a maximum of N iterations may be performed per time step.

[2] If KAUTO $\neq 0$, automatic increases of time step could be made; otherwise, every time step increase should be explicitly specified.

Macro Commands: A list of macro commands available in ITFECC-A is given below; for details, see user manual for ITFECC-A.

Control Macro Commands

Command	Description
ITFC	Starts the program (code ITFECC-A).
MACR	Starts the macro-program mode.
END	Terminates the analysis.

Macro-type Commands For Mesh Input

Command	Description
COOR	Read, generate and print nodal coordinate data.
ELEM	Read, generate and print element connectivity data and material set numbers.
END	Signifies the end of mesh data input excluding the boundary condition data.
MATE	Read and print element material data.
POLA	Convert polar coordinates to cartesian.
SPHE	Convert spherical coordinates to cartesian.
NOPR	Suppress output of subsequent data.
PAGE	Change carriage control for output.
PRIN	Resume printing of subsequent data.

Programming Macro Commands

Command	Description
ATDT	Controls automatic check/increase of time increment.
AUTO	Signals the automatic increase of time increment.
BOUN	Controls input of boundary condition codes.
CHNG	Signals a change in boundary conditions.
CREP	Signals the start of creep analysis, (prior to CREP, the program conducts elastic analysis).
DATA	Controls reading of specified data from specified disk/tape units (for resuming a previously terminated analysis).
DISK	Specifies the disk/tape unit number for output of specified displacement quantities with time.
DISP	Prints nodal displacement at specified steps.
DT	May be used to specify initial time step.
END	Signals the end of macro command sequence.
FORC	Controls input of boundary condition forces and displacements.
FORM	Forms the right hand side for global equilibrium equation system.
INDT	Increases length of time increment whenever this macro is encountered, by a specified amount.
ITER	Controls the start of an iteration loop.
ITNX	Marks the end of an iteration loop, and automatically checks for convergence.
LOOP	Controls the start of a particular solution loop for a specified number of time steps.
NEXT	Marks the end of a solution loop started by a macro LOOP.
NOCR	Terminates creep analysis and returns to elastic analysis.
NOMC	Suppresses printing of macro commands during analysis.
NOPR	Suppresses printing of boundary condition details.
NOPS	Suppresses all activities invoked by macro PRST.
PLOT	Writes specified displacement quantities at specified intervals to a specified disk/tape unit (in a form suitable for plotting).
PMAC	Enables printing of all macro commands during analysis.

Programming Macro Commands *cont.*

Command	Description
PRST	Can be used to control output of results for stresses.
PUNC	Controls writing specified results to specified disk/tape units.
RATE	Controls the input of rate boundary conditions.
RDSK	Selects nodes/elements for reaction evaluation.
REAC	Controls the computation and printing of reactions.
REPT	Compiles selected sums of reactions (in a form suitable for plotting).
RITE	Prints specified current arrays as output.
SDSK	Selects stress quantities (for plotting) and relevant disk/tape units.
SOLV	Solves the global equilibrium equation system.
SRDK	Selects elements for monitoring strain rates.
SRTP	Compiles selected strain rates (in a form suitable for plotting).
STPT	Compiles selected stress quantities with time (for plotting).
STRE	Evaluates stress increments.
STRS	Prints stress values at specified steps in a time-incrementing loop.
TANG	Forms the symmetric tangent stiffness matrix.
TIME	Updates elapsed time by the length of the current time step.
TOLD	Controls tolerance limit for the convergence check.
UTAN	Forms the unsymmetric tangent stiffness matrix.

Element Library

Each type of element is given a designated name as ELMT*nn* , where *nn* is the allocated number for that element subroutine. Note that all elements under power law are capable of handling multiple load steps under Power Law Extension II. The available element subroutines are:

Name	Description
ELMT01	Plane strain axisymmetric frozen soil/ice element under power law.
ELMT02	1-D element under power law.
ELMT03	1-D element under Fish's model.
ELMT04	Plane strain axisymmetric frozen soil/ice element under Fish's model.
ELMT05	Axisymmetric frozen soil/ice element under power law.
ELMT06	Axisymmetric linear elastic element (for use in creep analysis).

Element Library *cont.*

ELMT07	Axisymmetric frozen soil/ice element under Fish's model.
ELMT08	Plane strain frozen soil/ice element under power law.
ELMT09	Plane strain linear elastic element (for use in creep analysis).
ELMT10	Plane strain frozen soil/ice element under Fish's model.
ELMT11	Plane stress frozen soil/ice element under power law.
ELMT12	Plane stress linear elastic element (for use in creep analysis).
ELMT13	Plane stress frozen soil/ice element under Fish's model.
ELMT14	3-D frozen soil/ice element under power law.
ELMT15	3-D linear elastic element (for use in creep analysis).
ELMT16	3-D frozen soil/ice element under Fish's model.
ELMT17	Adfreeze/bond strength (interface) element for 2-D analysis.

(II). Code ITFECC - B

This code is very similar to ITFECC-A in organization and structure. Most of the macros employed in ITFECC-A are available here. The element library includes two element subroutines, ie.:

Name	Description
ELMT01	Plane strain axisymmetric frozen soil/ice element under Power Law Extension I.
ELMT02	Axisymmetric frozen soil/ice element under Power Law Extension I.

(III). Code ILFENP

The computer code ILFENP employs a basic modular structure, an execution sequence, and a macro-programming language similar to code ITFECC-A, except for the basic difference that ILFENP is written using a load incremental algorithm. A brief description of global control parameters, macro commands, and element subroutines for code ILFENP is provided here; for details, **reference should be made to the user manual** for the code ILFENP.

Global Control Parameters

These parameters are identical to those listed earlier for the code ITFECC-A, except that the parameters TTIME, NAFE, LAGS are not used, and NLD is not relevant.

Control Macro Commands

These are similar to those listed earlier for the code ITFECC-A, except that the macro command to start the program is ILFN.

Macro-type Commands For Mesh Input

These are identical to those listed earlier for the code ITFECC-A.

Programming Macro Commands

Following macro commands are functionally identical to corresponding macro commands listed earlier under code ITFECC-A:

BOUN, DATA, DISK, DISP, END, FORC, FORM, ITER, ITNX, NEXT, NOMC, NOPR, NOPS, PLOT, PMAC, PRST, PUNC, RITE, SDSK, SOLV, STPT, STRE, TANG, TOLD, UTAN.

Following additional/different macro commands are available:

Command	Description
CONV	Performs a convergence check for non-linear elastic problems.
LOOP	Divides the applied load into a specified no. of load steps and starts a load incrementing solution loop.
STRS	Prints stress values at specified steps in a load-incrementing loop.
TIME	Increments the applied load by a specified increment.

Element Library

Element designation is similar to that in ITFECC-A. The subroutine list is:

Name	Description
ELMT01	Plane strain axisymmetric frozen soil/ice element under Domaschuk's model.
ELMT02	Axisymmetric element under Domaschuk's model.
ELMT03	Plane strain element under Domaschuk's model.
ELMT04	Plane stress element under Domaschuk's model.
ELMT05	3-D element under Domaschuk's model.

The same element subroutines above can be used to represent linear elastic elements by specifying time of solution = 0, and by using elastic bulk and shear modulii appropriately (see user manual for code ILFENP).

APPENDIX E

Sample Input Data File:

```
ITFC * I-6* Creep in Beam w Plane Stress- S.S. beam*Demo *22/06/91*
   55   10    1    2    2    8    3    1    1
   -1    185645        0.5   20960.0
COOR
    1    1        0.0      150.0
   11           500.0      150.0
   12    1        0.0      112.5
   22           500.0      112.5
   23    1        0.0       75.0
   33           500.0       75.0
   34    1        0.0       37.5
   44           500.0       37.5
   45    1        0.0        0.0
   55           500.0        0.0

ELEM
    1    1    1   23   25    3   12   24   14    2    2
    6    1   23   45   47   25   34   46   36   24    2

MATE
    1   11
  2.0D+05       0.49  0.001300       2.00       0.40
      0.0        0.0        2.0      100.0

END
MACR
BOUN                1
FORC                1
TANG,FORM
SOLV
DISP
NOPS
STRE
CREP
TOLD              0.1
NOMC
AUTO             0.01       50.0
LOOP              200
ATDT              0.5
TIME
ITER
TANG,FORM
SOLV
STRE
ITNX
DISP              200
STRS              200
NEXT
END
BOUN                1
   13    2   -1   -1
   21         1    1
   35    2   -1   -1
   43         1    1
    1   11        -1
   45                1
   11   11   -1
   55         1

FORC                1
   33                     200.0

STOP
```

Output File from ITFECC-A:

```
0ITFC * I-6* Creep in Beam w Plane Stress- S.S. beam*Demo *22/06/91*

     NUMBER OF NODAL POINTS          =    55
     NUMBER OF ELEMENTS              =    10
     NUMBER OF MATERIAL SETS         =     1
     DIMENSION OF COORDINATE SPACE=     2
     DEGREE OF FREEDOMS / NODE       =     2
     NODES PER ELEMENT (MAXIMUM)     =     8
     NUMBER OF STRESSES INVOLVED     =     3
     NO OF GAUSS PTS FOR STRESSES    =     1
     NO OF LOAD INCREMENTS           =     1
     EXTRA D.O.F. TO ELEMENT         =     0
     ITERATION CODE                  =    -1
     AUTO TIME SELECTION CODE        =     1
     MAX NO OF SOLUTION CYCLES       = 85645
     THETA (FOR STRESSES)            =  0.50
     TOTAL TIME FOR AUTO ANALYSIS    = 20960.000
     NO OF ADFREEZE/BOND ELEMENTS    =     0
     NO OF GAUSS PTS FOR ADFR ELMS=     0


0ITFC * I-6* Creep in Beam w Plane Stress- S.S. beam*Demo *22/06/91*
     NODAL COORDINATES
      NODE       1 COORD       2 COORD
         1          0.          150.0
         2       50.00          150.0
         3       100.0          150.0
         4       150.0          150.0
         5       200.0          150.0
         6       250.0          150.0
         7       300.0          150.0
         8       350.0          150.0
         9       400.0          150.0
        10       450.0          150.0
        11       500.0          150.0
        12          0.          112.5
        13       50.00          112.5
        14       100.0          112.5
        15       150.0          112.5
        16       200.0          112.5
        17       250.0          112.5
        18       300.0          112.5
        19       350.0          112.5
        20       400.0          112.5
        21       450.0          112.5
        22       500.0          112.5
        23          0.          75.00
        24       50.00          75.00
        25       100.0          75.00
        26       150.0          75.00
        27       200.0          75.00
        28       250.0          75.00
        29       300.0          75.00
        30       350.0          75.00
        31       400.0          75.00
        32       450.0          75.00
        33       500.0          75.00
        34          0.          37.50
        35       50.00          37.50
        36       100.0          37.50
        37       150.0          37.50
        38       200.0          37.50
        39       250.0          37.50
        40       300.0          37.50
        41       350.0          37.50
        42       400.0          37.50
```

```
        43     450.0          37.50
        44     500.0          37.50
        45        0.             0.
        46     50.00             0.
        47     100.0             0.
        48     150.0             0.
        49     200.0             0.
        50     250.0             0.
0ITFC * I-6* Creep in Beam w Plane Stress- S.S. beam*Demo *22/06/91*
     NODAL COORDINATES
      NODE       1 COORD       2 COORD
        51     300.0             0.
        52     350.0             0.
        53     400.0             0.
        54     450.0             0.
        55     500.0             0.
0ITFC * I-6* Creep in Beam w Plane Stress- S.S. beam*Demo *22/06/91*
     ELEMENTS
   ELEMENT  MATERIAL  1 NODE  2 NODE  3 NODE  4 NODE  5 NODE  6 NODE  7 NODE  8 NODE
         1         1       1      23      25       3      12      24      14       2
         2         1       3      25      27       5      14      26      16       4
         3         1       5      27      29       7      16      28      18       6
         4         1       7      29      31       9      18      30      20       8
         5         1       9      31      33      11      20      32      22      10
         6         1      23      45      47      25      34      46      36      24
         7         1      25      47      49      27      36      48      38      26
         8         1      27      49      51      29      38      50      40      28
         9         1      29      51      53      31      40      52      42      30
        10         1      31      53      55      33      42      54      44      32
0ITFC * I-6* Creep in Beam w Plane Stress- S.S. beam*Demo *22/06/91*
     MATERIAL PROPERTIES
     MATERIAL SET  1 FOR ELEMENT TYPE11
          PLANE STRESS CREEP/ELASTIC ELEMENT
          YOUNGS MODULAS          =     0.20000E+06
          POISSONS RATIO          =     0.49000
          PARAMETER "A"           =     0.13000E-02
          PARAMETER "B"           =      2.0000
          PARAMETER "C"           =     0.40000
          BODY FORCES IN R,Z      =          0.                0.
          ORDER OF NUMER INTGRN   =      2.0000
          THICKNESS OF DOMAIN     =      100.00

1 M A C R O - P R O G R A M  M O D E
0ITFC * I-6* Creep in Beam w Plane Stress- S.S. beam*Demo *22/06/91*

   *     1   BOUN            1.0000             0.      *
   *     2   FORC            1.0000             0.      *
   *     3   TANG FORM          0.              0.      *
   *     4   SOLV               0.              0.      *
   *     5   DISP               0.              0.      *
   *     6   NOPS               0.              0.      *
   *     7   STRE               0.              0.      *
   *     8   CREP               0.              0.      *
   *     9   TOLD           0.10000             0.      *
   *    10   NOMC               0.              0.      *
   *    11   AUTO          0.10000E-01      50.000      *
   *    12   LOOP            200.00             0.      *
   *    13   ATDT            0.50000             0.      *
   *    14   TIME               0.              0.      *
   *    15   ITER               0.              0.      *
   *    16   TANG FORM          0.              0.      *
   *    17   SOLV               0.              0.      *
   *    18   STRE               0.              0.      *
   *    19   ITNX               0.              0.      *
   *    20   DISP            200.00             0.      *
   *    21   STRS            200.00             0.      *
```

```
   *   22   NEXT                0.              0.     *
   *   23   END                 0.              0.     *
0ITFC * I-6* Creep in Beam w Plane Stress- S.S. beam*Demo *22/06/91*
  **MACRO INSTRUCTION    1 EXECUTED**  BOUN          V1 =      1.000      , V2 =          0.
0ITFC * I-6* Creep in Beam w Plane Stress- S.S. beam*Demo *22/06/91*
     NODAL B.C.
      NODE       1 B.C.        2 B.C.
         1            0            -1
        11           -1             0
        12            0            -1
        13           -1            -1
        15           -1            -1
        17           -1            -1
        19           -1            -1
        21            1             1
        22           -1             0
        23            0            -1
        33           -1             0
        34            0            -1
        35           -1            -1
        37           -1            -1
        39           -1            -1
        41           -1            -1
        43            1             1
        44           -1             0
        45            0             1
        55            1             0
  **MACRO INSTRUCTION    2 EXECUTED**  FORC          V1 =      1.000      , V2 =          0.
0ITFC * I-6* Creep in Beam w Plane Stress- S.S. beam*Demo *22/06/91*
     NODAL FORCE/DISPL
      NODE       1 FORCE       2 FORCE
        33         0.          200.0
  **MACRO INSTRUCTION    3 EXECUTED**  TANG  FORM    V1 =          0.      , V2 =          0.


  **MACRO INSTRUCTION    4 EXECUTED**  SOLV          V1 =          0.      , V2 =          0.
  **MACRO INSTRUCTION    5 EXECUTED**  DISP          V1 =          0.      , V2 =          0.
0ITFC * I-6* Creep in Beam w Plane Stress- S.S. beam*Demo *22/06/91*
     NODAL DISPLACEMENTS     TIME           0.          (LOAD INCR. NO =    1)
      NODE       1 COORD       2 COORD       1 DISPL       2 DISPL
         1        0.0000      150.0000   -0.3364E-03    0.0000E+00
         2       50.0000      150.0000   -0.3331E-03    0.2319E-03
         3      100.0000      150.0000   -0.3231E-03    0.4592E-03
         4      150.0000      150.0000   -0.3064E-03    0.6778E-03
         5      200.0000      150.0000   -0.2831E-03    0.8828E-03
         6      250.0000      150.0000   -0.2531E-03    0.1070E-02
         7      300.0000      150.0000   -0.2163E-03    0.1235E-02
         8      350.0000      150.0000   -0.1733E-03    0.1374E-02
         9      400.0000      150.0000   -0.1228E-03    0.1480E-02
        10      450.0000      150.0000   -0.6574E-04    0.1555E-02
        11      500.0000      150.0000    0.0000E+00    0.1578E-02
        12        0.0000      112.5000   -0.1659E-03    0.0000E+00
        13       50.0000      112.5000    0.0000E+00    0.0000E+00
        14      100.0000      112.5000   -0.1592E-03    0.4629E-03
        15      150.0000      112.5000    0.0000E+00    0.0000E+00
        16      200.0000      112.5000   -0.1392E-03    0.8903E-03
        17      250.0000      112.5000    0.0000E+00    0.0000E+00
        18      300.0000      112.5000   -0.1059E-03    0.1246E-02
        19      350.0000      112.5000    0.0000E+00    0.0000E+00
        20      400.0000      112.5000   -0.5882E-04    0.1496E-02
        21      450.0000      112.5000    0.0000E+00    0.0000E+00
        22      500.0000      112.5000    0.0000E+00    0.1602E-02
        23        0.0000       75.0000   -0.6652E-19    0.0000E+00
        24       50.0000       75.0000   -0.8894E-19    0.2343E-03
        25      100.0000       75.0000    0.2033E-19    0.4642E-03
        26      150.0000       75.0000    0.4743E-19    0.6851E-03
```

```
        27      200.0000       75.0000    0.2033E-18    0.8928E-03
        28      250.0000       75.0000    0.5997E-18    0.1083E-02
        29      300.0000       75.0000    0.4608E-18    0.1251E-02
        30      350.0000       75.0000    0.6200E-18    0.1391E-02
        31      400.0000       75.0000    0.1897E-18    0.1502E-02
        32      450.0000       75.0000   -0.1736E-18    0.1574E-02
        33      500.0000       75.0000    0.0000E+00    0.1615E-02
        34        0.0000       37.5000    0.1659E-03    0.0000E+00
        35       50.0000       37.5000    0.0000E+00    0.0000E+00
        36      100.0000       37.5000    0.1592E-03    0.4629E-03
        37      150.0000       37.5000    0.0000E+00    0.0000E+00
        38      200.0000       37.5000    0.1392E-03    0.8903E-03
        39      250.0000       37.5000    0.0000E+00    0.0000E+00
        40      300.0000       37.5000    0.1059E-03    0.1246E-02
        41      350.0000       37.5000    0.0000E+00    0.0000E+00
        42      400.0000       37.5000    0.5882E-04    0.1496E-02
        43      450.0000       37.5000    0.0000E+00    0.0000E+00
        44      500.0000       37.5000    0.0000E+00    0.1602E-02
        45        0.0000        0.0000    0.3364E-03    0.0000E+00
        46       50.0000        0.0000    0.3331E-03    0.2319E-03
        47      100.0000        0.0000    0.3231E-03    0.4592E-03
        48      150.0000        0.0000    0.3064E-03    0.6778E-03
        49      200.0000        0.0000    0.2831E-03    0.8828E-03
        50      250.0000        0.0000    0.2531E-03    0.1070E-02
0ITFC * I-6* Creep in Beam w Plane Stress- S.S. beam*Demo *22/06/91*
     NODAL DISPLACEMENTS      TIME          0.          (LOAD INCR. NO =    1)
      NODE       1 COORD      2 COORD       1 DISPL      2 DISPL
        51      300.0000        0.0000    0.2163E-03    0.1235E-02
        52      350.0000        0.0000    0.1733E-03    0.1374E-02
        53      400.0000        0.0000    0.1228E-03    0.1480E-02
        54      450.0000        0.0000    0.6574E-04    0.1555E-02
        55      500.0000        0.0000    0.0000E+00    0.1578E-02
  **MACRO INSTRUCTION    6 EXECUTED**  NOPS          V1 =          0.      , V2 =          0.
  **MACRO INSTRUCTION    7 EXECUTED**  STRE          V1 =          0.      , V2 =          0.
0ITFC * I-6* Creep in Beam w Plane Stress- S.S. beam*Demo *22/06/91*
     INITIAL AVERAGED ELASTIC STRESSES  (TIME = 0)
 ELEMENT TYPE      1-COORD     2-COORD     11-STRESS     22-STRESS     12-STRESS
        1    1      50.0000    112.5000    0.1333E-01   -0.1027E-04    0.1333E-01
        2    1     150.0000    112.5000    0.4001E-01   -0.4051E-04    0.1333E-01
        3    1     250.0000    112.5000    0.6657E-01   -0.1756E-03    0.1333E-01
        4    1     350.0000    112.5000    0.9351E-01   -0.9017E-03    0.1333E-01
        5    1     450.0000    112.5000     0.1181      -0.2617E-02    0.1333E-01
        6    1      50.0000     37.5000   -0.1333E-01    0.1027E-04    0.1333E-01
        7    1     150.0000     37.5000   -0.4001E-01    0.4051E-04    0.1333E-01
        8    1     250.0000     37.5000   -0.6657E-01    0.1756E-03    0.1333E-01
        9    1     350.0000     37.5000   -0.9351E-01    0.9017E-03    0.1333E-01
       10    1     450.0000     37.5000    -0.1181       0.2617E-02    0.1333E-01
  **MACRO INSTRUCTION    8 EXECUTED**  CREP          V1 =          0.      , V2 =          0.
  **MACRO INSTRUCTION    9 EXECUTED**  TOLD          V1 =     0.1000       , V2 =          0.
  **MACRO INSTRUCTION   10 EXECUTED**  NOMC          V1 =          0.      , V2 =          0.
 **  M12  LOOP  = = = NEXT  M22  (NO. OF REPETITION = 200)  ------------------------------
0ITFC * I-6* Creep in Beam w Plane Stress- S.S. beam*Demo *22/06/91*
    NODAL DISPLACEMENTS      TIME   4.0625000          (LOAD INCR. NO =    1)
      NODE       1 COORD      2 COORD       1 DISPL      2 DISPL
         1        0.0000     150.0000   -0.2132E-01    0.0000E+00
         2       50.0000     150.0000   -0.2174E-01    0.1452E-01
         3      100.0000     150.0000   -0.2106E-01    0.2893E-01
         4      150.0000     150.0000   -0.2101E-01    0.4320E-01
         5      200.0000     150.0000   -0.1973E-01    0.5697E-01
         6      250.0000     150.0000   -0.1878E-01    0.7018E-01
         7      300.0000     150.0000   -0.1648E-01    0.8216E-01
         8      350.0000     150.0000   -0.1430E-01    0.9297E-01
         9      400.0000     150.0000   -0.1050E-01    0.1012E+00
        10      450.0000     150.0000   -0.6334E-02    0.1082E+00
        11      500.0000     150.0000    0.0000E+00    0.1088E+00
        12        0.0000     112.5000   -0.9897E-02    0.0000E+00
```

```
        13      50.0000     112.5000   0.0000E+00   0.0000E+00
        14     100.0000     112.5000  -0.9790E-02   0.2903E-01
        15     150.0000     112.5000   0.0000E+00   0.0000E+00
        16     200.0000     112.5000  -0.9159E-02   0.5730E-01
        17     250.0000     112.5000   0.0000E+00   0.0000E+00
        18     300.0000     112.5000  -0.7559E-02   0.8284E-01
        19     350.0000     112.5000   0.0000E+00   0.0000E+00
        20     400.0000     112.5000  -0.4501E-02   0.1027E+00
        21     450.0000     112.5000   0.0000E+00   0.0000E+00
        22     500.0000     112.5000   0.0000E+00   0.1119E+00
        23       0.0000      75.0000  -0.2319E-17   0.0000E+00
        24      50.0000      75.0000  -0.1065E-17   0.1455E-01
        25     100.0000      75.0000  -0.4105E-17   0.2907E-01
        26     150.0000      75.0000  -0.2960E-17   0.4341E-01
        27     200.0000      75.0000  -0.5472E-17   0.5742E-01
        28     250.0000      75.0000   0.4263E-17   0.7073E-01
        29     300.0000      75.0000  -0.9555E-18   0.8315E-01
        30     350.0000      75.0000   0.3786E-17   0.9392E-01
        31     400.0000      75.0000   0.1498E-17   0.1033E+00
        32     450.0000      75.0000   0.1381E-17   0.1091E+00
        33     500.0000      75.0000   0.0000E+00   0.1143E+00
        34       0.0000      37.5000   0.9897E-02   0.0000E+00
        35      50.0000      37.5000   0.0000E+00   0.0000E+00
        36     100.0000      37.5000   0.9790E-02   0.2903E-01
        37     150.0000      37.5000   0.0000E+00   0.0000E+00
        38     200.0000      37.5000   0.9159E-02   0.5730E-01
        39     250.0000      37.5000   0.0000E+00   0.0000E+00
        40     300.0000      37.5000   0.7559E-02   0.8284E-01
        41     350.0000      37.5000   0.0000E+00   0.0000E+00
        42     400.0000      37.5000   0.4501E-02   0.1027E+00
        43     450.0000      37.5000   0.0000E+00   0.0000E+00
        44     500.0000      37.5000   0.0000E+00   0.1119E+00
        45       0.0000       0.0000   0.2132E-01   0.0000E+00
        46      50.0000       0.0000   0.2174E-01   0.1452E-01
        47     100.0000       0.0000   0.2106E-01   0.2893E-01
        48     150.0000       0.0000   0.2101E-01   0.4320E-01
        49     200.0000       0.0000   0.1973E-01   0.5697E-01
        50     250.0000       0.0000   0.1878E-01   0.7018E-01
0ITFC * I-6* Creep in Beam w Plane Stress- S.S. beam*Demo *22/06/91*
     NODAL DISPLACEMENTS     TIME   4.0625000          (LOAD INCR. NO =    1)
      NODE      1 COORD      2 COORD      1 DISPL      2 DISPL
        51     300.0000       0.0000   0.1648E-01   0.8216E-01
        52     350.0000       0.0000   0.1430E-01   0.9297E-01
        53     400.0000       0.0000   0.1050E-01   0.1012E+00
        54     450.0000       0.0000   0.6334E-02   0.1082E+00
        55     500.0000       0.0000   0.0000E+00   0.1088E+00
0ITFC * I-6* Creep in Beam w Plane Stress- S.S. beam*Demo *22/06/91*
     AVERAGED ELEMENT (TOTAL) STRESSES AT TIME =    4.0625000
 ELEMENT TYPE     1-COORD    2-COORD    11-STRESS    22-STRESS    12-STRESS
       1    1     50.0000   112.5000   0.1742E-01  -0.2998E-04   0.1333E-01
       2    1    150.0000   112.5000   0.5183E-01  -0.8514E-04   0.1333E-01
       3    1    250.0000   112.5000   0.8528E-01  -0.2294E-03   0.1333E-01
       4    1    350.0000   112.5000   0.1185      -0.1104E-02   0.1333E-01
       5    1    450.0000   112.5000   0.1483      -0.2909E-02   0.1333E-01
       6    1     50.0000    37.5000  -0.1742E-01   0.2998E-04   0.1333E-01
       7    1    150.0000    37.5000  -0.5183E-01   0.8514E-04   0.1333E-01
       8    1    250.0000    37.5000  -0.8528E-01   0.2294E-03   0.1333E-01
       9    1    350.0000    37.5000  -0.1185       0.1104E-02   0.1333E-01
      10    1    450.0000    37.5000  -0.1483       0.2909E-02   0.1333E-01
          E N D  O F  L O O P  -  N E X T  M12-M22
                                      ******* END OF MACRO EXECUTION *******
                                      END OF JOB
```

APPENDIX F

FE Analysis Of Laterally Loaded Piles

(I). Code FEPILE - I

The computer code FEPILE-I is functionally equivalent to the code ITFECC-A described earlier in Appendix D. A brief description of control parameters, macro commands, and element subroutines are provided below; however, for detailed description of features of the code, preparation of input data, and interpretation of output results, **reference should be made to the user manual** for code FEPILE-I.

Global Control Parameters:

These parameters are identical to those listed earlier in Appendix D for the code ITFECC-A, except that the parameters NAFE, LAGS are not used, and that NSN stands for number of soil reactions which is equal to 1.

Control Macro Commands

These are similar to those listed earlier in Appendix D for the code ITFECC-A, except that the macro command to start the program is PILE.

Macro-type Commands For Mesh Input

These are identical to those listed earlier in Appendix D for the code ITFECC-A.

Programming Macro Commands

Following macro commands are functionally identical to corresponding macro commands listed earlier commands listed earlier in Appendix D under code ITFECC-A: ATDT, AUTO, BOUN, CHNG, CREP, DATA, DISK, DISP, DT, END, FORC, FORM, ITER, ITNX, LOOP, NEXT, NOCR, NOMC, NOPR, NOPS, PLOT, PMAC, PRST, PUNC, RATE, RITE, SDSK, SOLV, TANG, TIME, TOLD, UTAN. Following additional/different macro commands are available:

Command	Description
STPT	Compiles soil/ice reactions with time in a way suitable for plotting.
STRE	Evaluates increments of ice/soil reaction at Gauss points.
STRS	Prints element end forces and ice/soil reactions at specified steps in a time-incrementing loop.

Element Library

Element designation is similar to that in ITFECC-A. The subroutine list is:

Name	Description
ELMT01	Pile element on a spring-dashpot medium.
ELMT02	Linear elastic pile element for creep analysis.

(II). The Alternative Algorithm And Code FEPILE-II

Equation (5.16) can be written as,

$$\chi_k = \sum_e \int_0^1 \{[B]^T EI[B] + [N]^T k_w[N]\} l\, ds\, \mathbf{q}_k + \sum_e \int_0^1 k_w[N]^T[N] l\, ds\, \mathbf{q}_{c,k} + \sum_e \mathbf{F}_{e,k} = \mathbf{0}\ , \qquad (F.1)$$

where $q_{c,k}$ is the vector of nodal creep deformations at time t_k, and all other notations are as defined in Chapter 5 (note: q_k is the vector of total nodal deformations and $[N]$ is given by eqn. 5.13c). For a 2-node element at time t_k:

$$\mathbf{q}_k = \langle w_1,\ \alpha_1,\ w_2,\ \alpha_2 \rangle_k^T\ , \qquad (F.2)$$

$$\mathbf{q}_{c,k} = \langle w_{c1},\ 0,\ w_{c2},\ 0 \rangle_k^T \qquad (F.3)$$

The additional creep displacement at a given node for the $(k+1)$th time step Δt_k is given by,

$$\delta w_{c,k+1} = \dot{w}_{c,k+\theta} \cdot \Delta t_k \qquad (F.4)$$

and

$$\dot{w}_{c,k+\theta} = (1-\theta)\dot{w}_{c,k} + \theta \dot{w}_{c,k+1}\ , \qquad 0 < \theta < 1 \qquad (F.5)$$

The lateral soil/ice reaction at this node is given by,

$$R_k = k_w\{w_k - w_{c,k}\} = k_w[N]\{\mathbf{q}_k - \mathbf{q}_{c,k}\} \qquad (F.6)$$

and creep displacement rate is given by eqn. (5.21). Thus eqn. (F.4) yields,

$$\delta w_{c,k+1} = \Delta t_k \, C_1 \, t^{C_2} \Big\{ (1-\theta) \big[k_w (w_k - w_{c,k}) \big]^b + \theta \big[k_w (w_{k+1} - w_{c,k+1}) \big]^b \Big\} \quad (F.7)$$

By using the Newton-Raphson procedure as described in Chapter 5, the following two equations can be finally obtained to solve for the cumulative iterative correction of the global vector of total deformations $\delta \mathbf{q}^n_{k+1}$ and the cumulative iterative correction of the global vector of creep deformations $\delta \mathbf{q}^n_{c,k+1}$ (where superscript n denotes the nth iterative cycle):

$$\delta \mathbf{q}^n_{c,k+1} = \Delta t_k \, C_1 \, t^{C_2} \Big\{ (1-\theta) \big[k_w (\mathbf{q}_k - \mathbf{q}_{c,k}) \big]^b + \theta \big[k_w (\mathbf{q}^n_{k+1} - \mathbf{q}^n_{c,k+1}) \big]^b \Big\} \quad (F.8)$$

and

$$\begin{aligned} \int_L \big\{ [B]^T EI[B] + [N]^T k_w [N] \big\} dL \, \delta \mathbf{q}^n_{k+1} = & - \int_L \big\{ [B]^T EI[B] + [N]^T k_w [N] \big\} dL \, \mathbf{q}_k \\ & + \int_L \big\{ [N]^T k_w [N] \big\} dL \, \big(\mathbf{q}_{c,k} + \delta \mathbf{q}^n_{c,k+1} \big) - \mathbf{F}_{k+1} = \mathbf{0} \end{aligned} \quad (F.9)$$

The convergence criterion is identical to eqn. (3.53). After covergence, the total deformation vector and creep displacement vector are updated, and solution process proceeds to the next time step. Whenever required, eqn. (F.6) is used to compute lateral ice/soil reactions at a node point. By combining eqns. (F.6) and (5.29), the element end forces for each element are calculated.

Code FEPILE-II was developed by incorporating the above algorithm. Details (macro commands etc.) needed for using this code are provided in the user manual for code FEPILE-II.

APPENDIX G

Expressions For Adfreeze Element

The 6-node adfreeze (interface) element is as shown in Fig. 6.1. The local curvilinear coordinate system is denoted by (s, n), with coordinate s parallel to the interface. The global coordinate system is denoted by (x, y). $[N(s)]$ in eqn. (6.5) is:

$$[N(s)] = \langle\, N_i,\ N_j,\ N_k \,\rangle = \langle\, \frac{(1-s)}{2} - \frac{(1-s^2)}{2},\ \frac{(1+s)}{2} - \frac{(1-s^2)}{2},\ (1-s^2) \,\rangle \quad (G.1)$$

Let the relative displacements at mid-points i, j, k be expressed in local coordinate system as $\mathbf{w}$ and in global coordinate system as $\mathbf{W}$.

$$\mathbf{w} = \langle\, d_{si},\ d_{ni},\ d_{sj}, d_{nj},\ d_{sk}, d_{nk} \,\rangle^T \quad (G.2)$$

$$\mathbf{W} = \langle\, d_{xi},\ d_{yi},\ d_{xj}, d_{yj},\ d_{xk}, d_{yk} \,\rangle^T \quad (G.3)$$

In view of Fig. 6.2,

$$\{\mathbf{w}\} = \begin{bmatrix} \cos\vartheta_i & \sin\vartheta_i & 0 & 0 & 0 & 0 \\ -\sin\vartheta_i & \cos\vartheta_i & 0 & 0 & 0 & 0 \\ 0 & 0 & \cos\vartheta_j & \sin\vartheta_j & 0 & 0 \\ 0 & 0 & -\sin\vartheta_j & \cos\vartheta_j & 0 & 0 \\ 0 & 0 & 0 & 0 & \cos\vartheta_k & \sin\vartheta_k \\ 0 & 0 & 0 & 0 & -\sin\vartheta_k & \cos\vartheta_k \end{bmatrix} \{\mathbf{W}\} \quad (G.4)$$

where ϑ_l is the orientation angle (Figure 6.2) at the l th mid-point. Let the nodal displacement vector be denoted by $\mathbf{a}^e$. Let (u_p, v_p) denote the nodal displacements at the pth local node in the global x and y directions, respectively.

$$\mathbf{a}^e = \langle\, u_1,\ v_1,\ u_2,\ v_2,\ u_3,\ v_3,\ u_4,\ v_4,\ u_5,\ v_5,\ u_6,\ v_6 \,\rangle^T \quad (G.5)$$

$$\{\mathbf{W}\} = \begin{bmatrix} -1 & 0 & 0 & 0 & 0 & 0 & 1 & 0 & 0 & 0 & 0 & 0 \\ 0 & -1 & 0 & 0 & 0 & 0 & 0 & 1 & 0 & 0 & 0 & 0 \\ 0 & 0 & -1 & 0 & 0 & 0 & 0 & 0 & 1 & 0 & 0 & 0 \\ 0 & 0 & 0 & -1 & 0 & 0 & 0 & 0 & 0 & 1 & 0 & 0 \\ 0 & 0 & 0 & 0 & -1 & 0 & 0 & 0 & 0 & 0 & 1 & 0 \\ 0 & 0 & 0 & 0 & 0 & -1 & 0 & 0 & 0 & 0 & 0 & 1 \end{bmatrix} \{\mathbf{a}^e\} \quad (G.6)$$

The relative displacement vector in local coordinates at an arbitrary point on the mid-plane is denoted by $\mathbf{d}$ (see eqn. 6.8). Thus,

$$\{\mathbf{d}\} = \begin{bmatrix} N_i & 0 & N_j & 0 & N_k & 0 \\ 0 & N_i & 0 & N_j & 0 & N_k \end{bmatrix} \{\mathbf{w}\} \quad (G.7)$$

Combining eqns. (G.4), (G.6), and (G.7), the eqn. (6.9) for the 6-node interface element can be obtained, as:

$$\{\mathbf{d}\} = \langle\ -[M]_1,\ -[M]_2,\ -[M]_3,\ [M]_1,\ [M]_2,\ [M]_3,\ \rangle \qquad (G.8)$$

where

$$[M]_l = \begin{bmatrix} N_l \cos\vartheta_l & N_l \sin\vartheta_l \\ -N_l \sin\vartheta_l & N_l \cos\vartheta_l \end{bmatrix} \qquad (G.9)$$

where N_l, ϑ_l are defined for the lth mid-point.

Matrix $[S]^n$ in eqn. (6.23) is dimensionally (2×2), but only one of its components is non-zero, ie.,

$$[S]^n = \begin{bmatrix} H h\, \sigma_s^{h-1}\, t^g & 0 \\ 0 & 0 \end{bmatrix} \qquad (G.10)$$

where all notations are as defined in Chapter 6 (eqn. 6.4). Matrix $[\bar{C}]^n$ in eqn. (6.26) has the form:

$$[\bar{C}]^n = \begin{bmatrix} X & 0 \\ 0 & C_n \end{bmatrix}, \quad \text{where} \quad X = \frac{C_s}{1 + C_s \Delta t_k\, \theta\, H h\, \sigma_s^{h-1}\, t^g} \qquad (G.11)$$

where all notations are defined in Chapter 6.